

INFORMATION TO USERS

This material was produced from a microfilm copy of the original document. While the most advanced technological means to photograph and reproduce this document have been used, the quality is heavily dependent upon the quality of the original submitted.

The following explanation of techniques is provided to help you understand markings or patterns which may appear on this reproduction.

- 1. The sign or "target" for pages apparently lacking from the document photographed is "Missing Page(s)". If it was possible to obtain the missing page(s) or section, they are spliced into the film along with adjacent pages. This may have necessitated cutting thru an image and duplicating adjacent pages to insure you complete continuity.**
- 2. When an image on the film is obliterated with a large round black mark, it is an indication that the photographer suspected that the copy may have moved during exposure and thus cause a blurred image. You will find a good image of the page in the adjacent frame.**
- 3. When a map, drawing or chart, etc., was part of the material being photographed the photographer followed a definite method in "sectioning" the material. It is customary to begin photoing at the upper left hand corner of a large sheet and to continue photoing from left to right in equal sections with a small overlap. If necessary, sectioning is continued again — beginning below the first row and continuing on until complete.**
- 4. The majority of users indicate that the textual content is of greatest value, however, a somewhat higher quality reproduction could be made from "photographs" if essential to the understanding of the dissertation. Silver prints of "photographs" may be ordered at additional charge by writing the Order Department, giving the catalog number, title, author and specific pages you wish reproduced.**
- 5. PLEASE NOTE: Some pages may have indistinct print. Filmed as received.**

Xerox University Microfilms
300 North Zeeb Road
Ann Arbor, Michigan 48106

74-5438

NIIIMURA, Masanobu, 1939-
PLASMA-SOLID INTERFACE ENERGY TRANSPORT.

Colorado State University, Ph.D., 1973
Physics, plasma

University Microfilms, A XEROX Company, Ann Arbor, Michigan

DISSERTATION

PLASMA-SOLID INTERFACE ENERGY TRANSPORT

Submitted by

Masanobu Niimura

In partial fulfillment of the requirements

for the Degree of Doctor of Philosophy

Colorado State University

Fort Collins, Colorado

August, 1973

COLORADO STATE UNIVERSITY

June, 1973

WE HEREBY RECOMMEND THAT THE THESIS PREPARED
UNDER OUR SUPERVISION BY MASANOBU NIIMURA ENTITLED
PLASMA-SOLID INTERFACE ENERGY TRANSPORT BE ACCEPTED
AS FULFILLING IN PART REQUIREMENTS FOR THE DEGREE OF
DOCTOR OF PHILOSOPHY.

Committee on Graduate Work

Daniel F. Edwards

Cyiao-yao Bge

R. J. Churchill
D. W. Chan

Adviser

R. J. Churchill
Head of Department

ABSTRACT OF DISSERTATION

PLASMA-SOLID INTERFACE ENERGY TRANSPORT

This thesis deals with a quantitative investigation of the arc energy transport across a plasma-solid interface. In particular, the effect of external and internal electric fields on the thermal conductivity has been investigated in detail. High electric fields exist at the interface due to large gradients in the plasma parameters causing a departure from the local-thermodynamic-equilibrium (LTE). This situation makes accurate energy transport calculations at the interface difficult. A unified theory to treat the effect of electric fields has been developed by introducing a generalized thermal conductivity and/or generalized correction factor for the conventional thermal conductivity. The radial and axial energy equations including all the important transport terms and the field correction factors have been evaluated. The state of plasma is described by a two-temperature gas in the high electric field regions. A comprehensive formula useful for the calculation of both the anode and cathode fall energy transports has been presented.

This thesis also presents the results of theoretical and experimental investigations of Thomson scattering technique as employed for the plasma-solid interface diagnostics. A direct method to

measure energy transport coefficients from Thomson scattered laser line profiles has been proposed and the results of numerical calculations for the purpose are presented. Experimentally, the distribution of the electron temperature and density of an argon arc plasma at the reduced and atmospheric pressures has been measured by Thomson scattering. From these data the degree of non-LTE and the anode fall energy transfer rate have been calculated. The experimental results are discussed in relation to the theoretical predictions performed in this thesis.

Masanobu Niimura
Plasma Dynamics Laboratory
Electrical Engineering
Department
Colorado State University
Fort Collins, Colorado 80521
August, 1973

ACKNOWLEDGMENTS

This thesis represents the culmination of several years of research at Colorado State University. During the course of this research several individuals aided the program development. First of all, I wish to express my most sincere gratitude to Dr. R. J. Churchill for his invitation to this institution and for his continuous support and guidance throughout the course. Without him this work would never have been completed. It is my pleasure to extend my thanks to Dr. P. W. Chan for his never failing supervision and criticism during the whole experimentation and thesis writing. My thanks also goes to Dr. D. F. Edwards and Dr. C. Y. She for their support of equipments and valuable discussions.

To Dr. J. P. Rybak, Dr. R. P. Davidson and Mr. Marvin Estes, the former fellow staff members at the Plasma Dynamics Laboratory, and to all graduate students in Electrical Engineering, I wish to express my appreciation for the memories of their association that I will always cherish.

To my parents, Mr. and Mrs. Niimura and to my special friend in heart, I send my many thanks for their emotional encouragement and immense love that kept me going when all else failed.

Last but not least, I wish to thank the Chief of Drafting Center, Miss H. Akari for her quick and beautiful drawing of these figures and many useful ideas for the thesis design.

I am further grateful to the U.S.-Japan Binational Fulbright Committee for their Fulbright-Hays Grant. All their combined efforts made my study here possible.

"The research reported in this thesis was supported in part by the Air Force Cambridge Research Laboratories, Air Force Systems Command under Project THEMIS, Contact No. F 19628-70-C-0035, and in part by NSF under Grand No. GK-32473, but the report does not necessarily reflect endorsement by the sponsors."

TABLE OF CONTENTS

<u>Chapter</u>		<u>Page</u>
I INTRODUCTION		1
II ENERGY TRANSPORT IN THE ARC PLASMA (LTE THEORY)		7
A. BASIC ENERGY EQUATIONS AND PROPERTIES OF THE ARC PLASMA		8
B. RADIAL AND AXIAL ENERGY TRANSPORT OF THE ARC PLASMA		83
III VALIDITY OF THE LOCAL THERMODYNAMIC EQUILIBRIUM (LTE) FOR THE ARC PLASMA . .		133
A. COMPLETE AND PARTIAL LTE CRITERIA IN THE STATIONARY, INHOMOGENEOUS ARC		135
B. EXACT, DIRECT SOLUTION OF SAHA- EGGERT EQUATION		150
IV DIAGNOSTICS BY THOMSON SCATTERING . . .		158
A. THEORY OF INCOHERENT SCATTERING BY PLASMAS		160
B. THOMSON SCATTERING EXPERIMENT . . .		188
V ANALYSES AND DISCUSSIONS		245
A. LTE VALIDITY IN THE LOW CURRENT ARGON ARC PLASMA		245
B. HEAT TRANSFER ACROSS THE ARC PLASMA-ANODE INTERFACE		250
C. THOMSON SCATTERING AS A PROBE FOR THE PLASMA-SOLID INTERFACE DIAGNOSTICS		258

<u>Chapter</u>	<u>Page</u>
VI CONCLUSIONS	261
A. SUMMARY	261
B. FUTURE WORK	264
REFERENCES	266
APPENDIX	272
A. COMPUTER PROGRAM OF SAHA-EGGERT EQUATION	273

LIST OF TABLES

<u>Table</u>		<u>Page</u>
IIA1 Electrical Transport Coefficient, γ_E		16
IIA2 Thermal Transport Coefficient, γ_T		25
IIB1 Correction Factor, ϵ		105
IVA1 Frequency Response Function, $F(\vec{k}, \omega)$		165
IVB1 Thomson Scattering Experiment, Past Data		189
IVB2 Scattering Data		219
V A1 Plasma Parameter at the Axis of 15 Amp Argon Arc		247
V A2 Degree of Non-LTE, 15 Amp Argon Arc		248

LIST OF FIGURES

<u>Figure</u>		<u>Page</u>
IIA1	Schematic Energy Balance in a Stationary Plasma	9
IIA2	Equilibrium Concentrations of the Argon Arc Plasma	18
IIA3	Temperature Dependence of the Electrical Conductivity	19
IIA4	Electrical Conductivity to be Compared with Fig. (IIA3)	20
IIA5	Formation of the Plasma Boundaries due to the Saturated Conductivity and the Large Electric Field near the Anode	22
IIA6	Temperature Dependence of the Electron Mean Free Path (MFP) Length	24
IIA7	Temperature Dependence of the Thermal Conductivity	28
IIA8	Conductive Heat Transfer Flux and Dissipation Energy	29
IIA9	Temperature Dependence of the Coefficient of Viscosity	33
IIA10	Temperature Dependence of the Internal Energy	35
IIA11	Temperature Dependence of the Enthalpy	36
IIA12	Temperature Dependence of the Specific Heat	37
IIA13	Temperature Dependence of the Mass Density	39
IIA14	Temperature Dependence of the Prandtl Number	40

<u>Figure</u>		<u>Page</u>
IIA15	Cathode Jet	46
IIA16	Hydrodynamic Flow of a Low Intensity Arc Plasma	48
IIA17	Arc Current Dependence of the Maximum Arc Temperature.	52
IIA18	Sheath Boundaries for Electrically Floating Walls	59
IIA19	Inverse Coulomb Cutoff Parameter, $\lambda (= \Lambda / 12\pi)$, (Eq. II A15-a)	61
IIA20	Radial Electric Field Distribution (Primitive Electric Field) (a) Without Wall, (b) With Wall	64
IIA21	Cathode and Anode Fall Boundaries	67
IIA22	Axial Electric Field Distribution (Actual and Primitive Electric Fields)	73
IIA23	Vector Relations of Primitive and actual Currents with $\vec{\nabla}n$, $\vec{\nabla}T$, and \vec{E}	76
IIA24	Thomson's Graph of Bremsstrahlung Power Density as a Function of Temperature	79
IIB1	Two Calculation Methods of the Conductive Heat Flux, q	88
IIB2	Polygon Curves for $Q_{rad}(S)$ and $\sigma(S)$, where $S = \int \tilde{k}(T) dT$	91
IIB3	Conductive Heat Transfer Flux, $q(\xi)$, where $\xi = r/R$	97
IIB4	Thermionic Current Density Plotted from Schoeck's Experimental Data	100
IIB5	Energy Partition of an Arc with $T = 10^4$ °K for $I = 15$ Amps	104

<u>Figure</u>		<u>Page</u>
IIB6	Axial Energy Transport	113
IIB7	Corrected Energy Partition of an Arc with $T = 10^4$ °K for $I = 15$ Amps	115
IIB8	Stagnation Temperature Profile Near the Anode Surface	120
IIB9	Temperature Boundaries Near the Anode	123
IIB10	Energy Flow Evaluation, Two Different Methods	128
IIIA1	Radial Non-LTE Model	143
IIIA2	Non-LTE by Axial Electric Field	147
IIIA3	Non-LTE by Radial Ambipolar Diffusion	148
IVA1	A Linear Electric Dipole with Moment- Vector along z-axis. $R \gg \lambda/2$	161
IVA2	Scattering Geometry	167
IVA3	Frequency Response of Q_e^0 -Function	170
IVA4	Ion-Acoustic Line Profiles for Collision- less Plasma	172
IVA5-a	Electron-Plasma Line Profiles for Collision Dominated Plasmas	176
IVA5-b	Electron-Plasma Line Profiles for Collision- Landau Damping Competing Plasmas	177
IVA5-c	Electron-Plasma Line Profiles for Landau Damping Dominated Plasmas	178
IVA6	Collision Dominated Plasma Waves: (1) Electron-Plasma Wave (b) Ion-Acoustic Wave	180

<u>Figure</u>		<u>Page</u>
IVA7	Resonance Frequency of Ion-Acoustic Line	181
IVA8	Differential Scattering Cross Section for Collision Dominated Plasmas	182
IVA9	Feynmann Diagrams of Incoherent Scattering Processes	184
IVB1	Limits of Applicability of Thomson Scattering Experiment	191
IVB2	Scattering Volume	192
IVB3	Waveforms of the Power Supply Current and of the Xe-Lamp Light with Giant Pulsed Ruby Laser	200
IVB4	Laser Out-Put Energy	202
IVB5	Xe-Lamp Triggering Module with a Synchrounous Gate Pulse for Pockels' Cell Power Supply	203
IVB6	Power Supply for DC Arcs	204
IVB7	Arc I-V Characteristics	205
IVB8	Photomultiplier	207
IVB9	Tilting Interference Filter	208
IVB10	Narrow Band Interference Filter	209
IVB11	Thomson Scattering in Reduced Pressure	211
IVB12	Scattering Geometry	212
IVB13	Scattering Chamber (Top View)	213
IVB14	Rayleigh and Wall Scattering	215
IVB15	Typical Oscilloscope Trace for 100 Torr Plasma	216

<u>Figure</u>		<u>Page</u>
IVB16	Scattering Intensity Distribution	217
IVB17	Scattering Intensity vs. Electron Energy, z = 5 mm	220
IVB18	Scattering Intensity vs. Electron Energy, z = 3, 2 mm	221
IVB19	Scattering Intensity Vs. Electron Energy, z = 5, 3, 2 mm	222
IVB20	Electron Doppler Broadened Line	224
IVB21	Axial Electron Temperature Distribution	226
IVB22	Thomson Scattering Experiment in Atmospheric Pressure	228
IVB23	Atmospheric Arc Device with Cooling, Gas Feeding and Translational Units	229
IVB24	Rayleigh Scattering from One Atmospheric Argon	230
IVB25	Rejection Raio of IF Filter	231
IVB26	Scattering Intensity Calibration	233
IVB27	Back Ground Intensity Distribution	235
IVB28	Typical Oscilloscope Trace for 1 Atm Plasma	236
IVB29-a	Scattering Intensity Distribution, z = 5 mm	237
IVB29-b	Scattering Intensity Distribution, z = 3 mm	239
IVB29-c	Scattering Intensity Distribution, z = 2 mm	240
IVB30	Electron Density Distribution	241

<u>Figure</u>		<u>Page</u>
IVB31	Anode Temperature Measurement	243
IVB32	Gas Flow Rate Dependence on the Arc Feature	244
VA1	Plasma Parameter Distribution	246
VA2	Anode Fall Potential	251
VA3	Static (or Heavy Particles') Temperature Distribution	252

CHAPTER I

INTRODUCTION

In recent years accurate evaluation of the energy transport across plasma-solid interfaces has become a highly desired subject not only because of the need for the development of practical devices where plasmas are used as light sources, switches, rectifiers, etc., but because of the relatively new interest in designing thermonuclear fusion reactors, magneto-hydrodynamic (MHD) machines and space vehicles where plasmas are in direct contact with walls.

Questions encountered in the process of the design are these: "What is the actual plasma heat transfer rate?" "Will plasma turbulence and instabilities which might occur in the boundary layers adjacent to the wall alter the thermal conductivity to intolerably high levels?" "What about the linear effects of the imposed electric and magnetic fields on the thermal conductivity tensor?" "How does one deal with the problems of non-LTE plasma caused by the external (or imposed) and internal (or electrostatic) fields?" "How would the solution of the energy equation change if the effects of radiation cooling and electromagnetic force of the plasma are taken into account?" All these questions are intrinsically related to the plasma and have not been encountered in the conventional heat transfer study of neutral

gases. The heat transfer rate is also influenced by the conditions of the hydrodynamic flow (turbulent or laminar), the nature of the wall (conductor or insulator, electrically connected or floating) and of the wall surface.

This thesis attempts to answer some of those questions, especially on the linear effects of the external and internal electric fields by the detailed investigation of the arc plasma.

The first Section, IIA of this thesis is devoted to a review of the basic energy balance equation and to the recalculation of some of the important transport coefficients and plasma parameters for the purpose of solving the energy equation accurately. All the electrical, thermal, mechanical and radiative properties of the arc plasma are summarized and the contributions from all the electrons, ions and neutral atoms are taken into account for the calculations. The reason of the recalculation is that presently available basic data for the arc plasma have originated from the German literature, during post-war era (the works have been summarized by Finkelnburg and Maecker¹) and are lacking in accuracy upon comparison with the modern theory.^{2, 3)} The physical bases by which the data are calculated will be explained in some detail so that one can estimate the degree of accuracy of the data. In the next Section, IIB, a theory to treat general energy transport problem of spatially inhomogeneous, radiative and non-LTE plasmas under an external electric field is to be developed. A

generalized thermal conductivity will be introduced to correct the effect of external and internal electric fields on the heat transfer rate. The reduction of the thermal energy flow, especially, due to the internal electric field has been neglected from the practical energy calculations in the past literature¹⁾ but one will find that this thermo-electric correction is important for spatially inhomogeneous plasmas like arcs and at plasma boundaries. Next, the influence of the Joule heating source on the thermal boundary layer thickness is calculated. At the last part of Chapter II, a unified formula by which one can calculate either anode fall-, cathode fall-, or the other boundary layer-energy transfer rate to the solid surface will be presented. The theory throughout Chapter II can be applied either for electrically connected walls (where the charge replenishment occurs) or floating walls. The theory developed in Chapter II will be checked experimentally in Chapter V.

Chapter III deals with the problem of non-LTE (Local Thermo-dynamic Equilibrium) caused by the high external electric field and spatial inhomogeneity (ambipolar diffusion) of the arc. The degree of non-LTE at the main body of the positive column is theoretically predictable and experimentally observable⁴⁾ but not in the vicinity of the electrodes. A formula is suggested for the prediction of non-LTE at the electrode surface. Non-LTE at the periphery due to the ambipolar diffusion has been observed recently⁵⁾ and the theoretical

calculation has just started.⁶⁾ These situations emphasize the necessity of a multi-temperature model for the energy transport calculation and of a new diagnostic technique free from the LTE-condition for the temperature measurement of the individual plasma constituents. Thomson scattering technique is employed in the present research for this reason. Section IIIB presents the computer calculation of Saha-Eggert equation to obtain the exact Saha equilibrium temperature which is to be compared with the solution of the one-temperature model energy balance equation.

Section IVA describes the incoherent scattering theory where DuBois' theory⁷⁾ is extended so that one can measure the transport properties, such as the thermal conductivity and viscosity, directly from the Thomson scattered laser line profiles and the resonance frequency shifts. Section IVB gives a description of the experiment in which the spatial distribution of the electron temperature and density is measured by the Thomson scattering technique. The experimental results are analyzed and discussed in Chapter V toward the following three main subjects:

- A. LTE validity in the low current argon arc plasma.

(How is the degree of non-LTE distributed spatially?)

- B. Heat transfer across the arc plasma - anode interface.

(How much and by which mechanisms is the anode fall energy transferred? Is the thermo-electric correction important?)

C. Thomson scattering as a probe for the plasma-solid interface diagnostics. (Can the Thomson scattering be a very powerful probe in the proximity of the solid surface?)

The conclusion of this thesis is given in Chapter VI, where the main contributions of the present work are summarized and the recommended future works are listed.

Historically, a few researchers such as Thomson (1897, 1935),⁷⁾ Compton (1923)⁸⁾ and Tonks and Langmuir (1929)⁹⁾ referred to the arc energy transfer but very briefly and their interest is restricted to the energy balance at the cathode and positive column. After the long blank era (1932 when Nuclear Physics appeared, to 1946) in the arc physics, numerous literatures of this area have been published in Germany during the post-war era (1946 to 1952) but the situation is as aforementioned. The closest work to the present work has been done by Schoeck (1961),¹⁰⁾ where the anode energy transport is investigated for the high current arc. However problems of non-LTE and thermo-electric correction are disregarded and the plasma parameter has not been measured actually. Present research thus extends the Schoeck's work in both the theoretically and experimentally weak fields. More detailed historical survey will be seen in each separate chapter.

The term, "interface," frequently used in this thesis does not always mean an infinitely thin layer but the dimension depends on the

physical quantity considered. The terminology of interface is used throughout this thesis in the sense equivalent to the sum of boundaries in which the variation of the physical quantities (such as temperature, velocity, pressure, electric field, electron and ion densities, etc.) is large.

All physical quantities and formula in the final form are converted to and shown in the MKS units.



CHAPTER II

ENERGY TRANSPORT IN THE ARC PLASMA

(LTE THEORY)

This chapter presents the theoretical formulation for the calculation of the energy transport in an arc plasma. Section A is a review of the basic energy balance equations and arc properties. In order to solve the energy balance equations correctly, accurate data on the electrical, thermal, mechanical and radiative properties of the plasma are required. Presently available these data are not consistent in accuracy and are often based on the assumptions not well justified. The same is true for the energy transport equations and for the transport coefficients. The relatively long sub-sections in Section A in this chapter are devoted to the summary of accurate data pertinent to both the low current (or low temperature) and high current (or high temperature) atmospheric argon arc plasmas under the assumption of the local thermal equilibrium (LTE).

In Section B the energy balance equations and energy transport vectors are evaluated for several cases. Formulas are presented so that energy partitions of the plasma can be calculated from any type of temperature profiles experimentally obtained.

A. BASIC ENERGY EQUATIONS AND PROPERTIES OF THE ARC PLASMA

[II A1] Basic Energy Equations

Plasma or ionized gas is a conductive medium through which an electric current can flow. The bulk of an arc plasma is heated by the interaction of the current (or electron motion) with the applied electric field. The thermal energy produced in the plasma per unit time per unit volume is

$$\vec{j} \cdot \vec{E} = \sigma E^2, \quad [\text{Watt}/\text{m}^3] \quad (\text{IIA1})$$

where j [Amp/m²] is the current density vector; E [Volt/m] is the local gradient of the externally applied potential; and σ [Ohm⁻¹ m⁻¹] is the electrical conductivity of the plasma medium. This mechanism is called Joule or ohmic heating.

The heat produced in the plasma is transported by (i) conduction due to the diffusional mass flow generated by the temperature, density, and pressure gradients and due to the drift current generated by the externally applied electric field, and by (ii) convection due to the macroscopic motion of the plasma fluid. The net energy transferred per unit time per unit area is expressed by the vector field, \vec{q} in units of [Watt/m²]. If the rotational symmetry is assumed with respect to the axis of the plasma-column, as is the case of the arc plasma, the quantity \vec{q} can be described by two components of the cylindrical coordinates, i.e., the radial (q_r) and the axial (q_z)

components. When the convective heat transfer is negligible, the amount of heat dissipation, D in units of [Watt/m³] can be expressed simply by $\vec{\nabla} \cdot \vec{q}$ and the first energy balance equation will be

$$\begin{aligned}\sigma E^2 &= D_{\text{cond.}} \\ &\equiv \vec{\nabla} \cdot (\vec{q}_r + \vec{q}_z).\end{aligned}\quad (\text{IIA2})$$

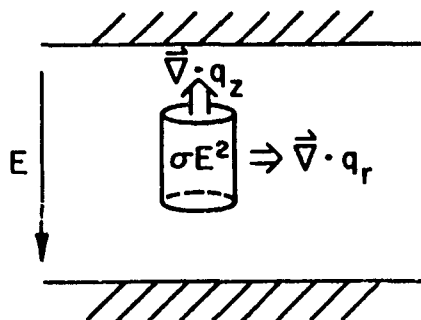


Figure (IIA1) Schematic Energy Balance in a Stationary Plasma.

In the arc plasma, however, there exists considerable hydrodynamic mass flow either due to the natural thermal expansion (buoyancy force), the forced gas flow, or the self-induced electromagnetic pinch force. The macroscopic fluid flow velocity, u [m/sec] can also be described by two components, i.e., the radial (u_r) and axial (u_z) components. The difference, $(\sigma E^2 - \vec{\nabla} \cdot \vec{q})$ will be transported away by the convection:

$$\rho c_p \frac{DT}{Dt} \equiv \rho c_p \left(\frac{\partial T}{\partial t} + \vec{u} \cdot \vec{\nabla} T \right)$$

$$= \sigma E^2 - \vec{\nabla} \cdot \vec{q}. \quad (\text{IIA3})$$

Here, D/Dt is the hydrodynamic derivative of the moving fluid mass with density $\rho [\text{kg}/\text{m}^3]$, specific heat at constant pressure $c_p [\text{Joule}/\text{kg}^{\circ}\text{K}]$, and temperature $T(r + u\Delta t, t + \Delta t) [{}^{\circ}\text{K}]$.

When the conduction mechanism is due to the temperature gradient, the transfer vector \vec{q} is expressed by

$$\vec{q} = -k \vec{\nabla} T, \quad [\text{Watt}/\text{m}^2] \quad (\text{IIA4})$$

where $k [\text{Watt}/\text{m}^{\circ}\text{K}]$ is the coefficient of thermal conductivity.

Notice that for more complete form the other conduction terms such as due to the gradients of density ($\vec{\nabla} n$), pressure ($\vec{\nabla} p$), and potential ($\vec{\nabla} V$) should also be added to the right hand side of Eq. (IIA4).

Substituting Eq. (IIA4) into Eq. (IIA3), one has another energy balance equation where the convection at stationary state ($: \partial T / \partial t \approx 0$) is included:

$$\rho c_p \vec{u} \cdot \vec{\nabla} T = \sigma E^2 + k \nabla^2 T \quad (\text{IIA5})$$

In addition one must take into account the internal energy changes of the plasma due to the friction, the compression, and the radiation:

$$\left. \begin{aligned}
 Q_{\text{friction}} &= -(\tau : \vec{\nabla} u) \\
 &= \eta \phi_u \text{ for Newtonian fluid}^{11)} \\
 Q_{\text{compression}} &= \left(\frac{\partial \ln V}{\partial \ln T} \right)_p \frac{Dp}{Dt} \\
 &= (\vec{u} \cdot \vec{\nabla}) p \text{ for stationary ideal gas}^{11)} \\
 D_{\text{radiation}} &= f(n_e, T_e).
 \end{aligned} \right\} \text{(IIA6)}$$

Here, Q and D are used to distinguish the heating and cooling effects, respectively; τ is the viscous stress tensor which can be expressed by the coefficient of viscosity, $\eta [\text{kg}/\text{m} \cdot \text{sec}]$ and the velocity gradient for Newton Fluids; ϕ_u is the dissipation function expressed by velocity gradients¹¹⁾; p [Newton/m²] is the pressure; and $f(n_e, T_e)$ denotes the radiation cooling effect which is a function of the electron number density, n_e and temperature, T_e of the plasma. Thus adding those terms to Eq. (IIA5), the most general energy balance equation is obtained as

$$\sigma E^2 + \eta \phi_u + (\vec{u} \cdot \vec{\nabla}) p - \vec{\nabla} \cdot \vec{q} - \frac{c}{p} \vec{u} \cdot \vec{\nabla} T - Q_{\text{rad.}} = 0 \quad \text{(IIA7-a)}$$

or

$$\begin{aligned}
 -\vec{\nabla} \cdot \vec{q} + \sigma E^2 - Q_{\text{rad.}} &= \frac{c}{p} \vec{u} \cdot \vec{\nabla} T + \eta \phi_u + (\vec{u} \cdot \vec{\nabla}) p \\
 &= 0 \text{ (when } u = 0).
 \end{aligned} \quad \text{(IIA7-b)}$$

Here, Eq. (IIA7-a) is written so that the heating (positive sign) and cooling (negative sign) mechanisms can be distinguished from each

other, while in Eq. (IIA7-b) the hydrodynamic flow-dependent-terms are separated from the flow-independent-term. When the velocity u is equal to zero (or negligibly small), Eq. (IIA7-b) reduces to the well-known Elenbass-Heller differential equation. These equations will be evaluated in Section IIB for obtaining radial and axial energy transfer rates of the arc plasma. Before this can be done, we need to know the various quantities such as the transport coefficients (σ , k , α , β); hydrodynamic parameters (n , c_p , ρ , u); plasma parameters (n_e , n_i , T_e , T_i); electrical properties (\vec{E} , \vec{j}); and radiative power coefficient ($Q_{rad.}$). The rest of this section is provided for the evaluation of these quantities pertinent to argon arc plasmas.

Electrical and Thermal Energy Transport Coefficients

[II A-1] Electrical Conductivity (σ)

The electrical conductivity of a plasma is a measure of the drift of current carriers (i.e., electrons and ions) under the presence of unit external electric field. The magnitude of the electrical conductivity is given by the ratio of the drift current density (j) to the electric field strength (E):

$$\begin{aligned}\sigma \equiv j/E &= - (en_e \mu_e + z_i n_i \mu_i) \\ &\approx - en_e \mu_e\end{aligned}\quad (\text{IIA8})$$

where μ_e and μ_i are the mobilities of electrons and ions, respectively; and z_i is the charge number of the ion. The approximation in

Eq. (IIA8) is justified because of the heavier mass of ions than that of electrons which contribute predominantly to the electrical conductivity.

The large conductivity of electrons means that the electrons have strong coupling with an external electric field and are Joule heated preferentially compared to the ions. The Joule heat is stored once in the form of the random kinetic energy of electrons:

$$\sigma_e E^2 = \frac{n_e}{2} m \langle \mu_e E \rangle^2 = \frac{3}{2} n_e k_B T_e, \quad [\text{Joule}] \quad (\text{IIA9})$$

where m is the electron mass (9.11×10^{-31} kg), k_B is the Boltzmann constant (1.38×10^{-23} Joule \cdot ${}^\circ\text{K}^{-1}$), and, n_e and T_e are the electron density [m^{-3}] and temperature [${}^\circ\text{K}$], respectively. The electron energy is then transferred to ions and reduced to an equilibrium temperature (thermalization) through the collisions. The energy exchange of the electron-ion (e - i) mutual collisions is such that

$$\frac{dT_e}{dt} = - \frac{T_e - T_i}{\tau_{ei}}, \quad (\text{IIA10-a})$$

where T_i is the ion temperature and τ_{ei} is the e - i thermalization (or relaxation) time given by²⁾

$$\begin{aligned} \tau_{ei} &= \frac{3mMk_B^{3/2}}{8(2\pi)^{1/2} n_i e^4 \ell n} \left(\frac{T_i}{M} + \frac{T_e}{m} \right)^{3/2} \\ &\approx 5.87 \times 10^6 \frac{A_i}{n_i \ell n \Lambda} T_e^{3/2} \quad [\text{sec}] \end{aligned} \quad (\text{IIA10-b})$$

where A_i is the ratio of ion mass to proton mass ($A_i = 39.95$ for Argon); n_i is the ion density in [m⁻³]; Λ is the Coulomb cut off parameter to be described later and $\ln \Lambda = 3 \sim 5$ for atmospheric high temperature arcs. Thus the relationship between the Joule heating energy and the plasma temperatures is given by

$$\sigma_e E^2 = \kappa \frac{3}{2} n_e k_B (T_e - T_i) / \tau_{ei}, \quad (\text{IIA10-c})$$

where κ is the energy transport coefficient of e-i collision ($\approx 2m/M$).

The electron conductivity of Eq. (IIA8) can be further written as

$$\begin{aligned} \sigma_e &\equiv -en_e \mu_e = -e^2 n_e / m v_e \\ &= \epsilon_0 \omega_p^2 / \nu_e = (\epsilon_0 / 2\pi) \omega_p^2 \tau_e, \quad [\text{Ohm}^{-1} \text{m}^{-1}] \end{aligned} \quad (\text{IIA11})$$

where $\omega_p = (n_e e^2 / \epsilon_0 m)^{1/2}$ [rad/sec] is the plasma frequency ($\epsilon_0 = 9.954 \times 10^{-12}$ F/m); ν_e [rad/sec] is the electron radial collision frequency which is the sum of the collision frequencies between electron-ion (ν_{ei}), electron-neutral (ν_{en}) and electron-electron (ν_{ee}); and $\tau_e (= 2\pi / \nu_e)$ is the corresponding relaxation time which is related to the mean free path (MFP) length of the electron by

$$\begin{aligned} l_e &\equiv \tau_e \langle \nu_e \rangle = \tau_e \left(\frac{3k_B T_e}{m} \right)^{1/2} \\ &= (n_i Q_{ei} + n_n Q_{en} + n_e Q_{ee})^{-1}, \quad [\text{m}] \end{aligned} \quad (\text{IIA12})$$

where the Q_e 's are collisional cross-sections between various plasma constituents.

According to Spitzer²⁾ the conductivity due to the e-i collision is given by

$$\begin{aligned}\sigma_{ei} &= 2(2k_B T_e)^{3/2} \gamma_E^{3/2} m^{\frac{1}{2}} z e^2 c^2 \ln \Lambda [\text{emu}] \\ &= (3.80 \times 10)^{-1} \gamma_E^{3/2} T_e^{-1} (\ln \Lambda)^{-1}, [\text{Ohm}^{-1} \text{m}^{-1}] \quad (\text{IIA13})\end{aligned}$$

where Λ is the Coulomb cutoff parameter:

$$\begin{aligned}\Lambda &= \frac{3}{2(\pi)^{\frac{1}{2}}} \cdot \frac{(k_B T_e)^{3/2}}{z e^3 n_e^{\frac{1}{2}}} \\ &= \frac{12\pi}{\lambda} = \frac{1.23 \times 10^7 T_e^{3/2}}{n_e^{\frac{1}{2}}} [\text{Dimensionless}] . \quad (\text{IIA14})\end{aligned}$$

Here the inverse Coulomb cutoff parameter,

$$\lambda = k_D^3 / n_e . \quad (\text{IIA15-a})$$

In Eq. (IIA13),

$$z = \sum_i n_i z_i^2 / n_e \quad (\text{IIA15-b})$$

is the average charge number summed over all positive ions of species i; and γ_E is the electrical transport coefficient for correcting the deviation of the real plasma from Lorenz gas model ($z = \infty$),

the values of which have been tabulated by Spitzer and Härm¹³⁾ for a range of average charge number z:

Table (IIA1)

Electrical Transport Coefficient, γ_E

Ionic Charge, z	1	2	4	16	∞
γ_E	0.5816	0.6833	0.7849	0.9225	1.000

Since $\tau_{ee} / \tau_{ei} = m/M$ (M is the ion mass)¹⁴⁾, from Eq. (IIA11)

$$\sigma_{ee} = \frac{m}{M} \sigma_{ei} \cdot [\text{Ohm}^{-1} \cdot \text{m}^{-1}] \quad (\text{IIA16})$$

As one knows that $Q_{en} \approx 4 \times 10^{-20} [\text{m}^2]$ ¹⁴⁾ (argon gas atomic radius at 1 eV), then from Eqs. (IIA11) and (IIA12)

$$\begin{aligned} \sigma_{en} &= \omega_p^2 / 8\pi^2 v_e n_n Q_{en} \\ &= \frac{10^{16} e^2 (n_e/n_n)}{8\pi c^2 m^{1/2} (3k_B T_e)^{1/2}} [\text{emu}] \\ &= 1.45 \times 10^7 \left(\frac{n_e}{n_n}\right) T_e^{-1/2} [\text{Ohm}^{-1} \text{m}^{-1}], \end{aligned} \quad (\text{IIA17})$$

where n_n is the number density of neutrals. The total conductivity is given by

$$\sigma_e = \sigma_{ei} + \sigma_{ee} + \sigma_{en}. \quad (\text{IIA18})$$

Eq. (IIA18) can be evaluated from Eqs. (IIA13), (IIA16) and (IIA17) for an atmospheric argon arc plasma as a function of the electron temperature by assuming complete thermodynamic equilibrium and the result is shown in Fig. (IIA3). For the calculation of Fig. (IIA3), the equilibrium concentrations of argon arc plasma, Fig. (IIA2) has been calculated by using exact Saha-Eggert equation which will be explained in Chapter III.

Fig. (IIA3) is to be compared with Fig. (IIA4) which has been calculated by Busz and Finkelnberg¹⁵⁾ and which includes only the e-i contribution disregarding γ_E and $\ln\Lambda$ terms. Fig. (IIA4) is used by Shoeck¹⁰⁾ for the estimation of the temperature (T_ϵ) at the edge of ϵ -layer (anode fall space). The critical temperature at which the conductivity becomes almost insensitive by the temperature appears at approximately twice high temperature according to the exact calculation. This means that for the plasma whose maximum electron temperature is less than 20,000 °K, there should be no well-defined free-stream (or saturated) temperature, T_s . Thus the thermal boundary layer thickness δ_t , estimated by Shoeck for a plasma with the maximum temperature 12,000 °K, cannot be well determined for plasmas with temperature less than 20,000 °K, following the result of exact calculation.

This situation may be understood in Fig. (IIA5). Imagine two types of plasma equilibrium temperature profiles in an open space

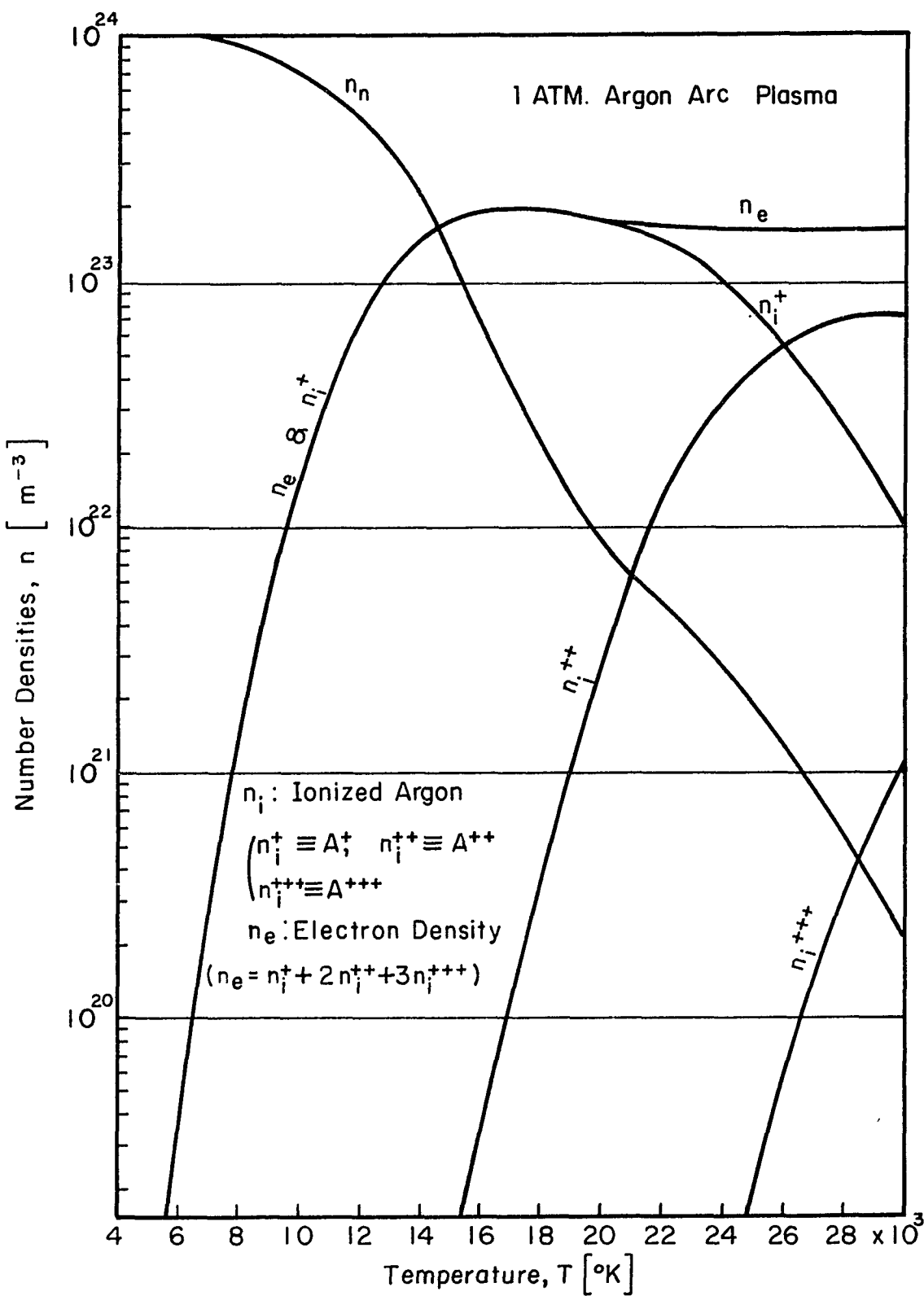


Fig. (II A 2) Equilibrium Concentrations of the Argon Arc Plasma

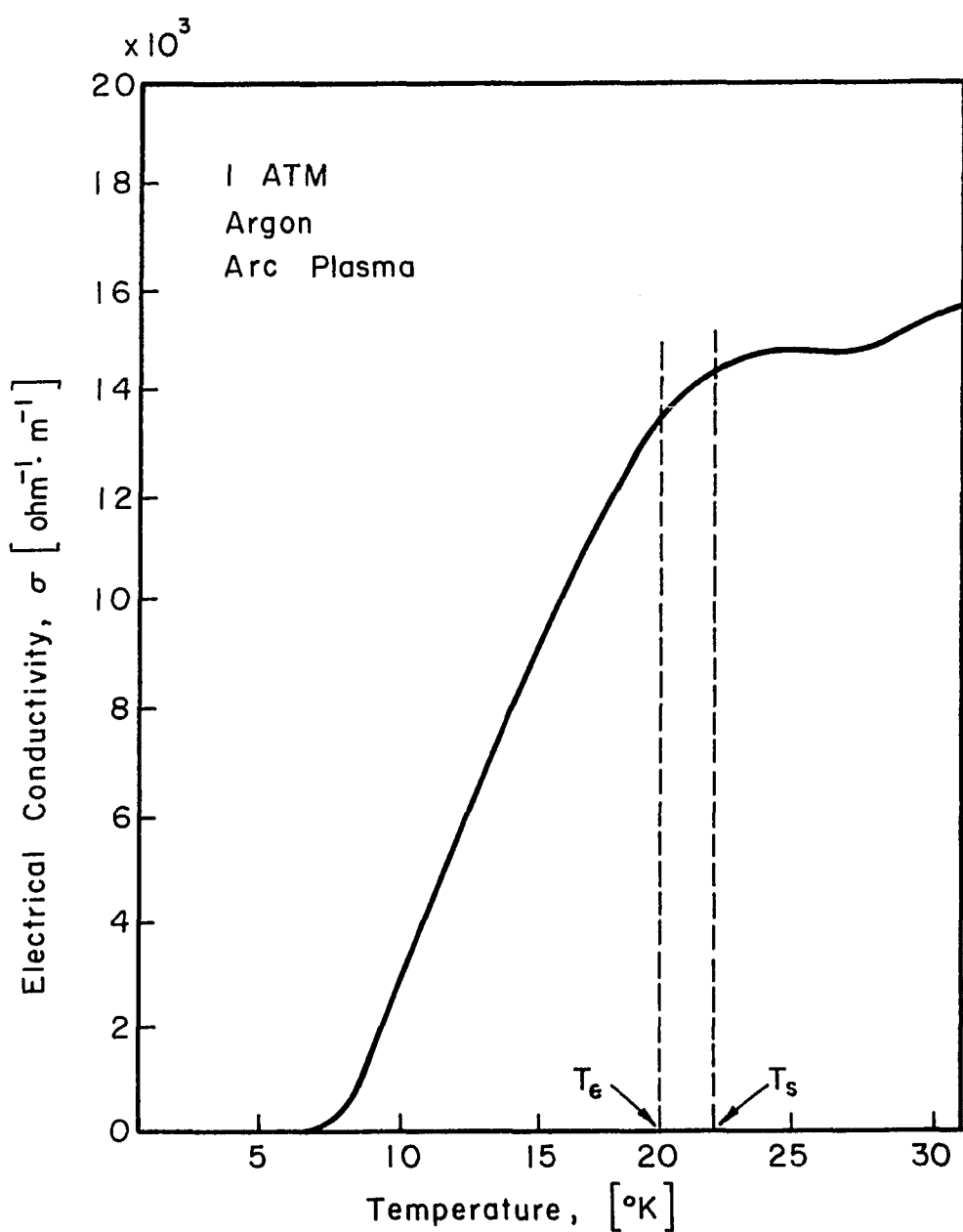


Fig. (II A 3) Temperature Dependence of the Electrical Conductivity.

T_s : Saturation Temperature

T_ϵ : Temperature at the Edge of ϵ -layer

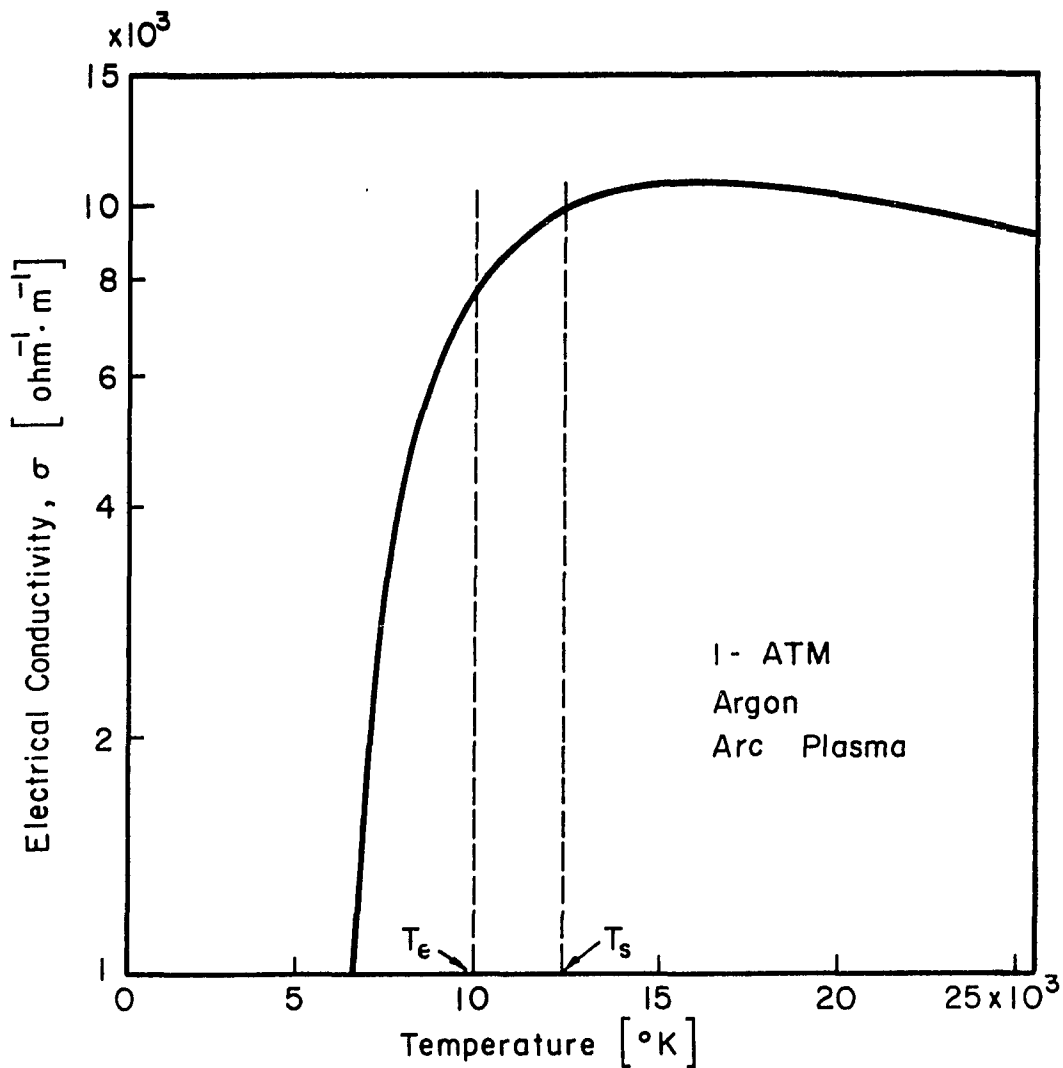


Fig. (II A 4) Electrical Conductivity to be Compared with Fig.(IIA 3).
[After Busz - Peukert and Finkelnburg]¹⁵⁾

T_s : Saturation Temperature

T_ϵ : Temperaturer at the Edge of ϵ - layer

such as shown in (a). Profile (1) has temperature higher than T_s ($\approx 22,000^{\circ}\text{K}$); while the maximum temperature of the profile (2) has temperature less than T_s . According to Fig. (IIA3) the conductivity is insensitive for temperature larger than T_s . Therefore the conductivity distribution shows a flat top for a high temperature plasma, profile (1) but not for a low temperature plasma, profile (2) as shown in (b). If the electric field distribution caused by the anode effect is as shown (c), the electron temperature distribution will be like (d) because of the strong coupling between electrons and electric field ($T_e \propto \sigma_e E^2$). The gas or ion temperature profile (T_g) will be like (e) which is similar to the conductivity profile (b) because of the weak coupling of the ions with electric field. For both T_e and T_g no temperature boundary thickness (δ_t) can be defined for the low temperature plasma as shown by curves (2) in (d) and (e). The anode fall space (ϵ -layer) can be defined from the T_e measurement for both cases of low and high temperature plasmas as shown (d).

Near the electrode an appreciable gradient of the electric potential exists due to the charge non-neutrality at the neighbor. The fall space (ϵ -layer in the previous terminology) has a thickness of the order of one MFP-length of electrons¹⁶⁾ and the electrons gain energy by $eE\ell_e$ during the passage of the fall space. The ℓ_e 's can be calculated using Eqs. (IIA11) through (IIA17) as

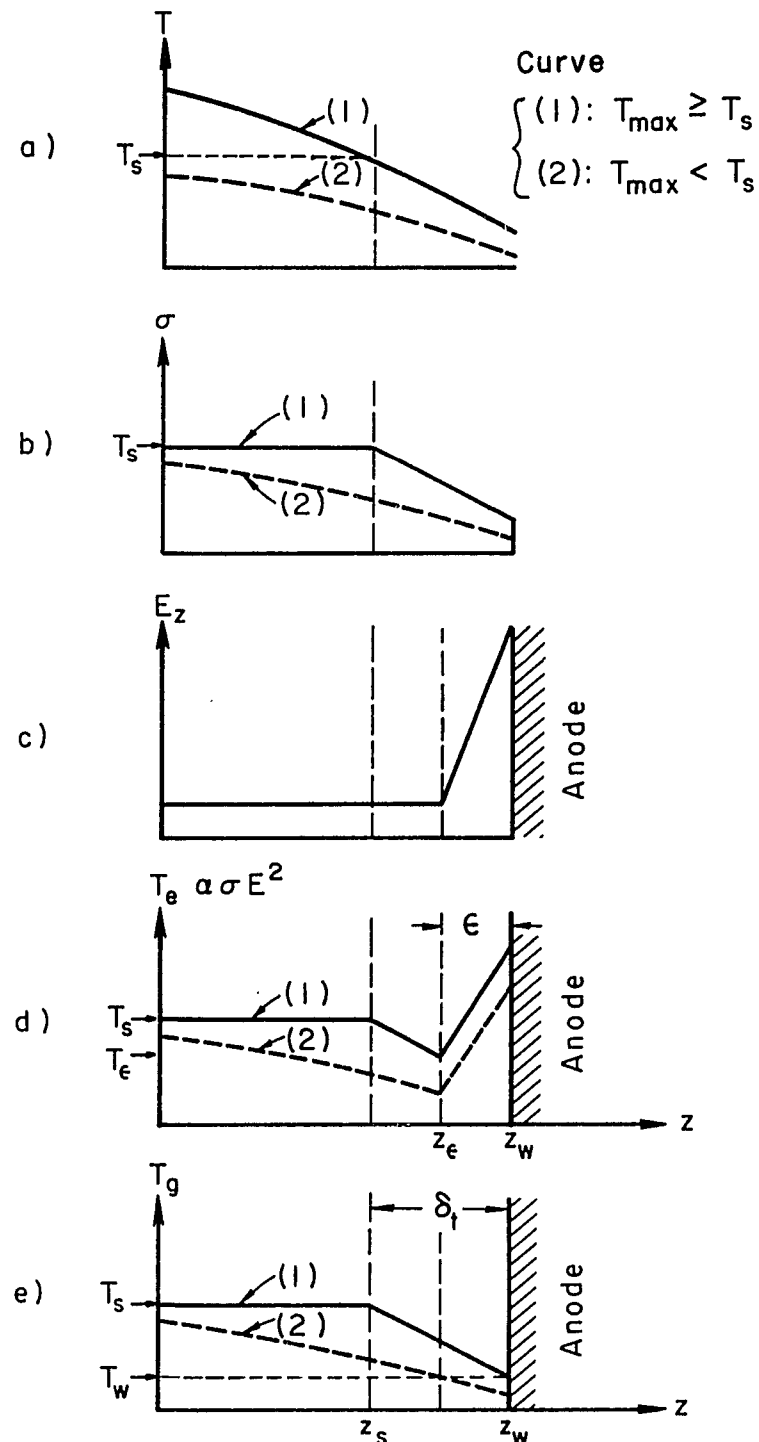


Fig. (II A5) Formation of the Plasma Boundaries due to the Saturating Conductivity and Sheath Electric Field.

T_s : Conductivity Saturation Temperature

T_ϵ : Temperature at the Edge of ϵ -layer

$$\begin{aligned}
 \ell_{ei} &\equiv (v_e / \epsilon_0 \omega_p^2) \sigma_{ei} \\
 &= \gamma_E (3k_B T_e)^2 / 8 \times 0.714 \pi n_i z c^2 e^4 \ell n \Lambda \\
 &= 1.61 \times 10^{10} \gamma_E T_e^2 / n_i z \ell n \Lambda \quad [m], \tag{IIA19}
 \end{aligned}$$

$$\ell_{ee} = \frac{m}{M} \ell_{ei} \quad [m], \tag{IIA20}$$

and

$$\begin{aligned}
 \ell_{en} &\equiv (n_n Q_{en})^{-1} \\
 &= 2.5 \times 10^{19} / n_n \quad [m], \text{ for } k_B T \approx 1 \text{ eV.} \tag{IIA21}
 \end{aligned}$$

The total electron MFP, $\ell_e = \ell_{ei} + \ell_{ee} + \ell_{en}$ is evaluated and the result is shown in Fig. (IIA6) as a function of the equilibrium temperature (T).

According to Fig (IIA6), $\ell_e \approx 6 \mu\text{m}$ at $T_e = 10^4 \text{ }^\circ\text{K}$. This is comparable to the experimental evidence of $2 \mu\text{m}$ obtained by Block and Finkelnburg.¹⁶⁾ The determination of the precise thickness of the ϵ -layer is not so important for the heat transfer calculation as will be seen in Section IIB because the energy transport due to the electron flow which forms the arc current does not depend on the ϵ -layer thickness and because the energy transport due to the temperature gradient does not depend on the electron temperature but on the ion or heavy particle's static temperature whose gradient size is δ_t .

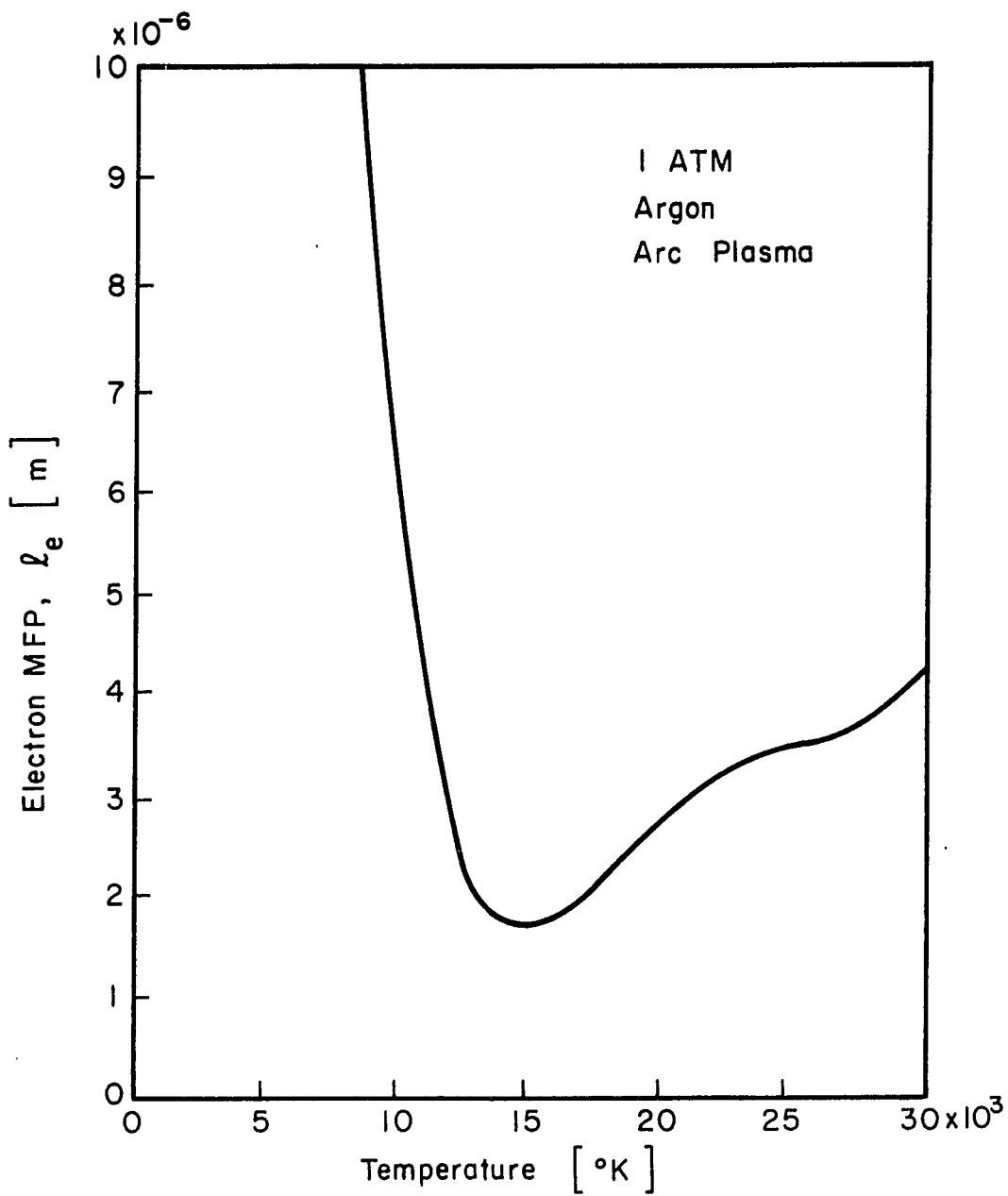


Fig. (II A 6) Temperature Dependence of the Electron Mean-Free-Path (MFP) Length. [After Olsen]³³⁾

[IIA-2] Thermal Conductivity (k)

There exists a close similarity between the thermal conductivity (k) and the electrical conductivity (σ) since the field vectors of the current density (\vec{j}) and the heat transfer flux (\vec{q}) are coupled through the electric field \vec{E} and the thermal gradient $\vec{\nabla}T$:

$$\left. \begin{aligned} \vec{j} &= \sigma \vec{E} + \alpha \vec{\nabla} T \\ \vec{q} &= -\beta \vec{E} - k \vec{\nabla} T, \end{aligned} \right\} \quad (\text{IIA22})$$

where $\alpha = 1.4 \sigma k_B / 2e$ and $\beta = \alpha T + 5\sigma k_B T / 2e = 3.2\sigma k_B T / e$.^{2, 13)}

Note that here again $\vec{\nabla}n$ and $\vec{\nabla}p$ are assumed to be zero.

According to Spitzer,^{2, 3)} the thermal conductivity due to electron-ion collision is given by

$$\begin{aligned} k_{ei} &= 20 \left(\frac{2}{\pi} \right)^{3/2} \frac{k_B (k_B T_e)^{5/2}}{m_e^{1/2} c e z \ell \ln \Lambda} \gamma_T \\ &= 1.95 \times 10^{-9} \gamma_T T_e^{5/2} z^{-1} (\ln \Lambda)^{-1} [\text{Watt/m/oK}] \quad (\text{IIA23}) \end{aligned}$$

where Λ is given by Eq. (IIA14) and γ_T is the correction term for the finite ion charges and is given by Spitzer and Härn¹³⁾ for a range of average charge number z :

Table (IIA2)

Thermal Transport Coefficient, γ_T

Ion Charge, z	1	2	4	16	∞
γ_T	0.2252	0.3562	0.5133	0.7907	1.000

If the ratio of Eq. (IIA23) to Eq. (IIA13) is taken,

$$\begin{aligned} k_{ei}/\sigma_{ei} &= 10 \frac{\gamma_T}{\gamma_E} \left(\frac{k_B}{e} \right)^2 T \\ &\approx \frac{10}{3} \left(\frac{k_B}{e} \right)^2 T \text{ for } z = 1 \end{aligned} \quad (\text{IIA24})$$

This can be compared with well-known Wiedemann-Frantz Law which states the ratio of thermal conductivity to electrical conductivity in metals:

$$k/\sigma = \frac{\pi^2}{3} \left(\frac{k_B}{e} \right)^2 T. \quad (\text{IIA25})$$

The close similarity between Eqs. (IIA24) and (IIA25) implies that fully ionized plasmas behave like metals in the electrical and thermal properties. Therefore the electron thermal conductivity can be calculated from the electron electrical conductivity as

$$\begin{aligned} k_e &= k_{ei} + k_{ee} + k_{en} \\ &= 7.45 \times 10^{-8} (\gamma_T/\gamma_E) T(\sigma_{ei} + \sigma_{ee} + \sigma_{en}) \\ &= 2.81 \times 10^{-8} T(\sigma_{ei} + \sigma_{ee} + \sigma_{en}) \text{ for } z = 1. \end{aligned} \quad (\text{IIA26})$$

Therefore, the graph (k_e/T) vs. T curve is essentially the same shape to the curve σ_e vs. T . The ion contribution to the thermal conductivity, (k_i) is small because the corresponding electrical conductivity (σ_i) is small.

The total k for rare gases is given by

$$k = k_e + k_n + k_I, \quad (\text{IIA27})$$

where k_n and k_I are contributions from neutral atoms and from diffusion of ionization energy generated by the recombination, respectively.

The value of k_n and k_I are given by¹⁷⁾

$$\begin{aligned} k_n &= \frac{0.661}{10^9} \frac{k_B}{Q_n} \left(\frac{k_B T}{m} \right)^{\frac{1}{2}} [\text{emu}/10^9] \\ &= 8.95 \times 10^{-3} T^{\frac{1}{2}}, \text{ for Argon } [\text{Watt}/\text{m}^\circ\text{K}] \end{aligned} \quad (\text{IIA28})$$

and

$$\begin{aligned} k_I &= ID \frac{d}{dT} \frac{1}{(p/K_p + q)^{\frac{1}{2}} + 1} \\ &= 2.63 \times 10^{-2} I Y_E T_e^{\frac{1}{2}} (z \ln \Lambda)^{-1}, \quad [\text{Watt}/\text{m}^\circ\text{K}] \end{aligned} \quad (\text{IIA29})$$

where I is the discharge current, D the diffusion constant, p the pressure, and K_p the equilibrium constant.¹⁷⁾

Fig. (IIA7) shows the result of the calculation of Eqs. (IIA26), and (IIA28) for an argon plasma assuming complete thermal equilibrium. Fig. (IIA7) can also be regarded as a plot of the heat transfer flux (q) of a plasma with constant temperature gradient, since $\vec{q} = -k\vec{\nabla}T$. The graph can be roughly divided into three regions, i.e., (1) constant k regions for $T < T_1$ and $T > T_2$ and logarithmically linear k

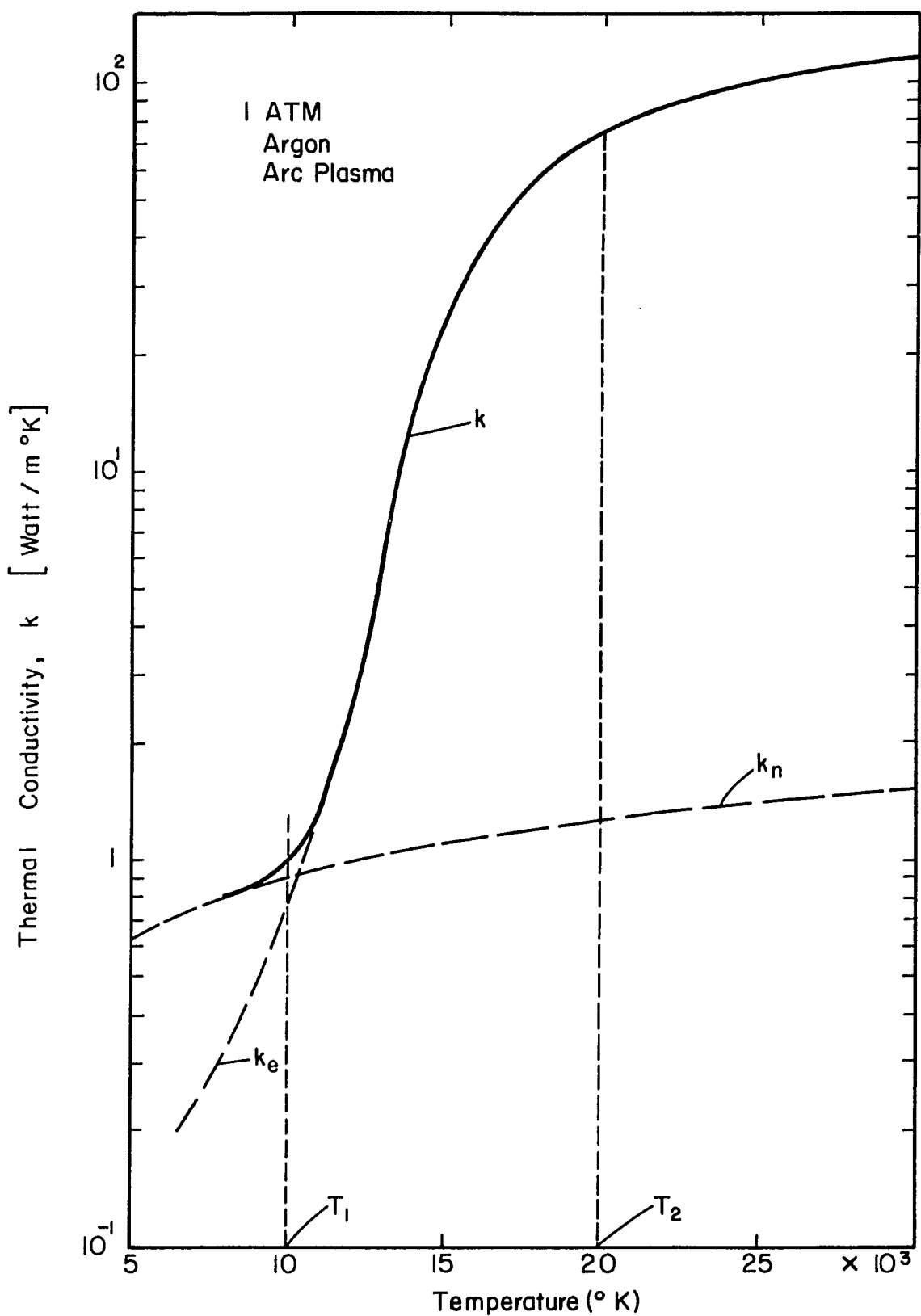


Fig (II A7) Temperature Dependence of Thermal Conductivity

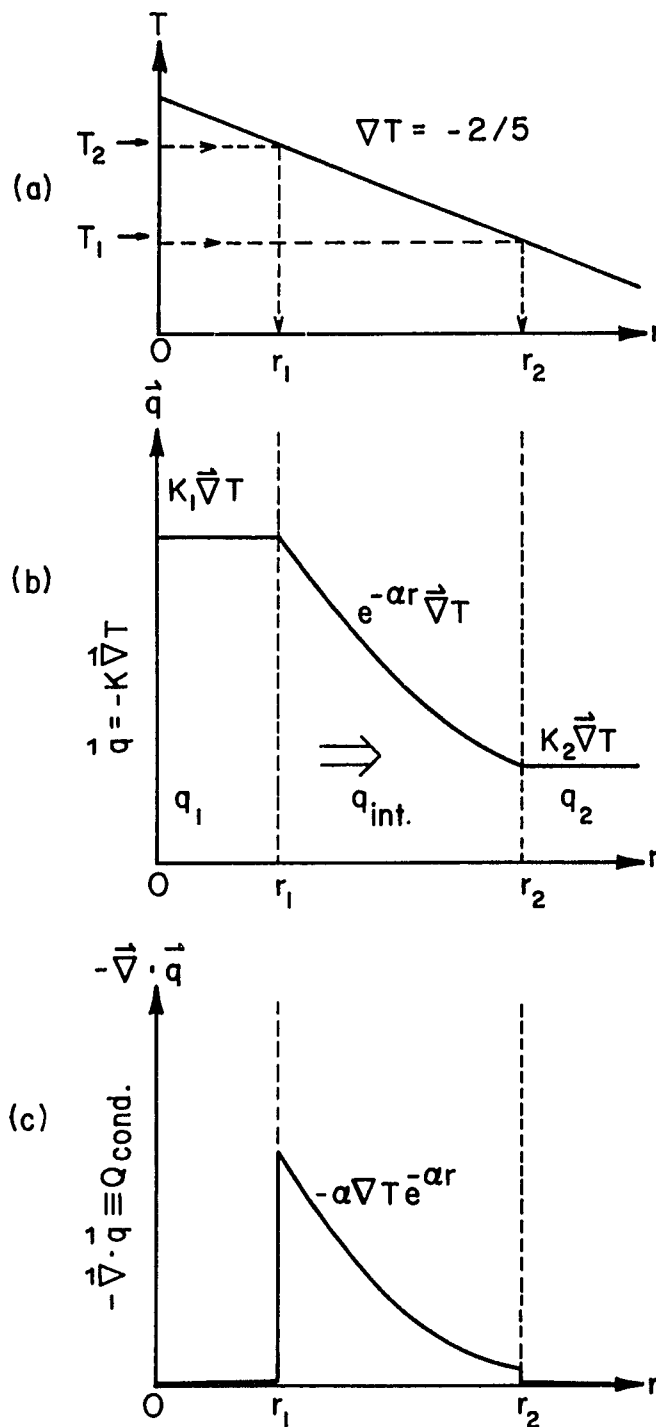


Fig. (II A 8) Conductive Heat Transfer Flux and Internal Dissipation Energy Change in the Radial Direction (r).
See Fig. (II A 7) for T_1 and T_2

region for $T_1 < T < T_2$. Fig. (IIA8) illustrates the effect of the heat conductivity on the heat transfer flux. If a plasma had a constant temperature gradient with respect to the radius (r), as shown in Fig. (IIA8-a), the heat transfer flux will change as shown in Fig. (IIA8-b) because of the constant k in the very high ($T > T_2$) and very low ($T < T_1$) temperature regions. Therefore the internal energy-change due to the conduction, $D_{\text{cond.}} = \vec{\nabla} \cdot \vec{q}$ will become as shown in Fig. (IIA8-c). The internal energy increases by conduction in the radius between r_1 and r_2 where the ionization process is active.

Near the solid surface the absolute magnitude of the conductive heat transfer is small. Therefore the net transfer rate of the heat, from plasma to the wall by conduction, can be approximated as

$$\begin{aligned} q_{p \rightarrow w} &= q_1 + q_{\text{int.}} + q_2 \\ &\approx q_1 + q_{\text{int.}}, \text{ when } T_{\max} \geq 20,000 \text{ } ^\circ\text{K} \\ &\approx q_{\text{int.}} = e^{-\alpha r} \nabla T, \text{ when } T_{\max} < 20,000 \text{ } ^\circ\text{K}. \quad (\text{IIA30}) \end{aligned}$$

Here q_1 , $q_{\text{int.}}$ and q_2 are the transfer flux in the three regions as shown in Fig. (IIA8-b); and α in Eq. (IIA30) is the slope of the thermal conductivity, $k(T)$.

Fluiddynamic and Thermodynamic Quantities

[IIA3] Coefficient of Viscosity (η)

The heat due to the internal friction (or viscous stress) force of plasma fluid is proportional to the coefficient of viscosity η . The viscosity of a fully ionized plasma has been analyzed by Braginskii.³⁾ In the absence of a magnetic field the coefficient of viscosity is given by

$$\eta_{i,e} = \frac{0.406 m_i e^{\frac{1}{2}} (k_B T_{i,e})^{5/2}}{e^4 \ln \Lambda}, \quad (\text{IIA31})$$

where $m_e \equiv m$ (electron mass) and $m_i \equiv M$ (ion mass). Apparently the η_e is negligible compared with the η_i ; the viscosity is due primarily to the positive ions:

$$\begin{aligned} \eta &= \eta_i + \eta_e \equiv \eta_i (1 + \sqrt{\frac{m}{M}}) \\ &\approx 7.5 \times 10^{-18} \frac{M}{m} \frac{T^{5/2}}{\ln \Lambda}. \quad [\text{kg/m} \cdot \text{sec}] \end{aligned} \quad (\text{IIA32})$$

($M/m = 7.3 \times 10^4$ for Argon). The plasma viscosity increases with increasing temperature according to Eq. (IIA32) at the high ionization (a_i , degree of ionization ≈ 1) region just as for low density neutral gases. In the low ionization region ($a_i < 10^{-1}$), where neutral-neutral ($n - n$) collisions are the predominant mode of the momentum transfer, the viscosity increases with increasing temperature following the next expression:¹⁷⁾

$$\eta_n = 0.176 \frac{1}{Q_n} (Mk_B T)^{\frac{1}{2}}, \quad (\text{IIA33})$$

where Q_n is the n - n collisional cross section for viscosity. In the transient region ($10^{-1} \leq a < 1$), however, the viscosity decreases with increasing temperature (like liquids) because the newly created electrons and ions in the gas obstruct the transfer of momentum. After fully ionized, the ion-electron system behaves like low density neutral gases. The solid line in Fig. (IIA9) is a theoretical curve calculated by Cambel¹⁸⁾ following the above mentioned text and agrees quite well with the experimental data obtained by Schreiber.¹⁹⁾ Using this data the dominant term of the frictional power density (Eq. IIA6) can be expressed for a plasma at $T \approx 10^4$ °K as

$$\begin{aligned} Q_{\text{fric}} &= \frac{n}{g_c} \left(\frac{du_r}{dz} \right)^2 \\ &\approx 2 \times 10^{-4} \left(\frac{du_r}{dz} \right)^2, \quad [\text{Watt/m}^3] \end{aligned} \quad (\text{IIA34})$$

where g_c is the dimensional conversion factor set equal to 1 [m/sec²]. This is to be compared with the Joule heating power density. For $T \approx 10^4$ °K, $\sigma = 3 \times 10^3$ ohm⁻¹ m⁻¹ (from Fig. IIA3) and $E \approx 10^3$ V/m (from Ref. 16);

$$\begin{aligned} Q_j &= \sigma E^2 \\ &\approx 3 \times 10^9. \quad [\text{Watts/m}^3] \end{aligned} \quad (\text{IIA35})$$

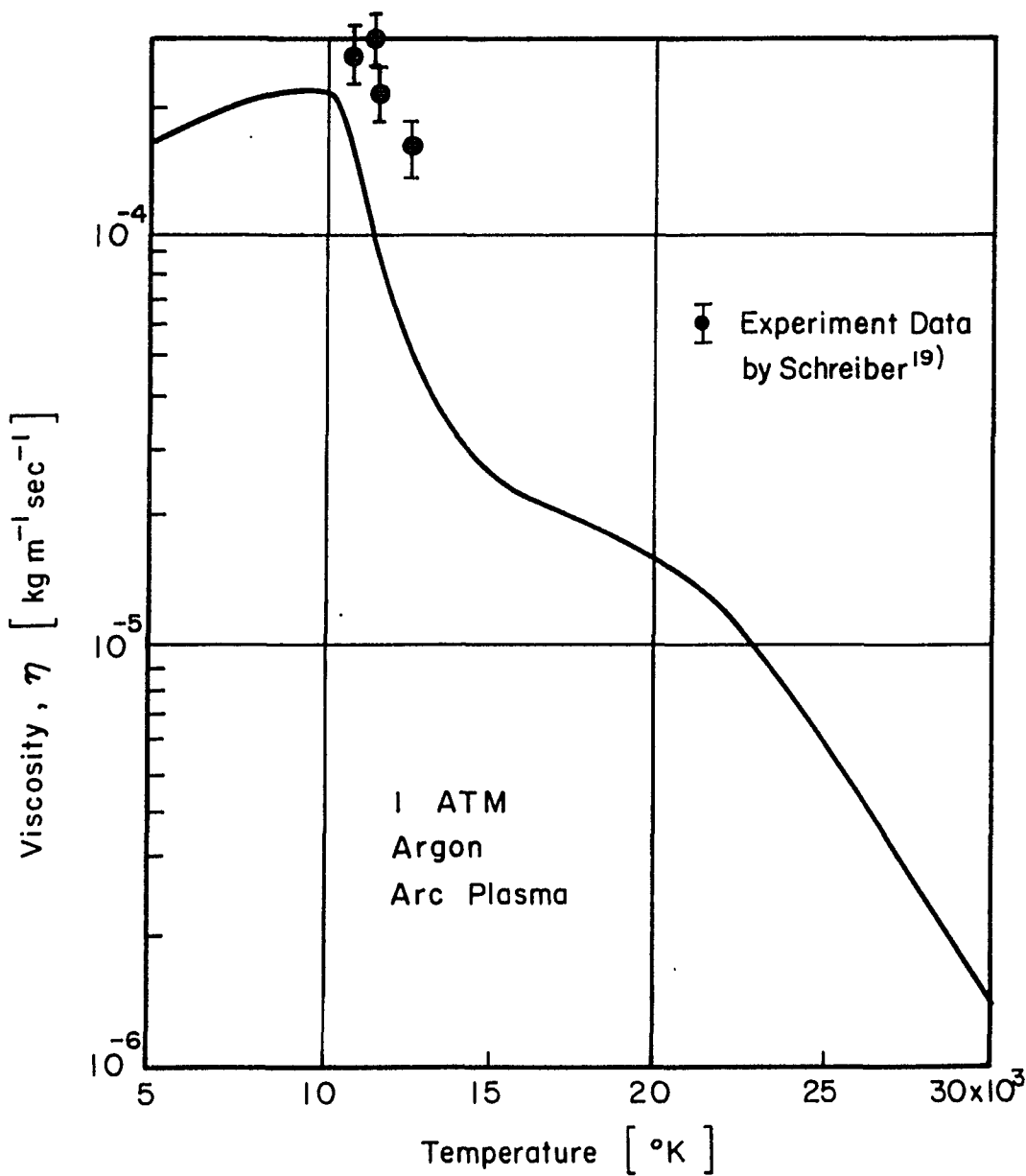


Fig. (II A9) Temperature Dependence of the Coefficient of Viscosity. [After Cambel]¹⁸⁾

Therefore Q_{fric} is smaller than Q_J unless $du_r/dz \geq 3.7 \times 10^6$ [sec⁻¹], which is very unlikely as will be seen later on.

[II A-4] Specific Heat (c_p), Enthalpy (H) and Internal Energy (U)

The specific heat at constant pressure is given by

$$c_p = \left(\frac{\partial H}{\partial T} \right)_p [\text{J/kg } {}^\circ\text{K}], \quad (\text{IIA36})$$

where H is the enthalpy or heat content of a system. The first law of thermodynamics says that

$$H = U + pV, \quad (\text{IIA37})$$

where U is the internal energy and pV represents the external work.

The dependences of U and H of an argon arc plasma with the respect to the temperature are shown in Figs. (IIA10) and (IIA11), respectively.¹⁸⁾ Thus the specific heat varies with temperature in the manner shown in Fig. (IIA12).¹⁸⁾ If $\partial V / \partial T$ (V is the volume) is negligible,

$H = (5/2) k_B T/M$ from Eq. (IIA37). Then from Eq. (IIA36), c_p is constant:

$$c_p \approx \frac{5}{2} \frac{k_B}{M} = 5.15 \times 10^2 [\text{J/kg } {}^\circ\text{K}] \quad (\text{IIA38})$$

for Argon. This is true only at very low temperature less than 10^4 °K as is seen from Fig. (IIA12). The peaks at the higher temperatures correspond to the higher ionization stages.

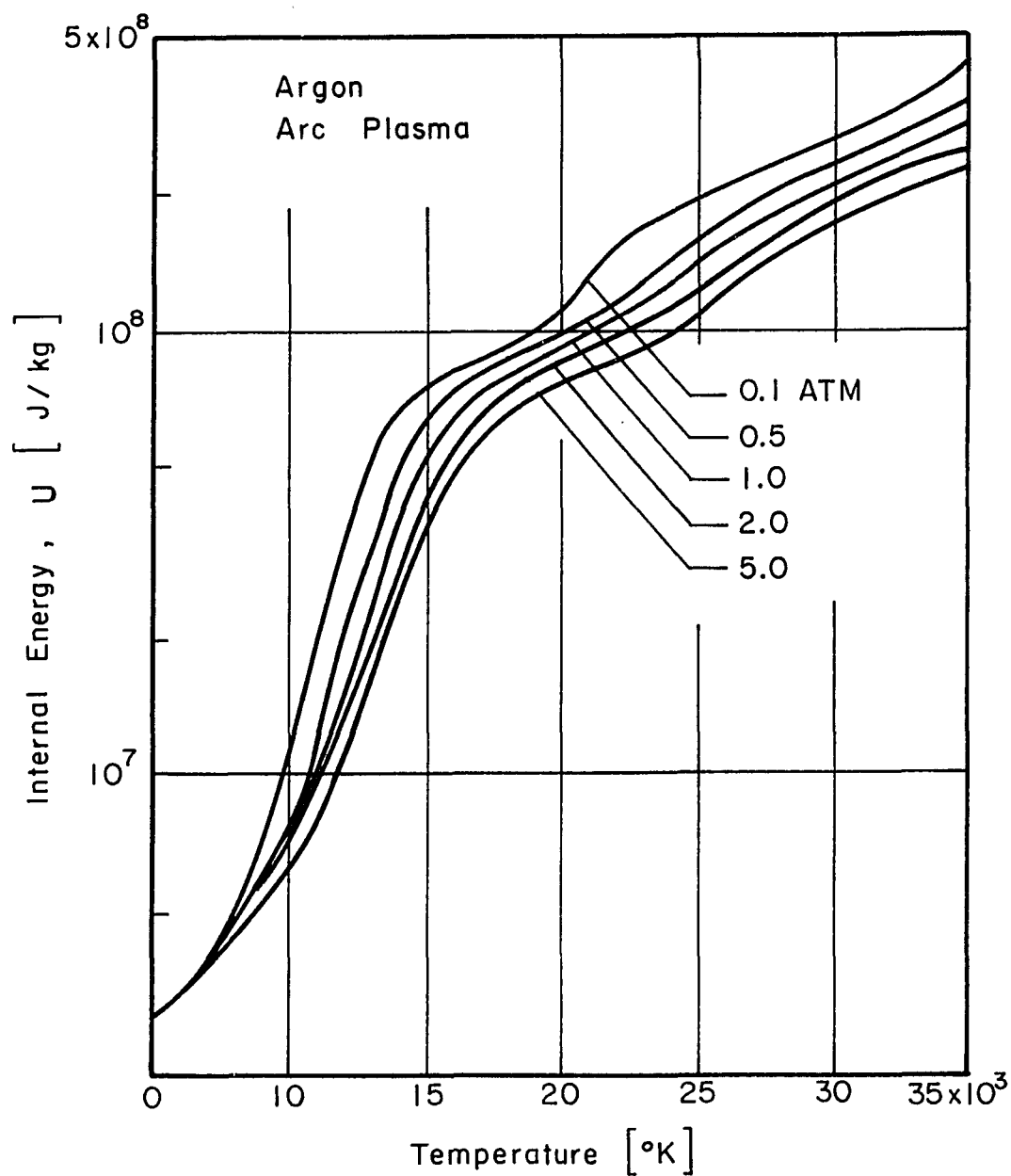


Fig. (II A 10) Temperature Dependence of the Internal Energy.
[After Cambel]¹⁸⁾

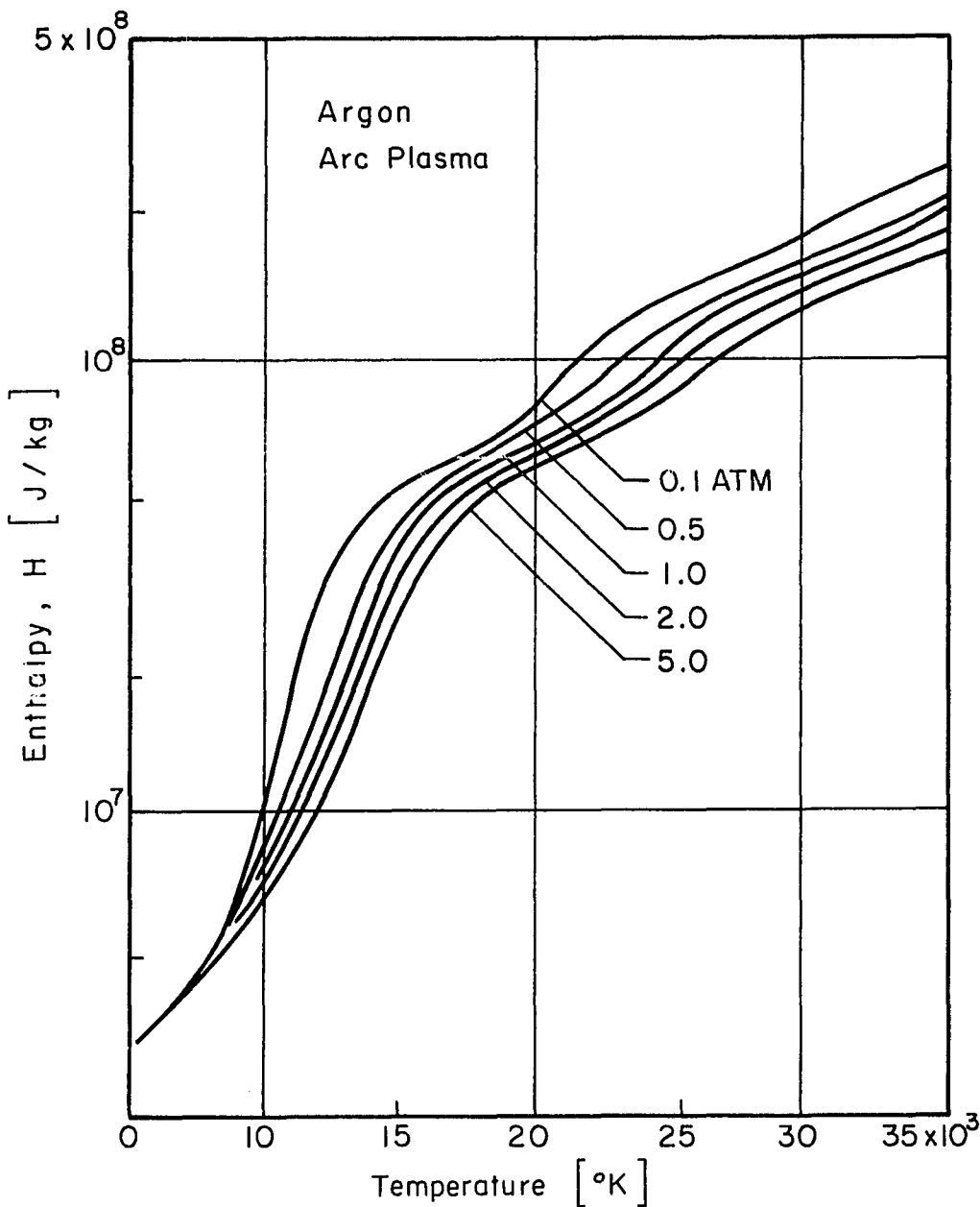


Fig. (II A 11) Temperature Dependence of the Enthalpy.
[After Cambel]¹⁸⁾

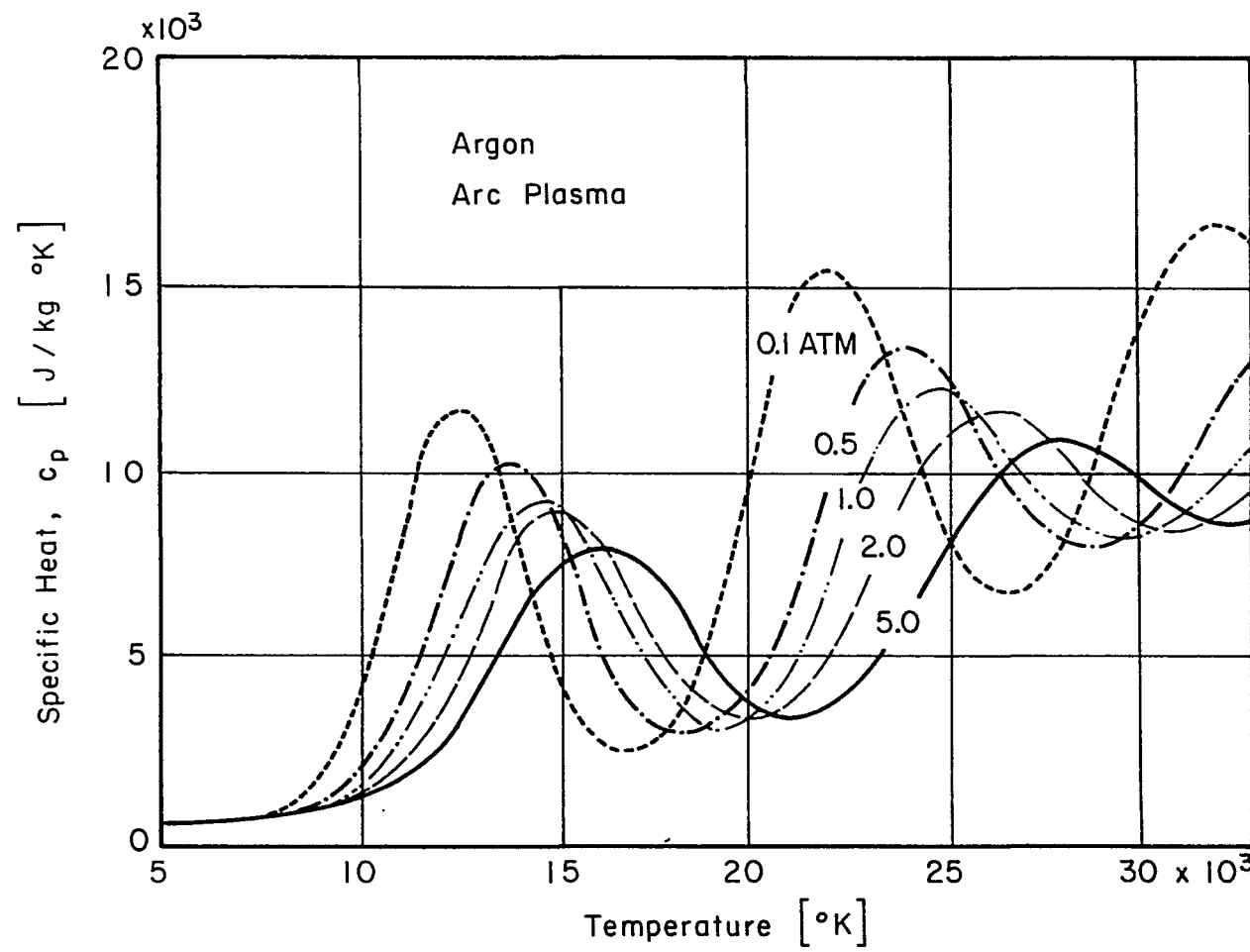


Fig. (II A 12) Temperature Dependence of the Specific Heat.
[After Cambel]¹⁸⁾

[IIA-5] Mass Density (ρ) and Prandtl Number (Pr)

Fig. (IIA13) and Fig. (IIA14) show the curves of mass density against temperature¹⁸⁾ and of Prandtl number against temperature²⁰⁾ for an argon plasma, respectively. The Prandtl number (Pr), defined as the ratio of kinetic viscosity (η) to thermal conductivity (k), gives relationship between the thermal boundary layer and mass flow boundary layer thicknesses. There are two definitions:

$$\text{Pr} = \frac{c}{p} \frac{\eta}{k} \quad (\text{Equilibrium Pr}) \quad (\text{IIA39})$$

and

$$\text{Pr} = \rho c \frac{\eta}{k} \quad (\text{Frozen Pr}). \quad (\text{IIA40})$$

These curves can be calculated from Figs. (IIA7), (IIA9), (IIA12) and (IIA13). For a fully ionized plasma Eqs. (IIA23) and (IIA32) can be used, resulting in

$$\begin{aligned} \text{Pr} &= \frac{c}{p} \frac{\eta}{k} \\ &\approx 3.84 \times 10^{-9} \frac{c}{p} \frac{M}{m} \left(\frac{T_i}{T_e} \right)^{5/2} \\ &= 2.80 \times 10^{-4} \frac{c}{p} \left(\frac{T_i}{T_e} \right)^{5/2} \text{ for Argon.} \end{aligned} \quad (\text{IIA41})$$

Fig. (IIA14) gives the upper limit of the Prandtl number for the 1 atm pressure plasma since c_p at 1 atm is smaller than that at 0.1 atm in the temperature range shown in Fig. (IIA14).

The Prandtl number relates the hydrodynamic mass flow with the thermal energy flow. As is already known, the power gain due to the

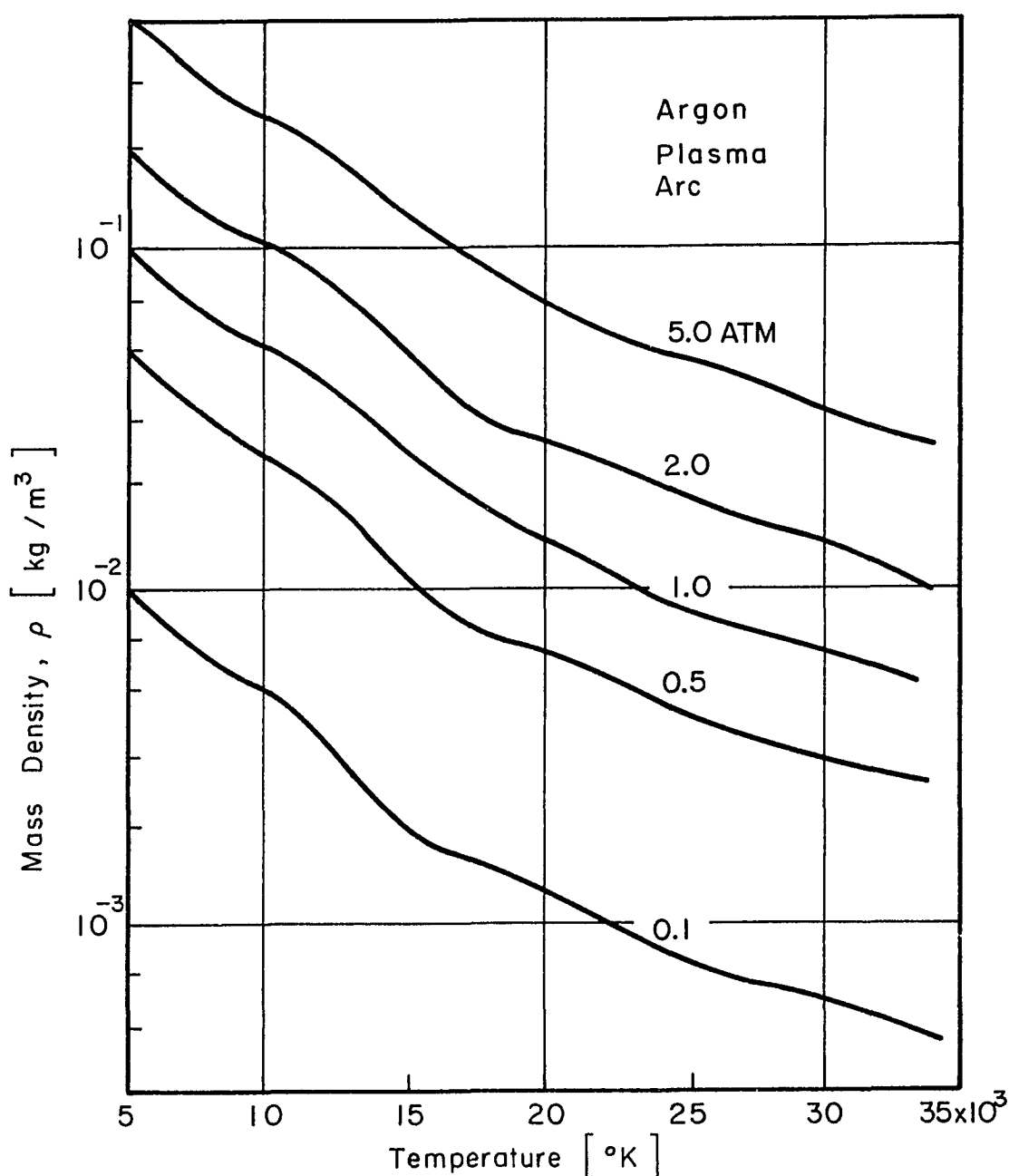


Fig. (II A 13) Temperature Dependence of the Mass Density.
[After Cambel]¹⁸⁾

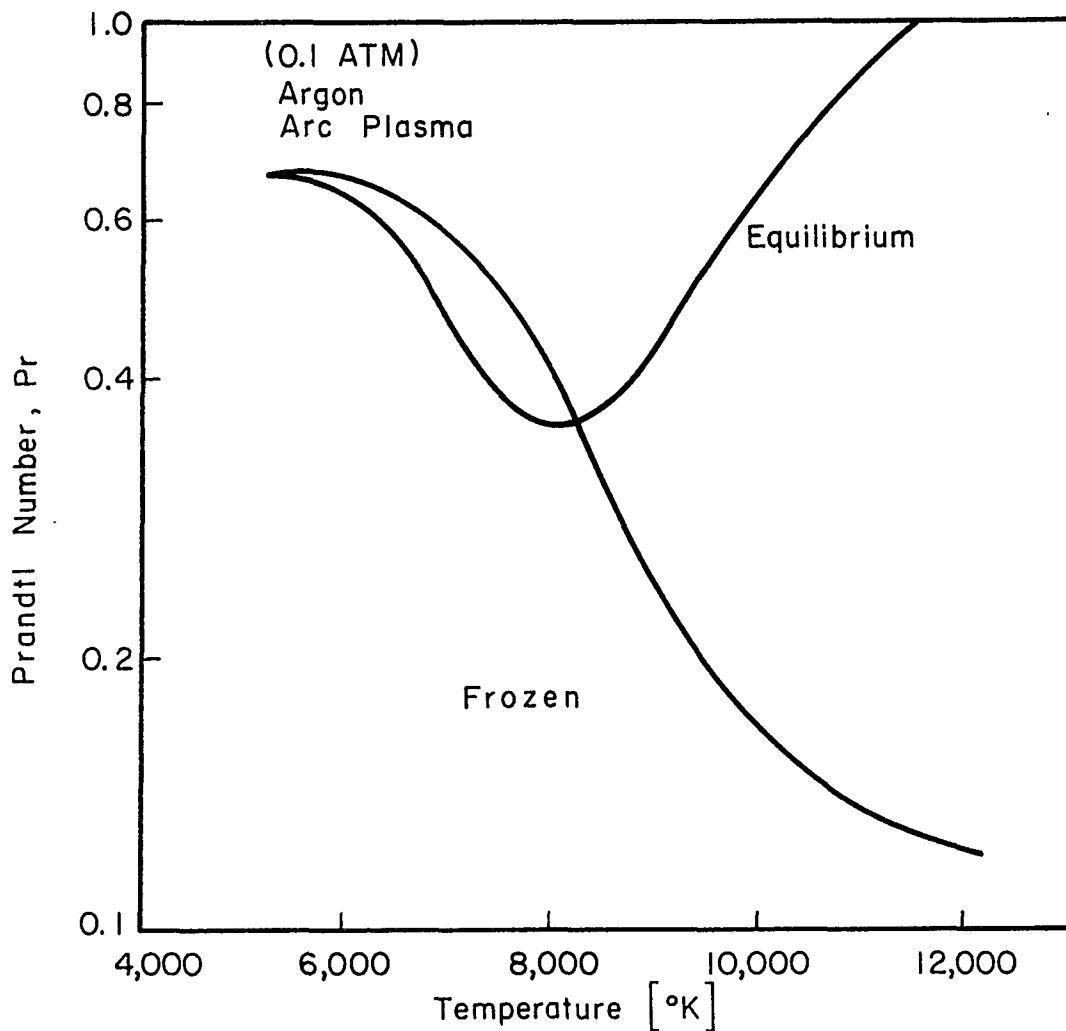


Fig. (II A 14) Temperature Dependence of the Prandtl Number.
[After Penski]²⁰⁾

internal friction is written as

$$Q_{\text{fric.}} = \eta \left(\frac{\partial u_r}{\partial z} \right)^2 \approx \eta \frac{u_r^2}{\delta_u^2}, \quad (\text{IIA42})$$

where δ_u is the characteristic length in which velocity variation is large (i.e., velocity boundary layer thickness). On the other hand, the power dissipation due to the conduction is written as

$$D_{\text{cond.}} = \frac{\partial}{\partial z} (k \frac{\partial T}{\partial z}) \approx k \frac{T}{\delta_t^2}, \quad (\text{IIA42})$$

where δ_t is the characteristic length in which temperature variation is large (i.e., temperature boundary layer thickness). The ratio $Q_{\text{fric.}}/D_{\text{cond.}}$ relates to the Prandtl number by

$$\begin{aligned} \frac{Q_{\text{fric.}}}{Q_{\text{cond.}}} &= \text{Pr} \frac{u_r^2}{c_p T} \left(\frac{\delta_T}{\delta_u} \right)^2 \\ &\approx \text{Pr} \frac{u_r^2}{(5k_B T/M)} \left(\frac{\delta_T}{\delta_u} \right)^2 \text{ at low temperature. } (\text{IIA43}) \end{aligned}$$

Case 1:

If the $Q_{\text{fric.}}$ is comparable with $D_{\text{cond.}}$, i.e.,

$$Q_{\text{fric.}} \approx D_{\text{cond.}}; \quad (\text{IIA44})$$

then

$$\left(\frac{\delta_T}{\delta_u}\right)^2 \approx \frac{c_p T}{u_r} \frac{1}{Pr}$$

>> 1 in most cases. (IIA45-a)

Hence, $\delta_T \gg \delta_u$. (IIA45-b)

Case 2:

If the $Q_{fric.}$ is very small compared with $D_{cond.}$, i.e.,

$$Q_{fric.} \ll D_{cond.}; \quad (\text{IIA46-a})$$

then

$$\delta_T \approx \delta_u. \quad (\text{IIA46-b})$$

Of these, Case 2 is the more probable as will be seen later on.

[IIA-6] Hydrodynamic Flow Velocity (\vec{u})

For the calculation of energy equations, the magnitude of hydrodynamic flow velocities is also important. Because of the high temperature and high current characteristics of the arc and because of the large spatial nonhomogeneities, there exist distinct hydrodynamic flows which affect the heat transfer rates.

(a) Natural-Convection Flow-Veloctiy

Natural (or free) convection of the arc plasma arises due to the fluid expansion by the temperature difference between the plasma axis and the surrounding atmosphere. The temperature in the axis of an

argon arc ($I \approx 15$ A) is estimated to be approximately $10,000^{\circ}\text{K}$, while the surrounding atmosphere located at the distance $R \approx 2.5 \times 10^{-3}$ m from the axis is in 300°K . Then from Fig. (IIA11),

$$\begin{aligned}\Delta\rho &\equiv \rho_R - \rho_{\text{axis}} \\ &\equiv 1.8 - (2.5 \times 10^{-2}) [\text{kg/m}^3].\end{aligned}\quad (\text{IIA47})$$

The equation of motion for a free-convection system is given by¹¹⁾

$$\rho_1 \frac{D\vec{u}}{Dt} = -[\vec{\nabla} \cdot \vec{\tau}] - \rho_1 \beta_1 \vec{q}(T - T_1), \quad (\text{IIA48})$$

where ρ_1 is the mass density for a reference temperature T_1 and $\beta_1 = -\rho_1^{-1} (\partial\rho/\partial T)_p$, the coefficient of volume expansion near T_1 .

When the term of viscous force, $\vec{\nabla} \cdot \vec{\tau}$ is neglected, Eq. (IIA48) gives the maximum flow velocity \vec{u} . For cylindrical coordinates at steady state, the axial and radial components of Eq. (IIA48) are given by

$$\left\{ \begin{array}{l} u_r \frac{\partial U_z}{\partial r} + u_z \frac{\partial U_z}{\partial z} = -\beta_1 g_z (T - T_1) \\ u_r \frac{\partial U_r}{\partial r} + u_z \frac{\partial U_r}{\partial z} = 0. \end{array} \right. \quad \begin{array}{l} (\text{IIA49-a}) \\ (\text{IIA49-b}) \end{array}$$

Here θ variation is assumed to be zero and the arc axis is parallel to the vector of the gravitational force (or $g_r = 0$). Near the arc axis, $\partial u_z / \partial r \approx 0$ and $\beta_1 (T - T_1) = -(\rho - \rho_{\text{axis}})/\rho_{\text{axis}}$ then Eq. (IIA49-a) gives

$$u_z \lesssim (2\Delta\rho g_z z / \rho_{\text{axis}})^{\frac{1}{2}} = 2.9 [\text{m/sec}] \quad (\text{IIA50})$$

for z (electrode spacing) = 6×10^{-3} m. From the Eq. (IIA50) and continuity equation, $\nabla \cdot (\rho \vec{u}) = 0$ for cylindrical coordinates,

$$r \rho(r) u_r + \int_0^r r \rho(r) \frac{\partial u_z}{\partial r} dr = 0; \quad (\text{IIA51-a})$$

one has

$$u_r \approx \frac{r}{3} (\Delta \rho g_z / 2 \rho_{\text{axis}} z)^{\frac{1}{2}} = 0.27 \text{ [m/sec]} \quad (\text{IIA51-b})$$

From Eq. (IIA52),

$$(du_r/dz)^2 = \frac{r^2}{36} (\Delta \rho g_z / 2 \rho_{\text{axis}})^2 z^{-3} = 2.25 \times 10^{-3} \quad (\text{IIA52})$$

typically. Thus from Eq. (IIA34),

$$\begin{aligned} Q_{\text{fric.}} &= 2 \times 10^{-4} (du_r/dz)^2 \\ &= 0.45 \text{ [Watt/m}^3], \end{aligned} \quad (\text{IIA53})$$

which is very small compared with the Joule heating power density, 3×10^{12} [Watt/m³].

(b) Axial Velocity, u_z

Because the current density is very high (\sim millions Amps/m²) at the cathode spot, the arc experiences strong pinch force near the cathode. This force drives plasma fluid toward the anode direction for the following reasons. The pinch effect occurs due to the Lorentz force of $\vec{v} \times \vec{b}$ term. The magnetic field, \vec{b} is self-induced by the

current density of the axial direction, j_z through the Maxwell's equation:

$$(\vec{\nabla} \times \vec{b})_z = \mu_0 \vec{j}_z . \quad (\text{IIA54})$$

In the cylindrical coordinates this becomes

$$\frac{1}{r} \left[\frac{\partial}{\partial r} (rb_\theta) - \frac{\partial b_r}{\partial \theta} \right] = \mu_0 \sigma E, \quad (\text{IIA55})$$

where the second term in the square bracket vanishes because of the symmetry in the θ direction. The integration of Eq. (IIA55), assuming E_z is constant in the interior of the plasma, yields

$$b_\theta = \mu_0 r \frac{\sigma E_z}{2} . \quad (\text{IIA56})$$

The Lorentz force subjected to an electron is given by

$$\begin{aligned} \vec{F}_r &= -e(\vec{v}_z \times \vec{b}_\theta) \\ &= -e(j_z/ne) \times (\mu_0 r \sigma E_z / 2) \\ &= -\mu_0 r \frac{(j_z)^2}{2n} . \quad [\text{Newton}] \end{aligned} \quad (\text{IIA57})$$

This is a centripetal pinch force which is proportional to the quadratic of the current density. The corresponding force density f_r at a radial distance, r is given by

$$f_r = (\rho/m) F_r = -\mu_0 r \frac{(j_z)^2}{2} \quad [\text{Newton}/m^3] . \quad (\text{IIA58})$$

This force can be converted into the equivalent pressure:

$$p = \int f dr = \frac{\mu_0 j_z^2}{2} \int_r^R r dr = \frac{\mu_0}{4\pi} I j_z \left(1 - \frac{r^2}{R^2}\right) [\text{Newton/m}^2]. \quad (\text{IIA59})$$

The maximum pressure occurs at the center of the plasma column

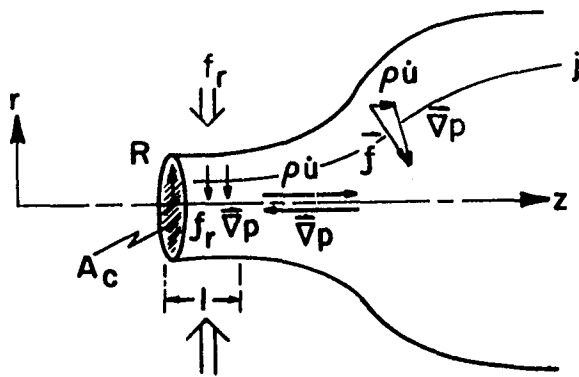


Figure (IIA15). Cathode Jet

(i.e., $r = 0$):

$$p_{\max} = \frac{\mu_0}{4\pi} I j_z, \quad [\text{Newton/m}^2] \quad (\text{IIA60})$$

where $\mu_0 = 4\pi/10^7$ [Henry/m], $I = \pi R^2 j_z$ [Amps], and j_z is in units of $[\text{Amps}/\text{m}^2]$. This is the same result which Maecker²¹⁾ obtained in the cgs-Gauss units:

$$p_{\max} = c^{-2} I j_z \quad [\text{dyne/cm}^2], \quad (\text{IIA61})$$

where $c = 3 \times 10^{10}$ [cm/sec], and \mathbf{j} and \mathbf{u} are in the cgs-Gauss units.

Since we can assume that the ion motion is strongly coupled with electrons via the Coulomb force, the hydrodynamic flow arises so that the force density vectors balance on the streamline. (See Fig. II A15):

$$\begin{aligned}\vec{f} &= \vec{\nabla} p + \rho \frac{D\vec{u}}{Dt} \\ &= \vec{\nabla} p + \rho [\vec{\nabla}_z^2 \vec{u}^2 - \vec{u} \times (\vec{\nabla} \times \vec{u})].\end{aligned}\quad (\text{IIA62})$$

Since $\vec{\nabla} \times \vec{u} = 0$ for irrotational flows, the integration form of Eq. (IIA62) is

$$\int f ds = p + \frac{1}{2} \rho u^2. \quad (\text{IIA63})$$

The maximum flow velocity occurs along the axis of the plasma column where all the radial forces are converted into the axial pressure gradient. Since the maximum axial pressure is given by Eq. (IIA60) approximately, one has finally

$$\begin{aligned}u_{z, \max} &\approx (2p_{\max}/\rho_{\text{axis}})^{\frac{1}{2}} \\ &= (2 I j_z / 10^7 \rho_{\text{axis}})^{\frac{1}{2}} \quad [\text{m/sec}].\end{aligned}\quad (\text{IIA64})$$

An excellent agreement of Eq. (IIA61) and therefore of Eq. (IIA64) has been proved by Schoeck's¹⁰⁾ experiment within 20% of error. A

correction factor to adjust Eq. (IIA61) with experimental data is introduced by Wienecke.²²⁾

For a plasma with $I = 15$ Amps, $j_z \approx 3.15 \times 10^6$ Amps/m² is expected by the extrapolation of Schoeck's experimental data.¹⁰⁾ And since $\rho_{\max} = 2.5 \times 10^{-2}$ kg/m³ at the arc axis, Eq. (IIA64) gives the value:

$$u_{z, \max} \approx 16 \text{ [m/sec].} \quad (\text{IIA65})$$

This cathode jet velocity is about 5 times larger than the velocity due to the natural convection given by Eq. (IIA50) and corresponds to the forced gas flow velocity of 3[l-min] from a 1[mm] diameter orifice.

Fig. (IIA16) shows a schematic of the hydrodynamic velocity distribution in 15-Amp arc.

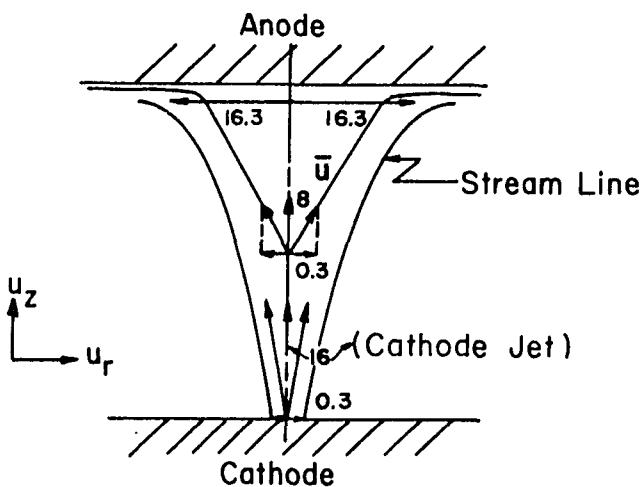


Fig. (IIA16). Hydrodynamic Flows of a Low Intensity Arc Plasma.

Generally speaking, compared with the high current arc ($I > 30$ Amps), the low current arc diverges more quickly toward anode for instance as is the case of Fig. (IIA16).

Plasma Parameters:

[IIA-7] Arc Plasma Temperatures (T)

In local thermal equilibrium (LTE) plasma, the system is uniquely determined by the equilibrium temperature, T ($= T_e = T_i = T_n$), since the all plasma constituents (n_e , n_i and n_n) are essentially those determined by the Saha-Eggert equation. The maximum temperature of a LTE plasma depends on the energy transfer mechanisms of the arc system and can be calculated using the energy equation (IIA7). For simplicity, let us consider a system where only one energy source σE^2 (or $\vec{j} \cdot \vec{E}$) is balanced with only one loss mechanism $\vec{\nabla} \cdot (k \vec{\nabla} T)$:

$$\vec{\nabla} \cdot (k \vec{\nabla} T) + \vec{j} \cdot \vec{E} = 0. \quad (\text{IIA66})$$

In the cylindrical coordinates this becomes

$$\frac{1}{r} \frac{\partial}{\partial r} (r k \frac{\partial T}{\partial r}) + \frac{\partial}{\partial z} (k \frac{\partial T}{\partial z}) + j_z E_z = 0, \quad (\text{IIA67})$$

where we have again neglected θ -variations because of the symmetry. For the positive plasma column the axial conduction loss term in Eq. (IIA67) is negligible since $\partial T / \partial z \approx 0$. Then the twice integrations of Eq. (IIA67) are

$$rk \frac{\partial T}{\partial r} + \int_0^r rjE dr = 0 \quad (\text{IIA68})$$

and

$$\int_{T_{\max}}^{T_R} kdT + jE \int_0^R \frac{1}{r} \int_0^r r dr dr = 0. \quad (\text{IIA69})$$

Here, T_{\max} and T_R are the temperatures at $r = 0$ and $r = R$ (edge of the plasma column), respectively. Eq. (IIA69) can be further written as

$$\int_{T_{\max}}^{T_R} kdT = -EI/4\pi. \quad (\text{IIA70})$$

where $I = j\pi R^2$. Here the thermal conductivity k is a function of temperature as is shown in Fig. (IIA7). If the positive column is fully ionized, $k \approx k_e$ which is given by Eq. (IIA23). Since $(\ln \Lambda)^{-1} \approx 1/3$ for typical arc plasmas, Eq. (IIA70) becomes

$$6.50 \times 10^{-10} \gamma_T z^{-1} \int_{T_{\max}}^{T_R} T^{5/2} dT = EI/4\pi. \quad (\text{IIA71})$$

This results in

$$T_{\max} \approx (4.56 \times 10^8 z/\gamma_T)^{2/7} (EI)^{2/7} [\text{°K}], \quad (\text{IIA72})$$

assuming $T_R \ll T_{max}$. Thus in the fully ionized plasma, T_{max} is only the function of the input power per unit length, EI and is proportional to the $2/7$ -power of EI. On the other hand if the positive column is a partially ionized plasma the thermal conductivity is due to k_n which is given by Eq. (IIA28). The maximum temperature in such a plasma is calculated as

$$T_{max} = (1.84 \times 10^2 z/\gamma_E)^{2/3} (EI)^{2/3} [{}^\circ\text{K}] \quad (\text{IIA73})$$

$$= (1.68 \times 10^2)^{2/3} (EI)^{2/3}. \quad (\text{IIA74})$$

Generally $E = 10^2 \sim 10^3 \text{ V/m}$ in the positive column. Thus T_{max} is only a function of I, arc current.

These predictions are compared with the experimental data (Fig. IIA17) obtained by the spectroscopic measurement for wall-stabilized argon arc plasma with tungsten cathode reported by Emmons²³⁾ and Schreiber and Hunger.²⁴⁾ These data show that the electric field E is constant and the maximum temperature is only the function of (EI) as was predicted. However, the current dependence of the maximum temperature is weaker than the prediction of Eqs. (IIA72) and (IIA74) by a factor of about 2 and 4 in the high and low current regions, respectively. To predict the experimental data much better, the temperature dependence of the effective thermal conductivity should be much steeper or additional loss mechanisms should be accounted. The difference between the experimental curves (1) and

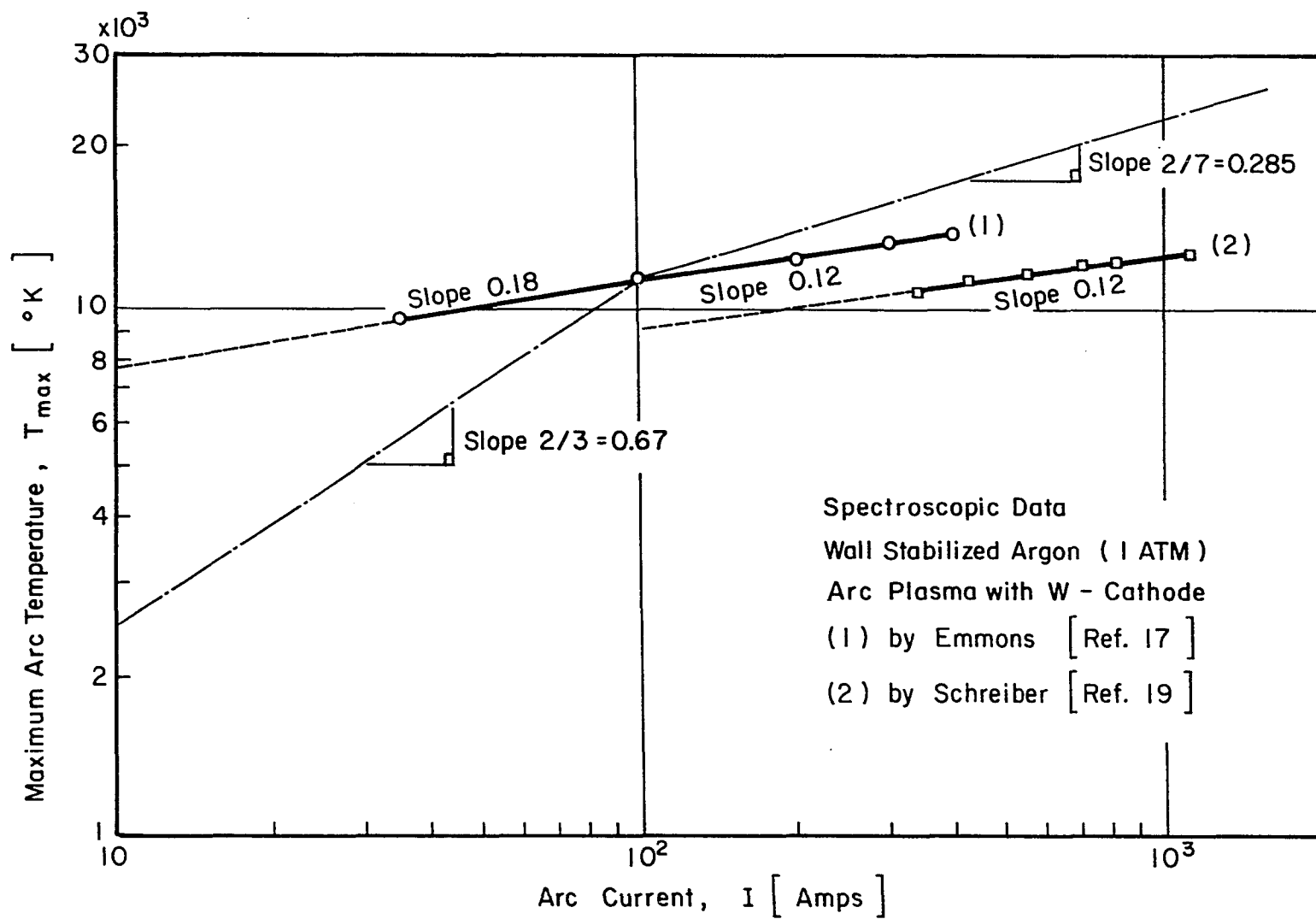


Fig. (II A 17) Arc Current Dependence of the Maximum Arc Temperature

(2) can be attributed to the different E due to the different arc spacing or different probing position along the arc axis. From the Fig. (IIA17) one also sees that the maximum temperature of more than 8000°K is difficult to obtain in a 15-amp free burning arc because the maximum temperature of the free burning arc is lower than that of the wall-stabilized arc.

Consider next the case where the axial conduction is much more dominant than the radial conduction as is true near the anode surface. The double-integration of the energy equation (Eq. IIA67) yields

$$\begin{aligned} \int_{T_s}^{T_w} k dT &= - \int_{z_s}^{z_w} dz \int_{z_s}^z j E_z dz \\ &= - \frac{jE}{2} (z_w - z_d)^2 \\ &= - \frac{IE}{2\pi} \left(\frac{\delta_t}{R} \right)^2, \end{aligned} \quad (\text{IIA75})$$

where T_w and T_s ($\gg T_w$) are the temperatures at z_w (anode wall surface) and z_s (edge of the thermal boundary layer), respectively; and $\delta_t = |z_s - z_w|$, see Fig. (IIA5-e). The change of E_z in the sheath (or ϵ -layer) has been neglected in Eq. (IIA75) for the reason that $\epsilon \ll \delta_t$. As we have seen in the Sub-Section [IIA2], $k \approx k_n$ in the thermal boundary layer. Thus Eq. (IIA75) can be calculated using Eq. (IIA28) as

$$\begin{aligned}
 T_s &= \left[\frac{1.68 \times 10^2}{2\pi} EI(\delta_t/R)^2 \right]^{2/3} \\
 &= (26.7 EI)^{2/3} (\delta_t/R)^{4/3} \quad [{}^\circ K]
 \end{aligned} \tag{IIA76}$$

This shows that the temperature at the temperature boundary edge T_s is a function of the ratio of boundary layer thickness (δ_t) to arc radius (R).

Spectroscopic temperature measurements are not reliable for low current arcs and low temperature regions (such as boundaries) of the high current arc where the arc is actually in non-LTE. In this thesis the temperature of the plasma is measured by Thomson scattering method which does not depend on the validity of LTE.

[II A8] Arc Plasma Constituent Number Density (n)

If LTE is assumed for the plasma, the concentrations can be calculated uniquely by Saha-Eggert equation for a given equilibrium temperature. The graph of equilibrium concentrations has been shown in Fig. (IIA2). Since the maximum temperature of a 15-Amp arc is expected to be $8000 {}^\circ K$ from Fig. (IIA17), the corresponding maximum electron density (n_e) is found from Fig. (IIA2) to be $1.4 \times 10^{21} \text{ cm}^{-3}$ and the maximum degree of ionization, $n_e/n_n = 1.56 \times 10^{-3}$. Secondary ionized argon ions, n_i^{++} are completely negligible in the temperature range of $8000 {}^\circ K$ as seen in Fig. (IIA2).

If the local thermodynamic equilibrium is not assumed for the plasma, the concentrations of the constituents cannot be determined from the conventional temperature measurements such as spectroscopy and Langmuir probe because those theories are based on the Boltzmann distribution of all plasma constituents. Only scattering and interferometric methods using light or microwave frequency can give reliable data of the electron number density for non-LTE plasmas. In this thesis, the electron number density is determined from the intensity measurement of Thomson scattering calibrated against that of Rayleigh scattering.

Electric Parameters in the Arc Plasma

[IIA-9] Electric Field Distribution

The electric field (\vec{E}) is directly related to the Joule heating power density σE^2 , the heat transfer flux vector $\vec{q} = -k\vec{\nabla}T - \beta\vec{E}$, and the validity criterion of LTE condition. The needed information is the absolute magnitude of \vec{E} and the distribution in the radial and axial directions.

(a) Radial Electric Field $E(r)$, Perpendicular to the Line of Arc Current

An important radial motion in the arc plasma is due to ambipolar diffusion. The free electron diffusion¹⁴⁾ takes place if the electron density is less than 10^{14} m^{-3} ; and if the plasma is fully ionized, the plasma diffusion²⁵⁾ takes place. Along the line of the

ambipolar diffusion a space charge field \vec{E}_s is set up to accelerate slow ions and decelerate fast electrons so that the local charge neutrality is maintained. The magnitude of this static field is given by¹⁴⁾

$$\begin{aligned}\vec{E}_s(r) &= - \frac{D_e - D_i}{\mu_e + \mu_i} \frac{\vec{\nabla}n}{n_o} \\ &\approx - \frac{k_B T_e}{e} \frac{\vec{\nabla}n}{n_o},\end{aligned}\quad (\text{IIA77})$$

where n_o is the density at the center; $\vec{\nabla}n = \partial n / \partial r$; and the relationships: $D_e \gg D_i$ and $\mu_e \gg \mu_i$ are used for the approximation. The term $\nabla n_r / n_o$ can be calculated from the (ambipolar) diffusion equation:

$$\frac{\partial n}{\partial t} - \nabla^2 n - \frac{n}{\Lambda_a^2} = 0. \quad (\text{IIA78})$$

In the steady state and in cylindrical coordinates, the solution is given by the Bessel function of the zeroth order, i.e., $n = n_o J_0(r/\Lambda_a)$. Hence the density gradient is given by

$$\vec{\nabla}n_r / n_o = \Lambda_a^{-1} J_1(r/\Lambda_a), \quad (\text{IIA79})$$

where J_1 is the Bessel function of the first order and Λ_a is the ambipolar diffusion length equal to $(R/2.405)$ such that the density becomes zero at the column edge, $r = R$. Thus the static electric field

distribution of the plasma with density variation given by Eq. (IIA79) can be written as

$$\begin{aligned} E_s(r) &= \frac{k_B T_e}{e} \frac{2.405}{R} J_1(2.405 r/R) \\ &= 8.62 \times 10^{-5} T_e(K^o) \frac{2.405}{R} J_1(2.405 r/R) [V/m]. \end{aligned} \quad (\text{IIA80})$$

For an arc plasma with $T \approx 10^4 K$ and $R \approx 10^{-3} m$, the maximum radial field strength can be calculated from Eq. (IIA80) to be

$$E_s(R) = 1.08 \times 10^3 [V/m]. \quad (\text{IIA81})$$

This is comparable with the axial electric field strength of the main positive column to be discussed in the part (b). Notice that the radial static field is very large for the arc because of the large density gradient or the small arc radius.

If a solid wall is constricting the plasma, the ambipolar diffusion is no longer true near the wall. Due to the large mobility, the electrons hit the wall much more frequently than the ions and are absorbed to the wall resulting in the extreme deficiency of the number of electrons near the wall. Ambipolar diffusion which brought about local charge neutrality is limited beyond a certain layer called sheath edge.^{9, 26)} However, in order to satisfy the boundary condition such that the current densities of the two species cancel each other locally (in the case of insulating wall) or as a whole (in the case of conducting but electrically floating wall), a strong electric field called sheath

electric field builds up in the sheath. Since the sheath consists of the positive space charges as shown in Fig. (IIA18) in the case of electrically floating walls, the electron flow is greatly reduced and the ion flow is enhanced by the established sheath field and/or sheath potential.

The sheath thickness and the sheath field strength depend on the nature of the plasma and wall.

When the ion mean free path (MFP) lengths which are given by²⁷⁾

$$\left. \begin{aligned} \ell_{ii} &= \ell_{ee} = \left(\frac{m}{M}\right) \ell_{e \rightarrow i} \approx \frac{\Lambda}{\ell n \Lambda} \lambda_D \\ \ell_{i \rightarrow e} &= \left(\frac{m}{M}\right)^{\frac{1}{2}} \ell_{ee} \approx \left(\frac{m}{M}\right)^{\frac{1}{2}} \frac{\Lambda}{\ell n \Lambda} \lambda_D \end{aligned} \right\} \quad (\text{IIA82})$$

are much longer than the sheath thickness the plasma is called collisionless. For the collisionless plasma the sheath potential (V_{sh}) is given by

$$\begin{aligned} V_{sh} &= -0.7722 \frac{k_B T}{e} \text{ (Tonks-Langmuir⁹⁾) or} \\ &= -0.854 \frac{k_B T}{e} \text{ (Caruson²⁶⁾ and Self²⁸⁾, [V]} \end{aligned} \quad (\text{IIA83})$$

and the sheath thickness is

$$\begin{aligned} d_{sh} &= 0.7722 \ell_{ii} \text{ (Tonks-Langmuir⁹⁾) or} \\ &= 0.4046 \ell_{ii} \approx (2 \sim 10) \lambda_D \text{ (Self²⁸⁾, [m]} \end{aligned} \quad (\text{IIA84})$$

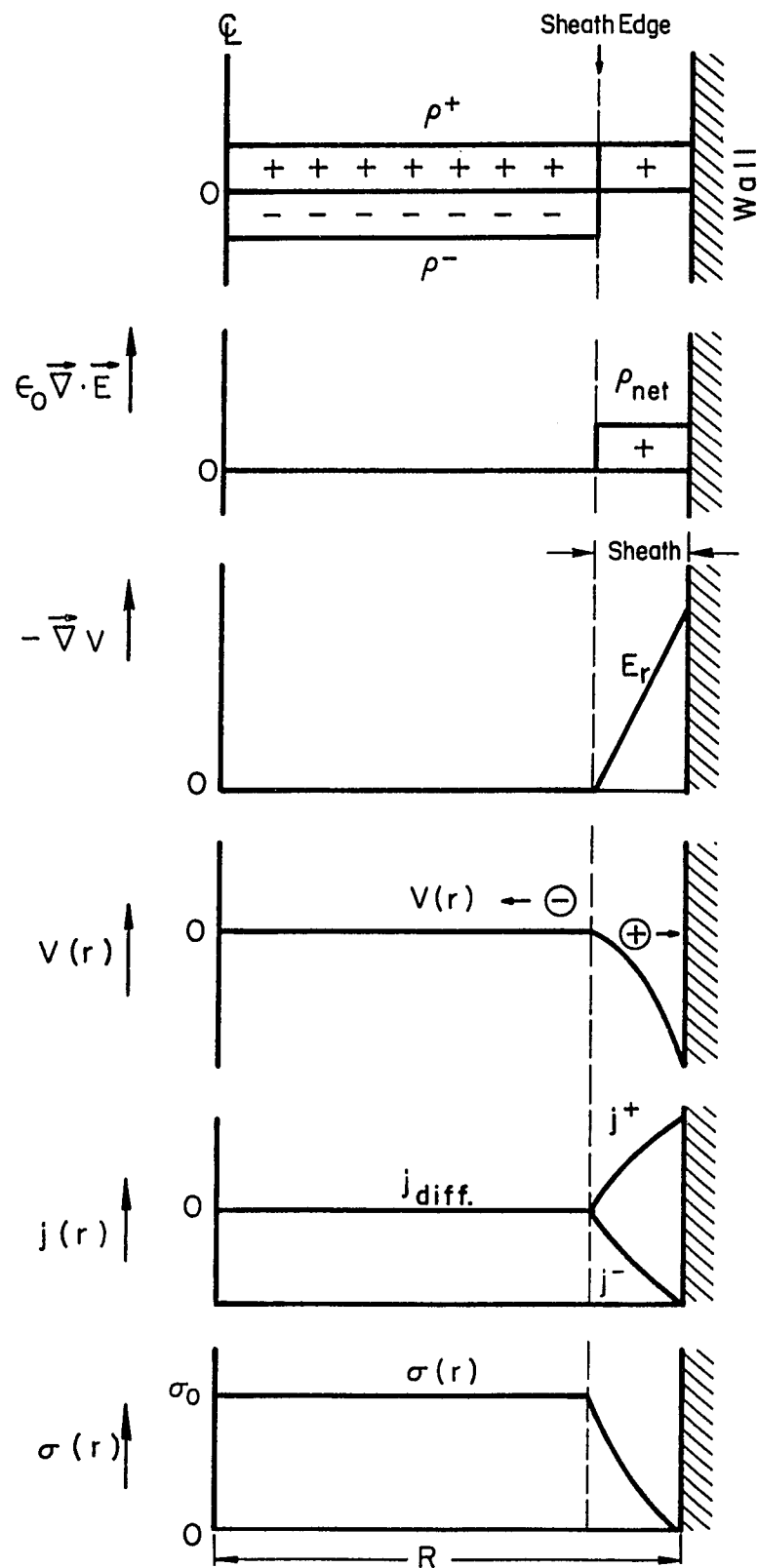


Fig. (II A 18) Sheath Boundaries for Electrically Floating Walls in the Radial Direction.

for electrically floating walls. Above results by Self²⁸⁾ are the solutions of the complete plasma-sheath equation. The relationship

$d_{sh} \approx (2 \sim 10) \lambda_D$ (where λ_D is the electron Debye length) has been recently verified experimentally by Gordon and Yaldowsky.¹⁹⁾ Thus the average sheath electric field ($E_{sh} = - V_{sh}/d_{sh}$) is given by

$$E_{sh} = 0.854 \times 10^{-2} \frac{k_B T}{e d_{sh}} \approx 1.84 \times 10^{-6} T(^{\circ}\text{K}) \frac{l \ln \Lambda}{\lambda_D \Lambda} [\text{V/m}] . \quad (\text{IIA85})$$

If we assumed that a plasma with $T = 10^4 ^{\circ}\text{K}$ [$n_e = 10^{22} \text{ m}^{-3}$, $\lambda_D = 10^{-7} \text{ m}$, $\Lambda = 10$ (See Fig. IIA19), $l_{ii} \approx 4.3 \times 10^{-7} \text{ m}$] was collisionless, Eq. (IIA85) would give the value:

$$\left. \begin{aligned} E_{sh} &= 4.25 \times 10^3 [\text{V/m}] \\ \text{for } d_{sh} &= 0.40 l_{ii} = 1.72 \times 10^{-7} [\text{m}] . \end{aligned} \right\} \quad (\text{IIA86})$$

But the $10^4 ^{\circ}\text{K}$ plasma is obviously not collisionless and the real sheath field and sheath thickness are different from what is given by Eq. (IIA86) as will be shown soon.

For collision dominated arc plasmas the ambipolar diffusion limited sheath is formed.³⁰⁾ The voltage drop across the sheath is given by³⁰⁾

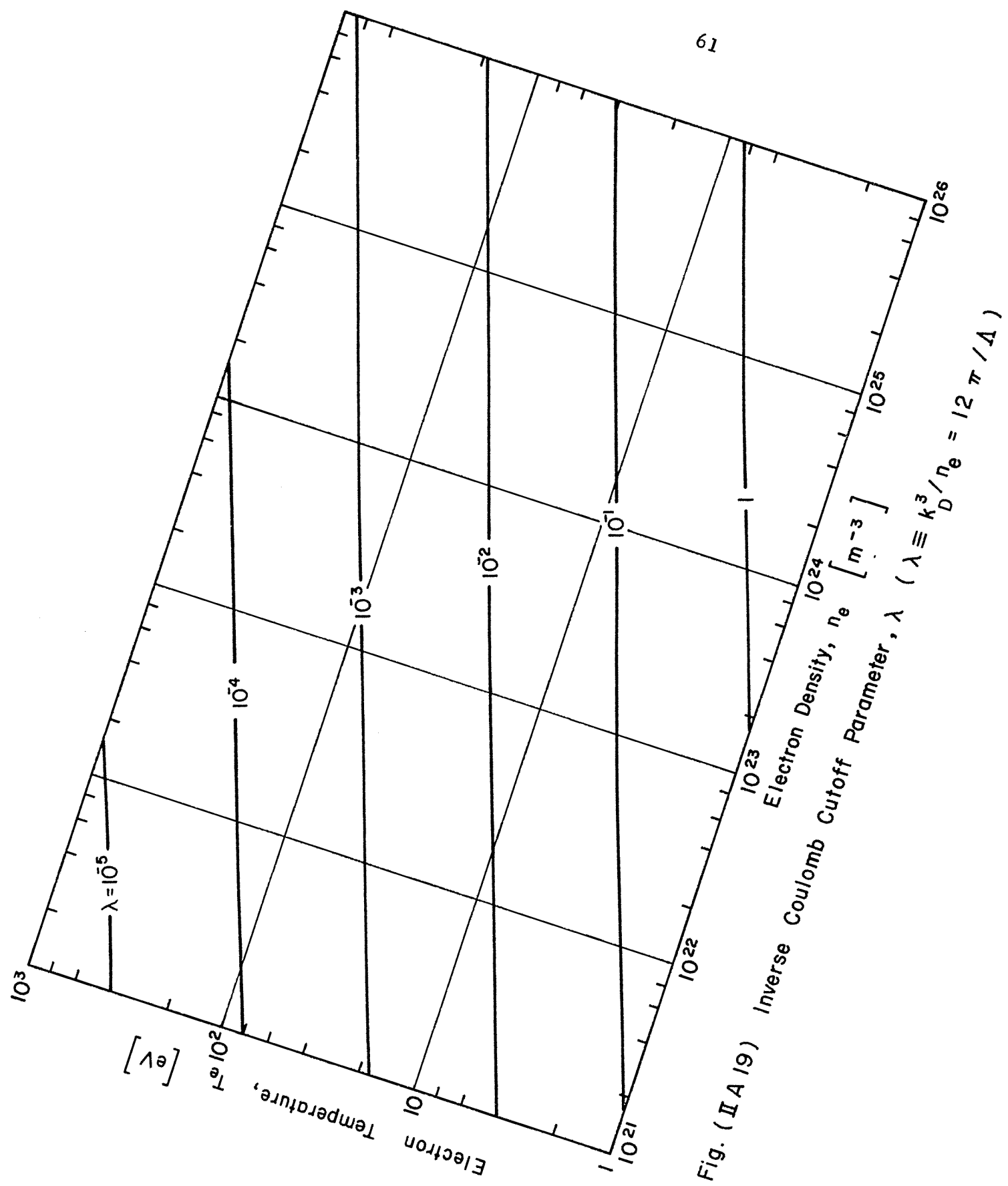


Fig. (II A 19)

61

$$10^{26}$$

$$10^{25}$$

$$10^{24}$$

$$10^{23}$$

$$10^{22}$$

$$10^{21}$$

$$10^{20}$$

$$10^{19}$$

$$10^{18}$$

$$10^{17}$$

$$10^{16}$$

$$10^{15}$$

$$10^{14}$$

$$10^{13}$$

$$10^{12}$$

$$10^{11}$$

$$10^{10}$$

$$10^9$$

$$10^8$$

$$10^7$$

$$10^6$$

$$10^5$$

$$10^4$$

$$10^3$$

$$10^2$$

$$10^1$$

$$10^0$$

$$10^{-1}$$

$$10^{-2}$$

$$10^{-3}$$

$$\begin{aligned}
 V_{sh} &= -\frac{k_B T_e}{2e} \ln \frac{v_i}{v_e} = \frac{k_B T_e}{2e} \ln \left[\left(\frac{T_e}{T_i} \right)_w \frac{M}{m} \right] \\
 &= - \int_0^{\ell_s} E_{sh} dr. \tag{IIA87}
 \end{aligned}$$

And the corresponding sheath thickness may be found as¹⁴⁾

$$d_{sh} = \left(\frac{\epsilon_0 T_e}{n_0 e} \right)^{1/3} = (\lambda_D)^{2/3}. \tag{IIA88}$$

Hence the average sheath electric field is

$$\begin{aligned}
 \vec{E}_{sh} &\approx 4.31 \times 10^{-5} T_e ({}^\circ K) \lambda_D^{-2/3} \ln \left(\frac{M}{m} \right) \\
 &= 4.82 \times 10^{-4} T_e ({}^\circ K) \lambda_D^{-2/3} \text{ for argon.} \tag{IIA89}
 \end{aligned}$$

Here, $(T_e / T_i)_w \approx (T_e / T_i)_{\text{sheath edge}} \approx 1$ has been used as an approximation. For an Argon plasma ($M/m = 7.4 \times 10^4$) with $T_e = 10^4$ (°K) and $n_0 = 10^{22} \text{ m}^{-3}$ ($\lambda_D = 10^{-7} \text{ m}$), Eq. (IIA89) gives

$$\vec{E}_{sh} \approx 2.42 \times 10^5 \text{ [V/m]}, \tag{IIA90}$$

$$\text{for } d_{sh} = (\lambda_D)^{2/3} \approx (\Lambda^{-1} \ln \ell_{ii})^{2/3} = 2 \times 10^{-5} [\text{m}].$$

For the high temperature plasma such that the thermal diffusion current is larger than the concentration diffusion current [i.e., $\vec{\nabla} T_e > (e^2 D_a / \sigma k_B) \vec{\nabla} n$], another type of sheath, the so-called thermo-electric power limited sheath, is formed.³⁰⁾ The well known

expression of the concentration diffusion current can be modified to that of the thermal diffusion current as

$$\vec{j}_T = -e \frac{k_B \vec{\nabla} T_e}{m v_e} n_e$$

$$= -\frac{k_B}{e} \sigma_e \vec{\nabla} T_e . \quad (\text{IIA91})$$

The thermoelectric sheath field (E_T) can be calculated by the formula,

$$a \vec{j}_T + \sigma_e \vec{E}_T = 0 , \quad (\text{IIA92})$$

where $a (\approx 0.7)$ is the correction factor given by Finkelnburg and Maecker.¹⁾ Hence from Eqs. (IIA91) and (IIA92),

$$\vec{E}_T = (0.7 k_B / e) \vec{\nabla} T$$

$$= 6.05 \times 10^{-5} \frac{\Delta T (^{\circ}\text{K})}{\Delta r (\text{m})} [\text{V/m}] . \quad (\text{IIA93})$$

If $\Delta T \approx 10^4 ^{\circ}\text{K}$ and $\Delta r \approx \epsilon \approx 10^{-4} \text{ m}$, values obtained by Block and Finkelnburg,¹⁶⁾ are substituted into Eq. (IIA93), the result is

$$E_T \geq 6.05 \times 10^3 [\text{V/m}] . \quad (\text{IIA94})$$

For usual plasmas, these two (i.e., ambipolar and thermoelectric) sheaths coexist.³⁰⁾ The distribution of the radial electric fields (which are primitive fields free from the externally imposed electric field) is shown schematically in Fig. (IIA20) for the case of an argon arc plasma with the temperature $10^4 ^{\circ}\text{K}$ and $n_0 = 10^{22} \text{ m}^{-3}$.

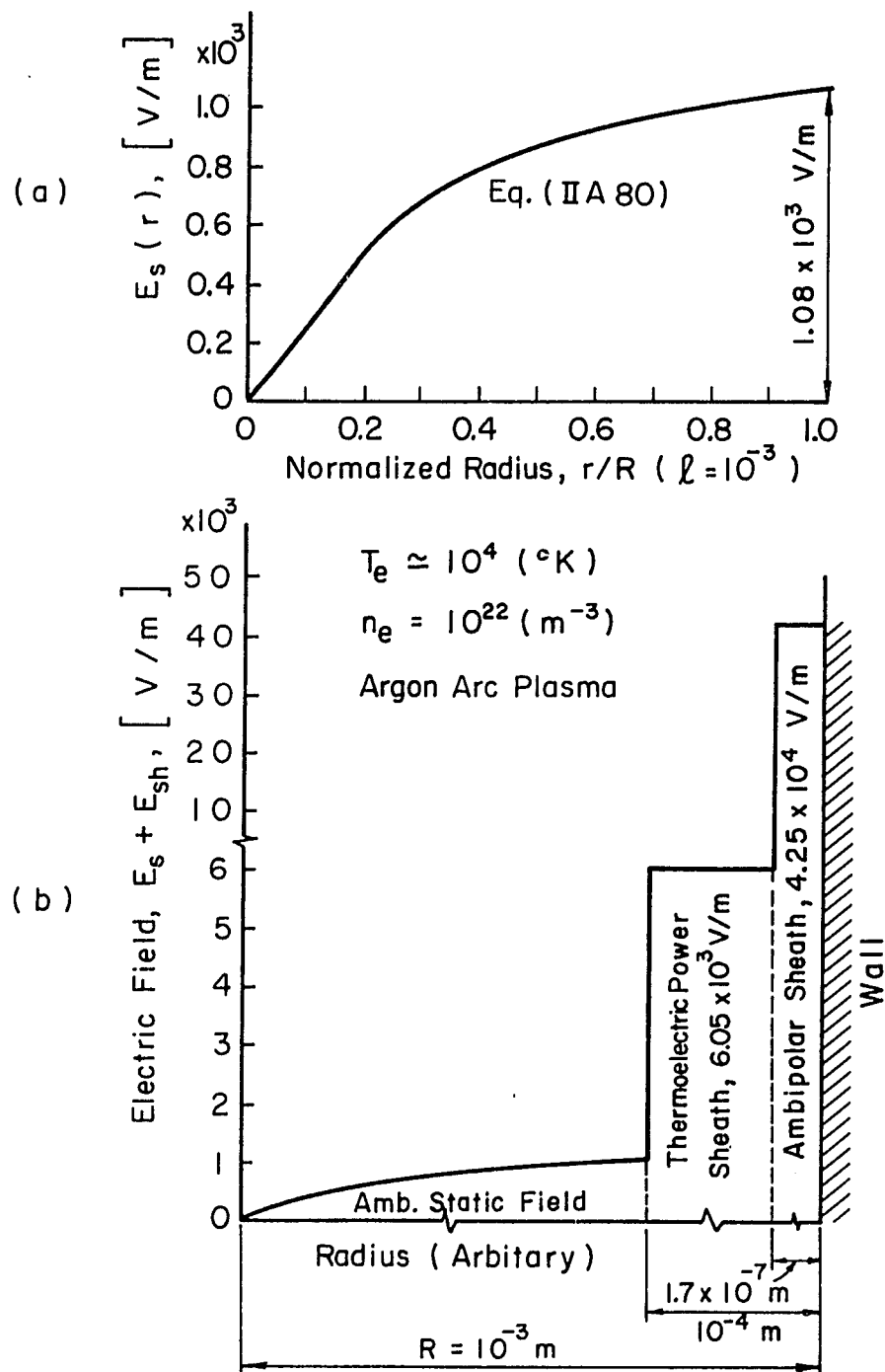


Fig. (II A 20) Static and Sheath Electric Field Distribution;
 (a) Without Wall, (b) With Wall in the
 Radial Direction

(b) Axial Electric Field $E(z)$, Parallel to the Line of Arc Current

The axial electric field in the positive column is given by balancing the energy the electrons gain from the electric field and the energy they lose by collisions:

$$\begin{aligned}
 eE_z v_d &= \kappa \frac{3}{2} k_B \frac{dT_e}{dt} \\
 &= \kappa \nu_{ei} \frac{3}{2} k_B (T_e - T_i), \\
 \therefore E_z &= \frac{3}{2} \frac{\kappa}{(v_d/v_e)} \ell_{ei}^{-1} k_B T_e^{\frac{1}{2}} (T_e - T_i)^{\frac{1}{2}} / e \\
 &\approx \frac{3\sqrt{2}}{2} \frac{\kappa}{\ell_{ei}} k_B T_e^{\frac{1}{2}} (T_e - T_i)^{\frac{1}{2}} / e \quad (\text{IIA95})
 \end{aligned}$$

where κ is the energy transport coefficient or the fraction of the electron's mean kinetic energy lost in one collision, ν_{ei} is the electron collision frequency and the relationship, ²⁵⁾ $v_d/v_e \approx (\frac{1}{2}\kappa)^{\frac{1}{2}}$ in the steady state has been used for the approximation. For an e - i collision κ is given by ³¹⁾

$$\kappa = \frac{2m}{M(1 + m/M)} \approx \frac{2m}{M} \quad (\text{IIA96})$$

Then Eq. (IIA95) becomes

$$\begin{aligned}
 E_z &= 2.58 \times 10^{-4} (m/M)^{\frac{1}{2}} \ell_{ei}^{-1} T_e^{\frac{1}{2}} [T_e(^0\text{K}) - T_i(^0\text{K})]^{\frac{1}{2}} \\
 &= 9.48 \times 10^{-7} \ell_{ei}^{-1} T_e^{\frac{1}{2}} [T_e(^0\text{K}) - T_i(^0\text{K})]^{\frac{1}{2}} \text{ for argon.} \quad (\text{IIA97})
 \end{aligned}$$

In order to obtain the value of E_z , both T_e and T_i should be measured. However no data of these temperatures are presently available.

For the local thermal equilibrium ($T_e = T_i$) plasma, $E = 0$.

Finkelnburg and Segal³²⁾ measured, by using a potential probe, $E_z = 10^3$ V/m in the main positive column of an air arc (average $m/M = 3.8 \times 10^{-5}$) with $T = 10^4$ °K and $\ell_{ei} = 2 \times 10^{-6}$ m. For these data Eq. (IIA97) gives

$$T_e - T_i = 1.59 \times 10^2, \quad [\text{°K}] \quad (\text{IIA98})$$

which means $(T_e - T_i) \times 100/T = 1.59\%$ deviation from the thermal equilibrium condition. Olsen³³⁾ calculated, from the spectroscopically measured temperature, that $E_z = 0.6 \times 10^3$ V/m at the main positive column of an argon arc plasma with $T = 1.4 \times 10^4$ °K and $\ell_{ei} = 2 \times 10^{-6}$ m. For these data Eq. (IIA97) gives

$$T_e - T_i = 1.13 \times 10^2 \quad [\text{°K}]. \quad (\text{IIA99})$$

This is 1.1% deviation from the equilibrium condition.

If there is no space charge distribution in the entire plasma, E_z is simply given by the ratio of arc voltage to electrode spacing. The actual E_z in the positive column is, however, always smaller than that simple ratio due to the space charges distributed near the electrodes. See Fig. (IIA21).

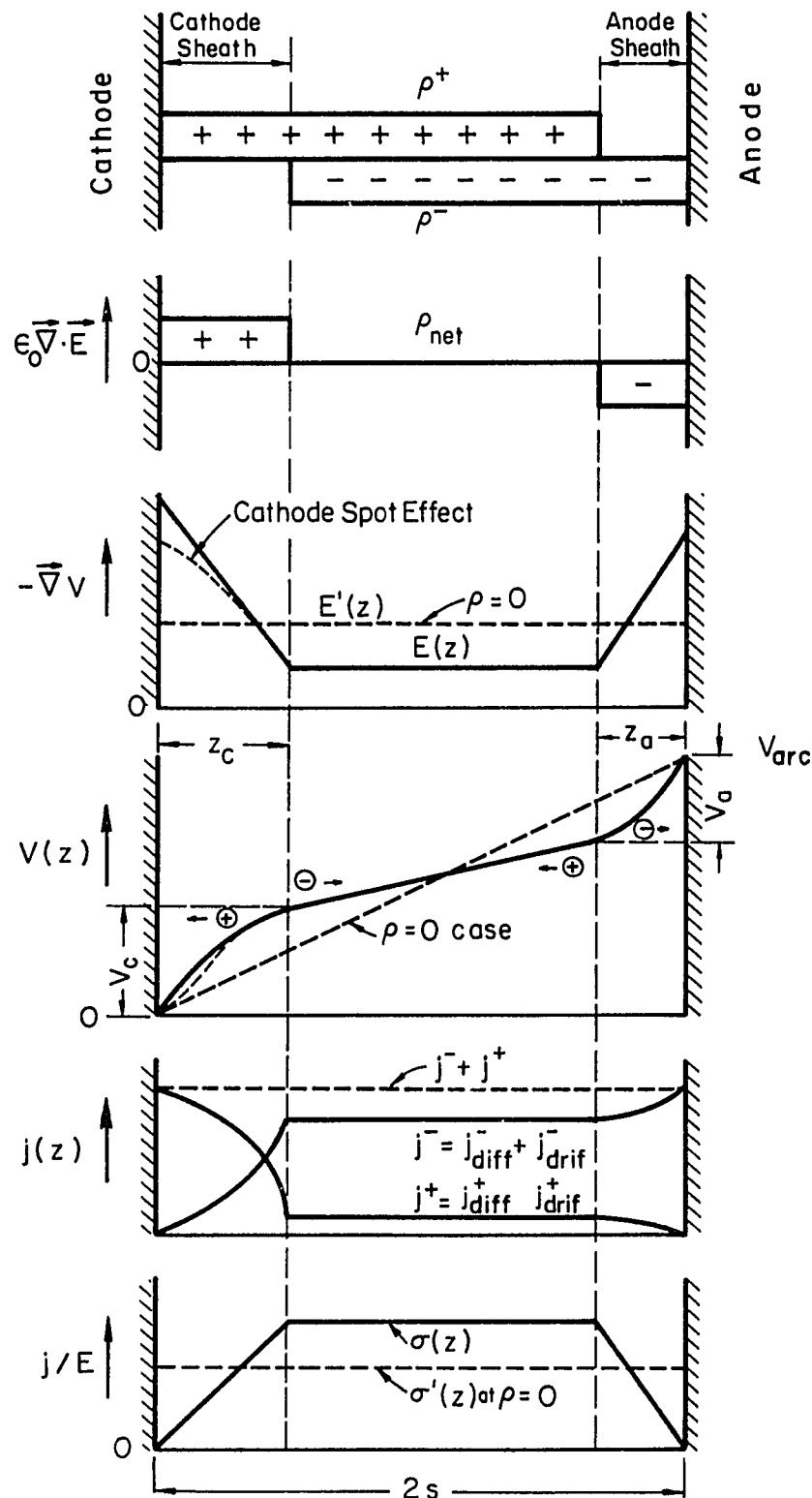


Fig. (II A 21) Cathode and Anode Fall Boundaries near Electrodes.

V_a and V_c : Anode and Cathode Falls

z_a and z_c : Anode and Cathode Fall Spaces or Sheaths

Near the electrodes there exist well-known cathode and anode falls, although the associated physics is not yet well known. The anode fall space of an atmospheric, high temperature arc has been directly measured by Block and Finkelnburg.¹⁶⁾ They used a potential probe connected with an optical grating which is placed on another fixed grating. A light beam passing through the two gratings and received by a photo-detector makes a fringe pattern on the oscilloscope screen. The counting of the number of fringes gives the knowledge of the precise distance of the probe from the anode surface. Their results show that the anode fall-space is 2μ which is on the order of one MFP length of the ions and that the maximum extension (or tail) of the anode fall-space is about 100μ . Near the anode, the positive ions are quickly repelled from the vicinity due to the externally applied positive charge on the anode surface. The anode fall-space, which is a sheath of extreme deficiency of ions, is usually understood to be on the order of one ion MFP length, ℓ_{ii} ($= \ell_{ee} / 4 \sqrt{2}$). The magnitude of the anode fall is influenced by the externally applied steady current which modifies the boundary condition and the space charge density. The effect of the steady current can be taken into account adding an extra factor in Eq. (IIA77) as³⁰⁾

$$\vec{E}_s(z) = - \frac{k_B T_e}{e} \left(1 + \xi \frac{\mu_i}{\mu_e}\right) (\vec{\nabla} n_z / n_o). \quad (\text{IIA100})$$

Here, $\xi (\gg 1)$ is the degree of velocity unbalance due to the steady current, which is defined by

$$v_e = (1 + \xi) v_i \approx \xi v_i. \quad (\text{IIA101})$$

Noticing that $\xi \gg 1$, one can further approximate:

$$\begin{aligned} \xi &\approx \frac{v_e}{v_i} \\ &= - \frac{j_e}{nev_i} \\ &\approx \frac{j_e}{eD_a} \left(\frac{dn}{dz} \right)^{-1} \\ &\approx \frac{j}{\mu_i k_B T_e} \left(\frac{dn}{dz} \right)^{-1}. \end{aligned} \quad (\text{IIA102})$$

Substituting this expression into Eq. (IIA100), one has

$$\begin{aligned} E_s(z) &= E_s^o + E_s^j \\ &= - \frac{k_B T_e}{e} \frac{\vec{\nabla} n_z}{n_o} - \frac{\vec{j}}{en_o \mu_e} \\ &= - \frac{k_B T_e}{e} \frac{\vec{\nabla} n_z}{n_o} - \frac{\vec{j}}{n_o} \frac{(3mk_B T_e)^{1/2}}{e^2 \ell_e}. \end{aligned} \quad (\text{IIA103})$$

In calculating the numerical factor, the last term (E_s^j), which is the correction due to the external current flow, is given by

$$E_s^j = -2.37 \times 10^{11} \frac{j}{n_o} \frac{\sqrt{T_e(^oK)}}{l_e} [V/m] \quad (\text{IIA104})$$

One can now calculate the magnitude for $T_e = 10^4$ °K plasma where $l_e = 6 \times 10^{-6}$ [m], $n_e = 10^{22}$ [m⁻³], and $j = 3 \times 10^6$ [Amps/m²].

For these values Eq. (IIA104) gives

$$E_s^j = -1.19 \times 10^3 [V/m]. \quad (\text{IIA105})$$

On the other hand the term E_s^0 , free from the external current flow, can be calculated as follows. Since the longitudinal ambipolar diffusion length, Λ_a is given by $2s/\pi$ (where s is the one half of the electrode spacing), the longitudinal density distribution is given by

$$n(z) = n_o \cos(\pi z/2s). \quad (\text{IIA106})$$

Taking the spatial derivative of Eq. (IIA106) and substituting it into Eq. (IIA103), one has

$$E_s^0 = -8.62 \times 10^{-5} T_e(^oK) \frac{\pi}{2s} \sin(\pi z/2s) [V/m]. \quad (\text{IIA107})$$

Hence for the arc with $s = 3 \times 10^{-3}$ m and $T = 10^4$ °K,

$$E_s^0 = -1.27 \times 10^2 [V/m]. \quad (\text{IIA108})$$

The external current dependent term (E_s^j) is therefore one order of magnitude larger than the pure ambipolar diffusion term (E_s^0). When one calculates Eq. (IIA104) for the data by Finkelnburg and Segal³²⁾

such that $T_e = 1.2 \times 10^4$ °K, $n_e = 6.5 \times 10^{22}$ m⁻³, $\ell_e = 4 \times 10^{-6}$ m and $j = (1 \sim 5) \times 10^7$ amps m², the calculation gives

$$E_s^j = - (1 \sim 5) \times 10^3 \quad [V/m], \quad (\text{IIA109})$$

which is in excellent agreement with their experimental value of $(1 \sim 4) \times 10^3$ V/m measured in the extended region of the cathode fall. Numbers in parentheses of Eq. (IIA109) and experimental values correspond to each other. (Note that the theoretical expression of Eq. (IIA100) is the same for the anode fall and for the cathode fall whose space is on the order of one electron MFP. However, in the proximity of the cathode, their experimental data suggests that the true sheath field is

$$E_{sh} \gg 4 \times 10^3 \quad [V/m]. \quad (\text{IIA110})$$

This is justified because of the existence of the thermionic emission in the proximity of the cathode surface. Since the anode has also very suppressed type of thermionic emission in the proximity of the anode,³⁰⁾ the accurate evaluation of Eq. (IIA104) is difficult without having the precise knowledge of T_e at the anode surface. On the other hand, an externally cooled anode acts as a heat sink. In such case again a thermoelectric power limited sheath will be formed but one has to include the effect of external current in Eq. (IIA93):

$$\begin{aligned}
 \vec{E}_T &= -0.7 \frac{k_B}{e} \left(1 + \xi \frac{\mu_i}{\mu_e} \vec{\nabla} T \right) \\
 &= -0.7 \frac{k_B \vec{\nabla} T}{e} - 0.7 \frac{j}{(\sigma k_B/e)} \sqrt{\frac{m}{M}} \\
 &\equiv -6.05 \times 10^{-5} \vec{\nabla} T - 3.45 \times 10^2 \frac{j}{\sigma}. \quad (\text{IIA111})
 \end{aligned}$$

Magnitude of the current free term is given by Eq. (IIA94) and for the same plasma ($j = 3 \times 10^6$, $\sigma = 3 \times 10^3$) the current dependent term becomes

$$\vec{E}_T = -3.45 \times 10^5. \quad [\text{V/m}] \quad (\text{IIA112})$$

Fig. (IIA22) shows a schematic of the axial electric field for a plasma with $T = 10^4 \text{ }^\circ\text{K}$ whose $\ell_e = 6 \times 10^{-6} \text{ m}$ and $n_e = 10^{22} \text{ m}^{-3}$. Notice that in Fig. (IIA22) the electric field due to the pure ambipolar diffusion is an internal (or primitive) electric field, while the others are externally applied electric fields.

[IIA-10] Current Density Distribution

(a) Radial Direction, $j(r)$

Only diffusional current is generated in the radial direction either by the density gradient ($\vec{\nabla} n$), temperature gradient ($\vec{\nabla} T$) or pressure gradient ($\vec{\nabla} p$) of the plasma. The expression of diffusion current densities can be derived from $e\vec{\nabla}(nk_B T/mv)$:

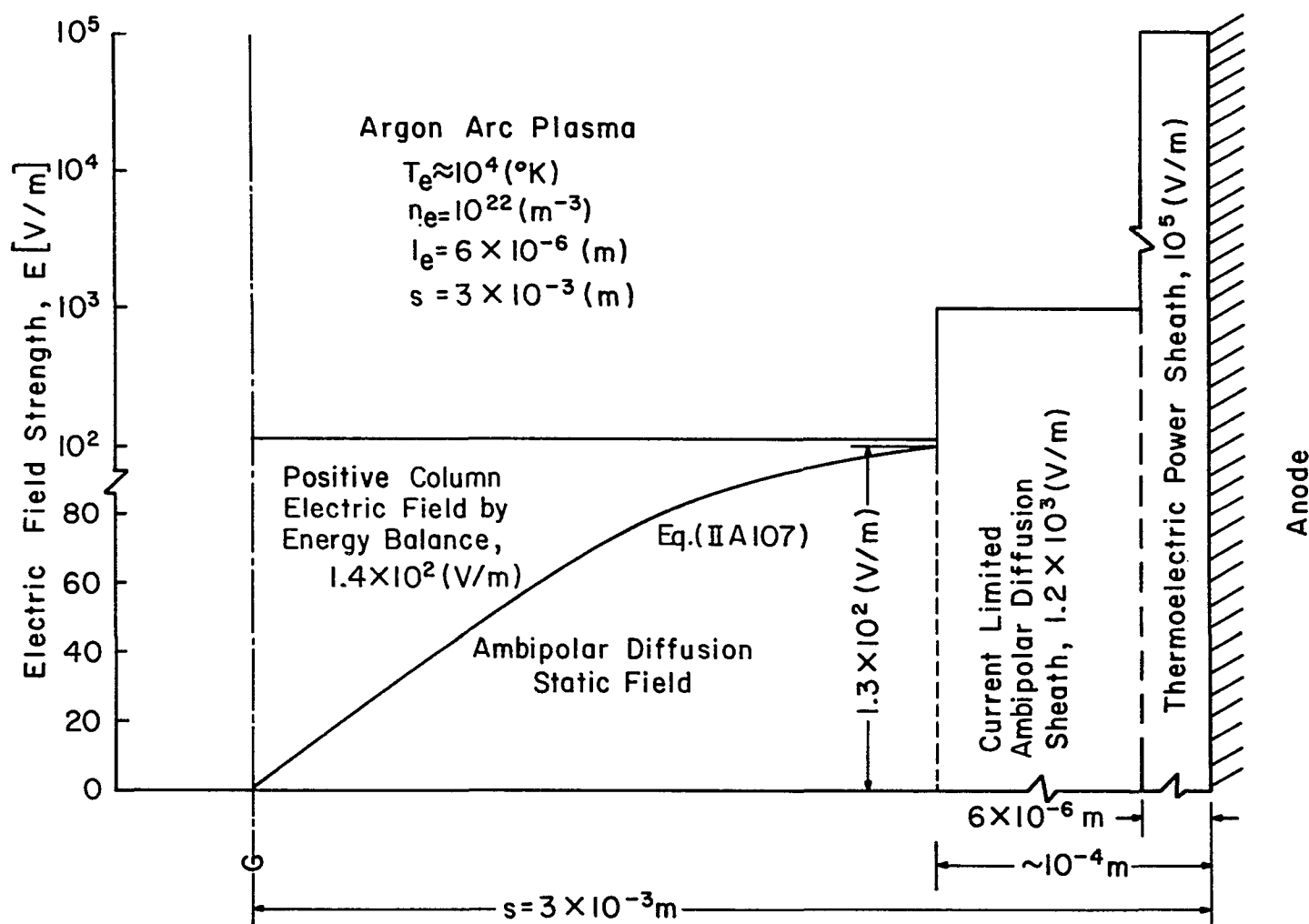


Fig. (IIA22) Axial Electric Field Distribution (Actual and Primitive Electric Fields).

$$\begin{aligned}
 j_{\text{diff.}}^-(r) &= -e\vec{\nabla}(nk_B T/mv) \\
 &= -eD_e \vec{\nabla}n - \frac{\sigma_0 k_B}{e} \vec{\nabla}T - \frac{\sigma_0}{en_0} \vec{\nabla}p \\
 &= -\sigma_0 \left\{ \frac{k_B T}{e} \frac{\vec{\nabla}n}{n_0} + \frac{k_B}{e} \vec{\nabla}T + \frac{1}{en_0} \vec{\nabla}p \right\} \\
 &\equiv \sigma_0 (\vec{E}_n + \vec{E}_T + \vec{E}_p), \quad [\text{Amp}/\text{m}^3] \quad (\text{IIA113})
 \end{aligned}$$

where $\sigma_0 = n_0 e^2 / mv$ and n_0 is the density from the center to the boundary edge. E_n , E_T and E_p denote the internal electric fields due to the density, temperature and pressure gradients, respectively.

The total diffusion current is

$$j_{\text{diff.}}^+(r) + j_{\text{diff.}}^-(r) = 0 \quad (\text{IIA114})$$

where j^+ and j^- designate the ion and electron current, respectively.

(b) Axial Direction, $j(z)$

If the plasma had no net space charge or was spatially homogeneous,

$$j_{\rho=0}(z) = \sigma' \left(\frac{V_{\text{arc}}}{2s} \right) = I_{\text{arc}} / \pi r^2 \quad [\text{Amp}/\text{m}^3] \quad (\text{IIIA115})$$

where $\sigma' = 2sI_{\text{arc}} / \pi r^2 V_{\text{arc}}$ is the conductivity for $\rho = 0$, $2s$ is the electrode spacing and I_{arc} is the externally applied arc current.

Since there are space charges near the electrodes, the net local current is given by

$$j_{\text{net}}(z) = j_{\text{drift}}(z) + \{ j_{\text{diff.}}^+(z) + j_{\text{diff.}}^-(z) \} \quad (\text{IIA116})$$

where the expression of $j_{\text{diff.}}$ is the same as in Eq. (IIA113) but the gradients are to be taken in the z-direction instead of the r-direction.

Fig. (IIA23) shows the vector relations of the diffusional (primitive) and drift (actual) currents with $\vec{\nabla}n$, $\vec{\nabla}T$ and \vec{E} .

Radiative Power Coefficient

[IIA-10] Radiation Power Density (Q_{rad})

The body of an arc plasma contains energy in two forms, namely in the form of matter (kinetic energies) and in the form of fields, such as the radiation field (black body, Bremsstrahlung excitation and recombination radiation energies). When the matter (plasma constituents) and the radiation field are in equilibrium, namely when $T_e = T_i = T_n \equiv T_g$, $\epsilon(\nu)_{\text{emission}} / k(\nu)_{\text{absorption}} = (2\nu^2/c^2)k_B T_{\text{BB}}$ and $T_g = T_{\text{BB}}$ (blackbody temperature) the system is in local thermodynamic equilibrium (LTE). Photons in such a system are absorbed and emitted by ground state atoms. The integrated radiation flux is isotropic and is only a function of the black body temperature ($T_{\text{BB}} = T_g$);

$$\begin{aligned} q_T &= \sigma_{\text{ST}} T_{\text{BB}}^4 \\ &= 5.67 \times 10^{-8} T_{\text{BB}}^4 (\text{°K}) [\text{Watt/m}^2]. \end{aligned} \quad (\text{IIA117})$$

where σ_{ST} is the Stefan's constant and q_T is called blackbody or

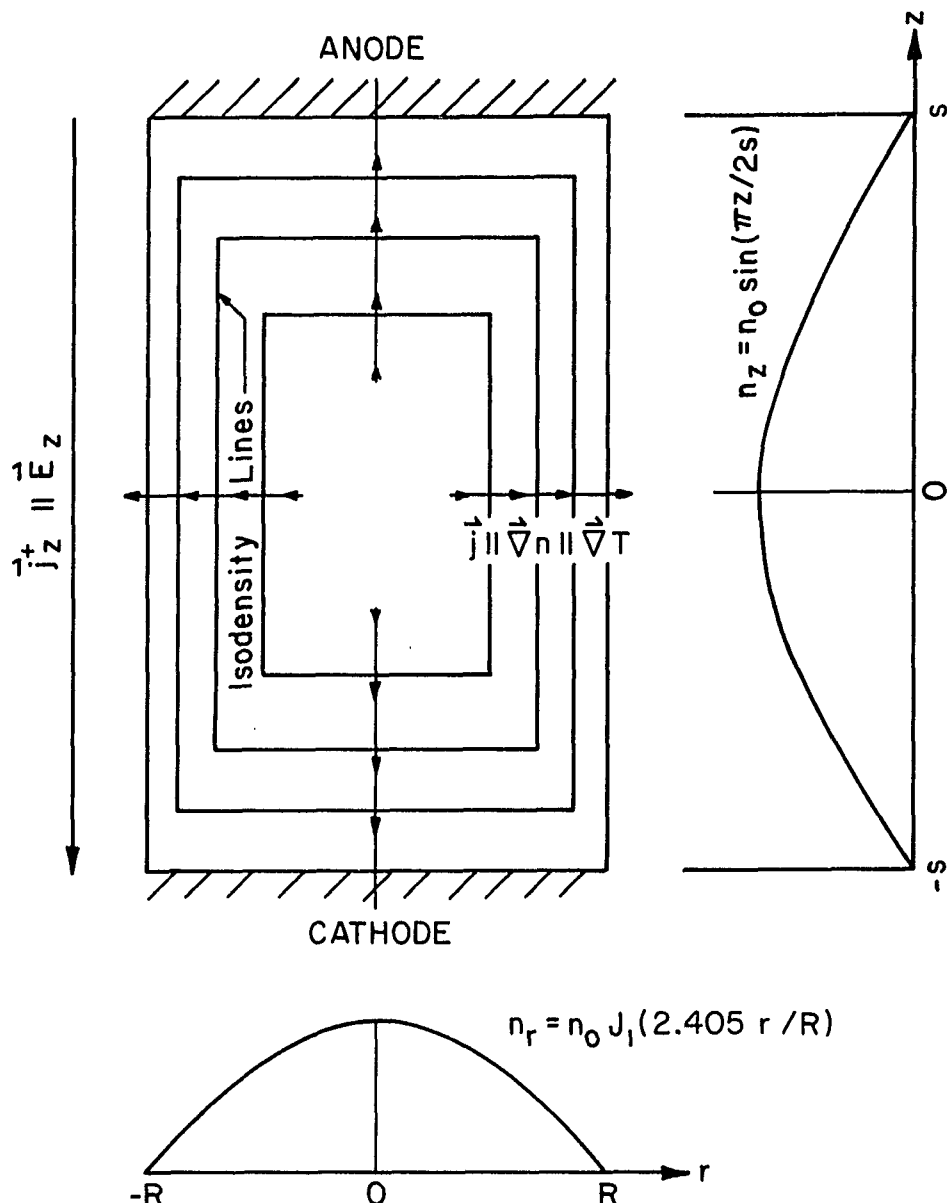


Fig.(IIA23) Vector Relations of Primitive and Actual Currents with $\vec{\nabla}n$, $\vec{\nabla}T$, and \vec{E} .

thermal radiation flux. Actually, only very dense and very extended plasma can be in pure thermodynamic equilibrium such as that produced in a nuclear explosion.³⁴⁾ In laboratory plasmas the emitted radiation is several orders of magnitude less than the corresponding black body radiation.³⁵⁾ Therefore Eq. (IIA117) simply presents the maximum radiation flux possible at the temperature. The actual radiation flux of a plasma at $T = 10^4 \text{ }^{\circ}\text{K}$ is therefore

$$q_{\text{rad}} \ll q_{\text{rad}}^{\text{BB}} = 5 \times 10^8 \text{ [Watt/m}^2\text{].} \quad (\text{IIA118})$$

Note that the Joule heating energy ($3 \times 10^9 \text{ Watt/m}^3$) of the corresponding plasma is still one order of magnitude larger than the radiation power density ($\nabla \cdot q_{\text{rad}}^{\text{BB}} \text{ Watt/m}^3$).

For a plasma whose radiation is not in thermodynamic equilibrium with matter (plasma-constituents) but which is hot, fully ionized, and free from magnetic field, the principal source of radiation is bremsstrahlung where photons are absorbed and emitted by free-free electron transitions. The total power density is given by Spitzer,²⁾ which was obtained by a quantum mechanical treatment:

$$\begin{aligned} Q_{\text{rad}}^{\text{BM}} &= \left(\frac{2\pi k_B T}{3m} \right)^{\frac{1}{2}} \frac{32\pi e^6}{3c^3 mh} z^2 n_e n_i \bar{g}_{\text{ff}} \\ &= 1.42 \times 10^{-40} z^2 n_e n_i T^{\frac{1}{2}} (\text{ }^{\circ}\text{K}) \bar{g}_{\text{ff}} \text{ [Watt/m}^3\text{]} \quad (\text{IIA119}) \end{aligned}$$

where $\bar{g}_{\text{ff}} = 1.103$ in the Born approximation (which is correct when

$T > 10^7 \text{ } ^\circ\text{K}$) and n_e and n_i are in the units of m^{-3} . The value calculated by Eq. (IIA119) is valid for temperatures less than $10^7 \text{ } ^\circ\text{K}$.

Thomson³⁶⁾ corrected Eq. (IIA119) for the region where the Born approximation cannot be assumed and the result is shown in Fig. (IIA24).

According to Eq. (IIA119), a plasma with $T = 10^4 \text{ } ^\circ\text{K}$ ($n_e = n_i = 10^{22} \text{ m}^{-3}$) produces bremsstrahlung (BM) power density

$$Q_{\text{rad}}^{\text{BM}} \leq 1.57 \times 10^6 \quad [\text{Watt/m}^3], \quad (\text{IIA120})$$

whereas Thomson's graph says

$$Q_{\text{rad}}^{\text{BM}} = 1.57 \times 10^2 \quad [\text{Watt/m}^3]. \quad (\text{IIA121})$$

This much energy is lost from electrons per unit volume during the encounters with ions. The continuum spectrum of bremsstrahlung radiation is limited such that $mv_e^2/2 \gg h\nu > \hbar w_p$ and has a sharp peak which occurs at the wavelength³⁷⁾

$$\lambda = \frac{7.2 \times 10^7}{T_e(\text{ }^\circ\text{K})} \quad [\text{\AA}]. \quad (\text{IIA122})$$

However the self-absorption coefficient of electrons for the continuum is given by³⁷⁾

$$\begin{aligned} k_{ab} &= 6.36 \times 10^{-47} \frac{n_e n_i}{(k_B T)^{3/2}} \frac{c^2}{2\nu^2} \quad [\text{cgs}] \\ &= 1.95 \times 10^{-28} \frac{n_e n_i}{T^{3/2}} \lambda^2 \quad [\text{MKS}]. \end{aligned} \quad (\text{IIA123})$$

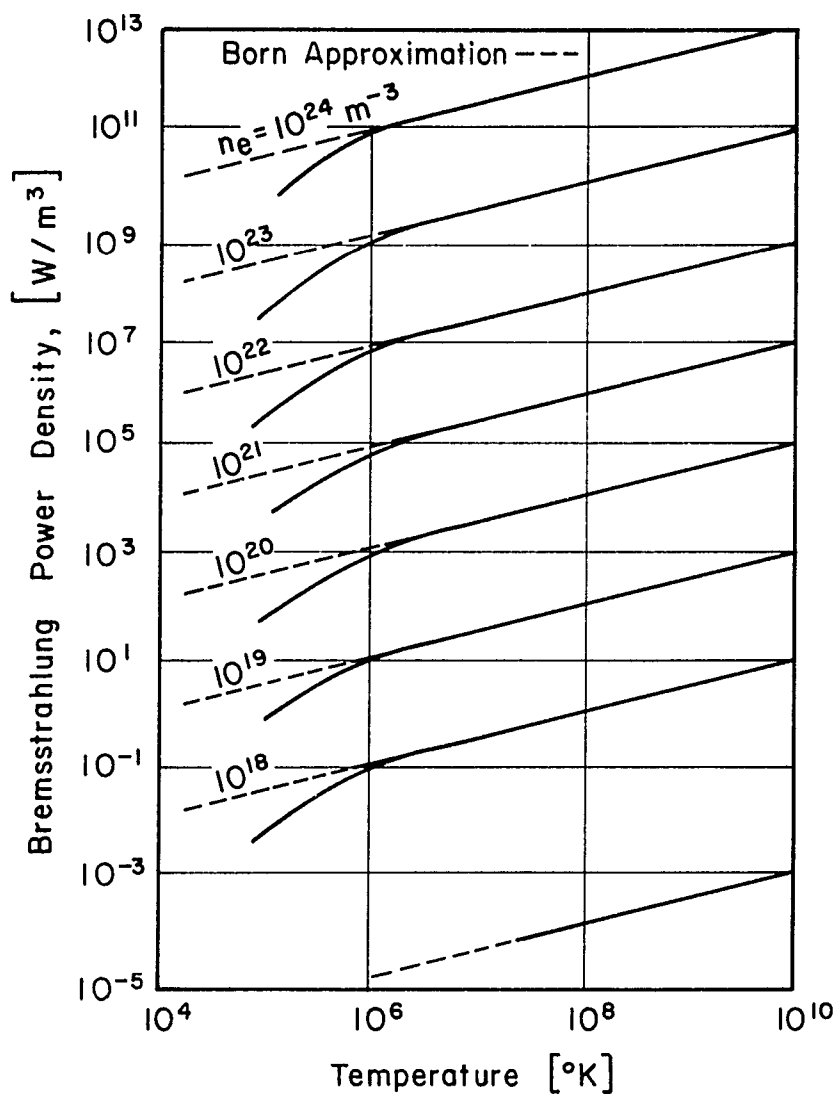


Fig. (IIA24) Thomson's Graph of Bremsstrahlung Power Density as a Function of Temperature. [After Thomson]³⁶⁾

Thus the absorption length $k_{ab}^{-1} = 97 \text{ m}$ from Eq. (IIA123) at the peak bremsstrahlung wavelength $\lambda = 7.2 \times 10^3 \text{ Å}^{\circ}$ for a plasma with $T = 10^4 \text{ K}$. This length is very long compared with the arc characteristic length ($\sim 10^{-2} \text{ m}$) and the reabsorption of bremsstrahlung radiation by electrons is negligible (optically thin) in this temperature range. Hence all the radiation energy is to be lost outside of the bulk of plasma.

Other radiation mechanisms can be attributed to excitation and recombination radiations where excited atoms interact with electrons. De-excitation (or bound-bound) readiation may take place when a bounded electron transits from an upper excited state (m) to a lower energy state (n) of an excited atoms due to the various collisional processes. The spectrum is therefore a line, centered at a frequency ν_{mn} and the power emitted per unit volume per unit solid angle is expressed by the emission coefficient $\epsilon_{mn}^{38)}$:

$$\begin{aligned}\epsilon_{mn}(T) &= \frac{1}{4\pi} A_{mn} h\nu_{mn} N_m [\text{Watt/m}^3 \cdot \text{sr}] \\ &= 2\pi c^2 r_o \frac{f_{nm}}{\lambda_{mn}^3} \frac{g_n}{g_m} N_m,\end{aligned}\quad (\text{IIA124})$$

where A_{mn} is the transition probability; $r_o = e^2/4\pi\epsilon_0 mc^2 \approx 2.82 \times 10^{-5} \text{ Å}^{\circ}$ is the classical electron radius; f_{mn} is the oscillation strength for the absorption; $\lambda_{mn} = c/\nu_{mn}$; and g_n/g_m is the ratio of the statistical weights of lower to upper states of the line. Eq.

(IIA124) is valid even if LTE does not exist. In case LTE exists, then the electron number density at the upper state, N_m can be calculated from

$$N_m = \frac{N_o(T)}{Z_o(T)} g_m \exp(-E_m/k_B T), \quad (\text{IIA125})$$

where $N_o(T)$ and $Z_o(T)$ are the total number density of atoms and the electronic partition function at temperature T , respectively.

Therefore, radiation power density of one spectral line can be calculated for LTE plasma if these line parameters are known. But it is a difficult task to sum up all possible line spectra of radiative transfer. Even in the experiment, measuring absolute intensities of all spectral lines is not easy. Thus the precise estimation of the contribution from the excitation radiation is left unknown.

When a free electron collides with an atom, the electron energy transits to a lower excited state of the atom and the recombination (or free-bound) radiation occurs. The radiation power density due to this process can be estimated analogously from Eq. (IIA124).

$$\begin{aligned} \epsilon_{f \rightarrow b}(T) &= -\frac{1}{4\pi} \left(\frac{dn_e}{dt} \right) h\nu \\ &= \frac{1}{4\pi} \rho_e n_e n_i h\nu \\ &= \frac{1}{4\pi} \rho_e n_e n_i \left(\frac{3}{2} k_B T_e + \chi_s^r \right), \quad [\text{Watt}/\text{m}^3 \cdot \text{sr}] \end{aligned} \quad (\text{IIA126})$$

where χ_s^r denotes the energy level s of r -times ionized atom, and

ρ_e is the radiative recombination probability of electrons summed over all possible capture states, which is on the order of 10^{-19} [m³/sec⁻¹].²⁵⁾ For an argon plasma with T ≈ 10⁴ °K, $0 < \chi_s^r \lesssim V_i^I = 15.75$ eV and $k_B T_e \approx 1\text{eV} = 1.6 \times 10^{-19}$ Joule; the recombination radiation can be found to be on the order

$$1.6 \times 10^6 < Q_{rad}^{Rec} \lesssim 1.8 \times 10^7. \quad [\text{Watt/m}^3] \quad (\text{IIA127})$$

This is more than four orders of magnitude larger than that of bremsstrahlung radiation and about 1% of the Joule heating energy.

The continuum spectrum of the recombination radiation is distributed through the range of 740 Å < λ ≪ 12,400 Å (because mv_e²/2 ≫ hν > ħω_p). For the shortest wavelength radiation, λ = 740 Å, the absorption length is 7×10^{-4} [m] from Eq. (IIA123), which is about the general arc dimension.

B. RADIAL AND AXIAL ENERGY TRANSPORT OF THE ARC

This section deals with energy transport calculations of the arc plasma using the basic data presented in Section IIA. Examples are executed in most cases for a typical free burning arc plasma with $T \approx 10^4$ °K, but formulae are presented so that the energy transport rates can be calculated for different types of temperature profiles encountered in the other plasma systems.

[IIB-1] Generalized Thermal Conductivity, $\tilde{k}(T)$ and the Heat Flux Potential, $S(T)$

The thermal energy in the plasma transported by the various collisional processes among plasma constituents is called conductive-heat-transport. While the heat of the heavy particles is conducted by the static temperature gradient, the thermal energy of the electrons is carried by the drift due to the electric field. The heat transfer flux due to the electric field (\vec{q}_E) is proportional to the drift current density ($j_{drif.}$):

$$\vec{q}_E = -U_i \vec{j}_{drif.} \quad [\text{Watt}/\text{m}^2]. \quad (\text{IIB1})$$

Here the proportionality constant, U_i , is the average ionization potential³⁹ given by

$$U_i = \frac{\pi}{3} \frac{k_B T}{e} . \quad [\text{Volt}] \quad (\text{IIB2})$$

The total conduction current density can be written as the sum of the drift (or Ohmic) and diffusion current densities:

$$\vec{j}_{\text{cond.}} = \vec{j}_{\text{drif.}} + \vec{j}_{\text{diff.}}$$

$$\equiv \sigma \vec{E}_{\text{eff.}} - \sigma (\vec{E}_n + \vec{E}_T + \vec{E}_p)$$

$$[\text{Amp/m}^2] \quad (\text{IIB3})$$

where $\vec{E}_{\text{eff.}}$ is the effective electric field (sum of the internal and external electric fields) in the plasma and E_n , E_T and E_p are the internal electric fields generated by the density, temperature and pressure gradients of the plasma, respectively. Substituting Eqs. (IIB2) and (IIB3) into Eq. (IIB1), one has

$$\begin{aligned} \vec{q}_E &= -\frac{\pi k_B T}{3 e} \vec{j}_{\text{cond.}} - \frac{\pi k_B T}{3 e} \sigma (\vec{E}_n + \vec{E}_T + \vec{E}_p) \\ &\equiv -\frac{\beta}{\sigma} \vec{j}_{\text{cond.}} - (k_n \vec{\nabla} n + k_T \vec{\nabla} T + k_p \vec{\nabla} p) \\ &\equiv \vec{q}_j + \vec{q}_n + \vec{q}_T + \vec{q}_p . \end{aligned} \quad (\text{IIB4})$$

Here β is a new transport coefficient given by

$$\beta \equiv k_E = \frac{2 k_B T}{3 e} \sigma = 2.84 \times 10^{-4} \sigma T, \quad (\text{IIB5})$$

and q_j is the heat transfer flux due to the externally applied steady current j ($= j_{\text{cond.}}$). Using expressions for E_n , E_T and E_p given by Eq. (IIA113), one can obtain the other transport coefficients:

$$\left. \begin{aligned} k_n &= \frac{\pi^2}{3} \left(\frac{k_B}{e} \right)^2 \frac{\sigma}{n_0} T^2 = 2.45 \times 10^{-8} \frac{\sigma}{n_0} T^2 \\ k_T &= \frac{\pi^2}{3} \left(\frac{k_B}{e} \right)^2 \sigma T = 2.45 \times 10^{-8} \sigma T \\ k_p &= \frac{\pi^2}{3} \frac{k_B}{e^2} \frac{\sigma}{n_0} T = 1.78 \times 10^{15} \frac{\sigma}{n_0} T \end{aligned} \right\} \text{(IIB6)}$$

where n_0 is the density from the center of the arc column to the boundary edge. Thus for a plasma with $T = 10^4$ °K ($\sigma = 3 \times 10^3$ ohm $^{-1}$ m $^{-1}$, $n_0 = 10^{22}$ m $^{-3}$, and $j_{\text{cond.}} = 5 \times 10^6$ Amps/m 2), the individual modes of the heat transport are given by:

$$\vec{q}_j = -\beta \vec{E}_{\text{ex}} = 8.5 \times 10^3 \vec{E}_{\text{ex}} \quad [\text{Watt}/\text{m}^2] \quad \text{(IIB7)}$$

(E_{ex} is the externally applied electric field), and

$$\begin{aligned} q_n &= k_n \vec{\nabla} n \simeq 7.35 \times 10^{-19} \vec{\nabla} n \\ q_T &= k_T \vec{\nabla} T \simeq 7.35 \times 10^{-19} \vec{\nabla} T \quad [\text{Watt}/\text{m}^2] \quad \text{(IIB8)} \end{aligned}$$

$$q_p = k_p \vec{\nabla} p \simeq 5.34 \vec{\nabla} p .$$

These expressions are to be used for the calculations of the conductive-heat-transport rates of electrons in the later Subsections.

Since the transport coefficients given by Eqs. (IIB5) and (IIB6) have different dimensions, the heat transfer rates must be evaluated individually as given by Eqs. (IIB7) and (IIB8). However, if a

generalized thermal conductivity, \tilde{k} is introduced and defined by

$$q_E dr = \tilde{k} dT \quad (\text{IIB9-a})$$

$$\equiv -\left(k_E \frac{dV}{dT} + k_n \frac{dn}{dT} + k_T + k_p \frac{dp}{dT}\right) dT,$$

i.e., $\tilde{k} = k_T + k_E (dV/dT) + k_n (dn/dT) + k_p (dp/dT)$; (IIB9-b)

then the \tilde{k} has the same dimension as k_T [Watt/m °K] and the theoretical treatment of the heat transfer can be greatly simplified.

Further, if one defines another new quantity, $S'(T)$ which is given by the integration of Eq. (IIB9-a) for the general q ,

$$S'(T) = \int_0^R q dr = - \int_{T_o}^{T_R} \tilde{k}(T) dT \quad [\text{Watt}/m] : \quad (\text{IIB10})$$

the heat transfer flux q can be calculated as a gradient of S' :

$$\vec{q} = \vec{\nabla} S' . \quad [\text{Watt}/m^2] \quad (\text{IIB11})$$

The S' -function, defined by the differentials $dS' = qdr = -\tilde{k}dT$, was first introduced by Schmitz³⁴ and is called heat flux potential because of the relationship of Eq. (IIB11). However, the S -function defined by $dS = -qdr = kdT$ is used more customarily than S' -function because of the symmetry in the energy equation expressed by S instead of T :

$$S(T) = \int_{T_R}^{T_o} \tilde{k}(T) dT, \text{ and } q = -\vec{\nabla} S. \quad (\text{IIB12})$$

Fig. (IIB1) is a schematic to show the two different calculation methods of the conductive heat flux (q), with and without using the heat flux potential (S). At this stage there is no special advantage to use S -functions since the temperature profile is supposed to have been measured. However, to predict the q -profile from the solution of the energy equation, the introduction of the S -function makes the mathematics very easy.

[IIB-2] Energy Equations for the Arc Plasma

Energies in the arc plasma are balanced in the manner given by Eq. (IIA7). The basic energy equation of Eq. (IIA7-b) can be expressed in cylindrical coordinates as

$$\begin{aligned} \frac{1}{r} \frac{\partial}{\partial r} (r \tilde{k}_r \frac{\partial T}{\partial r}) + \frac{\partial}{\partial z} (\tilde{k}_z \frac{\partial T}{\partial z}) + \sigma(T) E_z^2 - Q_{rad}(T) \\ = \rho c_p (u_r \frac{\partial T}{\partial r} + u_z \frac{\partial T}{\partial z}) - \frac{n}{g_c} \left(\frac{u_r}{\partial z} \right)^2 - u_r \frac{dp}{dr}, \end{aligned} \quad (IIB13)$$

where $q = -\tilde{k}\nabla T$ and \tilde{k} is the generalized heat conductivity defined in Eq. (IIB9). The orders of magnitude of the quantities in Eq. (IIB13) have been calculated in Section IIA and are summarized here. For a plasma with $T \approx 10^4$ °K:

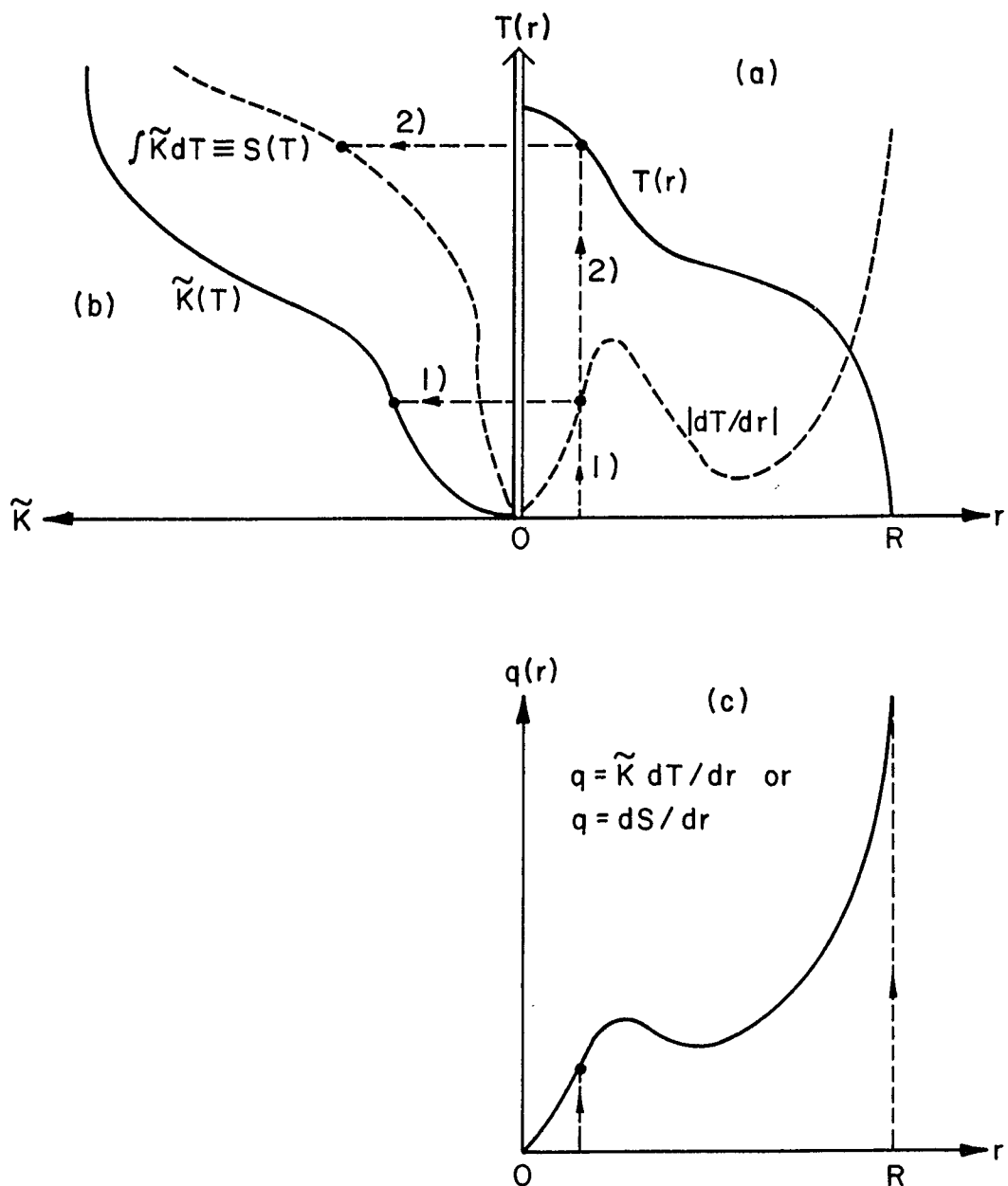


Fig. (II B 1) Two Calculation Methods of the Conductive Heat Flux, q :

Step: $\left\{ \begin{array}{l} 1) \frac{dT}{dr} \rightarrow K(T) \rightarrow \tilde{K} \frac{dT}{dr} = q \\ 2) T(r) \rightarrow S(T) \rightarrow \frac{dS}{dr} = q \end{array} \right.$

$$\left. \begin{aligned}
 Q_J &\equiv \sigma E_z^2 \approx 3 \times 10^9 \quad [\text{Watt}/\text{m}^3] \quad \text{from Eq. (IIA35)} \\
 Q_{\text{rad}} &\lesssim 2.8 \times 10^7 \quad [\text{Watt}/\text{m}^3] \quad \text{from Eq. (IIA127)} \\
 Q_{\text{fric.}} &\equiv \frac{\eta}{g_c} \left(\frac{\partial u_r}{\partial z} \right)^2 \approx 0.4 \quad [\text{Watt}/\text{m}^3] \quad \text{from} \\
 &\qquad\qquad\qquad \text{Eq. (IIA53)} \\
 \rho c_p &\approx 1.2 \times 10^2 \quad [\text{J}/\text{m}^3 \text{ }^\circ\text{K}] \quad \text{from Figs. (IIA12, 13)} \\
 u_r &\approx 0.3 \quad [\text{m/sec}] \quad \text{from Eq. (IIA51)} \\
 u_p &\lesssim 16 \quad [\text{m/sec}] \quad \text{from Eq. (IIA65)} \\
 p &\approx I j_z / 10^7 (1 - r^2/R^2) \quad [\text{Newton}/\text{m}^2] \quad \text{from} \\
 &\qquad\qquad\qquad \text{Eq. (IIA59)}
 \end{aligned} \right\} \text{(IIB14)}$$

From these data

$$\begin{aligned}
 Q_{\text{pinch}} &\equiv u_r \frac{dp}{dr} = - \frac{4r}{10^7 R^2} I j_z \\
 &\lesssim 1.8 \times 10^4 \quad [\text{Watt}/\text{m}^3]. \quad \text{(IIB15)}
 \end{aligned}$$

Therefore the energy modes in the plasma are of the order,

$$Q_{\text{Joule}} : Q_{\text{rad.}} : Q_{\text{pinch}} : Q_{\text{fric.}} \approx 1 : 10^{-2} : 10^{-5} : 10^{-10} \quad \text{(IIB16)}$$

Thus the plasma heating effects by friction and self-pinching are completely negligible for the energy equation of the plasma at $T \approx 10^4 \text{ }^\circ\text{K}$. However, the radiation cooling effect is not always negligible, especially on the axis where the conduction cooling is small.

It has been pointed out in Subsection (IIA-10) that an arc at $T \approx 10^4$ K is optically thin for the bremsstrahlung radiation (whose peak is at $\lambda \approx 7,200 \text{ \AA}$) and for the most of the recombination radiation ($740 \text{ \AA} < \lambda < 12,400 \text{ \AA}$). Thus, Q_{rad} is only the function of the local equilibrium temperature T as is true for $\sigma(T)$. It is convenient to change the variable T to S (heat potential) in order to solve the energy equation such as Eq. (IIB13) successfully. Since the thermal conductivity \tilde{k} is also a unique function of T in LTE plasma, the variable T is always convertible to the S -variable by using the relationship $dS = \tilde{k}(T)dT$. The obtained $Q_{\text{rad}}(S)$ and $\sigma(S)$ curves can be approximated by polygon (piecewise linear) curves as done by Frind⁴⁰ for $\sigma(S)$. One may write

$$Q_{\text{rad}}(S) = A_i S + B_i \quad (\text{IIB17})$$

$$\sigma(S) = C_i S + D_i ,$$

where A_i and C_i are the slopes of the polygon curves in the i -th subdivision for $Q_{\text{rad}}(S)$ and $\sigma(S)$, respectively with i being an integer number. (B_i and D_i are the intersections of the polygon curves with the ordinate.) The details are shown in Fig. (IIB2). Thus Eq. (IIB13) can be written in forms of the function S :

$$\begin{aligned} \frac{1}{r} \frac{\partial}{\partial r} (r \frac{\partial S}{\partial r}) + \frac{\partial^2 S}{\partial z^2} + (C_i E_z^2 - A_i) S + (D_i E_z^2 - B_i) \\ = \frac{\rho c_p u_r}{\tilde{k}_r} \frac{\partial S}{\partial r} + \frac{\rho c_p u_z}{\tilde{k}_z} \frac{\partial S}{\partial z} . \end{aligned} \quad (\text{IIB18})$$

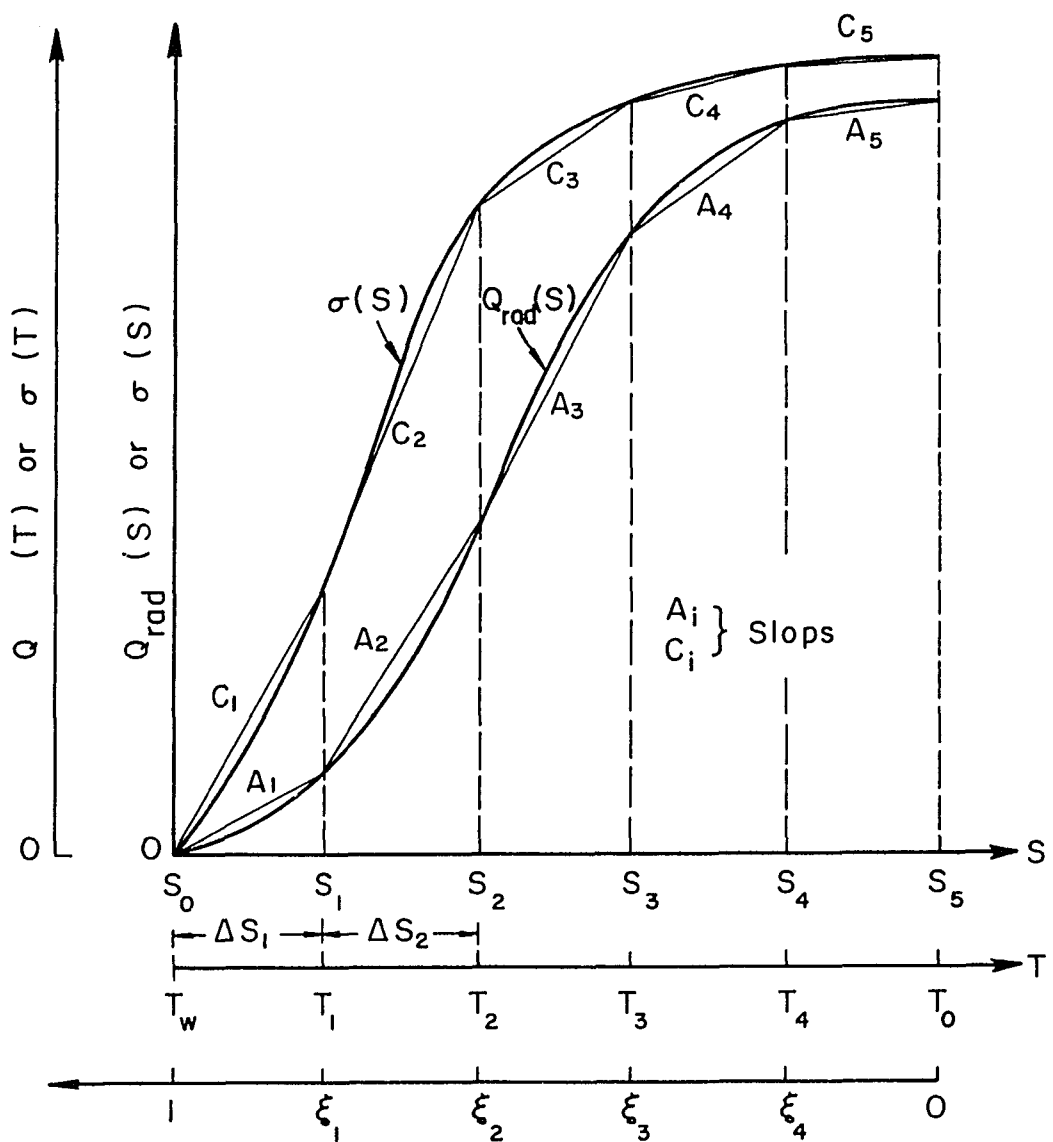


Fig. (II B 2) Polygon Curves for $Q_{rad}(s)$ and $\sigma(s)$,
where
 $S = \int \tilde{k}(T) dT$ and $\xi = r/R$.

Using the method of separation of variables

$$S = S_r(r) S_z(z) , \quad (\text{IIB19})$$

one can separate Eq. (IIB18) into two energy equations; the radial energy equation is given by

$$\frac{1}{r} \frac{d}{dr} \left(r \frac{dS_r}{dr} \right) + G_i S_r + H_i - \frac{\rho c_p u_r}{\kappa_r} \frac{dS_r}{dr} = \lambda_r \quad (\text{IIB20})$$

and the axial energy equation is given by

$$\frac{d^2 S_z}{dz^2} + G_i S_z + H_i - \frac{\rho c_p u_r}{\kappa_z} \frac{dS_z}{dz} = \lambda_z, \quad (\text{IIB21})$$

where λ_r and λ_z are constants for the separation variable. One can choose so that

$$G_i \equiv C_i E_z^2 - A_i \geq 0 \quad (\text{IIB22})$$

$$H_i \equiv D_i E_z^2 - B_i \geq 0 ,$$

since $\sigma(S)E_z^2 \geq Q(S)$ is always satisfied for general plasmas.

[IIB-3] The Radial Energy Transport

Introducing a dimensionless coordinate $\xi = r/R$ (R is the arc radius), Eq. (IIB20) can be written as

$$\frac{d^2 S(\xi)}{d\xi^2} + \left(\frac{1}{\xi} - \frac{\rho c_p u_r R}{\kappa_r} \right) \frac{dS(\xi)}{d\xi} + R^2 G_i S(\xi) = \lambda_\xi, \quad (\text{IIB23})$$

where $\lambda_\xi = R^2 (\lambda_r - H_i)$.

From Eq. (IIB14) and Fig. (IIA7) $\rho c_p u_r R / \tilde{k}_r \approx 2.4$ [dimensionless]. Next, Eq. (IIB23) is evaluated in the separate domains of ξ :

(i) For $\xi \ll \tilde{k}_r$ $\rho c_p u_r R \approx 0.4$ or for the case of no radial flow ($u_r = 0$), Eq. (IIB23) becomes

$$\frac{d^2 S}{d\xi^2} + \frac{1}{\xi} \frac{dS}{d\xi} + R^2 G_i S = \lambda_\xi . \quad (\text{IIB24})$$

The general solution of Eq. (IIB23) is the sum of the Bessel function of zeroth order and the particular solution, namely

$$S(\xi_i) = S_{i-1} + (S_i - S_{i-1}) J_0 [\xi_i R \sqrt{G_i}] + \lambda_\xi / R^2 G_i . \quad (\text{IIB25})$$

The boundary conditions are

$$\left. \begin{aligned} S(1) &= 0, \text{ minimum at the wall, and} \\ S(0) &= S_n + \lambda_r / (C_i E_z^2 - A_i), \text{ maximum at} \\ &\quad \text{the center.} \end{aligned} \right\} \quad (\text{IIB26})$$

The term $\lambda_\xi / R^2 G_i$ can be assumed constant with respect to ξ since A_i, B_i, C_i , and D_i are randomly distributed.

The heat transfer flux is given by the derivative of Eq. (IIB25),

$$\begin{aligned} q(\xi_i) &= - \frac{dS(\xi_i)}{d\xi_i} \\ &= R \sqrt{G_i} \Delta S_i J_1 [\xi_i R \sqrt{G_i}] , \end{aligned} \quad (\text{IIB27})$$

where $\Delta S_i = S_i - S_{i-1}$.

The boundary conditions are

$$q(1) = R\sqrt{G_i} \Delta S_1 J_1 [R\sqrt{G_i}], \text{ and} \quad (\text{IIB28})$$

$$q(0) = 0 .$$

The maximum occurs at ξ_i which satisfies

$$J_1 [\xi_i R \sqrt{G_i}] + 2R G_i^{3/2} J_0 [\xi_i R \sqrt{G_i}] = 0 . \quad (\text{IIB29})$$

For a strongly radiative plasma $G_i(\xi)$ - variation is weak [see, Eq. (IIB22)], then

$$q(\xi_i) \Big|_{\max} \simeq 0.58 R \sqrt{G_i} \Delta S_i \quad (\text{IIB30})$$

at $\xi_i \simeq 1.85/R\sqrt{G_i}$.

Since G_i is proportional to E_z^2 , this maximum becomes larger and appears closer to the arc axis when the externally applied electric field is increased.

(ii) For $\xi \gg \tilde{k}_r / \rho c_p u_r R \simeq 0.4$ or for the case with an explicit radial flow, Eq. (IIB23) becomes

$$\frac{d^2 S}{d\xi^2} - a \frac{dS}{d\xi} + R^2 G_i S = \lambda_\xi , \quad (\text{IIB31})$$

where $a = \rho c_p u_r R / \tilde{k}_r$. The general solutions of Eq. (IIB31) are as follows:

If $a^2 \geq 4R^2 G_i$ (strong radial flow)

$$S(\xi_i) = 2 P_1 e^{\frac{a}{2}\xi_i} \cosh(\xi_i \sqrt{a^2 - 4R^2 G_i}/2) + \lambda_\xi / R^2 G_i \quad (\text{IIB32})$$

and if $a^2 < 4R^2G_i$ (weak radial flow)

$$S(\xi_i) = 2P_1 e^{\frac{a}{2}\xi_i} \cos(\xi_i \sqrt{4R^2G_i - a^2/2}) + \lambda_\xi / R^2 G_i,$$

(IIB33)

where P_1 is the integration constant.

The heat transfer flux for each case is therefore given by

$$\begin{aligned} q(\xi_i) &= - \frac{dS(\xi_i)}{d\xi_i} \\ &= - a P_1 e^{\frac{a}{2}\xi_i} \left\{ \begin{array}{l} \cosh(\xi_i \sqrt{a^2 - 4R^2G_i}/2) \\ \cos(\xi_i \sqrt{4R^2G_i - a^2/2}) \end{array} \right\} \\ &\quad + \left\{ \begin{array}{l} -P_1 \sqrt{a^2 - 4R^2G_i} e^{\frac{a}{2}\xi_i} \sinh(\xi_i \sqrt{a^2 - 4R^2G_i}/2) \\ P_1 \sqrt{4R^2G_i - a^2} e^{\frac{a}{2}\xi_i} \sin(\xi_i \sqrt{4R^2G_i - a^2/2}) \end{array} \right\} \end{aligned} \quad (\text{IIB34})$$

From Eq. (IIB30) we see that the first case ($a^2 \geq 4R^2G_i$) has no physical reality since $q(\xi) < 0$ (heat flow inversion) happens for all ξ .

For the large hydrodynamic flow one must solve the energy equation coupled with the Navier Stokes equation.

For the case $4R^2G_i > a^2$, Eq. (IIB34) is rewritten as

$$\begin{aligned} q(\xi_i) &= P_1^{\frac{a}{2}\xi_i} \{ \sqrt{D_i} \sin(\xi_i \sqrt{D_i}/2) \\ &\quad - a \cos(\xi_i \sqrt{D_i}/2) \} \end{aligned}$$

$$= 2P_1 R \sqrt{G_i} e^{\frac{a}{2}\xi_i} \sin(\xi_i \sqrt{D_1} 2 - \phi), \quad (\text{IIB35})$$

where $D_i = 4R^2 G_i - a^2$ and $\phi = \tan^{-1}(\sqrt{a/D_i})$. Eq. (IIB35) shows that when there is a small radial flow ($a \neq 0$) the q-function deviates from a Bessel function type profile and the amount of q (heat transfer rate) is enhanced at the outer diameter of the plasma column due to the convection effect.

(iii) For $\xi \approx \tilde{k}_r \rho C_p u_r R \approx 0.4$, the general solution is given by the average of the cases i) and ii).

Fig. (IIB3) shows the schematic of $q(\xi)$ given by Eqs. (IIB27) and (IIB35). More precise curves can be obtained by the numerical evaluations of these equations.

The total amount of heat transfer from the plasma per unit length to the wall or to the surrounding atmosphere is given by

$$P_{p \rightarrow w} = 2\pi \int_0^R q(r) dr = 2\pi \int_0^1 q(\xi) d\xi \quad [\text{Watt}] \quad (\text{IIB36})$$

So far the total heat transfer flux $q(\xi)$ has been obtained as a solution of the basic energy balance equation. In the next part individual contributions of $q(\xi)$ are evaluated. Consider the simplest case where each curve of $\sigma(S)$ and $Q(S)$ can be approximated by single straight line. Then the heat potential $S(\xi)$ is obtained from Eq. (IIB25) setting $i = 1$. Substituting the boundary condition $S(1) = 0$, one has

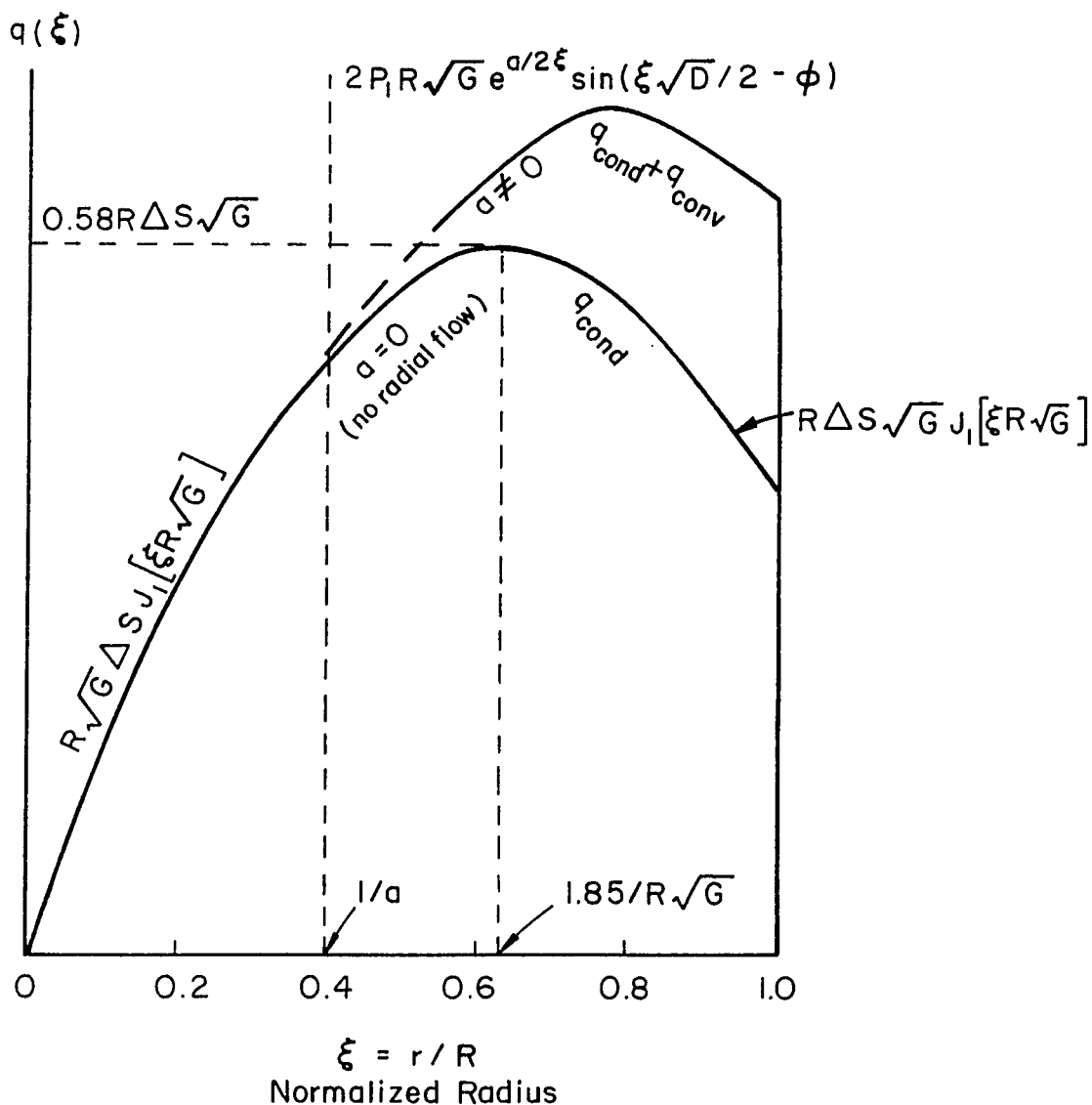


Fig. (II B 3) Conductive-Heat-Transfer Flux, $q(\xi)$, where $a = \rho c_p u_r R / \tilde{k}_r$, $G = C E_z^2 - A$, and $D = 4R^2 G - a^2$.

$$S(\xi) \equiv \int_{T_w}^T k dT \approx \Delta S_1 J_o (2.4\xi) \quad (\text{IIB37})$$

For a relatively low temperature plasma, the thermal conductivity k is almost constant with respect to temperature as is seen from Fig. (IIA7). Therefore Eq. (IIB37) can be easily integrated to yield a radial temperature profile

$$T(\xi) = T_o J_o (2.4\xi) + T_w, \quad (\text{IIB38})$$

where $T_o = \Delta S_1 / k$ is the temperature at $\xi = 0$ (axis) and T_w is the temperature at $\xi = 1$ (wall). The temperature gradient is given by

$$\vec{\nabla} T(\xi) = - T_o J_1 (2.4\xi). \quad (\text{IIB39})$$

The corresponding density gradient is given by Eq. (IIA79) with

$$\Lambda_a = r/2.4\xi :$$

$$\vec{\nabla} n(\xi) = - n_o J_1 (2.4\xi), \quad (\text{IIB40})$$

where n_o is the density at the axis. Using these gradients, individual heat transfer flux can be calculated from Eq. (IIB8) for a plasma with $T_o \approx 10^4$ °K:

$$\left. \begin{aligned} q_n(\xi) &= 1.75 \times 10^{-19} n_o J_1 (2.4\xi) \\ &\approx 1.75 \times 10^3 J_1 (2.4\xi) \\ q_T(\xi) &= 1.75 \times 10^{-1} T_o J_1 (2.4\xi) \\ &\approx 1.75 \times 10^3 J_1 (2.4\xi). \end{aligned} \right\} \quad (\text{IIB41})$$

The result $q_n = q_T$ is reasonable because $q_n/q_T = E_n/E_T$ from Eq. (IIB4) and $E_n/E_T = 1$ if

$$\frac{\nabla n}{n_o} = \frac{\nabla T}{T_o} \quad (\text{IIB42})$$

from Eq. (IIB113). Apparently Eq. (IIB42) holds when $\vec{\nabla}T$ and $\vec{\nabla}n$ are those given by Eqs. (IIB39) and (IIB40). Since the density distribution is given by $n(r) = n_o \exp(\phi/T(r))$, Eq. (IIB42) holds also when ϕ (plasma potential) = T_e (electron temperature).

On the other hand, $\vec{\nabla}p$ can be obtained from Eq. (IIB14) as

$$\vec{\nabla}p(\xi) = -2Ij_z\xi/10^7,$$

then from Eq. (IIB8)

$$q_p(\xi) = 1.07Ij_z/10^6 \approx 4.82 \times 10\xi. \quad (\text{IIB43})$$

This magnitude is about two orders of magnitude smaller than q_n or q_T since $\xi \leq 1$.

Actual amount of the heat flux depends on the plasma diameter R ,

$$q(r) = q(\xi)/R \quad [\text{Watt}/\text{m}^2]. \quad (\text{IIB44})$$

According to experimental data by Schoeck¹⁰ the current density (j) is a weak linear function with respect to the arc current (I) as is plotted in Fig. (IIB4). This means that a certain amount of current density is always needed for the thermionic emission of the arc and kept nearly constant. Thus, from Fig. (IIB4) one can assume that j_z

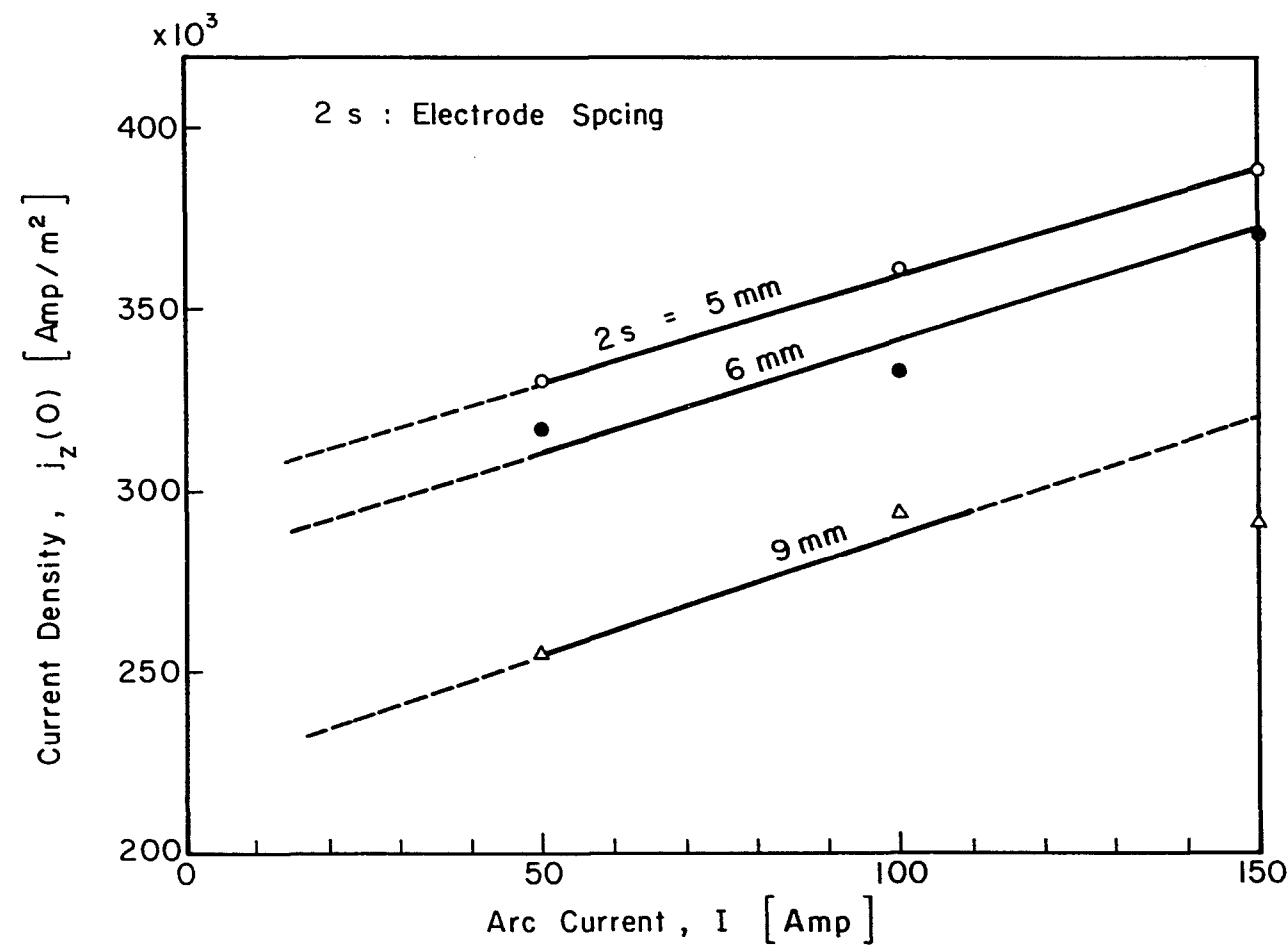


Fig. (II B 4) Thermionic Current Density Plotted from Schoeck's Experimental Data.¹⁰⁾

is about 3×10^6 Amps/m² for a 15 Amp arc at 2s (electrode spacing) = 6mm. The effective plasma diameter is given by

$$R = \sqrt{\frac{I}{\pi j_z(0)}} \simeq 1.3 \times 10^{-3} . \quad [m] \quad (IIB45)$$

The amount the conductive heat transfer flux is therefore given by

$$\begin{aligned} q_{cond}(r) &= \{ q_n(\xi) + q_T(\xi) + q_p(\xi) \} / R \\ &\simeq 2.7 \times 10^6 J_1(2.4 r/R) . \quad [Watt/m^2] \end{aligned} \quad (IIB46)$$

Using an approximate expansion for the integrated Bessel function:

$$\int_0^1 J_1(2.4\xi) d\xi \simeq \int_0^1 \left\{ \frac{2.4\xi}{2} - \frac{(2.4\xi)^3}{16} \right\} d\xi = 0.385, \quad (IIB47)$$

the power per unit length which conducted away from the plasma to surrounding atmosphere can be calculated:

$$\begin{aligned} P_{p \rightarrow w}^{cond} &= 2\pi \times 3.5 \times 10^3 \int_0^1 J_1(2.4\xi) \\ &= 8.5 \times 10^3 \quad [Watt/m] \\ &= 51 \quad [Watt] \quad \text{when } 2s = 6 \times 10^{-3} \text{ m.} \end{aligned} \quad (IIB48)$$

The joule heating energy contained in the main positive column per unit length is given by

$$\begin{aligned}
 P_{\text{Joule}} &= IE_z \\
 &= (15) \cdot (10^3) = 1.5 \times 10^4 \text{ [Watt/m]} \\
 &= 90 \text{ [watt] when } 2s = 6 \times 10^{-3} \text{ m.}
 \end{aligned}$$

(IIB49)

This is about 17% of the input power ($15 \text{ amp} \times 35 \text{ volt} = 525 \text{ watt}$). The rest of the energy may be contained in the boundaries near the electrodes.

The convective heat transfer flux can be calculated from Eqs. (IIA4) and (IIB14) as

$$\begin{aligned}
 q_{\text{conv}}(\bar{r}) &= \rho c_p \bar{u}_r \bar{T} \\
 &= 1.2 \times 10^6, \quad [\text{Watt}/\text{m}^2]
 \end{aligned} \tag{IIB50}$$

where \bar{r} , \bar{u}_r , and \bar{T} denote the average values. Hence, the average power carried away by convection is given by

$$\begin{aligned}
 P_{p \rightarrow w}^{\text{conv.}} &= 2\pi \left(\frac{R}{2}\right) q(\bar{r}) \\
 &= 4.9 \times 10^3 \quad [\text{Watt}/\text{m}] \\
 &= 30 \quad [\text{Watts}] \text{ when } 2s = 6 \times 10^{-3} \text{ m.}
 \end{aligned} \tag{IIB51}$$

The total transferred power by conduction and convection is radially about 80 watts (the remaining power, 10 watts might be transferred toward the axial direction) and the ratio between the two mechanisms is:

$$P_{p \rightarrow w}^{\text{cond.}} : P_{p \rightarrow w}^{\text{conv.}} = 0.63 : 0.37 \quad (\text{IIB52})$$

Fig. (IIB5) shows the schematic of the energy partition of an arc with $T \approx 10^4 \text{ K}$ at $I = 15 \text{ Amps}$.

[IIB-4] The Effect of Electric Field on the Plasma Heat Transfer

Unlike the neutral fluid the motion of the ionized particles is influenced by the electric field. Both the internal (or primitive) and external (or applied) electric fields alter the heat transfer rate via the thermoelectric effect which is expressed by Eq. (IIA22). The first equation of the coupled Eq. (IIA22),

$$\vec{j} = \sigma \vec{E} + \alpha \vec{\nabla} T \quad (\text{IIB54})$$

indicates that when a temperature gradient is present in a steady state, a diffusion current (of electrons) $\vec{\nabla} T$ flows. And if there is no steady current flow ($j = 0$), an electrostatic field (\vec{E}) builds up to such a value that the \vec{j} vanishes:

$$\vec{E} = - \frac{\alpha}{\sigma} \vec{\nabla} T, \quad (\text{IIB55})$$

where $\alpha = 0.7 \sigma k_B/e$ for $z = 1$ according to Spitzer²⁾ and Spitzer and Härm.¹³⁾ Then the second equation of Eq. (IIA22), which is the sum of the heat transfer flux due to the electron motion and the static temperature gradient of heavy particles,

$$\vec{q} = - \beta \vec{E} - k \vec{\nabla} T \quad (\text{IIB56})$$

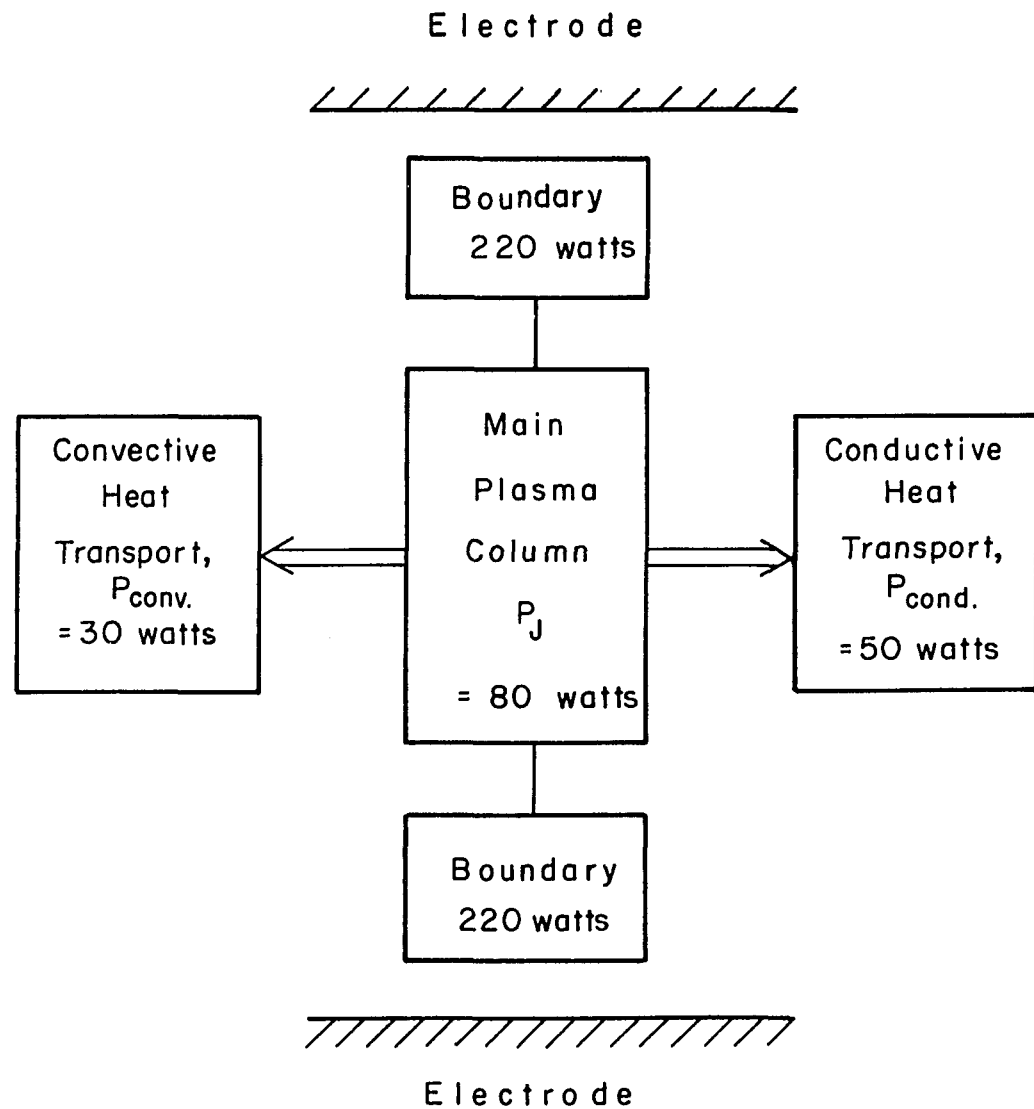


Fig. (II B 5) Energy Partition of an Arc with $T = 10^4$ °K for $I = 15$ Amps. Input Power 520 watts.

$$P_J : P_{rad} : P_{pinch} : P_{fric} = 1 : 10^{-2} : 10^{-5} : 10^{-10}$$

$$P_J : P_{cond} : P_{conv} = 1 : 0.63 : 0.37$$

(No Electric Field Correction)

where $\beta = 3.2 \sigma k_B T/e$ for $z = 1^{2, 13}$ becomes

$$\vec{q} = -\left(k - \frac{\alpha \beta}{\sigma}\right) \vec{\nabla} T$$

$$\equiv -k' \vec{\nabla} T. \quad (\text{IIB57})$$

Here k' is the effective thermal conductivity given by

$$k' = \left(1 - \frac{\alpha \beta}{\sigma k}\right) k$$

$$= 0.42 k \text{ when the conventional (field free)}$$

thermal conductivity is given by

$$k = \frac{10}{2.56} \left(\frac{k_B}{e}\right)^2 \sigma T \text{ for } z = 1. \quad (\text{IIB58})$$

This means that because of the electrostatic field given by Eq. (IIB55), the effective thermal conductivity reduces by 42% compared with the case of the field free. Generally, one can write as

$$k' = \epsilon k. \quad (\epsilon < 1) \quad (\text{IIB59})$$

Spitzer and Härm¹³ calculated the values of ϵ for the various charge number z as is shown in Table (IIB1):

Table (IIB1)

Correction Factor, ϵ

Ion charge, z	1	2	4	16	∞
ϵ	0.4189	0.4100	0.4007	0.3050	0.4000

Therefore the amount of the conductive heat transfer obtained in the last subsection may be "overestimated" for q_T by about 40%.

In the arc plasma the diffusion current arises not only due to the temperature gradient but also due to the density and pressure gradients. Further, there is a steady current flow in the axial direction. These currents are also coupled with the thermal effect and alter the thermal energy flow. The correction for these effects is possible by writing the most general thermoelectric equation:

$$\vec{j} = \sigma \vec{E}_{\text{eff}} + \tilde{\alpha} \vec{\nabla} T \quad (\text{IIB60})$$

$$\vec{q} = -\beta \vec{E}_{\text{eff}} - k_T \vec{\nabla} T.$$

Here $\tilde{\alpha}$ is the generalized transport coefficient given by

$$\tilde{\alpha} = \alpha_T + \alpha_n \frac{dn}{dT} + \alpha_p \frac{dp}{dT} \quad (\text{IIB61})$$

and, α_T and k_T are conventional α and k , respectively. α_n and α_p can be obtained so that the terms, $\alpha_n \vec{\nabla} n$ and $\alpha_p \vec{\nabla} p$ can express the currents due to the concentration and pressure diffusion, respectively. Although those have already given in Eq. (IIA113), they are shown here explicitly for the convenience together with α_T :

$$\left. \begin{aligned} \alpha_T &= 0.7 \frac{k_B}{e} \sigma \\ \alpha_n &= \frac{k_B T}{en} \sigma \\ \alpha_p &= \frac{1}{en} \sigma \end{aligned} \right\} \quad (\text{IIB62})$$

Thus, from Eq. (IIB60) the effective electric field, which is the sum of the external and internal electric fields, is given by

$$\vec{E}_{\text{eff}} = \sigma^{-1} (\vec{j} - \tilde{\alpha} \vec{\nabla} T). \quad (\text{IIB63})$$

Substituting this into the second equation of Eq. (IIB60),

$$\begin{aligned} \vec{q} &= -(\beta/\sigma) (\vec{j} - \tilde{\alpha} \vec{\nabla} T) - k_T \vec{\nabla} T \\ &= -(\beta/\sigma) \vec{j} - \tilde{\epsilon} k_T \vec{\nabla} T. \end{aligned} \quad (\text{IIB64})$$

Here, $\tilde{\epsilon}$ is the generalized correction factor given by

$$\begin{aligned} \tilde{\epsilon} &= 1 - \frac{\beta}{\sigma k_T} \approx \\ &= \epsilon_T + \epsilon_n + \epsilon_p, \end{aligned} \quad (\text{IIB65})$$

where $\epsilon_T = \epsilon$ which has been tabulated in Table (IIB1). The other correcting factors for $z = 1$ can be calculated as:

$$\begin{aligned} \epsilon_n &= 1 - \frac{\beta}{\sigma k_T} \propto_n \frac{dn}{dT} \\ &= 1 - 0.82 \frac{T}{n} \frac{dn}{dT} \\ &= 0.18 \end{aligned} \quad (\text{IIB66})$$

when Eq. (IIB42) holds. On the other hand,

$$\begin{aligned} \epsilon_p &= 1 - \frac{\beta}{\sigma k_T} \propto_p \frac{dp}{dT} \\ &= 1 - \frac{0.82}{nk_B} \frac{dp}{dT}. \end{aligned} \quad (\text{IIB67})$$

Thus for radial direction, where $j = 0$, the conventional heat transfer rates of q_T and q_n should be corrected as

$$\left. \begin{aligned} q'_T &= 0.42 q_T \\ q'_n &= 0.18 q_n \end{aligned} \right\} \quad (\text{IIB68})$$

Eq. (IIB63) represents all electrostatic fields generated in the plasma as well as the applied electric field, which have been calculated in Subsection [IIA-9]. As we have seen in Subsection [IIA-9] very high electric fields build up near the solid wall. These are the sheath electric field due to the large $\vec{\nabla}n$ as a result of the extreme drain of the electron charge by the wall and the boundary electric field due to the large $\vec{\nabla}T$ as a result of the forced cooling of the wall. These electrostatic fields are extremely large compared with that at the main bulk of the same plasma as seen in Fig. (IIA20) and proportional to the magnitude of the gradients, $\vec{\nabla}n$ and $\vec{\nabla}T$. However, the magnitude of the correction factor is still the same as given by Eq. (IIB68), although the magnitude of the heat transfer rate is proportional to these gradients. This situation is easy to understand in Eq. (IIB57).

Next, one has to correct the effect of the steady current flowing longitudinally. From Eq. (IIB63) the correction due to the steady (not the diffusion) current-flow is given by

$$\vec{q}_j'(z) = -\frac{\beta}{\sigma} j_z = -3.2 \frac{k_B}{e} T j_z \\ = -2.76 \times 10^{-4} T(z) j_z(z), \quad (\text{IIB69})$$

where the minus sign means that the electrons are moving against the steady current (Note that Eq. (IIB69) is the heat transfer flux carried by the electron motion.) For a plasma with $T \approx 10^4$ °K and $j_z = 3 \times 10^6$ Amps/m², this correction becomes

$$q_j'(z) = 8.3 \times 10^6 \text{ . [Watt/m}^2\text{]} \quad (\text{IIB70})$$

This is of the same order as the radial conduction given by Eq. (IIB46) and radial convection flows given by Eq. (IIB50). Thus, when those thermoelectric effects are taken into account, the new energy partition is as follows:

$$\left. \begin{aligned} P_{p \rightarrow w}^{\text{cond}}(r) &= 0.42 P_T + 0.18 P_n \\ &= 10.7 + 4.6 = 15.3 \text{ [watt]} \\ P_j^{\text{cond}}(z) &= 8.3 \times 10^6 q_j'(z) \pi R^2 \\ &= 26 \text{ [watt]} \end{aligned} \right\} \quad (\text{IIB71})$$

The convective transport does not change due to the field effect. It should be pointed out that this kind of thermoelectric correction has never been reported in the literature for the practical calculation of the heat transfer in the arc plasma.

[IIB-5] Axial Energy Transport

As is discussed in the last Subsection, there is a net heat flow in axial direction of the positive column due to the steady current, even if the axial temperature gradient is negligible. The formula is given by Eq. (IIB69).

The equation to be solved in this Subsection is the axial energy balance equation given by Eq. (IIB21). Taking the origin of the dimensionless coordinate ($z = z' / s$) at the center of the arc axis, Eq. (IIB21) becomes

$$\frac{d^2 S(z)}{dz^2} - a \frac{dS(z)}{dz} + s^2 G_i S(z) = \lambda'_z , \quad (\text{IIB72})$$

where $a = \rho c_p u_z s / \tilde{k}_z \approx 8.25$ for $u_z = 16 \text{ m/sec}$; $2s = 6 \times 10^{-3} \text{ m}$; and $\lambda'_z = s^2 (\lambda_z - H_i)$. The general solution is

$$S(z) = \exp(\frac{a}{2} z) (C_1 \exp \sqrt{D_i} z + C_2 \exp -\sqrt{D_i} z) + (\lambda'_z / s^2 G_i) , \quad (\text{IIB73})$$

where

$$D_i = a^2 - 4G_i . \quad (\text{IIB74})$$

i) When there is no hydrodynamic flow, i.e., ($a = 0$),

$$S(z) = C_1 \cos 2 \sqrt{G_i} z + (\lambda'_z / s^2 G_i) \\ \therefore q(z) = - \frac{dS(z)}{dz} = 2 C_1 \sqrt{G_i} \sin 2 \sqrt{G_i} z , \quad (\text{IIB75})$$

where we again assumed that $\lambda' z / s^2 G_i$ is a constant with respect to z because of the random distribution of H_i and G_i . From the boundary condition, $S(0) = 0$ and $2\sqrt{G_i} = \pi/2$. Then

$$q(z) = q_w \sin \frac{\pi}{2} z, \quad (\text{IIB76})$$

where $q_w = \pi C_1 / 2$ is the heat flux at the electrode surface.

ii) When there is a hydrodynamic flow (i.e., $a \neq 0$), D_i of Eq. (IIB74) should be negative quantity to obtain a physically meaningful answer of q . Then,

$$\begin{aligned} S(z) &= C_1 \exp \left(\frac{a}{2} z \right) \cos 2\sqrt{D_i} z + \left(\lambda' z / s^2 G_i \right) \\ \therefore q(z) &= q_w \exp \left(\frac{a}{2} z \right) \sin \frac{\pi}{2} z. \end{aligned} \quad (\text{IIB77})$$

Apparently the hydrodynamic flow enhances the heat transfer rate by a factor of

$$\exp \left(\frac{a}{2} \right) = \exp \left(\frac{\rho c_p u_z}{2k_z} s \right) \quad (\text{IIB78})$$

at the electrode surface ($z = 1$).

In Eq. (IIB77) the hydrodynamic flow (u_z) is assumed to start flowing from the origin of z . When u_z is the forced convection flow which start from the cathode (for example, the self-pinch and forced gas flows), q should be written as

$$q(z) = \rho c_p T(z) u(z) + q_w \sin \frac{\pi}{2} z, \quad (\text{IIB79})$$

where

$$T(z) \simeq \frac{1}{k_z} S(z) + T_w$$

$$= T_o \cos (\frac{\pi}{2} z) + T_w \quad (\text{IIB80})$$

$$u(z) = \sqrt{\frac{2p(z)}{\rho}} = \sqrt{\frac{2I}{10^7 \rho}} j_o(z) \text{ for self pinch}$$

and

$$u(z) = u_o \left\{ 1 - \frac{g(z+1)}{u_o} \right\} \quad (\text{IIB81})$$

$$\simeq u_o = 5.5 \text{ m sec for } 1-l/\text{min forced} \\ \text{gas flow from } \phi - \\ 1 \text{ mm orifice.}$$

Fig. (IIB6) shows a schematic of the axial energy flow in the main positive column. The total amount of the thermal energy transferred from the plasma to the electrode surface is given by

$$P_{p \rightarrow w} = \pi \int_0^l R^2(z) q(z) dz. \quad (\text{IIB82})$$

For a temperature profile given by Eq. (IIB80),

$$q_w = - k_z \frac{\partial T(z)}{\partial z} \Big|_{z=1} = \frac{\pi}{2} k_z T_o. \quad (\text{IIB83})$$

Thus, the power transferred from the plasma to the electrodes are calculated as follows:

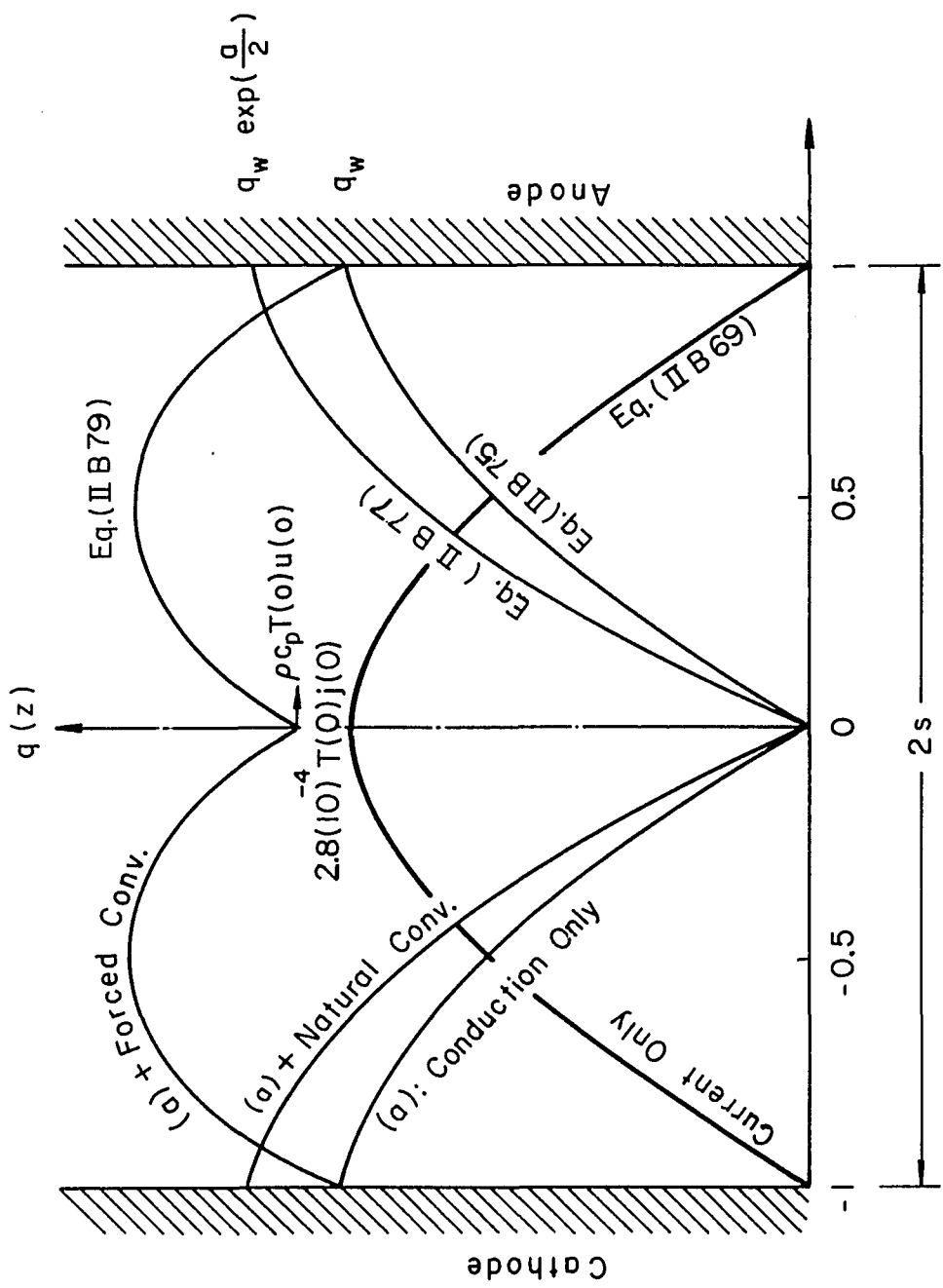


Fig. (II B 6) Axial Energy Transport, where $q_w = \frac{\pi}{2} k_z T_0$ and $a = \rho c_p u_z / k_z$

$$\left. \begin{aligned}
 P_{p \rightarrow A}^{\text{cond.}} &= \pi R^2 \frac{\pi}{2} k_z \frac{T_o}{s} \int_0^1 \sin\left(\frac{\pi}{2} z\right) dz \\
 &\simeq 11 \quad [\text{Watt}] \\
 P_{C \rightarrow A}^{\text{f. conv.}} &= \pi R^2 \rho c_p u_o T_o \int_0^1 \left\{ \cos\left(\frac{\pi}{2} z\right) + \frac{T_w}{T_o} \right\} dz \\
 &\simeq 38.3 \quad [\text{Watt}] \\
 P_{C \rightarrow A}^j &= 2.76 \times 10^{-4} \pi R^2 j_z T_o \int_0^1 \left\{ \cos\left(\frac{\pi}{2} z\right) + \frac{T_w}{T_o} \right\} dz \\
 &\simeq 16.6 \quad [\text{Watt}]
 \end{aligned} \right\} \text{(IIB84)}$$

where f.conv. \equiv forced convection, C \equiv cathode, A \equiv anode. The examples are taken again for a plasma with $T \simeq 10^4$ °K, $k_z \simeq 0.7$ Watt/m °K, $R \simeq 10^{-3}$ m, $u_o \simeq 16$ m/sec (pinch) and $j_z \simeq 3 \times 10^6$ Amp/m². $P^{\text{cond.}}$ in Eq. (IIB84) is the sum of conductances due to the temperature gradient and the density gradient. Multiplying the thermoelectric correction factors, the new $P^{\text{cond.}}$ becomes

$$\begin{aligned}
 P_{p \rightarrow w}^{\text{cond.}} &= 0.42 \times 5.5 + 0.18 \times 5.5 \\
 &= 3.3 \quad [\text{Watt}], \quad \text{(IIB85)}
 \end{aligned}$$

where the equal energy partition from the plasma to the anode and to the cathode is assumed. The total of these heat flows gives 106.3 watts, which is very close to 90 watts, the energy stored in the main positive column. Fig. (IIB7) shows the new energy partition including

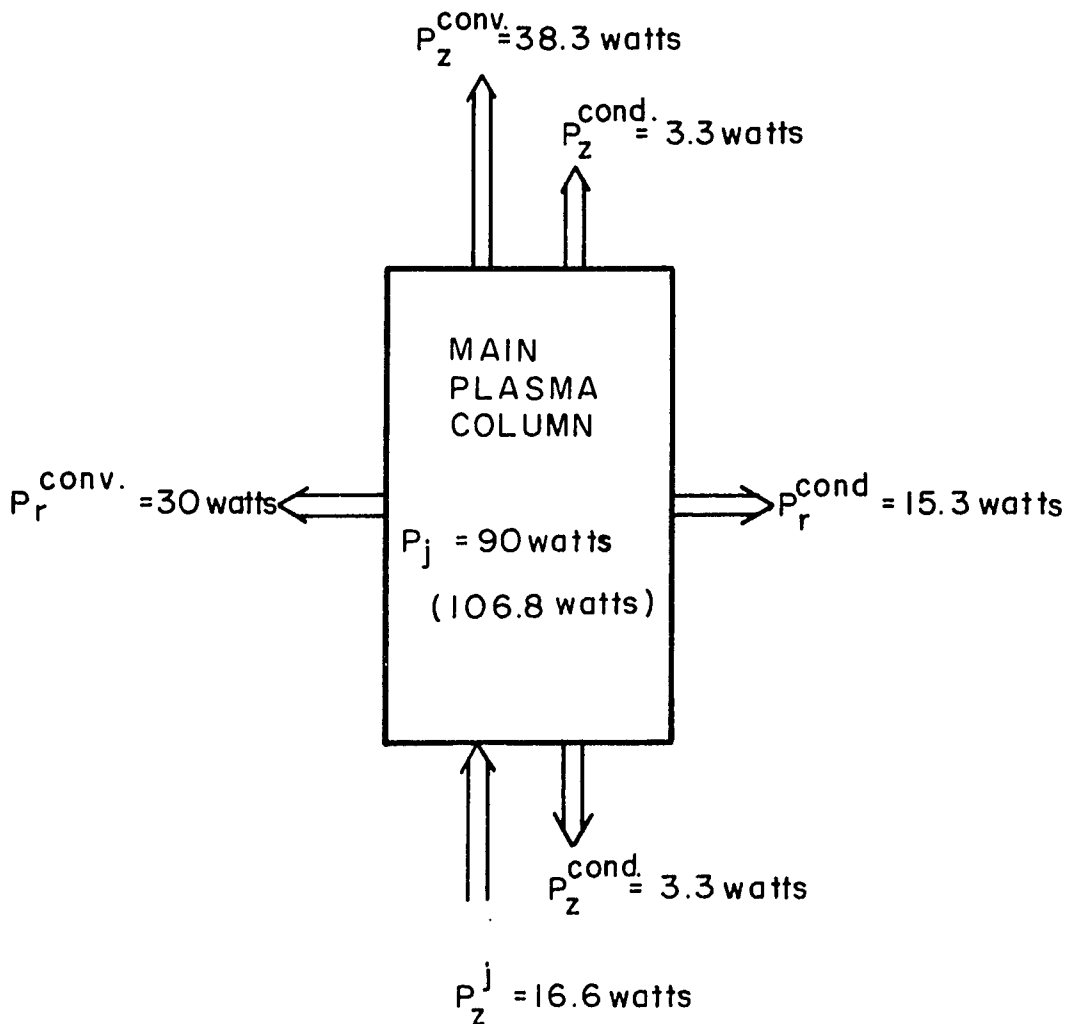


Fig.(II B7) Corrected Energy Partition of an Arc with
 $T = 10^4 \text{ }^{\circ}\text{K}$ for $I = 15 \text{ Amps}$. Input Power 520 watts.
 (Thermo-electric Correction is Included)

the thermoelectric correction and the axial energy flow of electrons due to the steady current. This Fig. (IIB7) is to be compared with Fig. (IIB5) where no electric field correction is made. However, no boundary effect has been included so far.

[IIB-6] Boundaries Near the Electrodes

Boundaries are the domains where the gradients of the hydrodynamic flow ($\vec{\nabla}u$), the temperature ($\vec{\nabla}T$), the density ($\vec{\nabla}n$), and of the pressure ($\vec{\nabla}p$) are large. As we have seen already, the heat transfer vectors and the thermoelectric effects are both directly related to these gradients. In other words, only the correct evaluation of these boundary parameters can have a chance to yield accurate values in the energy transport calculations. So far the order of magnitude of these gradients has been estimated individually. In this Subsection the relative relationships of these boundary layer thicknesses are investigated.

We write the basic energy balance equation in the form:

$$\vec{u} \cdot \vec{\nabla} T = \frac{k}{\rho c_p} \nabla^2 T + \frac{1}{\rho c_p} \left\{ \sigma E^2 - Q_{rad} + \frac{\eta}{g_c} \left(\frac{\partial u_r}{\partial r} \right)^2 + u_r \frac{\partial p}{\partial r} \right\}. \quad (\text{IIB85})$$

$\uparrow \quad \uparrow \quad \uparrow \quad \uparrow$
 $1 : 10^{-2} : 10^{-5} : 10^{-10}$

Here k is assumed to be independent of T , which is true in the low temperature domain such as $T \leq 10^4$ °K. The numbers in Eq. (IIB85) shows the relative importance of the energy source terms. On the

other hand, the corresponding Navier-Stokes' equation is given by

$$\vec{u} \cdot \vec{\nabla} u_r = \frac{\eta}{\rho} \nabla^2 u_r - \frac{g_c}{\rho} c_p \frac{\partial p}{\partial r}, \quad (\text{IIB86})$$

where the first and second terms denote the viscous force and pressure force, respectively.

Comparing Eq. (IIB85) with Eq. (IIB86), one sees that if

$$\sigma E^2 + g_c c_p \frac{\partial p}{\partial r} = 0 \quad (\text{IIB87})$$

and if the Prandtl number (P_r)

$$Pr^{-1} = \left(\frac{k}{\rho c_p} \right) / \left(\frac{\eta}{\rho} \right) = \frac{k}{c_p \eta} \quad (\text{IIB88})$$

is unity, the T-solution of Eq. (IIB85) is identical to the u-solution of Eq. (IIB86). However Eq. (IIB87) cannot be satisfied generally since $g_c c_p (\partial p / \partial r)$ is very small even near the cathode and zero near the flat anode surface while σE^2 (Joule heating) is not apparently zero in the arc plasma. Thus the two Eqs. (IIB85) and (IIB86) produce different results. The hydrodynamic flow profile is given by:⁴²

$$\frac{u_r(z)}{u_s} = \frac{3}{2} \left| \left(\frac{z}{\delta_u} \right) - \frac{1}{2} \left(\frac{z}{\delta_u} \right)^3 \right|, \quad (\text{IIB89})$$

which is a solution of Eq. (IIB86) satisfying the boundary conditions:

$u_r(z) = \partial^2 u_r(z) / \partial z^2 = 0$ at $z = 0$; $u_r(z) = u_s$ (free-stream velocity) and $\partial u_r(z) / \partial z = 0$ at $z = \delta_u$ (hydrodynamic boundary layer thickness. The

temperature profile, namely the $(T(z) - T_w)/(T_s - T_w)$ profile, is not the same form given by Eq. (IIB89) when the Joule heating (σE^2) is not negligible nor is the thermal boundary layer thickness δ_t the one given by⁴²

$$\frac{\delta_t}{u} = \frac{1}{1.026 \sqrt[3]{P_r}} \quad (\text{IIB90})$$

Thus unless the plasma is field free, the temperature profile has to be calculated from the energy equation given by

$$u_r \frac{\partial T}{\partial r} + u_z \frac{\partial T}{\partial z} = a \frac{\partial^2 T}{\partial z^2} + \frac{\sigma E^2}{\rho c_p} \quad (\text{IIB91})$$

where $a = k/\rho c_p$ is the thermal diffusivity.

Assume a solution of Eq. (IIB91) which satisfies the boundary conditions:

$$\begin{aligned} T'(z) &= 0 \text{ and } \frac{\partial^2 T'(z)}{\partial z^2} = P_J \text{ at } z = 0 \\ T'(z) &= 1 \text{ and } \frac{\partial T'(z)}{\partial z} = 0 \text{ at } z = \delta_t. \end{aligned} \quad (\text{IIB92})$$

$$\text{Here, } P_J = \sigma E^2 / k [{}^\circ\text{K}/\text{m}^2], \quad (\text{IIB93})$$

$$T'(z) = \frac{T(z) - T_w}{T_s - T_w} \equiv \frac{T'(z)}{T'_s}, \quad (\text{IIB94})$$

and T_s and T_w are the free-stream and wall (electrode) surface temperatures, respectively. Assuming the solution of the type

$$T'(z) = a + bz + cz^2 + dz^3, \quad (\text{IIB95})$$

one can obtain

$$\begin{aligned}
 T(z) = & T_w + \frac{3}{2} \frac{T_s - T_w}{\delta_t} \left(1 - \frac{1}{6} \frac{P_J}{T_s - T_w} \delta_t^2 \right) z \\
 & + \frac{1}{2} P_J z^2 - \frac{1}{2} \frac{T_s - T_w}{\delta_t^3} \left(1 + \frac{1}{2} \frac{P_J}{T_s - T_w} \delta_t^2 \right) z^3. \quad (\text{IIB96})
 \end{aligned}$$

The conductive heat transfer from the plasma to the wall surface is then given by

$$q_{(o)}^{\text{cond}} = -k \left. \frac{\partial T(z)}{\partial z} \right|_{z=0} = \frac{3}{2} \frac{k}{\delta_t} T' \left(1 - \frac{1}{6} \frac{P_J}{T'_s} \delta_t^2 \right), \quad [\text{Watt/m}^2] \quad (\text{IIB97})$$

where $T'_s = T_s - T_w$. The boundary temperature profile is depicted in Fig. (IIB8). Eq. (IIB96) shows that due to the existence of the energy source term P_J , the heat transfer rate decreases by a factor

$$\epsilon_B \equiv \left(1 - \frac{1}{6} \frac{P_J}{T'_s} \delta_t^2 \right). \quad (\text{IIB98})$$

This effect is neglected in the usual paper. Since $P_J \approx 4 \times 10^9 \text{ } ^\circ\text{K/m}^2$ and $T'_s \approx 10^4 \text{ } ^\circ\text{K}$, the correction term is

$$\epsilon_B \approx 1 - 6.6 \times 10^4 \delta_t^2 \quad (\text{IIB99})$$

$$\left\{ \begin{array}{l} = 0.934 \text{ for } \delta_t = 10^{-3} \text{ m} \\ = 0.999 \text{ for } \delta_t = 10^{-4} \text{ m.} \end{array} \right.$$

Thus the local thermal energy transferred per unit time from the plasma to the anode surface is, using Eq. (IIB97), given by

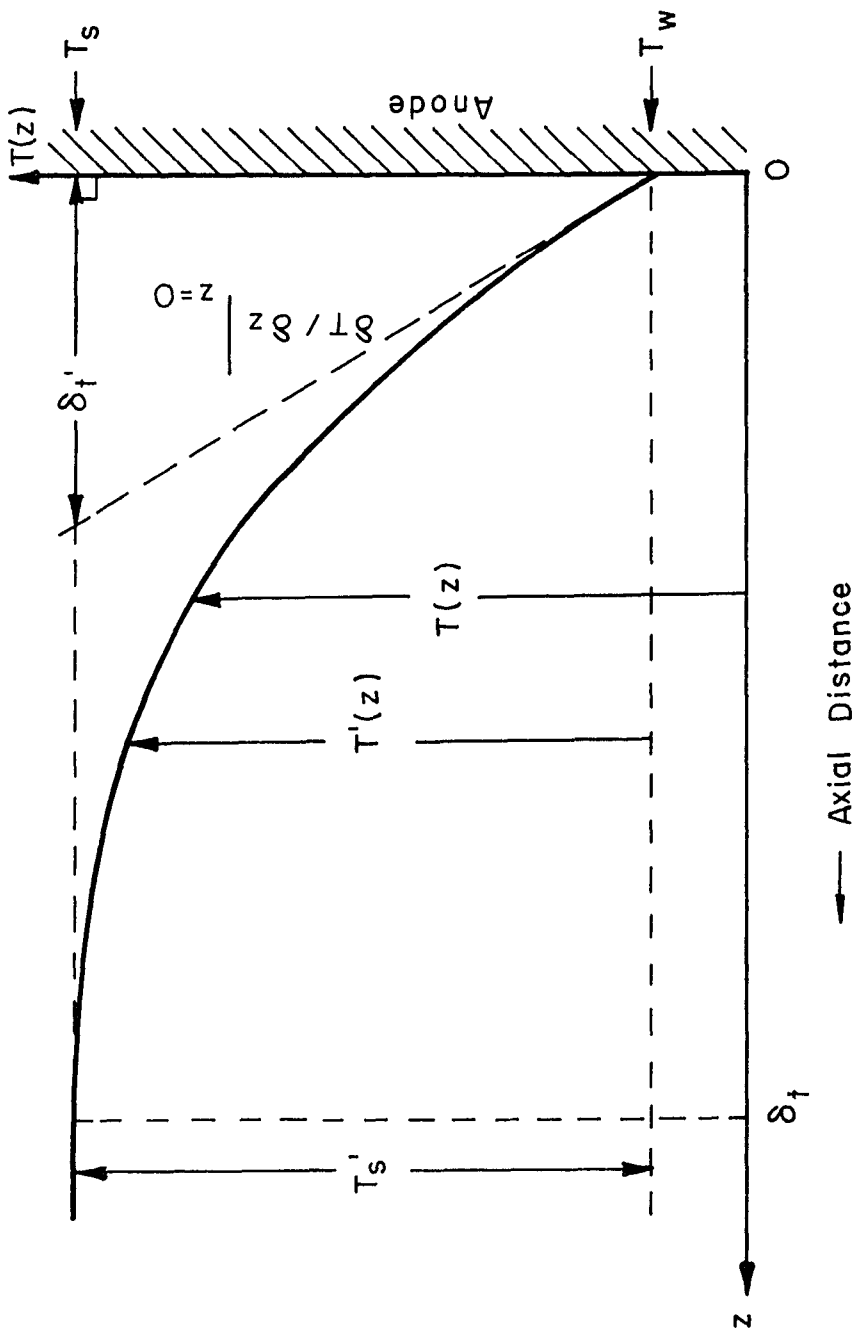


Fig. (III B 8) Stagnation Temperature Profile Near the Anode Surface , where

$$\left. \frac{\delta T(z)}{\delta z} \right|_{z=0} = \delta_t' / T_s' = \frac{3}{2} \frac{T_s'}{\delta_t'} \left(1 - \frac{1}{6} \frac{P_j}{T_s'} \delta_t'^2 \right)$$

$$Q_{P \rightarrow A} = \pi R^2 q_T$$

$$= \frac{3}{2} \pi R^2 k \frac{T_s - T_w}{(\delta_t / \epsilon_B)} , [\text{Watt}] \quad (\text{IIB98})$$

where R is the effective radius of the arc at the anode surface where T_w is constant and k is the thermal conductivity in the boundary.

Unlike the thermal boundary layer δ_t , the hydrodynamic boundary layer thickness δ_u is equal to zero at the stagnation point ($r = 0$).

Away from the stagnation point the hydrodynamic boundary layer builds up and the thickness as a function of r is given by⁴²

$$\delta_u(r) = 4.64 \left(\frac{\eta}{\rho u_s} \right)^{1/2} \sqrt{r} . \quad (\text{IIB99})$$

Including the correction factor ϵ_B , the hydrodynamic boundary layer thickness (δ_u) may be related to the thermal boundary layer thickness (δ_t) by

$$\delta_u(r) = 1.026 \sqrt[3]{Pr} \delta_t / \epsilon_B . \quad (\text{IIB100})$$

As we have seen in Subsection [IIB-5] the Prandtl number is smaller than unity for most plasmas. Therefore $\delta_u(r) \approx \delta_t(r)$ except at the stagnation point where only the thermal boundary exists.

The sheath boundary due to $\vec{\nabla}n$ is of the order of one ion MFP for the anode fall and of the order of one electron MFP for the cathode fall. The relative size of the sheath boundary layer and the temperature boundary layer depends on the plasma temperature and the surface temperature of the electrode which can be cooled externally. The

dynamic pressure boundary relates to the hydrodynamic boundary through the Bernoulli's equation as

$$\vec{\nabla} P = - \rho u \vec{\nabla} u . \quad (\text{IIB101})$$

[IIB-7] Exact and Unified Treatment of the Energy Transport Calculation In the Anode and Cathode Fall Boundary

Now that we have calculated all necessary properties for the arc energy calculations and corrected all the thermoelectric effects for the transport vectors and boundary layer thicknesses, we can now develop an exact and unified theory which is applicable to the both boundaries near the anode and cathode.

First, we start with the simplest boundary problem.

Here we have the temperature and velocity boundary near the electrode (say, anode), as is shown in Fig. (IIB9). From Eq. (IIB100),

$$\delta_u = 0.945 \delta_t \quad (\text{IIB102})$$

for $Pr = 0.67$ at $10^4 \text{ o K}^{5/4}$ and $\epsilon_B \approx 0.95$. Therefore the temperature boundary is almost equal to the velocity boundary in this special case, which means that the flow is in the radial direction (u_r) for $z \lesssim \delta_t$.

We consider only very small radius (r) where T_s and T_w are constant. Recalling that $\vec{q}^{\text{conv.}} = \rho c_p \vec{T} u$, the net heat flow by convection is given by

$$\begin{aligned} q^{\text{conv.}}(r) &\equiv q_s^{\text{conv.}} - q_r^{\text{conv.}} \\ &= \rho c_p \frac{\partial}{\partial r} \int_0^{\delta_t} \{ T_s - T(z) \} u_r(z) dz, \quad (\text{IIB103}) \end{aligned}$$

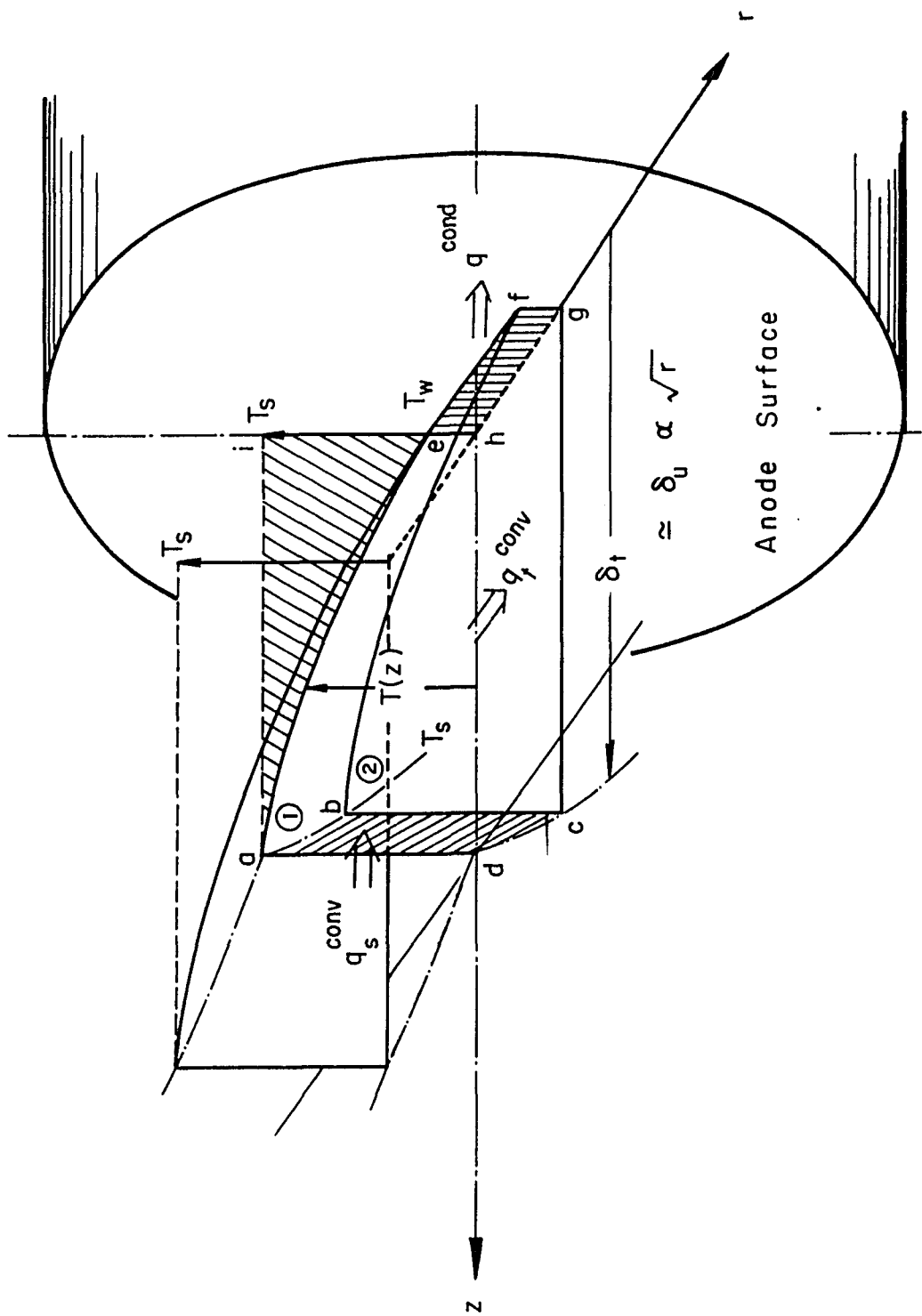


Fig. (II B 9) Temperature Boundaries Near the Anode

where $q_s^{\text{conv.}}$ is the flow coming in through the face (abcd) and traveling toward the radial direction, and $q_r^{\text{conv.}}$ is the radial net flow going out through the plates 1 and 2 in Fig. (IIB9). Therefore $q^{\text{conv.}}(r)$ is the r-derivative of the convection for the temperature corresponding to the area (aei) in Fig. (IIB9). Using Eq. (IIB96) for $T(z)$ and Eq. (IIB89) for $u_r(z)$, Eq. (IIB103) can be evaluated. Utilizing a similar calculation which is found in the text book,⁴³ one can evaluate Eq. (IIB103). Only the result is shown here:

$$q^{\text{conv.}}(r) = \frac{3}{20} u_s \rho c_p (T_w - T_s) \left(\frac{\delta_t}{\delta_u}\right)^2 \frac{\partial \delta_u(r)}{\partial r} . \quad (\text{IIB104})$$

Using Eq. (IIB99), this becomes

$$q^{\text{conv.}}(r) = -0.348(\eta \rho u_s)^{1/2} (T_s - T_w) \left(\frac{\delta_t}{\delta_s}\right)^2 \sqrt{r} . \quad (\text{IIB105})$$

This convection heat escapes toward the radial direction to reduce the thermal energy in the boundary but never contributes to heat the anode surface because $u_r(z) = 0$ at the surface of $z = 0$.

Only the conduction can heat (or cool) the impervious solid surface contacting gas at a finite temperature (T_w) and the amount of conduction is given by Eq. (IIB97); i.e.,

$$q^{\text{cond.}}(0) = 1.5 \frac{k}{\delta_t} (T_s - T_w) \epsilon_B . \quad [\text{Watt}/\text{m}^2] \quad (\text{IIB106})$$

Eq. (IIB106) is sometimes written in the form of the Newton's law using $k/\delta_t = h_c$ (film heat-transfer coefficient⁴² or convective heat

transfer coefficient⁴¹) and is called convective heat transfer flux between T_s and T_w separated by the displacement thickness, $\delta_t^* \equiv 0.375 \delta_t$. But in this thesis the terminology of convective heat transfer is restricted to the transfer of heat through the action of a moving fluid.⁴³ The conductive heat, $q^{\text{cond.}}$ (0) of Eq. (IIB106) heats up the anode through the face (efgh) in Fig. (IIB9).

If these temperatures are all the static temperatures consisting of the random thermal motion of the heavy particles and if there is no more heat source generated in or lost from the boundary region, the boundary energy balance equation is simply, $q^{\text{conv.}} = q^{\text{cond.}}$.

Namely,

$$0.348(\eta\rho u_s)^{1/2} (T_s - T_w) \left(\frac{\delta_t}{\delta_u} \right)^2 \sqrt{r} = 1.5 \frac{k}{\delta_t} (T_s - T_w) \epsilon_B.$$

(IIB107)

And the transferred energy to the anode surface is given by Eq. (IIB98). Conventional one-temperature, field-free theory holds up to here.

However, in the arc plasma there exist steady current flow and electrostatic field which modify the conductive-heat transfer rates. In other words in the boundary of the arc, the ions and electrons behave differently and a two-temperature gas treatment is necessary. The electrons drift in the opposite direction to the steady current and the motion couples strongly with the large electric field to raise the kinetic energy in the sheath. These effects can be treated by the careful evaluation of the kinetic energy distribution along the line of current, or by the detailed study of the thermoelectric correction.

What one needs is the accurate evaluation of the conductive-heat-transfer rate in the boundary. From Eq. (IIB64)

$$\begin{aligned}\vec{q}^{\text{cond.}}(z) &= -\left(\frac{\beta}{\sigma}\right)\vec{j}(z) - \tilde{\epsilon}k_T\vec{\nabla}T(z) \\ &= -U_i\vec{j}(z) - (\epsilon_T + \epsilon_n)k_T\vec{\nabla}T(z) \\ &\simeq -2.76 \times 10^{-4} T(z)\vec{j}(z) - 0.6k_T\vec{\nabla}T(z), \quad (\text{IIB108})\end{aligned}$$

where $U_i = \beta/\sigma = (\pi^2/3)k_B T/e$ is the average ionization potential given by Eq. (IIB2). The first term of Eq. (IIB108) represents the kinetic energy flow due to the steady current, which must be rewritten as a two-temperature-flow:

$$\begin{aligned}\vec{q}_j^{\text{cond.}}(z) &= -\vec{j}(z)U_i(z) = -\frac{\vec{j}(z)}{e} \frac{10}{3} k_B T(z) \\ &= -\frac{\vec{j}(z)}{e} \left[\frac{1}{2} \gamma_e k_B T_e(z) + \frac{1}{2} \gamma_i k_B T_i(z) \right], \quad (\text{IIB109})\end{aligned}$$

where $j = j_e + j_i$ and $\gamma_{e,i} = (2+m)/m = 5/3$ corresponding to $m = 3$ (numbers of degrees of freedom). And the second term of Eq. (IIB108) represents the conduction due to the diffusion currents caused by the temperature and density gradients. Further it is corrected for the effects of the electrostatic fields generated by the temperature and density gradients and is finally expressed by the conventional form of Fourier's law.

Thus, Eq. (IIB108) is useful when the local temperature $T(z)$ is known and shall be called the temperature method of correcting

Spitzer's theory. An alternative method shall be called the potential method in which the average ionization potential $U_i(z)$ is replaced by the conventional potential in the arc, $U(z)$ and is divided into two parts:

$$\begin{aligned}\vec{q}_j^{\text{cond}}(z) &= -\vec{j}(z)U(z) \\ &= -\{\vec{j}_e(z) + \vec{j}_i(z)\}U_o(z) \quad \text{for } z > \epsilon \\ &\quad - \vec{j}_e(z)U_A(z) \quad \text{for } 0 < z < \epsilon \quad (\text{IIB110})\end{aligned}$$

where $U_o(z)$ and $U_A(z)$ is the potential distribution in the positive column and in the anode fall, respectively. The coupling of ions with U_A is completely negligible because the ions are quickly swept away from the anode fall region.

Eq. (IIB108) can be written in the form

$$\vec{q}^{\text{cond.}}(z) = \vec{q}_j^{\text{cond.}}(z) - 0.6k_T \vec{\nabla} T(z). \quad (\text{IIB111})$$

Two different treatments for $\vec{q}_j^{\text{cond.}}(z)$ of Eqs. (IIB109) and (IIB110) are illustrated in Fig. (IIB10). The conductive heat transferred from the plasma to the anode surface is simply given by $\vec{q}^{\text{cond.}}(0)$. It is written in two forms; using Eq. (IIB97), by the temperature method:

$$\begin{aligned}q_{P \rightarrow A}^{\text{cond.}}(0) &= \frac{j(0)}{e} \frac{5}{3} k_B \{T_e(0) + T_i(0)\} \\ &\quad + 0.9 \frac{k_T}{\delta_t} \{T_i(\delta_t) - T_i(0)\} \epsilon_B \quad (\text{IIB112})\end{aligned}$$

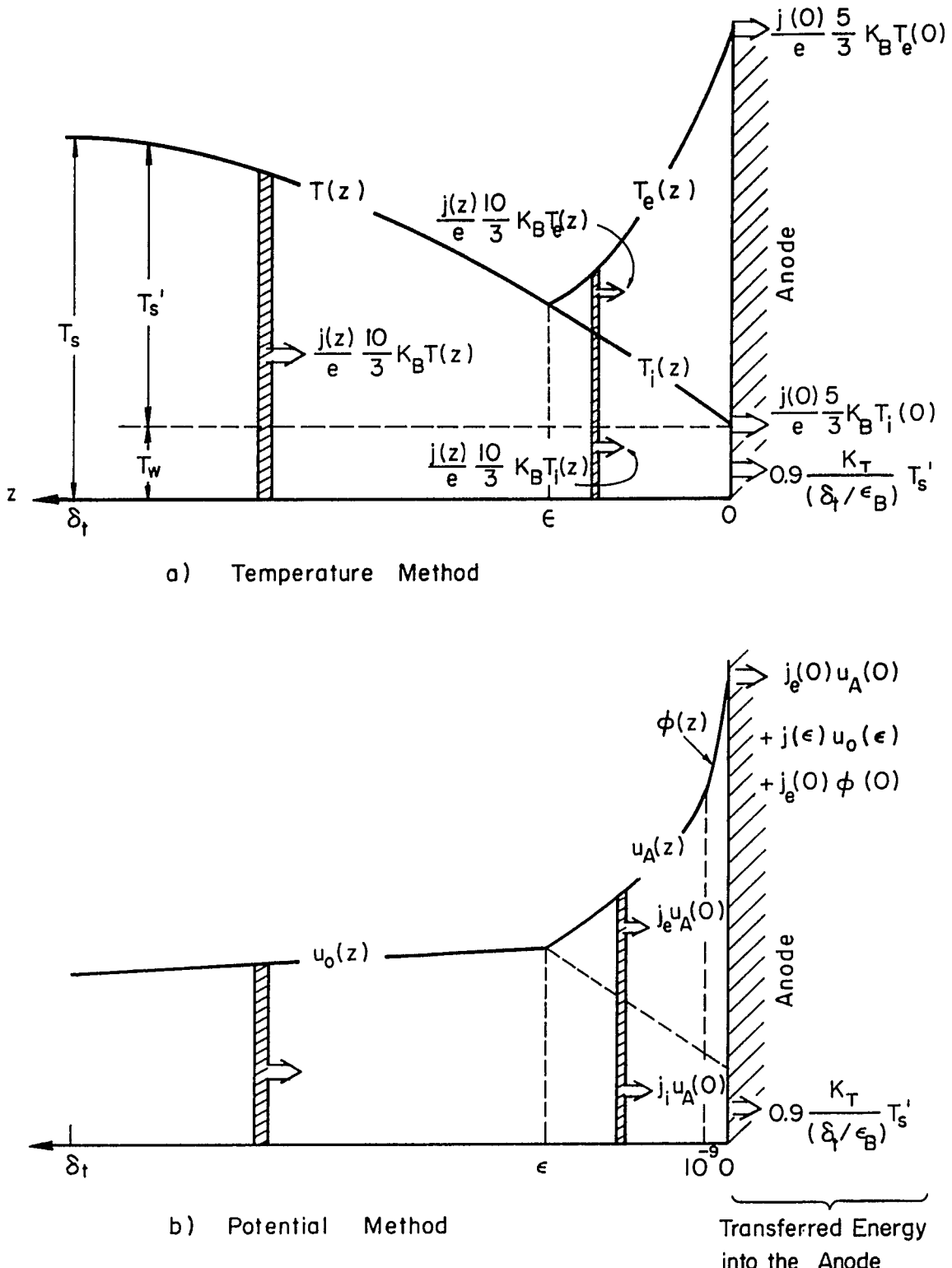


Fig. (II B 10) Energy Flow Evaluation; Two Different Methods, a) and b)

or by the potential method:

$$\begin{aligned} q_{p \rightarrow A}^{\text{cond.}}(0) &= j(\epsilon)U_o(\epsilon) + j_e(0)U_A(0) \\ &+ 0.9 \frac{k_T}{\delta_t} \{ T_i(\delta_t) - T_i(0) \} \epsilon_B \quad (\text{IIB113}) \end{aligned}$$

where $T_i(\delta_t) = T_s$ and $T_i(0) = T_w$ in more familiar notations. If the term $j(\epsilon)U_o(\epsilon)$ in Eq. (IIB113) is expressed by temperature method of Eq. (IIB112),

$$\begin{aligned} q_{p \rightarrow A}^{\text{cond.}}(0) &= \frac{j(\epsilon)}{e} \frac{10}{3} k_B T(\epsilon) + j(0)U_A(0) \\ &+ 0.9 \frac{k_T}{(\delta_t/\epsilon_B)} (T_s - T_w), \quad (\text{IIB114}) \end{aligned}$$

where $T_e(\epsilon) = T_i(\epsilon) = T(\epsilon)$ was assumed. Eq. (IIB114) can be compared with the Schoeck's expression:¹⁰

$$\begin{aligned} q_{\text{conv.}} + q_{jw} &= q_{je} + jU_a + h_i(i_s - i_w) \\ &= \frac{j(\epsilon)}{e} \left[\frac{5}{2} k_B T_e(\epsilon) + m_e \frac{(v_e^-)^2}{2} \right] + jU_A \\ &+ h_i(i_s - i_w) \quad (\text{IIB115}) \end{aligned}$$

which agrees with our result qualitatively although the physical interpretation of each term is rather vague in his case.

The electron is further accelerated by the surface potential-energy barrier at a distance of the order of 0.1 \AA before it enters into the conduction band of the metal. The difference between the metal conduction band and the plasma conduction band is called thermionic

work function, ϕ . The energy transfer flux due to this mechanism is given by

$$\vec{q}_{p \rightarrow A}^{\text{cond.}}(0) = j_e(0)\phi \quad [\text{Watt}/\text{m}^2]. \quad (\text{IIB116})$$

This term should be added to Eq. (IIB113). The work function of tungsten is $\phi = 4.4$ volts but depends on the face, $\phi = 3.95$ volts for Th and $\phi = 3.6$ volts for Cu.⁴⁵

The complete energy balance equation in the boundary can be summed up as

$$2\pi R \delta_t \vec{q}_{t}^{\text{conv.}}(r) = \pi R^2 [\{ \vec{q}_j^{\text{cond.}}(z) - 0.6k_T \nabla T(z) \} + \vec{q}_{p \rightarrow A}(z) - \vec{q}_{A \rightarrow p}(z)] \quad (\text{IIB117})$$

where

$$\vec{q}_{t}^{\text{conv.}}(r) = 0.348(\eta\rho u_s)^{1/2} (T_s - T_w) \sqrt{r} (\delta_t / \delta_u)^2, \quad (\text{IIB118-a})$$

$$\vec{q}_j^{\text{cond.}}(z) = -j(z) \{ U_o(z) + U_A(z) + \phi(z) \}, \quad (\text{IIB118-b})$$

and

$$\vec{q}_{p \rightarrow A}(z) = \vec{q}_{\text{rad.}}(z) = 10^{-2} \vec{q}_j^{\text{cond.}}(z) \quad (\text{IIB119})$$

$$\vec{q}_{A \rightarrow p}(z) = \vec{q}_{\text{rerad.}}(z) + \vec{q}_{\text{ablation}}(z). \quad (\text{IIB120})$$

In the above equations

$$q_{\text{rerad.}} = 5.68 \times 10^{-8} F \gamma T^4 (\text{°K}), \quad [\text{Watt}/\text{m}^2] \quad (\text{IIB121})$$

where F is an angle factor of the radiating arc regime (cone) with

respect to the area of energy transfer at the anode (base of cone) given by¹⁰ $F \approx 1/4$; and γ is the Grau factor or emissivity which is $1/2$ (1 for black body). And

$$q_{\text{ablation}} = 2k_T \gamma \theta, \quad [\text{Watt}/\text{m}^2] \quad (\text{IIB122})$$

where γ is the radius of the radiating arc regime (cone) and θ is the excess temperature of the cone over the electrode temperature.⁴⁵

The anode fall energy balance equation can be obtained from Eq. (IIB117) by simply replacing δ_t by ϵ and considering only the region $0 < z < \epsilon$.

Eq. (IIB117) can be used also for the cathode boundaries ($z \approx 2s$) by replacing A (anode) by K (cathode). Since the self-pinch force acts just like inverse flow near the anode, $\vec{\nabla}T(2s)$ profile may be close to $-\vec{\nabla}T(0)$ profile. This conduction heat will be convected away from the radial direction of the boundary toward the axial direction. Further, the potentials in Eq. (IIB118-b) should be corrected as⁴⁵

$$\dot{q}_j^{\text{cond.}}(z) = \vec{j}(z)U_o(z) + j_i(z)\{U_K(z) + U_i\}$$

$$-j_i(0)(1 - \alpha)U_K(0) - j(0)\phi, \quad (\text{IIB123})$$

where U_i is the ionization potential (15.75 volts for Ar and 13.53 volts for He), and α is the accommodation coefficient given by⁴⁶

$$\alpha = 1 - 7.8 \times 10^{-3} V/n_a \quad (\text{IIB124})$$

where V is the energy of the ion in electron volts and n_a is the number of sputtered atoms per incident ion. Notice that \vec{j} in Eqs. (IIB116) and (IIB121) is the vector pointing from the anode to cathode. The cathode loses the energies $j_i(0)(1 - \alpha)U_K(0)$ and $j(0)\phi$ as the results of the ion accommodation at the cathode surface and the thermionic emission of electrons from the cathode, respectively. The electrons emitted from the cathode combine with the positive ions outside the surface liberating energy $j_i(z)\{U_K(z) + U_i\}$, which is carried by ions together with the energy $j(z)U_o(z)$ to the cathode material.⁸ The validity of these analyses (especially Eq. (IIB114), etc.) are to be checked with present experiment.

CHAPTER III

VALIDITY OF LOCAL THERMODYNAMIC EQUILIBRIUM (LTE) FOR THE ARC PLASMA

In Chapter II the plasma transport properties are expressed as a function of the equilibrium temperature T , such as $\sigma(T)$, $k(T)$, $Q(T)$ and so forth, and the energy equations are mostly described and solved assuming the plasma to be a one-temperature gas-continuum except near the boundaries. As long as the local thermodynamic equilibrium ($T_e = T_i = T_n = T$) prevails, the data and theories developed in Chapter II are accurate because the state of the plasma can be uniquely described by the equilibrium temperature and ambient pressure, with no ambiguity. If some inconsistencies arise between the theory and experiment, the discrepancies can be attributed to the non-LTE origin of the plasma. Therefore, the data and theories in Chapter II, together with the exact solution of Saha-Eggert solution to be given in Section IIIB, can be used as a standard to be compared with the experiment.

If LTE does not prevail, the transport properties are functions of additional nonequilibrium variables and the energy equations must consist of multi-temperature equations coupled with rate equations. To avoid this complexity only LTE plasma, i. e., high pressure or high density plasma, should be used. Because of this arc plasmas have

been favored for the study of energy transfer. Argon arc plasma (including the arc jet plasma) is only a continuous laboratory plasma closest to LTE. However, even in the arc plasmas the existence of complete LTE has been a controversial subject.

This chapter reviews the LTE validity criteria for the arc. The problems being considered are the degree of non-LTE, the arc domains where LTE theory may break down, and the influence of non-LTE on the energy transfer calculation. Section B demonstrates the computer calculation of exact Saha-Eggert equation for LTE plasma for the purpose using the result as a standard temperature.

A. COMPLETE AND PARTIAL LTE CRITERIA IN THE STATIONARY,
INHOMOGENEOUS ARC

[IIIA-1] Effect of Electric Field on LTE

A free electron (mass m , charge e) subjected to an electric field E acquires velocity $v_e = (e/m)Et$ and the kinetic energy is $mv_e^2/2 = (eE)^2 t^2 / 2m$. Because of collisions, the longest time between collisions is limited and the electron velocities are randomized such that the electron temperature (T_e) is defined as an average of the random kinetic energy:

$$\frac{3}{2} k_B T_e = \frac{1}{2} m \langle v_e^2 \rangle$$

$$= \frac{(eE)^2}{2m} \langle t^2 \rangle = \frac{(eE)^2}{2m} \tau_e^2 , \quad (\text{IIIA1})$$

where τ_e is the average electron collision time and is equal to the inverse of the collision frequency (ν_e). Since electron-electron thermalization (or equilibration) time is faster than that of electron-ion by a factor m/M (M , ion mass), thermal equilibrium is established first among electrons. Thermal equilibrium is the state of the maximum entropy for the system at which the particle velocity distribution is Maxwellian. The electrons collide with the ions and raise their kinetic energy. After the electron-ion thermalization time, $\tau_{ei} \simeq 10^{-4}$ nsec (for 10^4 °K argon plasma) as given by Eq.(IIA10-b), the ion kinetic energy is randomized and an ion temperature (T_i) can be similarly defined. T_i can be approached to T_e locally. However, due

to the fact that the electron is receiving energy at a rate of eEv_d (v_d is the drift velocity) continuously from the external electric field, a finite temperature difference ($T_e - T_i$) exists. From Eqs. (IIA95) and (IIA99) of Chapter II this temperature difference can be calculated as

$$\begin{aligned}\epsilon &\equiv \frac{\Delta T}{T_e} = \frac{T_e - T_i}{T_e} \\ &= 1.62 \times 10^7 \frac{M}{m} \left(\frac{E \ell_{ei}}{T_e} \right)^2 \\ &= 1.12 \times 10^{12} \left(\frac{E \ell_{ei}}{T_e} \right)^2 \text{ for Argon,} \quad (\text{IIIA2})\end{aligned}$$

where $\ell_{ei} = v_e / v_{ei}$ is the $e \rightarrow i$ MFP length in [m]. Using ϵ , the ion temperature (T_i) can be expressed as

$$\begin{aligned}T_i &= (1 - \epsilon) T_e \\ &= (1 - \epsilon) \frac{2}{3\sqrt{2}} \left(\frac{e}{k_B} \right) \frac{E}{\gamma\kappa} \ell_{ei}, \quad (\text{IIIA3})\end{aligned}$$

where T_ϵ was calculated from Eq. (IIIA1) and the notations are the same as those used in Eqs. (IIA95) through (IIA97). Only when $\epsilon = 0$ (i.e., $E = 0$), the condition $T_e = T_i$ can be established, otherwise $T_e > T_i$. The electron gains surplus energy continually from the electric field and hence the thermal equilibrium between electron and ion ($T_e = T_i$) is never realized.

The degree of nonequilibrium, ϵ_{NE} can be defined as

$$\epsilon_{NE} = \epsilon \times 100 [\%]. \quad (\text{IIIA4})$$

In Chapter II we calculated that the arc with $E \simeq 10^3$ V/m is in about 1% nonequilibrium (Eqs. IIA98 and IIA99). Busz and Finkelnburg⁴⁷⁾ were the first to have used this approach to demonstrate the existence of thermal equilibrium in arcs. According to Olsen's calculation³⁾ the degree of nonequilibrium is 3% near the cathode tip and 0.6% near the anode. In the sheaths ϵ_{NE} can be very high due to the high electric field and the expression of Eq. (IIIA2) is inconvenient for expressing the degree of nonequilibrium because T_e in the sheath is not known. An alternative is to express the electron temperature in terms of the potential functions ($U = \gamma k_B T / 2e$) assuming no collision in the sheath:

$$\begin{aligned} \epsilon(z) &\equiv \frac{T_e(z) - T_i(z)}{T_e(z)} \\ &= U(z)^{-1} \left\{ U(z) - \frac{1}{2} \gamma_i \frac{k_B}{e} T_i(z) \right\} \\ &= 1 - 7.2 \times 10^{-5} \frac{T_i(z)}{U(z)}, \end{aligned} \quad (\text{IIIA5})$$

where $\gamma_i = 5/3$ (see Eq. IIB109 for notations). $U(z)$ is the imposed potential distribution and $U(z) = U_i/2$ at the outside of the sheath, where U_i is the average ionization potential defined by Eq. (IIB2). At the anode surface Eq. (IIIA5) becomes

$$\epsilon(0) = 1 - 7.2 \times 10^{-5} \frac{T_w}{(U_i/2) + U_A(0) + \phi(0)} . \quad (\text{IIIA6})$$

If one substitutes corresponding numbers for a 10^{40} K plasma:

$U_i = 2.88$ volts, U_A (anode fall potential) = 9.5 volts, ϕ (work function, for W) = 4.4 volts, and T_w (wall temperature) = 10^{30} K; Eq. (IIIA6) gives the degree of nonequilibrium, 99.0% when ϕ is excluded, and 99.4% when ϕ is included. This is obviously quite a large nonequilibrium and the electron temperature is about two orders of magnitude higher than the ion temperature at the anode surface. Thus, the electric arc (except the field-free arc jet) is in steady non-equilibrium ($T_e > T_i$) in the entire bulk and the degree of nonequilibrium is a function of position, being small ($\sim 1\%$) in the positive column and very large ($\sim 99\%$) in the proximity of the anode surface. Even under the steady nonequilibrium condition ($T_e \neq T_i$), thermal equilibrium does exist among ions themselves as well as among electrons themselves because the energy coupling rates with electric field are the constant for each species. If $T_e = T_i$ and if the velocity distributions of electrons and ions are Maxwellian characterized by a common temperature, then the electron-ion system is in the local thermodynamic equilibrium (LTE). But this is still "partial LTE" in the spectroscopic terminology since the neutral atoms are not yet involved. The complete LTE condition, where Saha equation can be applied, is established when⁵⁾

$$T_e = T_i = T_{ex,n} = T_n = T_I \quad (\text{IIIA7})$$

and when the populations of all the electronic energy levels as well as the velocities of electrons, ions, and atoms (excited and ground states) are all in Maxwell-Boltzmann distributions characterized by one equilibrium temperature, say T_I . In Eq. (IIIA7), $T_{ex,n}$, T_n and T_I designate the excitation temperature of neutrals, ground state temperature of neutrals, and the ionization temperature of the plasma characterizing the Saha equilibrium concentrations, respectively. The effect of electric field thus acts to raise T_e or to modify the electron velocity distribution.

[IIIA-2] Effect of Inelastic Collision on LTE

In the expression of Eq. (IIIA2) only the elastic collision is considered where the energy transport coefficient of electron-ion elastic collision ($\kappa = 2m/M$) is used. However if the electron-neutral collisional ionization prevails, κ is much larger than $2m/M$. As is seen from Eq. (IIIA3), a larger κ results in lowering electron temperature or reduction of ϵ_{NE} . This effect may be small in the arc core where only fully ionized particles exist. In the intermediate region between the core and periphery inelastic collision may occur because in that portion ionization process is active or the conductive heat transfer is large as is seen in Fig. (IIA8). This effect is very small, however, at the arc periphery because there few energetic electrons exist. Thus the degree of nonequilibrium may be minimum in the intermediate region if the inelastic collision actually prevails in that region. But

this is rather unlikely because the electron kinetic energy is about 1 eV while the first ionization energy is 15.75 eV for argon atom and a number of collisions is necessary for the collisional ionization. In the anode fall region the energetic electrons lose their energies to the neutrals by inelastic collisions but the average electrons may not lose their energies as much to ions because of the deficiency of the number of ions in that region. Therefore the inelastic collisions only serve to deplete the tail of the electron velocity distribution rather to bring T_e any closer to T_i .

[IIIA-3] Effect of Ambipolar Diffusion on LTE

It has been mentioned in Chapter II that one of the most prominent characteristics of the arc is the high number density and high temperature gradients resulting in the ambipolar diffusion of the plasma particles. Near the center of the arc there is a net production of free electrons (i.e., excess ionization relative to recombination), and accordingly the electron density (or temperature) is somewhat above its equilibrium value.

The electrons produced in the center then diffuse toward the outer region of the arc at a rate limited by ambipolar diffusion. In the intermediate region inelastic collision occurs. In the arc periphery net recombination occurs and produce neutral atoms. But because ions also diffuse at much higher rate than in the case of homogeneous plasma and because the diffusion velocity is very high at the periphery,

electrons experience a lack of recombination centers (ions). Thus at the arc periphery the measured electron density may be larger by many orders of magnitude than the Saha-equilibrium value³³⁾ and translational temperature T_n of the neutrals defined by the partial pressure for neutrals,

$$p_n = n_n k_B T_n \quad (\text{IIIA9})$$

is higher than the equilibrium value. In other words, the temperature of neutral atoms, T_n or $T_{ex,n}$ and the temperature of electrons, T_e both deviate from the Saha-equilibrium temperature, T_I .

Bott⁴⁸⁾ first observed a large deviation of $T_{ex,n}$ (obtained by slope method of relative line-spectrum intensities) from T_e (obtained by absolute continuum-spectrum intensities) in the outer region of a helium arc and suggested that the ground state populations depend not just on the local T_e but also in the region from which the atoms diffused. The work of Bott was extended by Hwang⁴⁹⁾, who verified that the measured electron temperatures agree well with values calculated using a two-temperature ambipolar diffusion model developed by Kruger⁵¹⁾.

Argon arc was investigated by Giannaris and Incropera⁵⁰⁾, who found the same effects as Bott found in a helium arc. Giannaris and Incropera also found that the critical radius (r_c) from which the electron temperature deviates from the equilibrium theory can be observed in the temperature range between 9,000 and 10,000°K and increases with

increasing arc current such that $r_c = 3.7$ mm ($I = 100$ Amps) and $r_c = 4.0$ mm ($I = 184$ Amps) for $R \sim 5$ mm arc.

Fig. (IIIA1) shows a schematic demonstrating non-LTE in the radial direction of an arc taking into account the experimental results of Ref. 48, 49 and 4 and the aforementioned effects. Notice that the local excitation temperature $T_{ex,n}$ exceeds the electron temperature in the periphery while the ion temperature (T_i) approaches the equilibrium value (T_I) in the periphery. It is seen from this figure that the equilibrium temperature (T_I), which is identical to the solution of the one-temperature energy balance equation in the radial direction, gives a standard temperature.

[IIIA-4] Effect of Inhomogeneity on LTE

To avoid the non-LTE due to diffusion, spatial variations of the plasma parameter should be small over the distance that a given particle can diffuse in time of the order of equilibration time. In the ambipolar diffusion range of the plasma, every particle diffuses with similar velocity, $D_a \bar{v}_n/n$ but the equilibration time is quite different among each species. The ground-state atoms have the longest equilibration time because of their smallest collision cross section. The average distance that the ground-state atom travels between the equilibrating collisions is given by Griem⁵⁰⁾

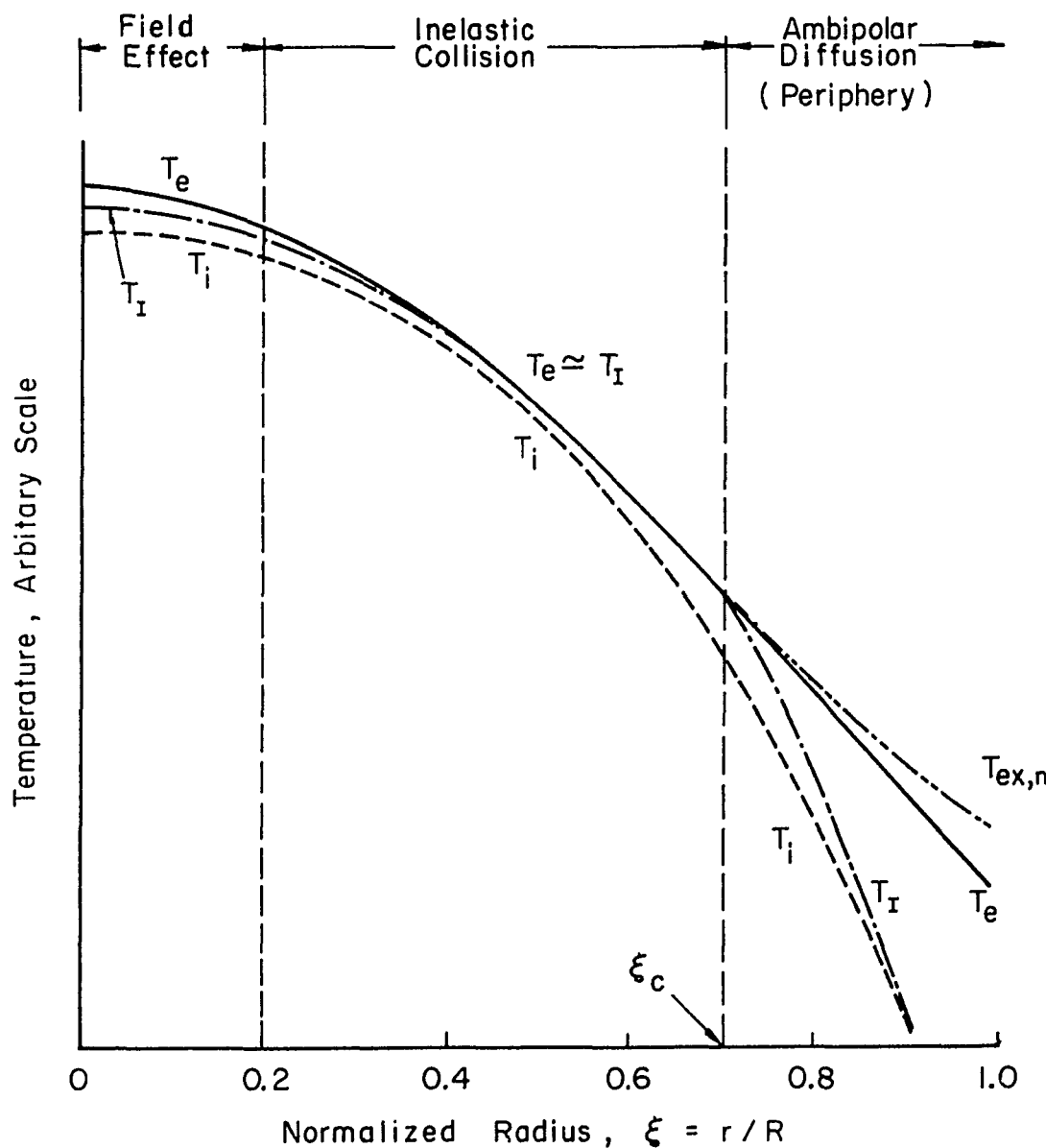


Fig. (III A 1) Radial Non - LTE Model Schematic

T_e = Electron Temperature

$T_{ex,n}$ = Excited-State Atom T.

T_i = Ion T.

T_x = Saha Equilibrium T.

ξ_c = Critical Radius, $0.7 < \xi < 0.8$

$$d_1^{o,a} \simeq 6 \times 10^{18} \left(\frac{M_H}{M_a} \right)^{\frac{1}{4}} \left(\frac{k_B T}{E_H} \right)^{\frac{1}{2}} \left(\frac{E_{21}^{o,a}}{f_{21} E_H} \right)^{\frac{1}{2}} \frac{1}{n_a}$$

$$\times \left[(1 + N_a^1 / N_a) (1 + 10 N_a^1 / N_a) \right]^{\frac{1}{2}} \cdot \exp \left(\frac{E_{21}^{o,a}}{2k_B T} \right), [m]$$

(IIIA10)

where M_H/M_a is the mass ratio of hydrogen and an atom $N_a = \sum_z N_a^z$ is the total density of atoms and ions of the chemical species, a ; $E_H = 13.6$ eV (ionization energy of hydrogen); $E_{21} = \Delta E = \hbar w_{12}$ is the first excited state (from $n = 1$ to $n = 2$) of the neutral atom; $f_{21} = 0.5$ ($f_{nn'} = 0.5n'$); and N_a^1 is the singly ionized atom density. For an argon plasma at $T \simeq 10^4$ K ($E_{21}^{o,a} = 12.9$ eV, $N_a = 7 \times 10^{23} m^{-3}$ and $N_a^1/N_a = 2 \times 10^{-2}$ from Fig. IIA2), Eq. (IIIA10) yields

$$d_1^{o,a} = 7.35 \times 10^{-4} [m]. \quad (\text{IIIA11})$$

If, for the radial temperature distribution $T(r)$,

$$\epsilon_d = \frac{T(o) - T(d_1^{o,a})}{T(o)} \ll 1, \quad (\text{IIIA12})$$

the non-LTE due to diffusion is negligible and the plasma can be said homogeneous within the distance $0 < r < d_1^{o,a}$. The above calculation shows

that the diffusion effect is negligible within about 1 mm radius from the axis of $T = 10^{40}$ K plasma, if the temperature at that radius is close to 9×10^{30} K. And if the temperature at $r = 1$ mm is lower than 9×10^{30} K, the spectroscopically obtained electron temperature, assuming complete LTE at the axis would be under-estimated by a factor ϵ_d compared with the actual electron temperature.

Complete LTE (or equilibrium down to the ground-state) thus cannot be expected except at the core for usual arcs even if the electron density is high enough to satisfy the complete LTE criterion of the homogeneous plasma as given by Griem⁵⁰⁾

$$n_e \geq 9 \times 10^{23} \left(\frac{E_2^{\text{o}, a}}{E_H} \right)^3 \left(\frac{k_B T}{E_H} \right)^{\frac{1}{2}}$$

$$\approx 1.08 \times 10^{23} [\text{m}^{-3}] \text{ for } 10^{40}\text{K, Argon.} \quad (\text{IIIA 13})$$

However the partial LTE (or equilibrium down to a certain excited state) can be realized. The lowest required electron density is given by the partial LTE criterion of homogeneous plasmas⁵⁰⁾:

$$n_e \geq 7 \times 10^{24} \frac{z^7}{p^{17/2}} \left(\frac{k_B T}{z^2 E_H} \right)^{\frac{1}{2}}, \quad (\text{IIIA 14})$$

where $z = 1$ for neutral atoms, $z = 2$ for singly charged ions, etc., and p is the principal quantum number to which level LTE is desired. For

the level $p = 14$ which is one level below the singly ionized argon atom, Eq. (IIIA14) yields

$$n_e \geq 2.09 \times 10^{16} [\text{m}^{-3}]. \quad (\text{IIIA15})$$

At least this much electron density is necessary for partial LTE within 10% between free electrons and singly ionized argon.

[IIIA-5] Summary

Classically arcs over 100 Torr pressure were believed to be in partial LTE with ions. However, even at atmospheric pressure, recent detailed investigation has revealed that the partial LTE with ions is not achieved, especially at currents less than 35 Amps. Figs. (IIIA2)⁴⁾ and (IIIA3)⁵¹⁾ are examples: these show the non-LTE caused by the axial electric field and by the radial diffusion, respectively.

Emmons⁵²⁾ and Giannaris and Incropera⁵³⁾ found near LTE at the core of an argon arc for over 75 Amps but not LTE at the periphery for all currents at least up to 180 Amps due to the ambipolar diffusion. The results have been schematically summarized in Fig. (IIIA1). Argon arcs are always nearer to LTE compared with helium arcs whose core is not in LTE until 400 Amps and whose behavior above 100 atm-pressure begins to be similar with that of argon arcs at 1 atm-pressure⁵³⁾. These results have been obtained only recently. An energy calculation using a two-temperature model has just been initiated by Kruger⁵¹⁾ based on the theoretical work by Kruger and Mitchner⁶⁾.

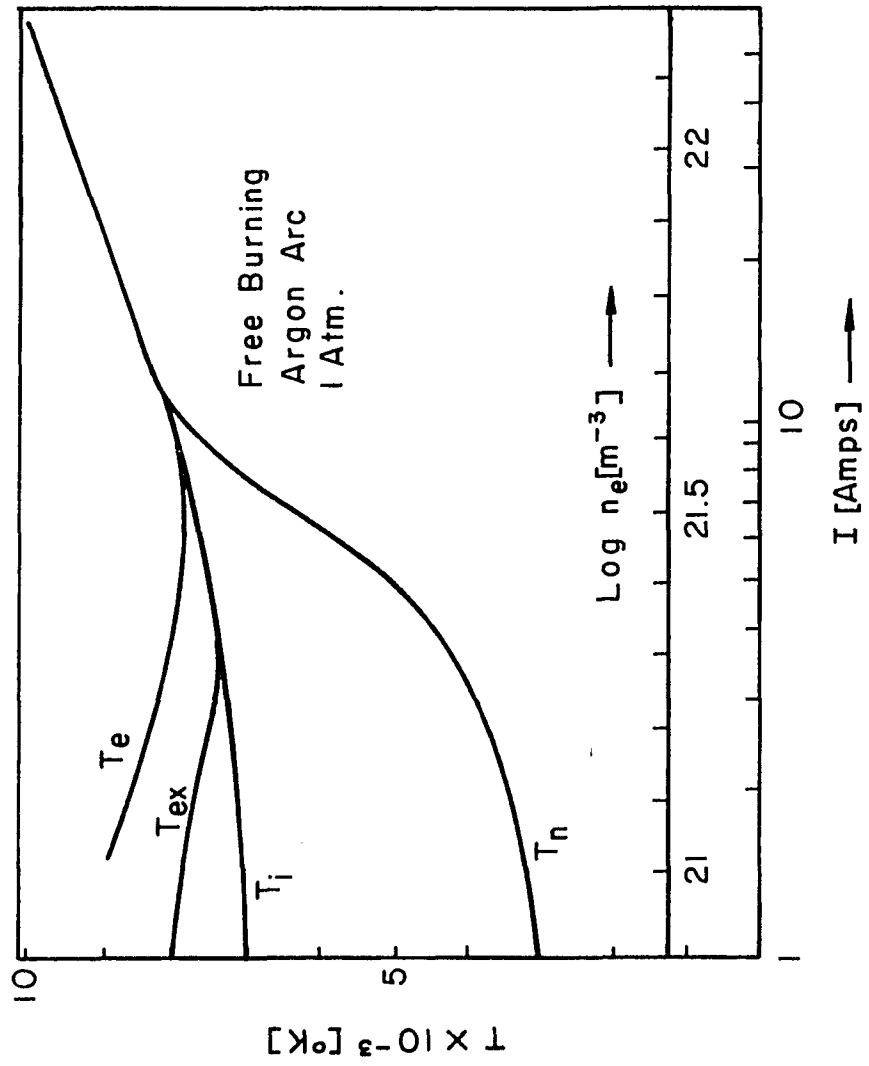


Fig. (III A 2) Non-LTE by Axial Electric Field. [After Kolesnikov]
4)

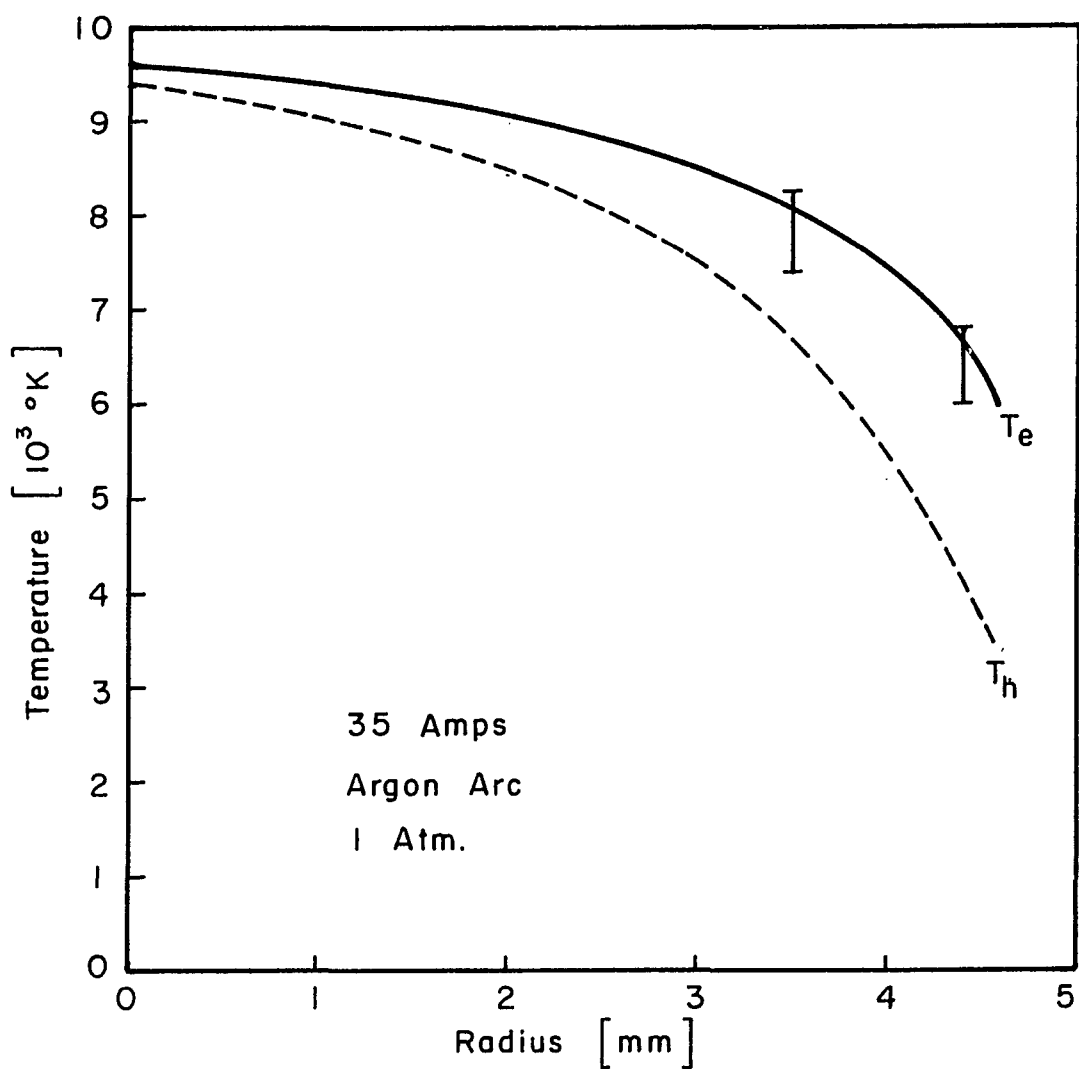


Fig. (III A 3) Non - LTE by Radial Ambipolar Diffusion

---- T_h is Calculated Temperature of Heavy-particles. [After Kruger]⁵¹⁾

In this thesis the axial distribution of degree of non-LTE has been investigated for a low current argon arc. The electron density and temperature distribution has been measured by using Thomson scattering technique which does not require LTE condition. Using the measured electron density, the corresponding Saha equilibrium temperature can be calculated and compared with the measured electron temperature, from which the degree of non-LTE can be calculated. The detail is described in Chapter V. The next section, B of this chapter, describes the computer solution of Saha-Eggert equation used to derive the Saha equilibrium temperature as a standard for the degree of non-LTE calculation.

B. EXACT, DIRECT SOLUTION OF SAHA-EGGERT EQUATION
FOR LTE PLASMAS

Exact solution of Saha-Eggert equation is important because the present basic energy equation is described by the Saha equilibrium temperature T ($= T_e = T_i = T_n$) and the exact solution can provide a standard for the non-LTE theory. Although similar calculations can be found in the literature^{54), 55)}, the computation procedure is not directly applicable to the present work. Thus the computation formulae and procedures of our case are presented here. Total 566 spectral lines of argon plasma have been used for the computation. When this program is combined with the energy equation to be solved numerically, the routine of the energy calculation may become very accurate.

[IIIB-1] Computation Formulae

The basic formula of Saha-Eggert equation is given by Griem⁵⁰⁾:

$$\frac{N_e N^z}{N^{z-1}} = 2 \left(\frac{m k_B T}{2\pi\hbar^2} \right)^{\frac{3}{2}} \frac{Z^z(T)}{Z^{z-1}(T)} \exp\left(-\frac{E_\infty^{z-1} - \Delta E_\infty^{z-1}}{k_B T}\right). \quad (\text{IIIB1})$$

The left-hand-side of the above equation expresses the equilibrium concentrations (N^0 = neutral density). For the convenience of computation we change $z - 1 \rightarrow z$, $Z^{z-1}(T) \rightarrow U^z(T)$, then Eq. (IIIB1) becomes

$$\frac{N^{z+1}(T)}{N^z(T)} = \frac{U_e}{N_e(T)} \frac{U^{z+1}(T)}{U^z(T)} \exp\left(-\frac{E_\infty^z - \Delta E_\infty^z}{k_B T}\right), \quad (\text{IIIB2})$$

where $z = 0$ for neutrals $z = 1$ for singly ionized atoms, etc.;

$$U_e = \frac{m e k_B T}{2 \pi \hbar^2} \frac{3}{2} = 4.88 \times 10^{15} \frac{T^3}{\text{cm}^2} \quad (\text{IIIB3})$$

is the partition function of electrons; and E_{∞}^z is the ionization energy of the atom ionized z times. The amount of reduction of the ionization energy by Coulomb interaction, ΔE_{∞}^z is given by Griem⁵⁰⁾:

$$\Delta E_{\infty}^z = (z + 1) e^2 / \rho_D \quad (\text{IIIB4})$$

where ρ_D is the effective Debye radius given by

$$\begin{aligned} \rho_D &= k_B T / 4\pi e^2 N_e (1 + z_{av.}) \text{ in CGS} \\ &= \epsilon_0 k_B T / e^2 N_e (1 + z_{av.}) \text{ in MKS} \end{aligned} \quad (\text{IIIB5})$$

with

$$\begin{aligned} z_{av} &= \frac{1}{N_e} \sum_{z=0}^z z^2 N_z \\ &= (N^1 + 2^2 N^2 + 3^2 N^3) / N_e \text{ if } z \leq 3 \\ &= 1 \text{ (for initial condition).} \end{aligned} \quad (\text{IIIB6})$$

$U^z(T)$ is the partition function of the atom ionized z times given by

$$U^z(T) = \sum_{n=1}^{p_{\max}^z} g_n \exp(-E_n/k_B T), \quad (\text{IIIB7})$$

where E_n is the energy of state n . We set $E_1 = 0$ for the ground state.

The maximum principal quantum number (p_{\max}^z) contributing to the partition function is given by the relation

$$p_{\max}^z \leq \left(\frac{z^2 E_H}{\Delta E_\infty^z} \right)^{\frac{1}{2}}, \quad (\text{IIIB8})$$

where $E_H = 12.595$ eV. In Eq. (IIIB7) g_n is the statistical weight which is equivalent to the values of the magnetic quantum number or degeneracy, namely

$$g_n = 2J_n + 1, \quad (\text{IIIB9})$$

where J_n is the total angular quantum number of each spectrum line specified by n .

If the p_{\max}^z obtained from Eq. (IIIB8) surpasses the number tabulated by Moore⁵⁶⁾, the following partition function is used assuming a hydrogenic structure for outer electrons:

$$U^z(T) = \sum_{n=1}^{p'_{\max}} g_n \exp(-E_n/k_B T)$$

$$+ \frac{2}{3} (2S_1^z + 1) (2L_1^z + 1) \left(\frac{e^2 E_z}{\Delta E_\infty^z} \right)^{\frac{3}{2}} \exp \left(- \frac{E_\infty^z - \Delta E_\infty^z}{k_B T} \right), \quad (\text{IIIB10})$$

where S_1^z and L_1^z are the spin and orbital momentums of the parent configuration (or ground state of the next higher ionization stage), respectively; and p'_{\max} is the highest principal quantum number for which the table still contains all levels of the configuration. The angular momentum of the outer electrons is $\ell = p'_{\max} - 1$. The number of p'_{\max} , i.e., the number of spectrum lines listed in Moore's table is as follows:

AI($z = 0$) . . . 309

AII($z = 1$) . . . 119

AIII($z = 2$) . . . 101

AIV($z = 3$) . . . 37

The imposed conditions are:

- (i) Total plasma particle number conservation

$$N = \sum_{z=0}^3 N^z = N^0 + N^1 + N^2 + N^3 \quad (\text{IIIB11})$$

(ii) Charge neutrality condition

$$N_e = \sum_{z=0}^3 z N^z = N^1 + 2N^2 + 3N^3 \quad (\text{IIIB12})$$

(iii) Average charge

$$z_{av.} = \frac{1}{N_e} \sum_{z=0}^3 z^2 N^z = \frac{1}{N_e} (N^1 + 4N^2 + 9N^3)$$

= 1 (for initial guess). (IIIB13)

[IIIB-2] Computation Procedure

The aim is to solve $z - 1$ simultaneous Saha equations given by Eq. (IIIB2). The method of solving those equations is as follows. At a given electron density and temperature, an initial guess ($z_{av} = 1$) is made for the plasma composition. From this, the lowering of ionization potential and the partition function are calculated and from these the composition is recalculated from the simultaneous Saha equations and the charge neutrality condition. The old and new values are compared and if agreement is good (within 10^{-10}) the solutions are retained, otherwise another iteration occurs and so on until self-consistent results are obtained.

A key point for the computation is that the first Saha equation (combining N^0 and N^1) need not be brought into the iterative loop, but

after the number densities of the ions have been calculated, N^0 is calculated substituting N^1 to the first equation.

First of all, E_∞^Z , S_1^Z , L_1^Z and p_{\max}^Z are read for $z = 0 \sim 3$, next J_n and E_n are read for $n = 1 \sim 309$ (for AI), $n = 1 \sim 119$ (for AII), $n = 1 \sim 109$ (for AIII), and $n = 1 \sim 39$ (for AIV). Fixed values are given for the electron number density N_e (or for the temperature, T) and for the initial guess, ($z_{av} = 1$). For a given temperature T (or for a given total number density) ΔE_∞^Z of Eq. (IIIB4), and $U^Z(T)$ of Eqs. (IIIB7) and (IIIB10) are calculated for $z = 0 \sim 3$ for all n . Next the Saha equation of the form (equivalent to Eq. IIIB2):

$$RN(Iz + 1, Iz) = \frac{DN(Iz + 1)}{DN(Iz)} = \frac{UE}{EN} \frac{U(Iz + 1)}{U(Iz)} \exp(-\frac{E(Iz) - DE(Iz)}{BK*T}) \quad (IIIB14)$$

is calculated for $Z(z) = 2 \sim 3$. From the charge neutrality condition of Eq. (IIIB12),

$$EN = DN(2) + 2. * DN(3) + 3. * DN(4); \quad (IIIB15)$$

$$\frac{EN}{DN(4)} = \frac{1}{RN(4, 3)} * \frac{1}{RN(3, 2)} + 2. * \frac{1}{RN(4, 3)} + 3. \quad (IIIB16)$$

Hence,

$$DN(4) = \frac{EN * RN(4, 3) * RN(3, 2)}{1. + 2. * RN(3, 2) + 3. * RN(4, 3) * RN(3, 2)}$$

$$DN(3) = \frac{DN(4)}{RN(4, 3)}$$

$$DN(2) = \frac{DN(3)}{RN(3, 2)}$$

(IIIB17)

can be computed. Calculating the average charge value of Eq. (IIIB13),

$$ZAV = (DN(2) + 4. * DN(3) + 9. * DN(4)) / EN; \quad (IIIB18)$$

check ZAV with the old guess of z_{av} . If $|ZAV - z_{av}| > 10^{-10}$, the program is returned to recalculate with the present value of ZAV. If $|ZAV - z_{av}| \leq 10^{-10}$, Eq. (IIIB14) is calculated for IZ = 1 and the result

$$DN(1) = \frac{DN(2)}{RN(2, 1)} \quad (IIIB19)$$

is printed out together with DN(2), DN(3), DN(4). The total plasma particle number density which is necessary to produce given N_e at given T is

$$DNT = DN(1) + DN(2) + DN(3) + DN(4)$$

$$= N^0 + N^1 + N^2 + N^3. \quad (IIIB20)$$

The corresponding program is shown in Appendix A. This program gives the equilibrium concentrations versus temperature for a given electron density. If the total number density, DNT, is fixed for a constant pressure considered, a slight modification of this program draws the curves of equilibrium concentrations versus temperature.

Fig. (IIA2) is the one of the results computed for the argon plasma at one atmospheric pressure.

CHAPTER IV

DIAGNOSTICS BY THOMSON SCATTERING

This chapter describes the theory and experiment of Thomson scattering used as a probe for the diagnosis of the plasma-solid interface.

Section A summarizes the differential scattering cross sections due to various Thomson scattering processes and discusses about the possibility of the plasma transport properties being measured in the collective scattering regime. Customarily, Thomson scattering technique has been used to measure the local plasma parameters (densities and temperatures), since the advent of the high power ruby laser. However the detailed investigation of the differential scattering cross section reveals that the plasma transport properties such as the electrical and thermal conductivities and the viscosity also can be measured without knowing the plasma paramters. This potentiality has been discussed in Section A and elsewhere^{59, 63 ~65)} intensively, for it would be a great help for the transport study if the properties could be obtained (by laser scattering) as local tensor quantities.

Section B is the experimentation. The electron density and temperature of an argon arc plasma have been measured by using Thomson scattering technique. The apparatus, experimental

procedures and scattered spectra are shown in detail. Several experimental difficulties in applying the light scattering technique for probing the region of the plasma near the anode surface are also discussed together with ways of overcoming them.

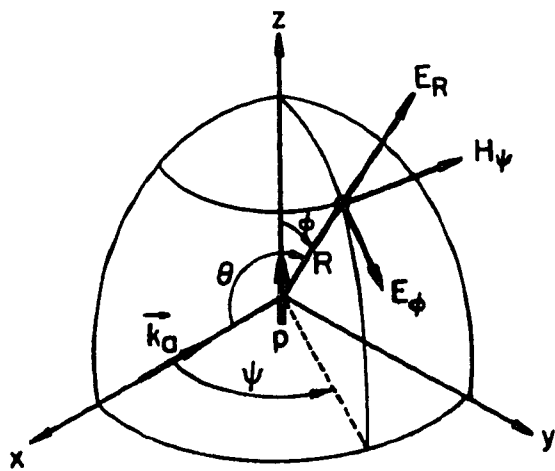
A. THEORY OF INCOHERENT SCATTERING BY PLASMAS

[IVA-1] Scattering Cross-Section by a Single Free Electron

Thomson scattering is a linear scattering process of electromagnetic waves by a single free electron in the vacuum. Customarily incoherent scattering by plasmas is also referred to the Thomson scattering. The classical theory is due to J. J. Thomson⁵⁷⁾ who discovered the existence of electrons in the ionized gas in 1897. Although the motion and damping of an electron in the plasma is influenced by the other plasma particles, the most elementary scattering process is mathematically the same as that of a linear dipole. That is, the electrons oscillate around the equilibrium position due to the external electric field. The amount of energy radiated from the harmonic oscillator per unit area across the spherical wave surface can be calculated by the integral of the Poynting vector (S) taken over this surface. In the wave zone ($R \gg \lambda/2\pi$) the Poynting vector is given by⁵⁸⁾ in MKS units:

$$\begin{aligned} S &= [\vec{E} \times \vec{H}] = |E_\phi H_\psi| \\ &= \frac{\{p\}^2}{c^4 R^2} \sin^2 \phi. \quad [\text{Watt/m}^2] \end{aligned} \quad (\text{IV A1})$$

The angles of ϕ and ψ are shown in Fig. (IV A1).



$$R \gg \lambda / 2\pi$$

$$p = p_0 e^{i\omega t}$$

$$E = E_0 e^{i\omega t}$$

Fig. (IV A1). A harmonic oscillator with moment-vector along the z-axis.

Here \ddot{p} is the double time derivative of the dipole moment $p = p_0 e^{i\omega t}$ which is induced by an external electric field $E = E_0 e^{i\omega t}$ and { } denotes the retarded dipole whose time is expressed by such preceding time $t - R/c$ as to reach the point of observation at the required time t . Since $p = ez$ (z is the amplitude of the oscillator), $\ddot{p} = e\ddot{z} = (e^2/m) E_0$, the energy flowing out across the area dA of the spherical surface is given by

$$\begin{aligned} dS &= \frac{e^2 \{ \dot{z} \}^2}{4R^2} \sin^2 \phi \, dA \\ &= \left(\frac{e^2}{mc^2} \right)^2 S_0 \sin^2 \phi \, d\Omega \end{aligned} \quad (\text{IV A2})$$

where $S_0 \equiv E^2$ is the incident power density and $d\Omega = dA/R^2$ the solid angle. Therefore the differential (with respect to the solid angle) scattering cross section for a single electron, defined by $d\sigma_s = dS/S_0$, is

$$\begin{aligned} d\sigma_s &= r_o^2 \sin^2 \phi d\Omega \\ &= 7.94 \times 10^{-30} \sin^2 \phi d\Omega \quad [m^2/sr] \end{aligned} \quad (\text{IIA3})$$

for polarized light, where $r_o^2 = e^2/mc^2 = 2.82 \times 10^{-15}$ [m] is the classical electron radius. The total cross section (σ_s) is the ratio of total amount of power over the whole spherical surface to incident power density:

$$\begin{aligned} \sigma_s &= \int_{\Omega} d\sigma_s \\ &= r_o^2 \int_0^{\pi} \int_0^{2\pi} \sin^2 \phi \sin \phi d\phi d\psi \\ &= \frac{8\pi}{3} r_o^2 = 6.65 \times 10^{-29} \quad [m^2]. \end{aligned} \quad (\text{IV A4})$$

Electrons are assumed to be in random position and they scatter incoherently. Therefore if there is no interaction of the electron with the other particles, the scattering cross section from a plasma with $n_e [m^{-3}]$ electron number density is simply given by

$$\frac{d\sigma_s}{d\Omega} = 7.94 \times 10^{-30} n_e \sin^2 \phi. \quad [m^2/sr] \quad (\text{IV A5})$$

However the actual electrons in a plasma are moving with random kinetic energy under the influence of the Coulomb electric field of the ions and electrons and one has to take into account the frequency response of the equivalent electric dipole and quadrupole.

[IV A-2] Unified Theory of the Differential Scattering Cross-Section for Thermal Equilibrium ($T_e = T_i$) Plasmas

Let $F(\vec{k}, w)$ be the gross frequency response of the electric dipole and quadrupoles in a plasma. Then the differential scattering cross section can be written in the form:⁶⁰⁾

$$\frac{d\sigma(\vec{k}, w)}{dw_b d\omega_b} = n_e r_o^2 \sin^2 \phi \frac{w_b}{w_a} \pi^{-1} F(\vec{k}, w), \quad [(m^2/sr)(rad/sec)], \quad (IV A6)$$

where a and b designate the incident and scattered frequencies, respectively; $\vec{k} \equiv \vec{k}_b - \vec{k}_a$ the scattering wave number; and $w \equiv w_b - w_a$ the scattering frequency. The frequency response function⁵⁹⁾ based on the DuBois' theory⁶⁰⁾ can be written as

$$F(\vec{k}, w) = \frac{k^{*2}}{w^2} \left| \frac{Q_e}{k^{*2} + Q} \right|^2 4\pi \text{Im}\sigma_L(\vec{k}, w), \quad [(rad/sec)^{-1}] \quad (IV A7)$$

where $k^* = k/k_D$ (Debye wave number) and Q is the induced polarization function which is related to the local electric conductivity $\sigma_L(\vec{k}, w)$ by

$$Q(\vec{k}, w) = k^{*2} 4\pi \sigma_L(\vec{k}, w) / w. \quad (IV A8)$$

The physical meaning of the terms in Eq. (IV A7) is as follows.

The local plasma property should be described by the local dielectric constant (ϵ) which relates to the polarizability (χ) or conductivity (σ) or polarization function (Q). Let ϵ_e and $\epsilon = \epsilon_e + \epsilon_i$ be the dielectric constants of the electrons and electron-ion system, then

$$\begin{aligned} \left| \frac{\epsilon_e - 1}{\epsilon} \right|^2 &= \left| \frac{4\pi \chi_e}{1 + 4\pi \chi} \right|^2 \\ &= \left| \frac{4\pi \sigma_e / w}{1 + (4\pi \sigma / w)} \right|^2 = \left| \frac{Q_e}{k^*{}^2 + Q} \right|^2. \end{aligned} \quad (\text{IV A9})$$

Here, the term $|\epsilon_e - 1|^2$ represents the excess dielectric constant due to the random density fluctuation of electrons and ϵ^2 represents the Coulomb screened interactions or collective phenomena of the plasma. The damping of the dipole oscillations is described by the term

$$4\pi \text{Im}\sigma_L(\vec{k}, w) = \Gamma_c / w^*{}^2, \quad [\text{rad/sec}] \quad (\text{IV A10})$$

where Γ_c is the collision frequency.

Eq. (IV A6) covers all scattering processes from the pure (or non-collective) Thomson scattering to the collective Thomson scattering. The corresponding $F(\vec{k}, w)$ -functions are tabulated in the Table (IV A1). For instance, if one uses $F(\vec{k}, w)$ for pure Thomson (column "a" Table IV A1), Eq. (IV A6) becomes

Scattering process	$-4\pi Im\sigma_L^{\epsilon\epsilon}$	$\frac{Q_\epsilon}{k^{*2} + Q}$	$4\pi Im\sigma_L$	$F(\vec{k}, \omega)$
(a) Pure Thomson (RPA)	0	1	$\frac{\omega}{k^{*2}} Im Q_\epsilon^0$	$\frac{(\pi/2)^{1/2}}{\omega_p k^*} e^{-1/2(\omega^*/k^*)^2}$
(b) Collective Thomson ion line (RPA)	0	$\frac{Q_\epsilon^0}{k^{*2} + Q^0}$	$\frac{\omega}{k^{*2}} Im Q_\epsilon^0$	$\frac{(\pi/2)^{1/2}}{\omega_p \alpha k^*} \left \frac{Q_\epsilon^0}{k^{*2} + Q^0} \right ^2 e^{-1/2(\omega^*/k^*)^2}$
(c) Collective Thomson plasma line (RPA)	0	$1 - \frac{Q_\epsilon^0}{k^{*2} + Q^0}$	$\frac{\omega}{k^{*2}} Im Q_\epsilon^0$	$\frac{(\pi/2)^{1/2}}{\omega_p k^*} \left 1 - \frac{Q_\epsilon^0}{k^{*2} + Q^0} \right ^2 e^{-1/2(\omega^*/k^*)^2}$
<hr/>				
(d) Collective Thomson resonance ion line (COLL.)	0	$\frac{4\pi\sigma_L^\epsilon}{\omega + 4\pi\sigma_L}$	$4\pi Im\sigma_L$	$\frac{k^{*2}}{\omega^2} \left \frac{4\pi\sigma_L^\epsilon}{\omega + 4\pi\sigma_L} \right ^2 4\pi Im\sigma_L$
(e) Collective Thomson ion line (res. and non res. part) (COLL.)	$-4\pi Im\sigma_L^{\epsilon\epsilon}$	$\frac{4\pi\sigma_L^\epsilon}{\omega + 4\pi\sigma_L}$	$4\pi Im\sigma_L$	$\begin{aligned} & \frac{k^{*2}}{\omega^2} \left\{ -4\pi Im\sigma_L^{\epsilon\epsilon} \right. \\ & \left. + \left \frac{4\pi\sigma_L^\epsilon}{\omega + 4\pi\sigma_L} \right ^2 4\pi Im\sigma_L \right\} \end{aligned}$
(f) Collective Thomson plasma line (COLL.)	0	$\frac{Q_\epsilon}{k^{*2} + Q}$	$\frac{\lambda}{6\sqrt{2}\pi^{3/2}} \frac{\omega_p}{\omega^{*2}} \cdot K_a(\omega^*)$	$\begin{aligned} & \frac{k^{*2}}{\omega^2} \left \frac{Q_\epsilon}{k^{*2} + Q} \right ^2 \\ & \times \left\{ \frac{\lambda}{6\sqrt{2}\pi^{3/2}} \frac{\omega_p}{\omega^{*2}} K_a(\omega^*) \right\} \end{aligned}$

RPA: Collisionless plasma theory.
 COLL.: Collisional plasma theory.

Table (IV A1) Frequency Response Function, $F(\vec{k}, \omega)$

$$\frac{d\sigma_s}{dw_b dw_a} = \frac{n_e r_o^2}{(2\pi)^{\frac{1}{2}}} \sin^2 \phi \frac{w_b}{w_a} \frac{k_D}{k} \frac{1}{w_p} e^{-\frac{1}{2}(w^*/k^*)^2}. \quad (\text{IV A11})$$

This is a Gaussian profile with half width at half height (HWHH) centering at the normalized frequency

$$w^* \equiv w/w_p = k^* \sqrt{2 \ln 2}$$

$$\text{or} \quad w_e = k v_e \sqrt{2 \ln 2}. \quad (\text{IV A12})$$

Since from the phase matching condition, $k^2 = k_a^2 + k_b^2 - 2k_a k_b \cos \theta$
 $= 4k_a^2 \sin^2(\theta/2) = 4(w_a/c)^2 \sin^2(\theta/2)$ (where θ is the scattering angle);
the HWHH is

$$w_e = 2w_a \sin \frac{\theta}{2} \sqrt{\frac{k_B T_e}{mc^2} 2 \ln 2}, \quad [\text{rad/s}] \quad (\text{IV A13})$$

where $mc^2 = 5.11 \times 10^5 \text{ eV}$ and $\ln 2 = 0.693$. Hence for $\lambda_a = 6943 \text{ \AA}^\circ$
(ruby laser), the Doppler half width is

$$\begin{aligned} \Delta \lambda_e &= \lambda_a \frac{\Delta w}{w_a} \\ &= 22.8 \sin \frac{\theta}{2} \sqrt{T_e(\text{K})/11,606} \quad [\text{\AA}^\circ] \\ &= 16.2 \sqrt{T_e(\text{K})/11,606} \quad [\text{\AA}^\circ] \text{ for } \theta = 90^\circ, \end{aligned} \quad (\text{II A14})$$

which agrees with the calculation based on Salpeter's theory.⁶¹⁾

However unlike Salpeter's formula, Eq. (IV A11) based on DuBois' theory⁶⁰⁾ can give the peak intensity explicitly:

$$\begin{aligned}
 \left. \frac{d\sigma_s}{d\omega_b} \right|_{w_b = w_a} &= \frac{n_e r_o^2}{\sqrt{2\pi}} \sin^2 \phi \frac{\Delta w}{\sqrt{2\ell n 2}} \\
 &= 1.24 \times 10^{-22} n_e (m^{-3}) \sin^2 \phi \Delta \lambda_e^o (\text{\AA}) \\
 &\quad [m^2 / sr] \quad (\text{IV A15})
 \end{aligned}$$

for $\lambda_a = 6943 \text{ \AA}^o$, where $\sin^2 \phi$ can be chosen to be unity experimentally as shown in Fig. (IV A2).

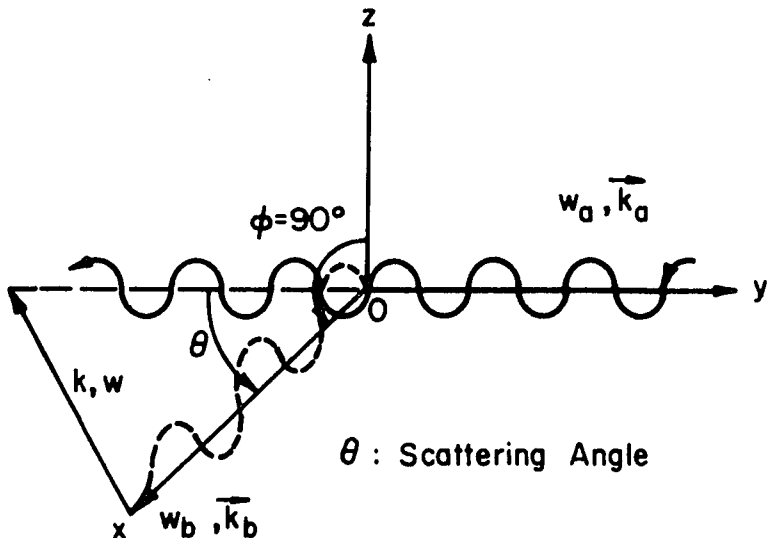


Fig. (IV A2). Scattering Geometry

As is well known, when the scattering wavelength $\lambda (= 2\pi/k)$ becomes longer than the Debye wave length $\lambda_D (= 2\pi/k_D)$, or when Salpeter's dimensionless parameter a_S defined by

$$a_S \equiv (k^*)^{-1} \equiv \frac{k_D}{k}$$

$$= \frac{7.4 \times 10^{-12}}{\sin \frac{\theta}{2}} \sqrt{\frac{n_e (m^{-3})}{T_e ({}^\circ K) / 11,606}}$$

$$= 1.05 \times 10^{-11} \sqrt{\frac{n_e (cm^{-3})}{T_e ({}^\circ K) / 11,606}} \text{ for } \theta = 90^\circ \quad (\text{IV A16})$$

becomes larger than unity, the collective effects of electrons influenced by ion-field begins to appear on the scattering spectra. The transient profiles from $a_S = 0$ to $a_S = 4$ can be found in the Salpeter's paper.⁶¹⁾ These can be calculated also using $F(k, w)$ of the column "c" in Table (IV A1) together with

$$Q^o = \text{Re}Q^o + i\text{Im}Q^o \quad (\text{IV A17})$$

where

$$\begin{aligned} \text{Re}Q^o \left(\frac{w^*}{k^*} \right) &= \text{Re}Q_e^o \left(\frac{w^*}{k^*} \right) + \text{Re}Q_i^o \left(\frac{w^*}{k^*} \right) \\ &= 2 - \frac{w^*}{k^*} \exp \left\{ -\frac{1}{2} \left(\frac{w^*}{k^*} \right)^2 \right\} \cdot \int_0^{w^*/k^*} dt \exp(t^2/2) \\ &\quad - \frac{w^*}{ak^*} \exp \left\{ -\frac{1}{2} \left(\frac{w^*}{ak^*} \right)^2 \right\} \cdot \int_0^{w^*/ak^*} dt \exp(t^2/2) \quad (\text{IV A18}) \end{aligned}$$

$$\begin{aligned}
 \text{Im}Q^O \left(\frac{w^*}{k^*} \right) &= \text{Im}Q_e^O \left(\frac{w^*}{k^*} \right) + \text{Re}Q_i^O \left(\frac{w^*}{k^*} \right) \\
 &= \left(\frac{\pi}{2} \right)^{\frac{1}{2}} \frac{w^*}{k^*} \exp \left\{ -\frac{1}{2} \left(\frac{w^*}{k^*} \right)^2 \right\} + \left(\frac{\pi}{2} \right)^{\frac{1}{2}} \frac{w^*}{ak^*} \exp \left\{ -\frac{1}{2} \left(\frac{w^*}{ak^*} \right)^2 \right\}.
 \end{aligned} \tag{IV A19}$$

Fig. (IVA3) shows the frequency $w^*/k^* \equiv z (\equiv \sqrt{2} x = \sqrt{2} w/w_e)$ response of Q_e^O -function. Q_i^O curve is identical to Q_e^O if the z is scaled by $\alpha z \equiv (m/M)^{\frac{1}{2}} z$.

The electron temperature (T_e) and density (n_e) of a plasma can be calculated from the width (Eq. IVA14) and peak intensity (Eq. IVA15) of the Gaussian Doppler profile of the pure Thomson scattering regime (where $\alpha_S \ll 1$), respectively. On the other hand the Lorenzian electron-plasma line in the collective scattering regime (where $\alpha_S \gg 1$) gives the information of electron density and damping rate (or collision frequency). The detailed resonance frequency of the electron-plasma line is given by

$$w_L = w_p [1 + 3k^{*2} (1 + \lambda/42.4)]^{\frac{1}{2}}, \tag{IV A20}$$

according to the calculation by Ichikawa;⁶⁾ or

$$w_L = w_p [1 + 3k^{*2} (1 + \lambda/408)]^{\frac{1}{2}}, \tag{IV A21}$$

according to the calculation by Niimura et al.^{63, 64)} The last term

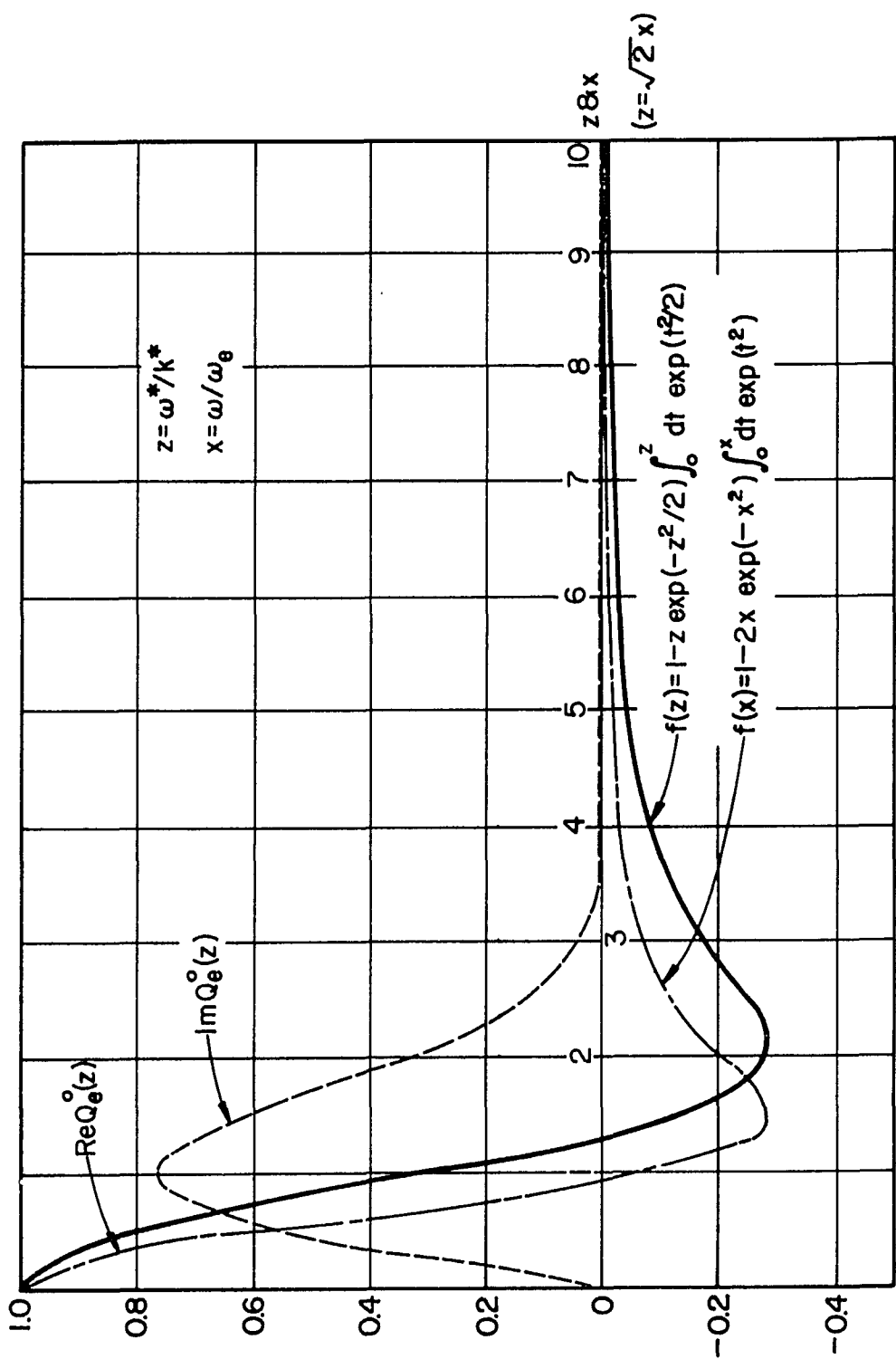


Fig.(IVA 3) Frequency Dependence of Q_e^0 - Function

involving λ ($\equiv k_D^3/n_e \equiv 12\pi/\Lambda$) is the correction factor for the dispersion term due to e - e collision. Using Eq. (IVA21), the position of the resonance peak in wavelength units is given by the next formula:

$$\Delta\lambda_L = 1.35 \times 10^{-10} \sqrt{n_e (m^{-3})} [1 + 3k^*^2 (1 + \frac{\lambda}{408})]^{\frac{1}{2}} [\text{Å}] . \quad (\text{IVA22})$$

The broadening of the electron-plasma line, due to the Landau and collision damping, has been calculated in fair detail by Niimura et al.^{64, 65)} with the intent to measure collision frequencies from the line broadening.

Using the $\vec{F}(k, w)$ function at column "b," the ion acoustic line profiles can be calculated. Fig. (IVA4) shows an example using this function for a collisionless ($\Gamma_{ii}/w_i \ll a$) plasma. The shoulder appears at

$$w^* = ak^* \\ \text{or at } w_i = kv_i = (\frac{5}{3})^{\frac{1}{2}} aw_e = (\frac{5}{3})^{\frac{1}{2}} a \frac{\Delta w_e}{\sqrt{2\ln 2}}, \quad (\text{IVA23})$$

where Δw_e is the Doppler width of the pure Thomson scattering given by Eq. (IVA30). Therefore the wavelength shift of the shoulder is given by the formula:

$$\Delta\lambda_i = \frac{\Delta\lambda_e}{0.66} a \\ = 34.6 (\frac{m}{M})^{\frac{1}{2}} \sin \frac{\theta}{2} \sqrt{T_i(\text{°K})/11,606}. \quad (\text{IVA24})$$

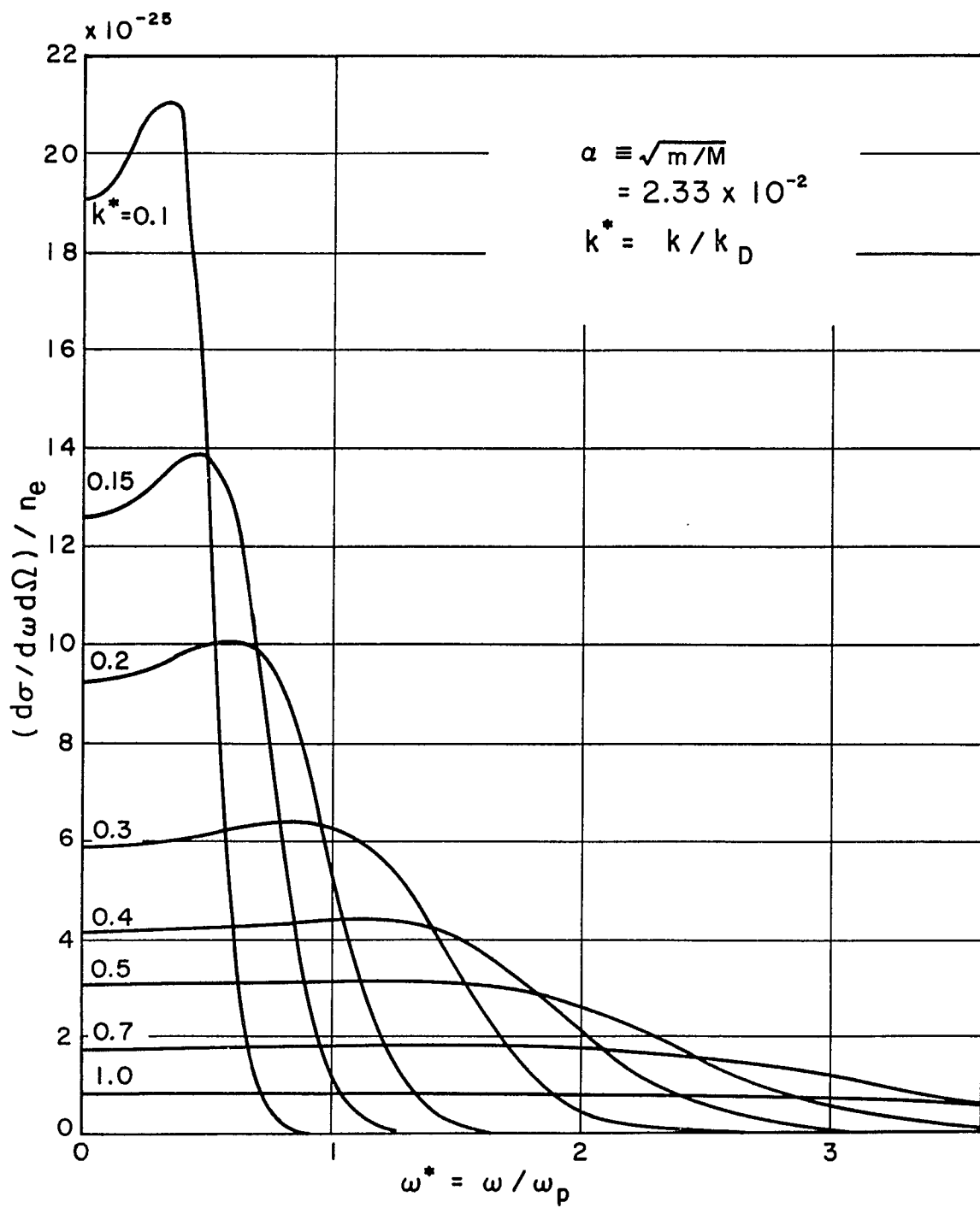


Fig.(IV A4) Ion Acoustic Line Profiles for Collision-less Plasmas

Notice that α is the square root ratio of electron to ion masses which should not be confused with Salpeter's parameter α_S .

[IVA-3] Scattering from Collision-Dominated Plasmas

So far DuBois' basic theory⁶⁰⁾ has been introduced and classified as in Table (IV A1). While the theories of incoherent scattering developed by Dougherty and Fareley,⁶⁶⁾ and Rostoker and Rosenbluth,⁶⁷⁾ as well as by Salpeter⁶¹⁾ are all based on the random phase approximation (RPA); the quantum electrodynamic theory of incoherent scattering developed by DuBois and Gilinsky⁶⁰⁾ includes the effects of wave mechanics, quantum statistics and close Coulomb collisions as well as distant collisions. This means that in the latter theory the velocity-dependent Coulomb collisions are calculated for all possible close- and distant-encounters of all species, which makes possible the study of the collisional damping. Coulomb collisional damping is manifested for the longitudinal waves (electron-plasma) and ion acoustic modes) in the plasma where an excess electron density fluctuation exists, i.e., $|\epsilon_e - 1| / |\epsilon| = |Q_e/k|^2 + Q \approx 1$.

Numerical studies^{64, 65)} of damping for the electron plasma line show that the electron-ion collisional damping surpasses overwhelmingly the Landau damping in the region,⁶⁵⁾ $\alpha_S \gtrsim 5$; while the electron-electron binary collision is dominant in the region,⁶⁴⁾ $5 \gtrsim \alpha_S > 1$. This fact can be used for the measurement of collision frequencies directly from the line width. Collision (e - i) broadened

line width is found to be an almost linear function against electron density at the region $\lambda < 1$ as shown graphically in Ref. 64, even if the complicated collision integral which involves the quantum effect of close collision is taken into account. The electron-electron collision frequency is, however, a much more complicated function as is also graphically shown in Ref. 65. Since the collision frequency is just another version of the local electrical conductivity (σ) and of the other transport coefficients (k, α, β), the direct measurement of collision frequencies is vital to the study of plasma energy transport.

Coulomb collisions influence not only the line broadening and narrowing of the resonance lines but also the resonance frequency shifts of the lines. In Eq. (IV A21), the resonance frequency of the electron plasma line is corrected for the e - e collision. If the effect of the e - i collisions is included, the resonance frequency can be written in the form:^{63, 64)}

$$w_L = w_p [(1 + \delta^{ei}) + 3k^*^2 (1 + \delta^{ee}) / (1 + \delta^{ei})]^{1/2} \quad (\text{IV A25})$$

where δ^{ei} and δ^{ee} is the small positive correction factors due to the e - i and e - e collisions, respectively. Then one can rewrite Eq. (IV A25) as

$$\begin{aligned} w_L &\approx (1 + \delta^{ei})^{1/2} w_p [1 + 3k^*^2 (1 + \delta^{ee}) (1 - 2\delta^{ei})]^{1/2} \\ &\approx (1 + \delta^{ei})^{1/2} w_p [1 + 3k^*^2 \{1 + (\delta^{ee} - 2\delta^{ei})\}]^{1/2}. \end{aligned} \quad (\text{IV A26})$$

If $\delta^{ee} - 2\delta^{ei} > 0$, the resonance frequency, w_L shifts toward the higher frequency due to collisions for all k^* . According to the calculation by Niimura et al.,^{63, 64)} $\delta^{ee} = \lambda/408$ and $\delta^{ei} = \lambda/118$. Therefore $\delta^{ee} - 2\delta^{ei} < 0$. Thus for small k^* (or for well isolated plasma lines) the resonance frequency shifts toward the higher frequency, but for large $k^* (\gtrsim 1)$ the resonance frequency can be shifted toward the lower frequency compared with the collisionless case. In either case, however, the shift is very small, about 1% correction at most even for the plasma with large coupling parameter $\lambda (\lesssim 1)$.

Figs. (IVA5-a), (IVA5-b) and (IVA5-c) show computed electron-plasma line profiles, using the formula of column "f" in Table (IVAl), for (a) collision dominated plasmas ($a_S^{-1} \equiv k^* \ll 1$ or $\Gamma_c/w_e \approx \lambda/k^* \gg 1$, Γ_c : collision frequency); (b) collision and Landau damping competing plasmas ($k^* < 1$ or $\Gamma_c/w_e > 1$); and (c) Landau damping dominated plasmas ($k^* \gtrsim 1$ or $\Gamma_c/w_e \gtrsim 2$). Much more detailed calculation procedure and explanation of these figures can be found in Ref. 64.

While the electron-plasma line shows the collision dominated feature when

$$w_p \gg \Gamma_{e \rightarrow i} \approx a^2 w_p \lambda \ell n \lambda^{-1}$$

or

$$1 \gg a^2 \lambda \ell n \lambda^{-1} \quad (IVA27)$$

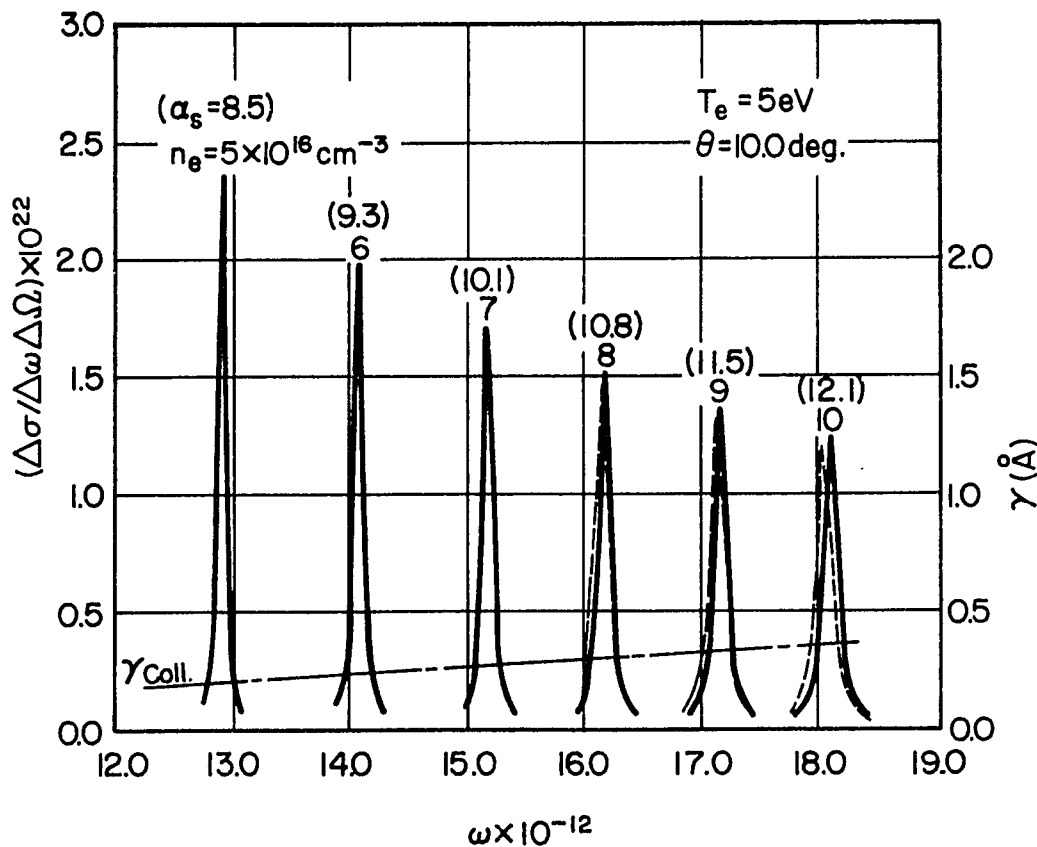


Fig.(IV A5-a) Electron-Plasma Line Profiles for Collision Dominated Plasmas

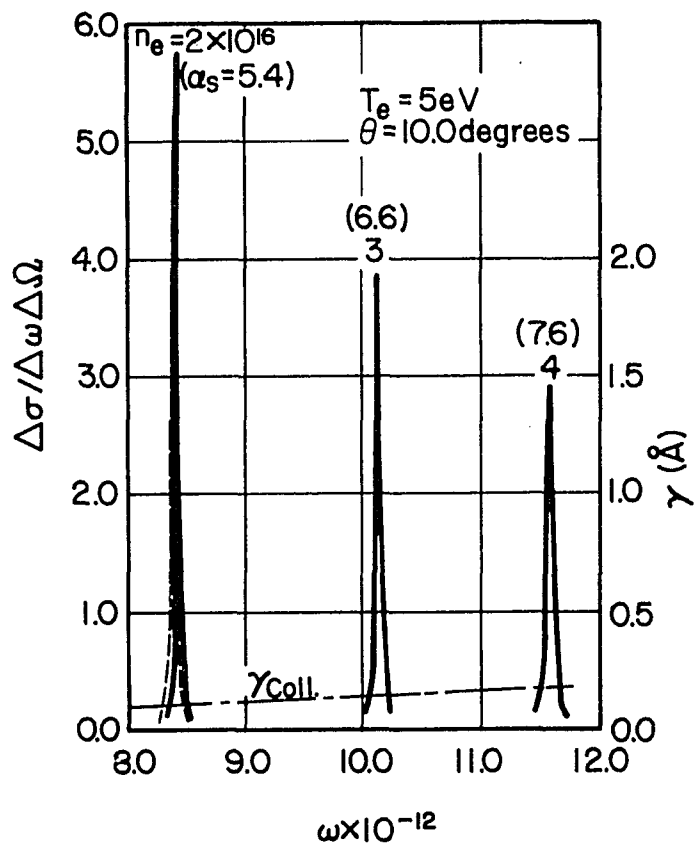


Fig.(IVA5-b) Electron-Plasma Line Profiles for Collision-Landau Damping Completing Plasma

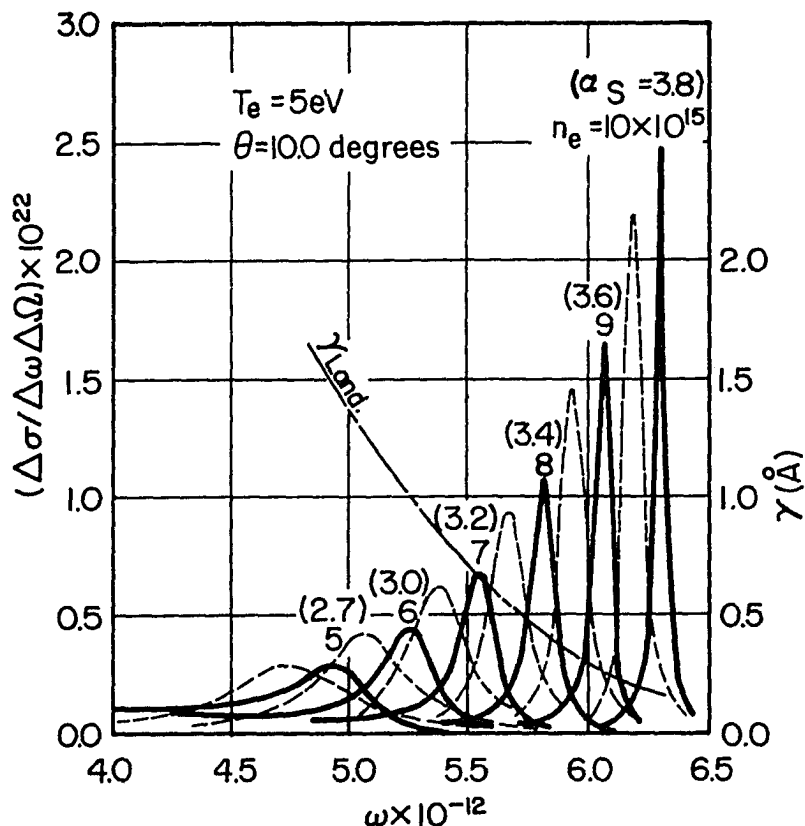


Fig.(IVA5-C) Electron-Plasma Line Profiles for Landau Damping Dominated Plasmas

or $\lambda_D \ll MFP^{ei};$

the ion-acoustic line shows the collision dominated feature when

$$w_i \ll \Gamma_{ii} \approx \alpha w_p \lambda \ell n \lambda^{-1}$$

or $k^* \ll \lambda \ell n \lambda^{-1}$ (IV A28)

or $\lambda_i \gg MFP^{ii}.$

Fig. (IV A6) shows the relationship between the longitudinal plasma waves (electron-plasma and ion-acoustic waves) and the mean free path (MFP) lengths in the collision dominated plasma.

The ion temperature can be measured from the resonance frequency of the ion-acoustic line. However for collision dominated plasmas the resonant frequency is not the ion doppler frequency w_i but shifts toward the higher frequency:

$$\begin{aligned} w_L &= k(\gamma_e + \gamma_i)^{\frac{1}{2}} \left(\frac{k_B T}{M} \right)^{\frac{1}{2}} = \sqrt{\frac{3}{5}} (\gamma_e + \gamma_i)^{\frac{1}{2}} w_i && \text{(IV A29)} \\ &= \sqrt{\frac{3}{5}} \left(\frac{5}{3} + 1 \right)^{\frac{1}{2}} w_i = \left(\frac{8}{5} \right)^{\frac{1}{2}} w_i \text{ for } \alpha^{-1} \gg \Gamma_{ii}/w_i \gg 1 \\ &= \sqrt{\frac{3}{5}} \left(\frac{5}{3} + \frac{5}{3} \right)^{\frac{1}{2}} w_i = 2^{\frac{1}{2}} w_i \text{ for } \Gamma_{ii}/w_i \gg \alpha^{-1}. \end{aligned}$$

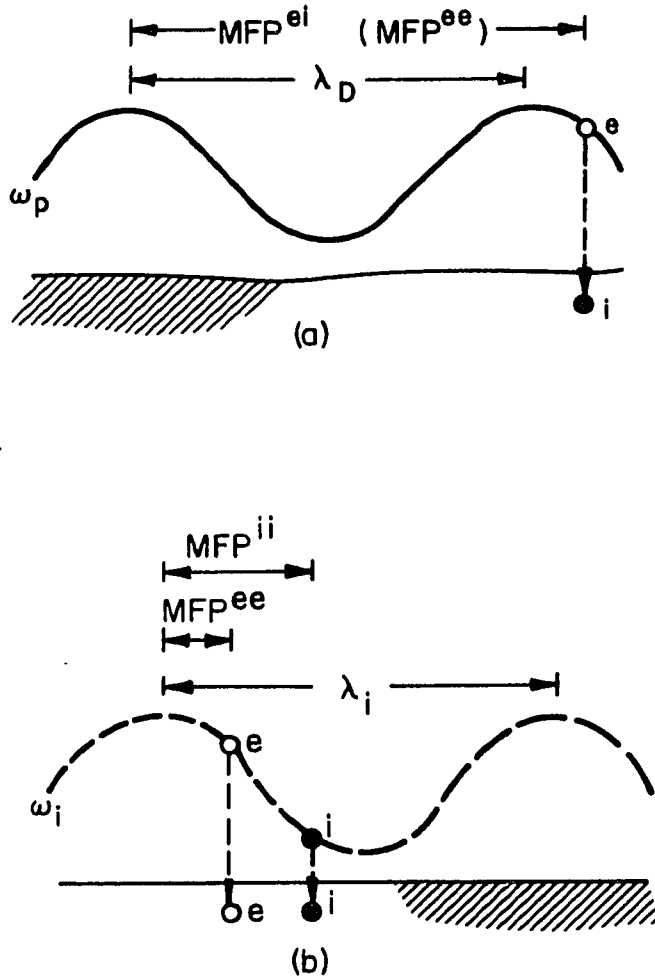


Fig. (IVA6). Collision Dominant Plasma Waves:
 (a) Electron-Plasma Wave
 (b) Ion-Acoustic Wave

Numerical result (Fig. IVA7) shows smooth transition of the resonance frequency from collisionless to collision dominated regimes.⁵⁹⁾

Fig. (IVA8) shows an example of ion-acoustic lines computed by using the formulae of columns "d" and "e" in Table (IVAl). The resonance line width is governed by various Coulomb collisions. The relationship between the collision frequency and the damping rate of the ion-acoustic line is shown in Ref. 59. Since the binary collision frequency

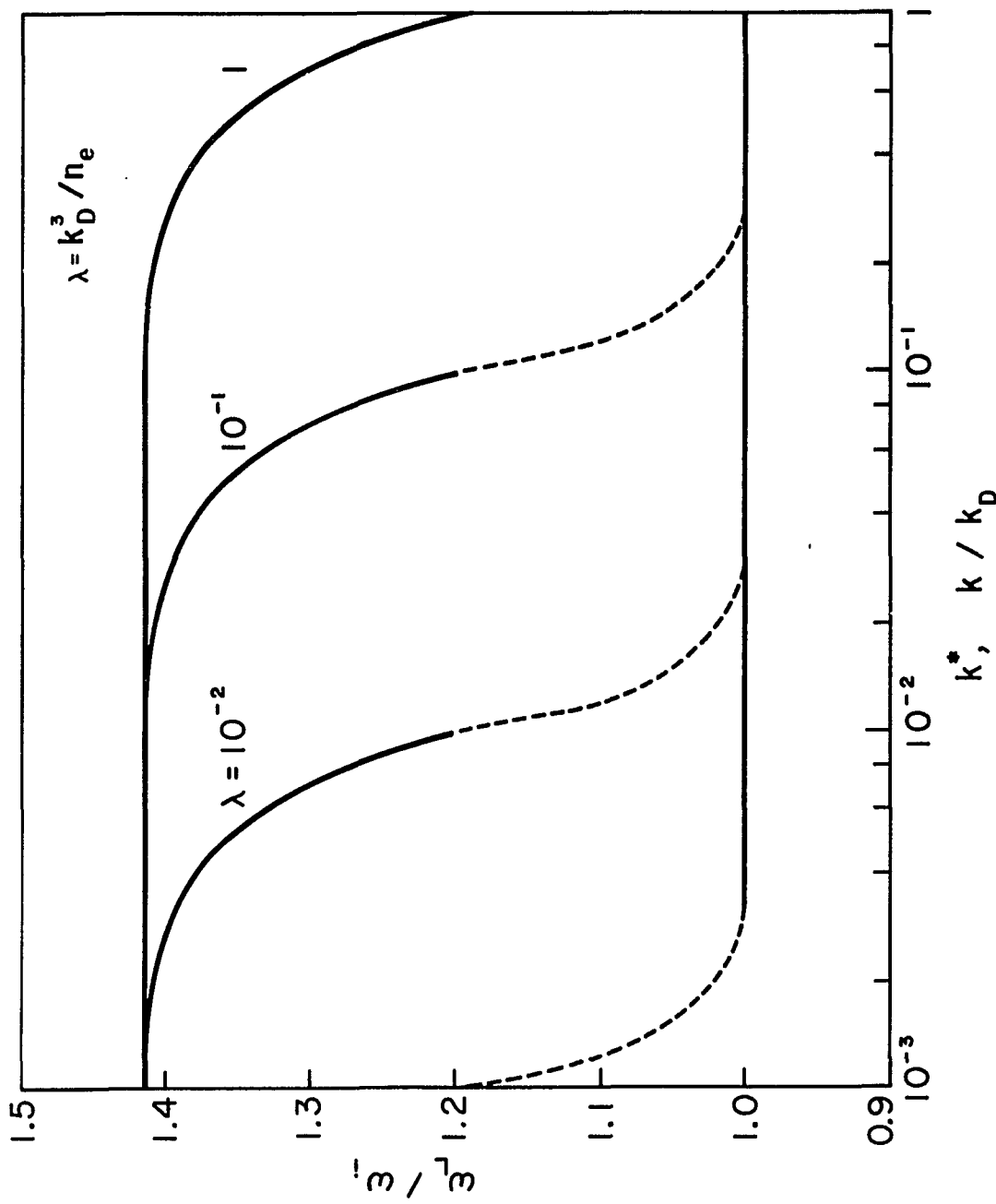


Fig (IVA7) Resonant Frequency of Ion-Acoustic Line

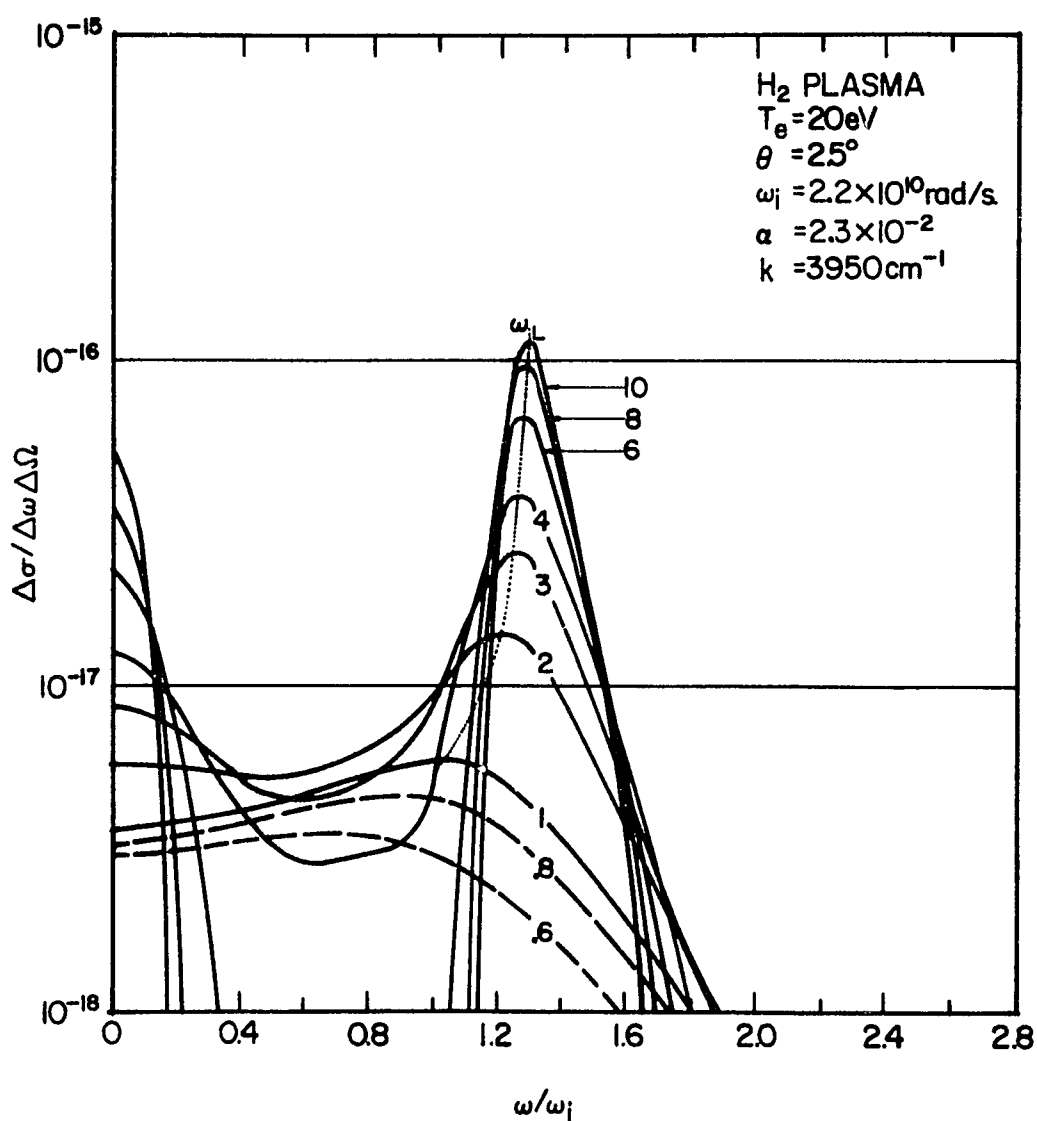


Fig. (IV A 8) Differential Scattering Cross Section of Ion-Acoustic Line for Collision Dominated Plasmas.
 Numbers for Curves are Electron Number Density, $n_e \times 10^{-25}$ [m⁻³].

is related to the thermal conductivity (k) and/or the coefficient of viscosity (η) as:⁶⁸⁾

$$\left. \begin{aligned} \Gamma_{ee} &= \frac{15}{4} \frac{c_e^2 n_e}{k_e} \times 0.75 = \frac{3}{4} \frac{c_e^2 n_e m}{\eta_e} \\ \Gamma_{ii} &= \frac{15}{4} \frac{c_i^2 n_i}{k_i} \times 0.75 = \frac{3}{4} \frac{c_i^2 n_i M}{\eta_i}, \end{aligned} \right\} \quad (\text{IVA30})$$

the precise measurement of the ion line gives the magnitude of those transport coefficients (where c_e and c_i are the sound velocities in the electron and ion media, respectively).

Fig. (IVA9) shows the Feynmann diagrams of incoherent scattering processes including the Landau and collisional damping of waves excited through Coulomb screening interaction.⁶⁰⁾ The complex amplitude of the differential scattering cross section is simply calculated by the multiplication of these factors shown in the Fig. (IVA9) in each scattering process:

$$\left(\left| \frac{d\sigma_s}{dw_b d\alpha_b} \right| \right)^{\frac{1}{2}} = \sqrt{\frac{n_e}{2}} r_o (\hat{e}_a \cdot \hat{e}_b) Q_e \frac{k^{*2}}{k^{*2} + Q} \frac{(\gamma_{\text{Land}} + \gamma_{\text{coll}})^{\frac{1}{2}}}{w} \quad (\text{IVA31})$$

where

$$\frac{1}{2} (\hat{e}_a \cdot \hat{e}_b)^2 = \frac{1}{2} (1 + \cos^2 \theta) \text{ for unpolarized light}$$

and $= \sin^2 \theta$ for polarized light.

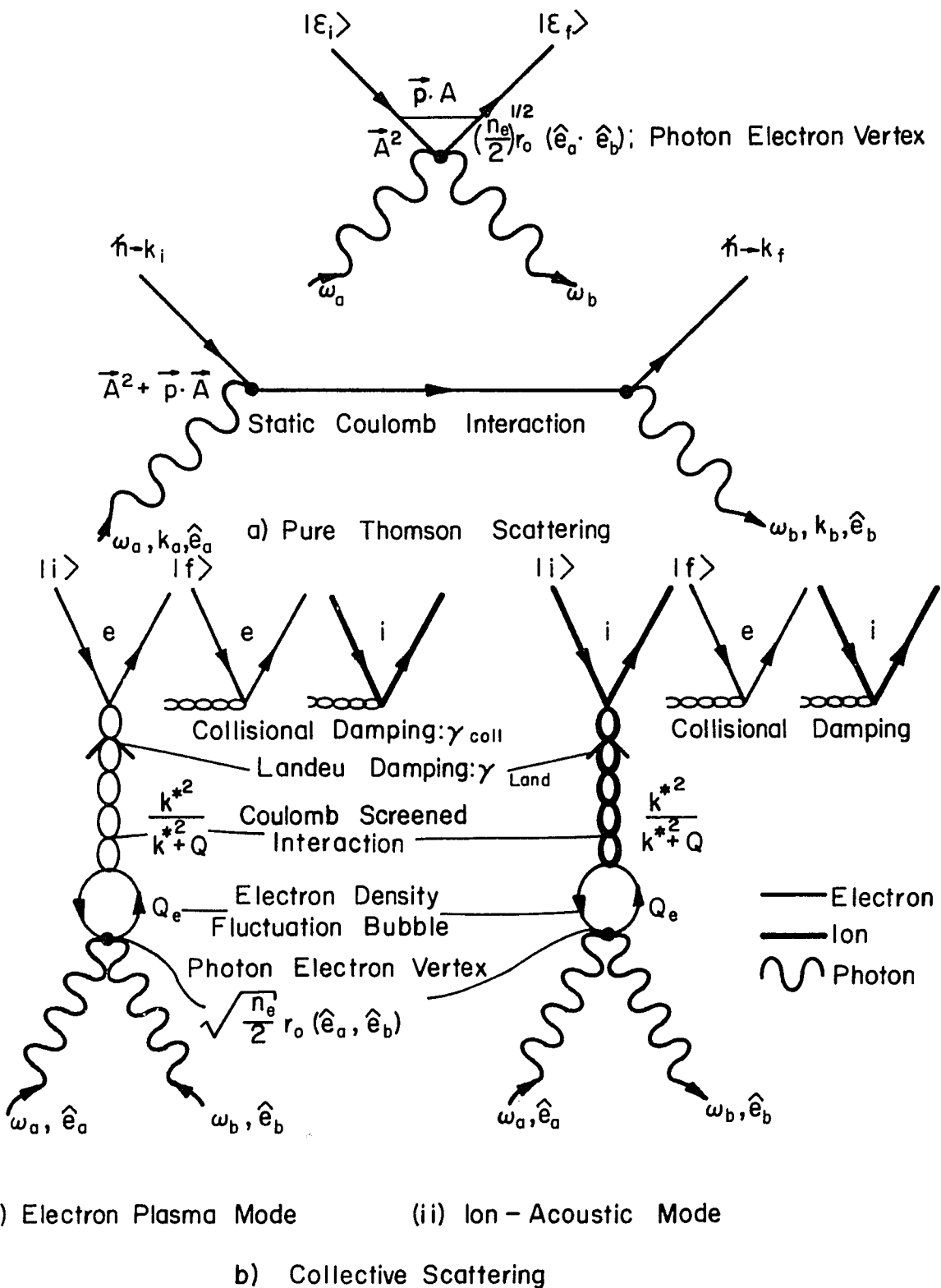


Fig (IVA9) Feynmann Diagrams for Incoherent Scattering Processes. [After Dubois]

[IVA-5] Differential Scattering Cross Section from Non-LTE Plasma

The theory by DuBois and Gilinsky,⁶⁰⁾ as well as the theory by Dougherty and Farley,⁶⁶⁾ assumes that temperatures of the electron and ion are equal each other (i.e., thermal equilibrium). However, Salpeter⁶¹⁾ and Rosenbluth and Rostoker⁶⁷⁾ consider the possibility of different electron and ion temperatures.

The non-local thermal equilibrium (LTE) effect becomes manifest in the scattered spectrum of the collective scattering region, because, during the non-collective (or pure Thomson) scattering regime, the contribution from ions are $a \equiv (m/M)^{\frac{1}{2}}$ -times smaller than that from electrons. Namely, the scattered spectrum from non-correlating ions (with electrons) is a very small Gaussian Doppler profile characterized by the ion temperature (T_i), mass (M) and density (n_i). Utilizing the expressions of Eqs. (IV A13) to (IV A15), one can obtain the width and peak intensity of the ion Doppler broadened profile as

$$\Delta\lambda_i = 22.8 \left(\frac{m}{M}\right)^{\frac{1}{2}} \sin \frac{\theta}{2} \sqrt{T_i(^{\circ}\text{K})/11,606} \quad [\text{\AA}] \quad (\text{IV A32})$$

and

$$\left. \frac{d\sigma_s}{dn_b} \right|_{w_b = w_a} = 1.24 \times 10^{-22} n_i (\text{m}^{-3}) \sin^2 \phi \Delta\lambda_i, \quad (\text{IV A33})$$

respectively. Therefore, by the comparison of Eqs. (IIA32) and (IIA14), one knows that the non-LTE condition does not appear on the

spectrum till $(m/M)T_i < T_e$, i.e., till $T_i \gg T_e$ if the experiment is in the non-collective scattering regime.

In the collective scattering region, the effect of non-LTE can be detected from the central feature but obviously not from the electron-plasma satellite lines. Because the collective scattering is due to the electrons correlating with ions the intensity of the central feature is as large as the order of magnitude of the pure Thomson scattering as is calculated from the column "b" of Table (IV A1):

$$\left. \frac{d\sigma_s}{dn} \right|_{w_b = w_a} = 1.24 \times 10^{-22} \left(\frac{M}{m} \right)^{\frac{1}{2}} n_i (m^{-3}) \sin^2 \phi \Delta \lambda_i. \quad (\text{IV A34})$$

However, the line width is very narrow as mentioned next.

The non-LTE effect on the ion-acoustic line has been investigated by Rosenbluth and Rostoker.⁶⁷⁾ When $T_i > T_e$, the only significant effect in this case is broadening of the central line which is consistent with its interpretation in terms of Doppler broadening characteristic of the ion thermal velocity, $v_i = (k_B T_i / M)^{\frac{1}{2}}$. When $T_e > T_i$, the ion contribution is small near the equilibrium resonance frequency, $w_L \approx w_i = kv_i$ but a sharp resonance peak appears in the neighborhood of the Langmuir frequency for ion oscillations, $w_L \approx (k/k_D)w_{pi} = k(k_B T_e / M)^{\frac{1}{2}}$. Thus, non-LTE effect cannot be detected in the experiment so long as one is probing the frequency range of w_e and/or of w_p . For the non-LTE detection the

experiment should be concentrated in the frequency range of w_i and/or w_i with electron temperature. The broadened line width and the enhanced resonance peak are the typical evidences of non-LTE plasma.

B. THOMSON SCATTERING EXPERIMENT AND THE RESULTS

[IVB1] General Experimental Considerations

A DC arc plasma with thoriated (~1%) tungsten electrodes, both water cooled, has been used for the investigation because of its simple geometry, reproducibility, fairly well-known plasma properties and suitable plasma conditions for applying the light scattering diagnostic technique. The arc has been run by a regulated DC power supply at current up to 15 Amps and operated at atmospheric and reduced pressures.

Argon arcs have been used primarily because of the well-known transport properties and the nearness to LTE compared, for example, with helium arcs. The argon arc is expected (from Chapter IIA) to produce a plasma of about 8,000°K equilibrium temperature with electron density of about $1.4 \times 10^{21} \text{ m}^{-3}$ at 15 Amps if LTE can be assumed near the atmospheric pressure. These plasma parameters are to be compared with the past plasmas studied by Thomson scattering experiments shown in Table (IVB1). Approximately forty experiments of light scattering from laboratory plasmas have been reported over the past ten years. The majority of these works deal with high density, high temperature plasmas and only a few reports deal with plasmas of relatively low electron temperatures less than 1 eV (11, 606°K).

The main difficulties encountered in the Thomson scattering experiment are due to: (a) the shot noise from discrete arrival of the weakly scattered photons, (b) the noise from natural plasma radiation,

AUTHORS	PLASMA	n_e (cm $^{-3}$)	T_e (eV)	AUTHORS	PLASMA	n_e (cm $^{-3}$)	T_e (eV)
Schwarz (1963-5)	Afterglow He Discharge	$10^5 - 10^{14}$	—	Daehler & Ribe (1966)	Scylla III Pinch	4×10^{16}	$T_e = 350$ $T_i = 2,200$
Funfer et al (1963)	θ Pinch	10^{17}	~ 100	Evans et al (1966)	Thetatron Discharge	1.1×10^{16}	$T_e = 256$
Davies & Ramsden (1964-6)	θ Pinch	5×10^{15} 2.4×10^{15}	33 1.0	Chan & Nodwell (1966)	Jet	$10^{16} - 10^{17}$	1 - 2
De Silva et al (1964)	Pulsed H, Arc	9×10^{14}	2.2	Izawa et al (1966)	Shock	10^{16}	33
Kunze et al (1964-5)	θ Pinch	3×10^{16}	4 - 215	Bottoms & Eisner (1966)	Conical Plasma Gun	10^{14}	2-5
Ascoli Bartoli et al (1964-5)	θ Pinch	2×10^{15}	$T_i = 70$	Weichel et al (1967)	Carbon Plasma	10^{19}	25
Gerry (1965-6)	Hollow Cathode Arc in Argon	$10^5 - 10^{14}$	3 - 8	Röhr (1967)	θ Pinch	5×10^{17}	$T_e = 32$ $T_i = 32$
Patrick (1965)	Annular Shock Tube	7×10^{15} $- 1.6 \times 10^{16}$	30 - 60	Dimock & Mazzucato (1968)	Model C Stellarator	$10^{12} - 10^{13}$	20-100
Consoli et al (1966)	θ Pinch	7×10^{15}	2 - 5	Nodwell & Van der Kamp (1968)	Jet	$10^{16} - 10^{17}$	1-2
Kunze et al (1966)	θ Pinch	2×10^{14}	2 - 160	Daehler et al (1969)	Scylla III	5×10^{16}	$T_e = 400$ $T_i = 2,200$
Malyshov et al (1966)	Glow Arc in Helium	2.5×10^{15}	1.8	Ringler & Nodwell (1969)	Arc	7.4×10^{15}	5
Kronast et al (1966)	θ Pinch	6×10^{16}	$T_i = 108$	Kellener (1970)	Arc	10^{16}	32
Anderson (1966)	Sheet Pinch (Triax)	2×10^{16}	2	Evans & Carolan (1970)	θ Pinch	10^{15}	20
John et al (1966)	θ Pinch	2×10^{17}	$T_i = 200$ $T_e = 800$	Daugherty et al (1970)	Shock	1.4×10^{14}	$T_e = 1.2$ $T_i = 12$
Ramsden et al (1966)	θ Pinch	6×10^{16} 2.4×10^{15}	$T_i = 150$ $T_e = 120$ eV	Kronast & Pietrzyk (1971)	π Pinch	10^{17}	$T_e = 3.2$ $T_i = 3.2$

Table (IVB1) Thomson Scattering Experiments Past Date

(c) unwanted Rayleigh (and Mei) scattering, (d) unwanted laser light scattered from the apparatus (and electrodes), and (e) unwanted direct heating effect of the laser upon the plasma. All of these produce spurious lights other than the Thomson scattering signal. For relatively low temperature plasmas, (b) is negligible but (c) and (d) are serious because the Doppler broadened line width of the pure Thomson scattering is narrow and becomes comparable with the instrumental width of the spectroscopic device. For low density plasmas (a) is not negligible while (e) becomes serious for high energy lasers.

The lowest electron number density that can be measured with reasonable accuracy is a function of various quantities such as the input laser energy, scattering volume, profile of the scattered light, band pass of the spectroscopic device, quantum efficiency of photocathode of the photodetector, minimum number of photoelectrons which exceed the noise photoelectrons, and the scattered geometry. On the other hand, the upper limit of the electron number density measurable is limited by the fact that the power of the scattered light must not be small compared with the power radiated from the plasma itself due to Bremsstrahlung and recombination radiation, whichever may become larger. Malyshev⁶⁹⁾ has calculated these conditions numerically and the graph is shown in Fig. (IVB1). This graph gives a rough estimation of the applicability of the Thomson scattering experiment. For instance, the range $10^{21} < n_e (\text{m}^{-3}) < 10^{24}$ is required for 10^{40}K plasma when a 6MW peak power, 0.2 Joule laser is used.

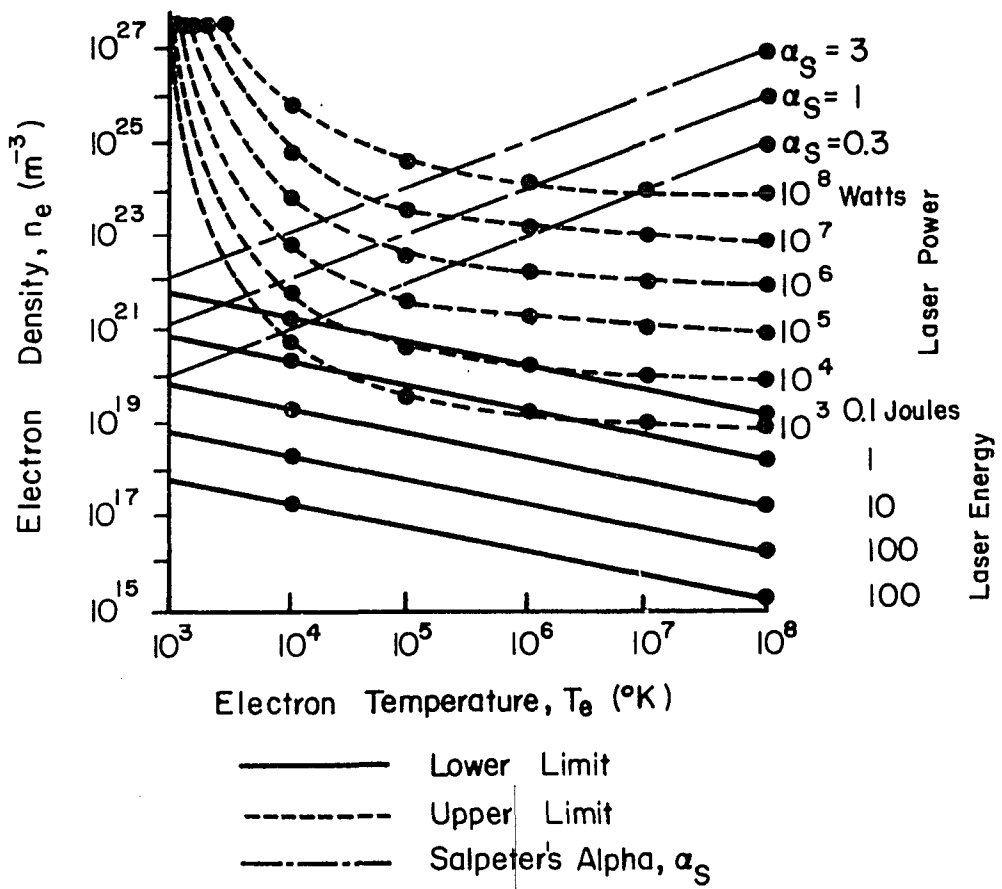


Fig.(IVB1) Limits of Applicability of Thomson Scattering Experiments

Assumed: 90° Scattering, Min. 1000 Photoelectrons, $10^{-3} m$ Laser Beam Diameter, Double Monochrometer as a Spectroscopic Device, Scattering Angle $\theta = 90^{\circ}$
 [After Malyshev⁶⁹⁾]

[IVB-2] Photon Statistics, Signal Estimation

Here the photon numbers of the pure Thomson scattering and of the Rayleigh scattering are calculated for the presently scheduled experimental conditions.

The definition of the total Thomson scattering cross section (σ_s) is

$$\sigma_s = \frac{\text{Scatt. Energy/electron}}{\text{Incident Energy/m}^2} \cdot [\text{m}^2/\text{electron}] \quad (\text{IVB1})$$

Let F_i be the incident energy, F'_s the total scattered energy in all solid angle, and V the scattering volume with cross section A , and ℓ the observed length as shown in Fig. (IVB2).

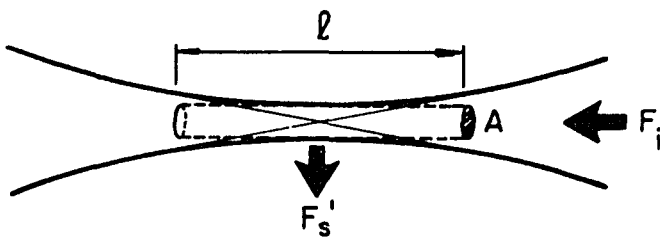


Fig. (IVB2). Scattering Volume

When the electron density is $n_e [\text{m}^{-3}]$ the total electrons contained in the scattering volume is $n_e A \ell$. Using these quantities Eq. (IVB1) can be written as

$$\sigma_s = \frac{F'_s / n_e A \ell}{F_i / A} = \frac{F'_s}{F_i} \frac{1}{n_e \ell}, \quad (\text{IVB2})$$

which is independent of A or beam focusing. Hence using the result of Eqs. (IVA4) and (IVA5), one has

$$\frac{F'_s}{F_i} = n_e \ell \sigma_s = 6.65 \times 10^{-29} n_e \ell \quad (\text{IVB3})$$

or

$$\frac{F_s}{F_i} = n_e \ell d\sigma_s = 7.94 \times 10^{-30} n_e \ell \sin^2 \phi d\alpha \quad (\text{IVB4})$$

where F_s is the scattered energy per unit solid angle.

Since the relationship of Eq. (IVB2) is the same for Rayleigh scattering by replacing n_e with n_n (neutral number density), one can write

$$\begin{aligned} \left(\frac{F_s}{F_i} \right) &= (d\sigma_s)_{Ra} n_n \ell \\ &= [(d\sigma_s)_{Ra} / (d\sigma_s)_{Th}] (d\sigma_s)_{Th} n_n \ell. \end{aligned} \quad (\text{IVB5})$$

Using the numerical value for Rayleigh scattering cross section,⁷⁰⁾ the ratio of Rayleigh to Thomson scattering is given by

$$(d\sigma_s)_{Ra} / (d\sigma_s)_{Th} = 1/423 \text{ for Argon}$$

$$= 1/26,800 \text{ for Helium} \quad (\text{IVB6})$$

When one chooses $\theta = 90^\circ$, Eq. (IVB5) becomes, for argon gas,

$$\left(\frac{F_s}{F_i} \right)_{Ra} = 1.88 \times 10^{-32} n_n l d\alpha \quad (\text{IVB7})$$

For helium gas the above numerical factor is 2.97×10^{-33} or two orders of magnitude smaller than the case of argon.

Solid angle is

$$d\alpha = \frac{\pi r^2}{f_o^2} = 3.5 \times 10^{-3} [\text{sr}]. \quad (\text{IVB8})$$

for the f/15 receiving lens of focal length $f_o = 45 \times 10^{-2} \text{ m}$ and diameter $2r = 3 \times 10^{-2} \text{ m}$. The neutral atom density (n_n) at 1 atm (= 620 Torr for the altitude 5,000 ft) is $1.9 \times 10^{25} \text{ m}^{-3}$ at 300°K and $7.13 \times 10^{23} \text{ m}^{-3}$ at $8,000^\circ\text{K}$. The observed length $l = 10^{-3} \text{ m}$. Then Eq. (IVB7) becomes

$$\left(\frac{F_s}{F_i} \right)_{Ra} = 1.25 \times 10^{-12} \quad (\text{IVB9})$$

for 300°K , 1 atm-pressure argon gas. The energy associated with one photon from the ruby laser is $h\nu = 2.87 \times 10^{-19} \text{ Joule}$ (or 1.79 eV) and a

1 Joule laser emits 3.48×10^{18} photons. If one assumes $F_i = 0.2$ Joule, Eq. (IVB9) yields

$$F_s = 8.7 \times 10^5 \quad (\text{IVB10})$$

The total transmission coefficient for the optical components of the receiving optics is

$$T = (0.86)^3 (0.06) (0.80) (0.50) = 0.0152 \quad (\text{IVB11})$$

↑ ↑ ↑ ↑
lenses IF filter color analyzer
 filter

Thus the number of photons arriving on the photocathode of a photomultiplier tube is

$$p = T \cdot F_s = 1.35 \times 10^4 \text{ [photons]} \quad (\text{IVB12})$$

The p number of photons create n_p number of photo-electrons in the photomultiplier with quantum efficiency ζ and gain G :

$$\begin{aligned} n_p &= \zeta G p \\ &= (3.2 \times 10^{-2})(1.3 \times 10^6)p \\ &= 4.16 \times 10^4 p \text{ [photoelectrons]} \quad (\text{IVB13}) \end{aligned}$$

for EMI9558QB(S - 20) photomultiplier at 1,150 Volt.

The corresponding photocurrent pulse with duration Δt is

$$I_p = e n_p / \Delta t = 1.66 \times 10^{-7} p \text{ [Amp]} \quad (\text{IVB14})$$

for a giant pulse laser with $t = 40 \text{ nsec}$, which yields

$$V = I_p R = 8.32 \times 10^{-6} p \text{ [Volt]} \quad (\text{IVB15})$$

for $R = 50\Omega$ load resistance. Then using Eq. (IVB12), the Rayleigh scattering signal from 1 atm-pressure argon is given by

$$\begin{aligned} V_{Ra} &= 0.112 \text{ [Volt] at } 300^\circ\text{K} \\ &= 4.20 \times 10^{-3} \text{ [Volt] at } 8,000^\circ\text{K}. \end{aligned} \quad (\text{IVB16})$$

On the other hand, the Thomson scattered signal from $8,000^\circ\text{K}$ plasma with $n_e \simeq 10^{21} \text{ m}^{-3}$ is given by

$$\begin{aligned} V_{Th} &= (423) \left(\frac{10^{21}}{7.13 \times 10^{23}} \right) \left(\frac{8}{27} \right) (4.20 \times 10^{-3}) \\ &= 7.35 \times 10^{-4} \text{ [Volt]}, \end{aligned} \quad (\text{IVB17})$$

which is smaller than the Rayleigh signal by a factor 0.175 at the center wavelength of the laser. In Eq. (IVB17), $(8/27)$ is the ratio of the spectrum width of a narrow-band interference filter to the Doppler width of $8,000^\circ\text{K}$ plasma (see Eq. IVA14). Thus the Thomson scattered signal can be detected where the intensity of the Rayleigh scattering profile (which is a convolution between Rayleigh scattering delta

function and transmission function of the narrow-band interference filter) has decreased to about 1/5 of that at the center wavelength.

The photocurrent corresponding to the Thomson scattering is

$$i_p = 1.4 \times 10^{-5} \text{ [Amps]} \quad \text{IVB18)$$

from Eq. (IVB17). This scattered signal must not be smaller than the shot noise current given by⁷¹⁾

$$i_s = \sqrt{\overline{(\Delta i)^2}} = \{2e(i_d + i_T)\Delta f\}^{\frac{1}{2}}, \quad \text{IVB19)$$

where i_d is the dark current and $i_T = i_p + i_{\text{stray}} + i_L$ is the total light current adding the scattered signal, stray light of laser, and plasma luminosity. For the practical experiment $i_T \approx i_p$ and Eq. (IVB19) yields

$$i_s = 3.3 \times 10^{-8}, \text{ [Amps]} \quad \text{IVB20)$$

which is negligibly small compared to i_p given by Eq. (IVB18). Since the ionization potential of argon (15.75 eV) is larger than the plasma potential (1 eV), the i_L is mainly due to recombination radiation rather than the Bremsstrahlung. In Eq. (IIA127) the power density of the recombination radiation has been estimated to be $10^6 \sim 10^7 \text{ Watt/m}^3$. On the other hand, the Thomson scattered power is, from Eq. (IVB3) for 6MW laser, 4.0×10^{-3} Watt per scattering volume of $7.85 \times 10^{-10} \text{ m}^3$

or equivalently 5.1×10^6 Watt/m³. Thomson scattered power is about the same order of magnitude as plasma radiation or $i_p \approx i_L$. [This relationship has been observed experimentally in the present plasma, which is a cross check of Eq. (IIA127).]

Finally one needs to check the direct effects of the laser upon the plasma. The main direct effect is the electron heating via inverse Bremsstrahlung. The absorption cross section for the laser photon is given by⁷²⁾

$$\sigma_A(n_e, T_e) = 3 \times 10^{-48} \frac{n_e(m^{-3})}{T_e(eV)} [m^2]. \quad (\text{IVB21})$$

The energy that an electron gains from the laser at P_o [Watt] during a time period τ_L is

$$\Delta E = h\nu\sigma_A \frac{P_o}{A} \tau_L \\ = 1.875 \times 10^{-19} \frac{n_e}{T_e} \frac{P_o}{A} \tau_L [eV]. \quad (\text{IVB22})$$

The quantity of interest is the relative change

$$\frac{\Delta E}{(3k_B T_e / 2)} = 1.25 \times 10^{-19} \frac{n_e}{T_e^2} \frac{P_o}{A} \tau_L. \quad (\text{IVB23})$$

When a laser of 6MW, 40 nsec is focused to 10^{-3} m diameter upon a $T_e = 1eV$, $n_e = 10^{22} m^{-3}$ plasma, Eq. (IVB23) yields 9.55×10^{-3} or

about 1% increment of the electron temperature. Since the electron loses its energy to the ion after τ_{ei} (relaxation time), τ_L should be replaced by τ_{ei} if $\tau_{ei} \leq \tau_L$. From Eq. (IIA10-b), $\tau_{ei} = 10$ nsec for the considered plasma. Thus the actual temperature rises about 0.1% above the thermal level.

[IVB3] Apparatus and Procedure

(i) Laser System

The DC power supply (Console, 3.2 kV, 1mA Max.) for the laser pumping consists of 54-stage energy storage capacitors (SPRAGUE, PQ-425; 25 μ F each) connected in parallel and a lumped inductance of total 518 μ H. Two linear xenon flashtubes (EG & G, FX47C-6.5 water cooled) are connected in series with the power supply and the total arc resistance of the flashtubes is 0.5 Ω during the discharge at the maximum energy input. Therefore the current wave form is close to the critical damping with damping constant $(1/2R)(L/C)^{1/2} = 0.6$, pulse-width $2(LC)^{1/2} = 1.65$ msec and undamped half period $\pi(LC)^{1/2} = 2.6$ msec. Fig. (IVB3) shows the actual waveform of (a) current pulse observed by a 35-turn Rogowski's pick-up coil and of (b) xenon lamp light with a giant pulsed ruby laser observed by a photodiode. (Preceding spikes before the giant pulse are the weak optical leaks from the Pockels cell Q-switching device.)

The ruby laser (Linde, standard-grade, 90°-cut, 6.5" long and 3/8" diameter) can produce average 1.65 Joule in normal mode and

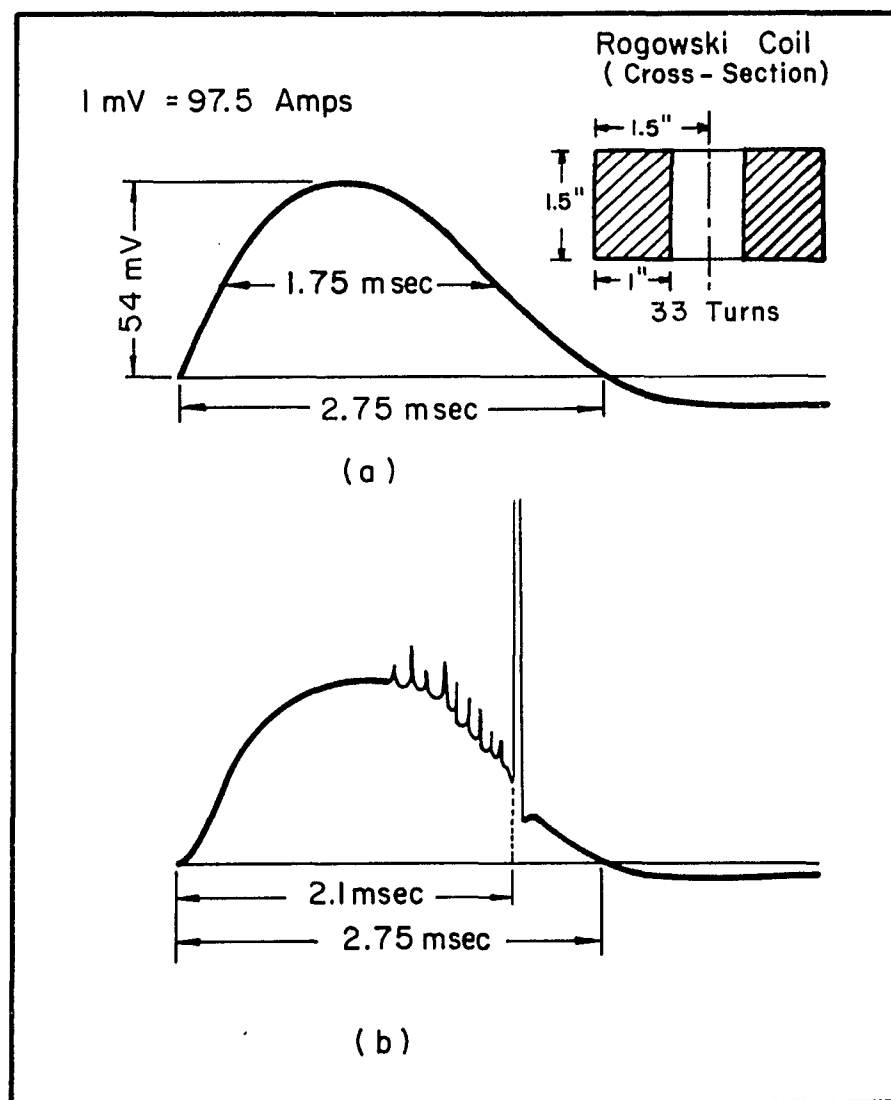


Fig. (IV B 3) (a) Current Waveform for Xe-Lamp Observed by a Rogowski Coil, (b) Xe-Lamp Light Profile with a Giant Pulsed Ruby Laser Observed by a Photodiode (Pockels Cell Q-Switching)

0.65 Joule in Q-switching mode when the charging voltage is 3 kV and when the full diameter of the ruby rod is used. Fig. (IVB4) shows the charging voltage dependence of the laser output energy. Only 0.03% and 0.01% of the input energy (6,000 Joules) are converted to the normal mode and to the Q-switching mode laser energy, respectively. High energy laser is favored for the Thomson scattering experiment as long as the laser heating effect on the plasma is negligible. Q-switched laser is used to reduce the background from the shot noise and plasma radiation.

Xenon lamps are triggered by a trigger module (EG & G, TM-11) which supplies 30 kV (max.) pulse with duration 1.5 μ sec. This trigger module has been modified to produce 8 V, 2 μ sec gate pulse for the Pockels cells Q-switching power supply (Crystal Lab., GP-3, dc 10 kV) as shown in Fig. (IVB5). Either Pockels cell or dye cell (cryptocyanine, 10^{-5} mol = 0.0048 g/l) are used for the Q-switching.

(ii) Arc System

The power supply for the dc arc is shown in Fig. (IVB6). Maximum current is 15 amps (with less than 0.1% ripple) and the open voltage 109 Volts. Fig. (IVB7) shows the I-V curve of operating arcs. Various materials (W, Cu, Steel, Al) as well as thoriated tungsten (Th. W) have been tested for the electrodes. The sputtering on the electrode surfaces has been found to be about the same when the environmental gas is same. Th. W was selected finally because of the

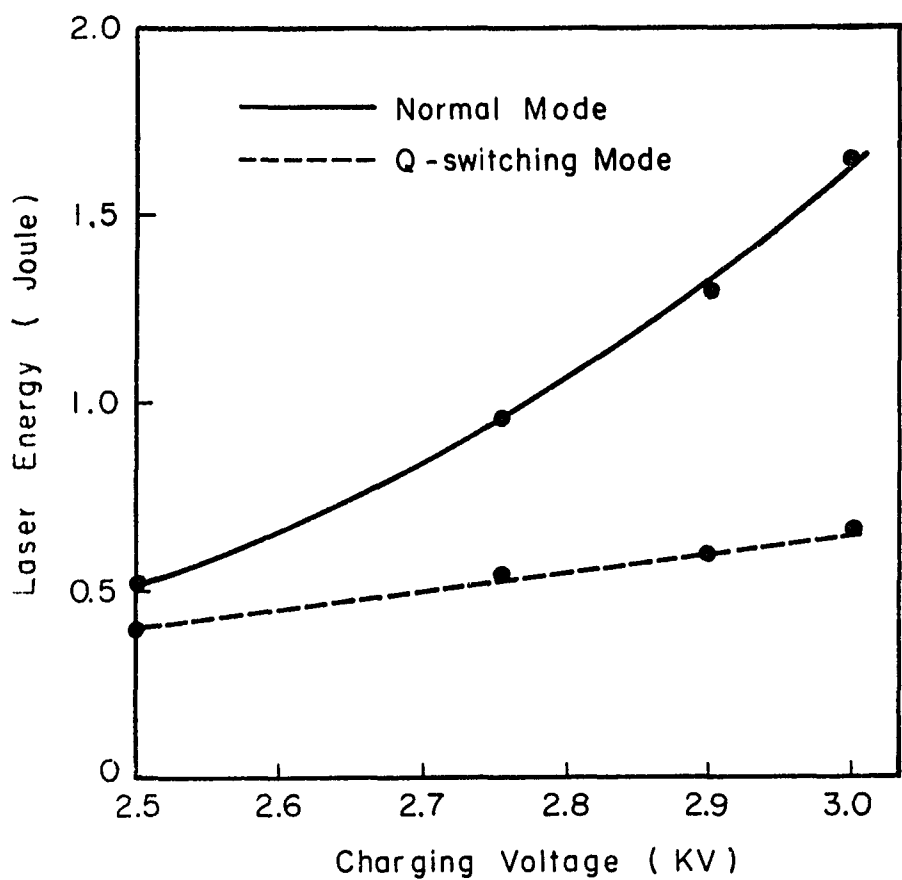


Fig. (IV B 4) Laser Output Energy Measured by Cu SO_4 Calorimeter

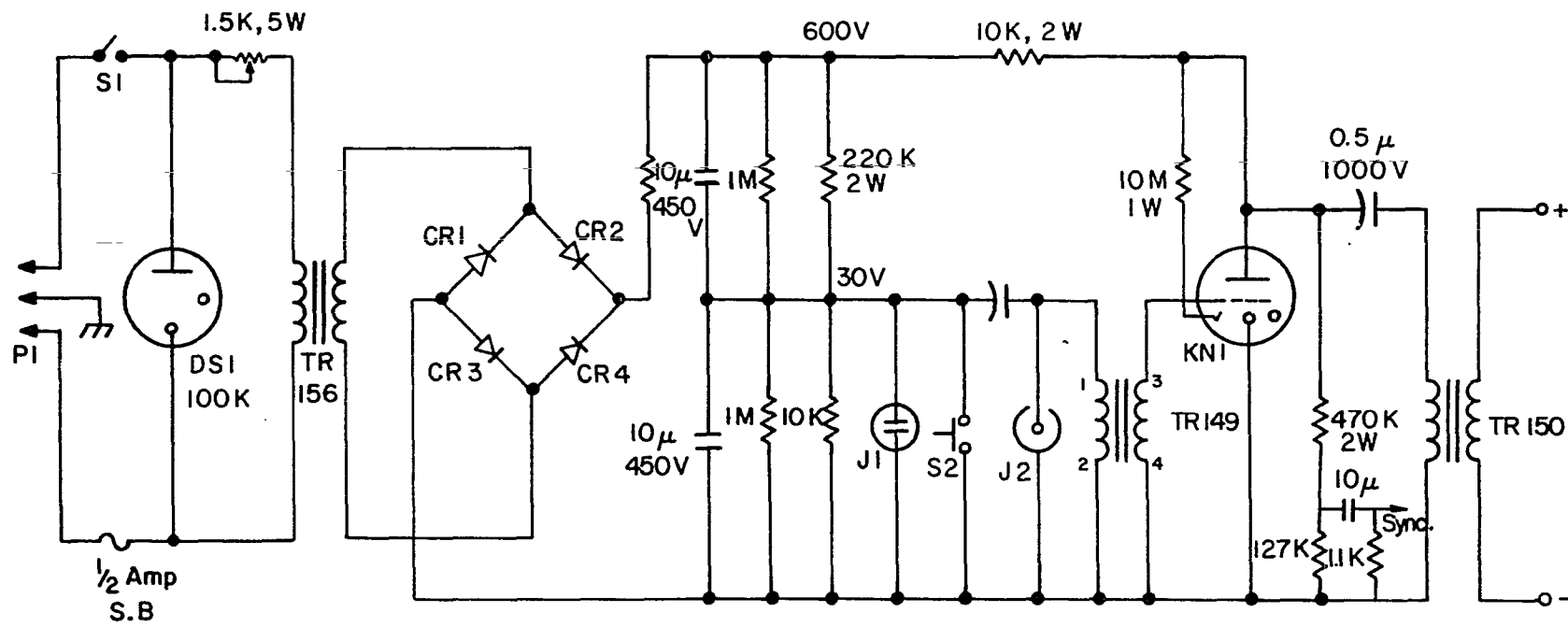


Fig. (IV B 5) Xe - Lamp Triggering Module with a Synchronous Gate Pulse for Pockels Cell Power Supply.

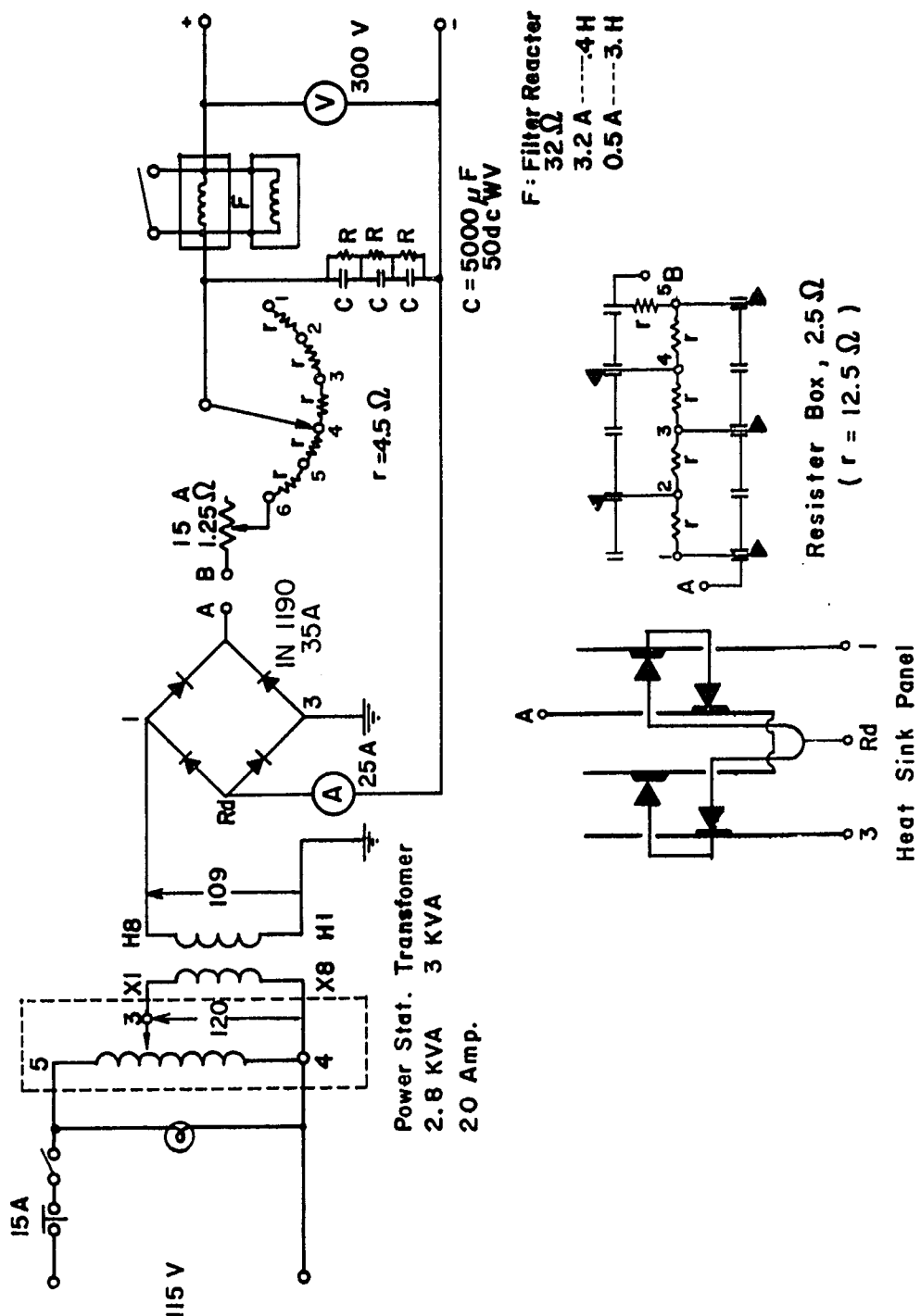


Fig. (IV B 6) Power Supply for DC Arcs.

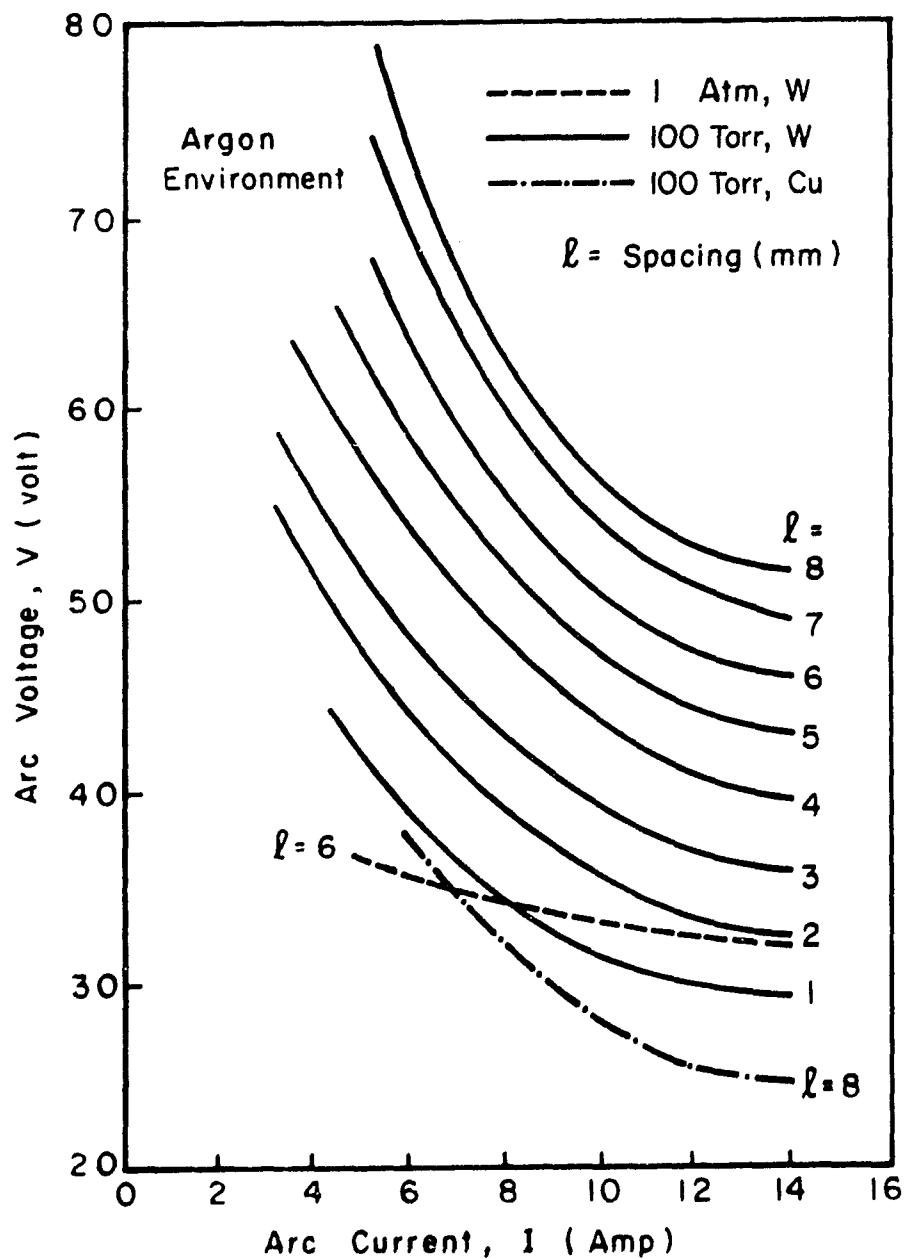


Fig. (IV B 7) Arc I - V Characteristics

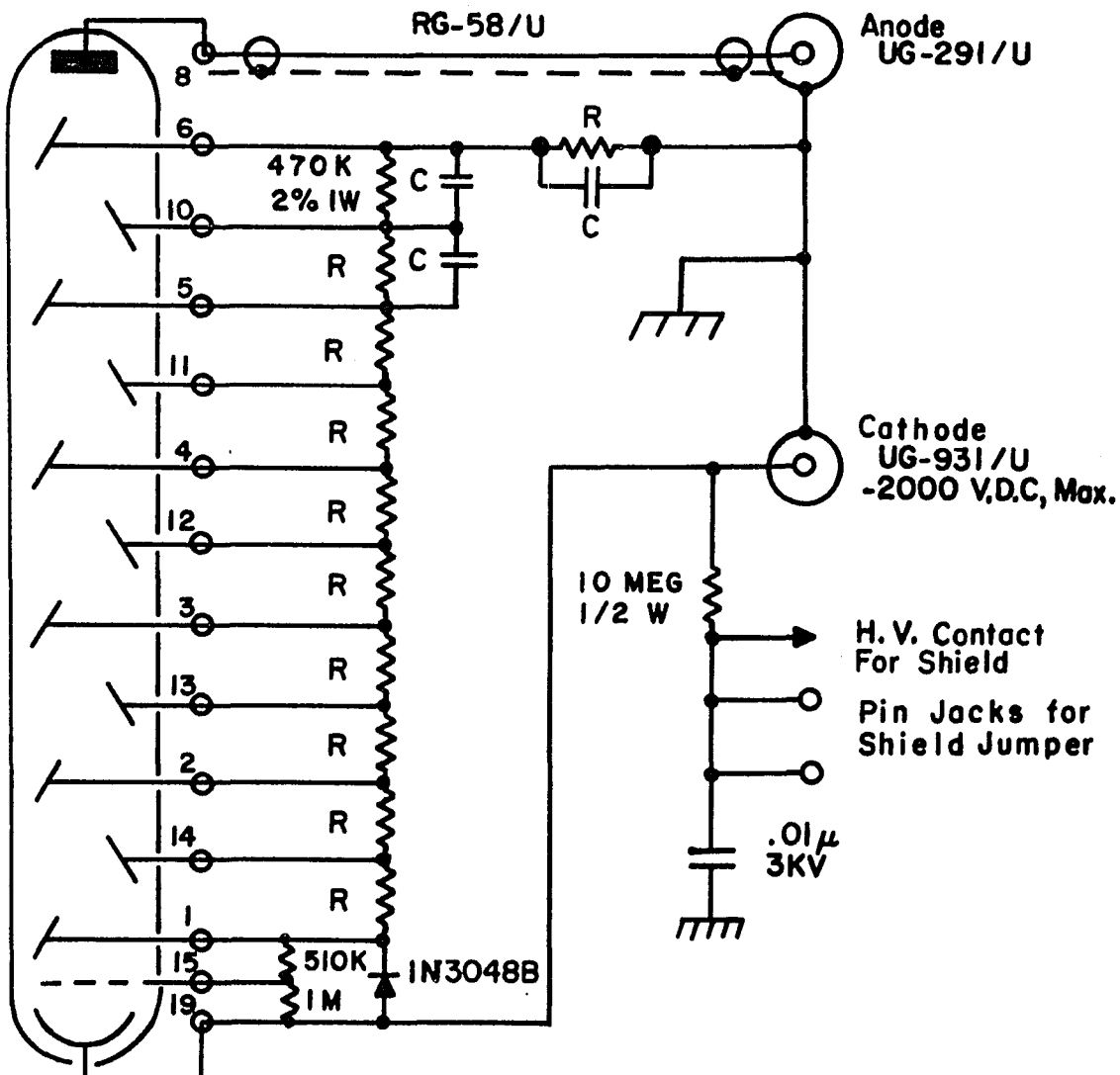
highest melting point (3653°K) in metals and lower work function (3.35 eV) compared with that of non-thoriated tungsten (4.4 eV). Dust free gases (Ar, H_e, N₂) are fed through a gas-filter filled with optical fiber glasses. Lighter gases give less sputtering but He arc is difficult to initiate and more difficult to realize LTE plasma because of the high ionization potential (24.46 eV) compared to Ar (15.75 eV).

(iii) Detector and Analyzer System

The laser output is monitored by photodiodes (RCA922 and HP5052-4201) and the scattered power is detected by a photomultiplier (EMI9558QB, S-20, 11-stages) shown in Fig. (IVB8). Linearities of the detectors have been carefully checked whenever the experimental condition changed.

A tilting interference filter (occasionally a monochrometer) has been used as the spectroscopic device. According to the theory of Fabry-Perot interferometer, the transmitted wavelength of the narrow band interference filter shifts toward longer wavelengths when it is tilted from the position of normal incidence. Fig. (IVB9) shows the peak wavelength shift against tilt angle.

Transmission band of the first order $\lambda^{(1)}$ changes by the equation written in Fig. (IVB9) where n^* is the effective refractive index of the coating material. Experimentally calibrated wavelength shift was $\Delta\lambda = 0.47 \phi^2$ as shown in Fig. (IVB10) for a specific IF filter (Spectrum System, C83671) with center transmission at $\lambda_0 = 6947 \text{ \AA}$, which gives



EMI 9558 Q
Circuit Schematic
Shield Dynode Assembly

(R = 220 K 2% 1 W, C = .01 μ 1000 V)

Fig. (IV B 8) Photomultiplier

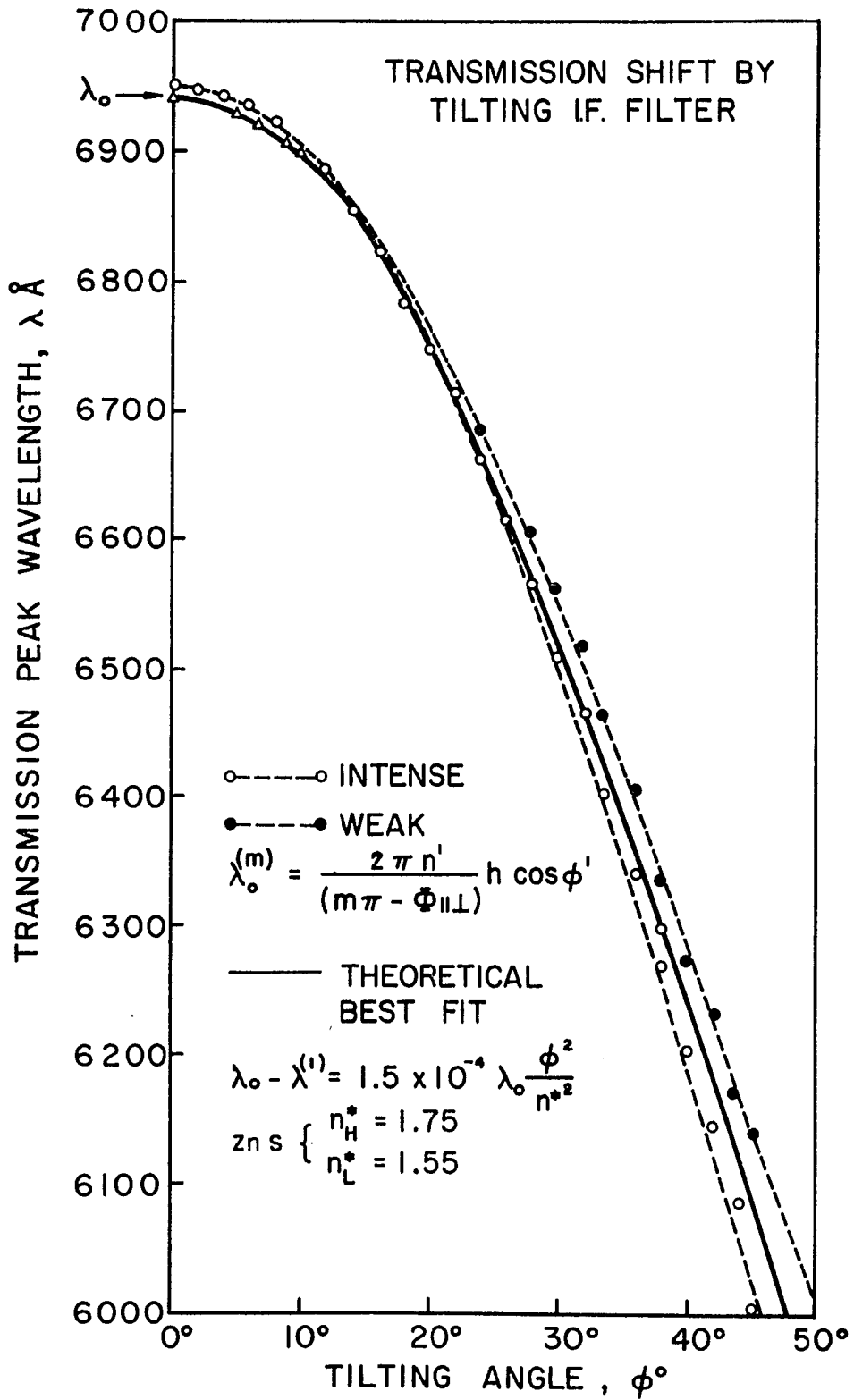


Fig. (IV B 9) Tilting Interference Filter

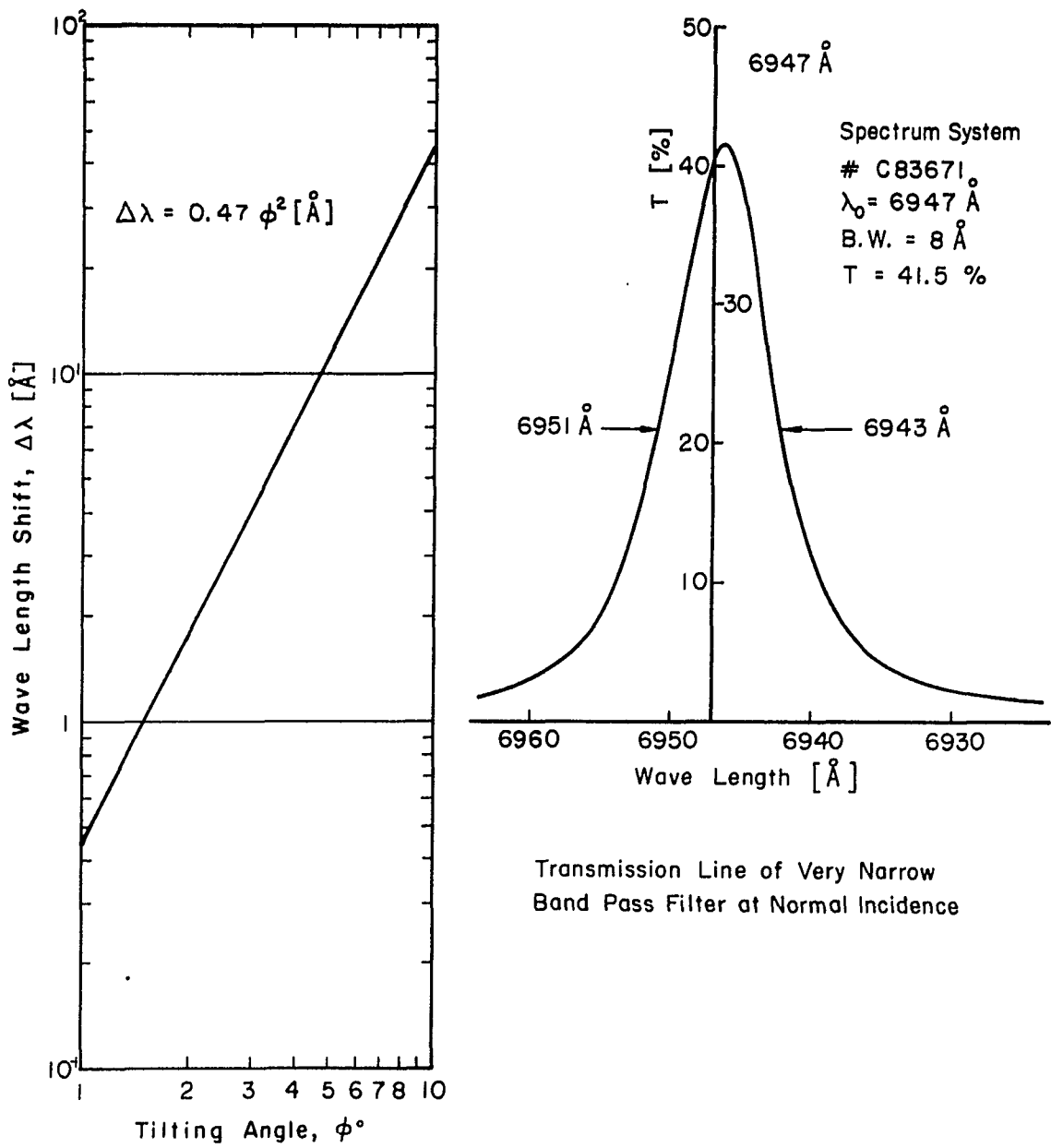


Fig. (IV B 10) Narrow Band Interference Filter

us $n^* = 1.55$, which equals exactly the theoretical value of n^*_L for ZnS listed in Fig. (IVB9). The narrow band pass (8 \AA) IF filter is mounted on the precision rotation stage measurable to $1/10$ of degree.

(iv) Optical System

For the reduction of laser stray light a polarizer-analyzer system is used in addition to the 90° -cut ruby rod. The linear polarized light is dumped, after focused in the arc, by a colored Brewster window. An offset viewing dump and Raman horn (both darkened) are installed to reduce the wall scattered background of the viewing lens. The complete optical system is aligned by using a CW He-Ne laser beam. Any slight off-axis of the relative optical components causes serious enhancement of the noise background. Normal incidence of the scattered light on to the narrow band pass interference filter has been checked in each experiment.

[IVB4] Experiments at Reduced Pressure

The schematic diagram of the experimental set-up is shown in Fig. (IVB11). A giant pulse ruby laser of 8 MW (40 nsec) is focused on the axis of a dc argon arc plasma at 100 Torr pressure. The geometry is shown in Fig. (IVB12). Electrodes are set at 6 mm apart and the arc draws 15 amps at 45 volts. The arc is housed in a special scattering chamber (shown in Fig. IVB13) equipped with a Brewster angle beam dump and a darkened Raman horn opposite the collecting

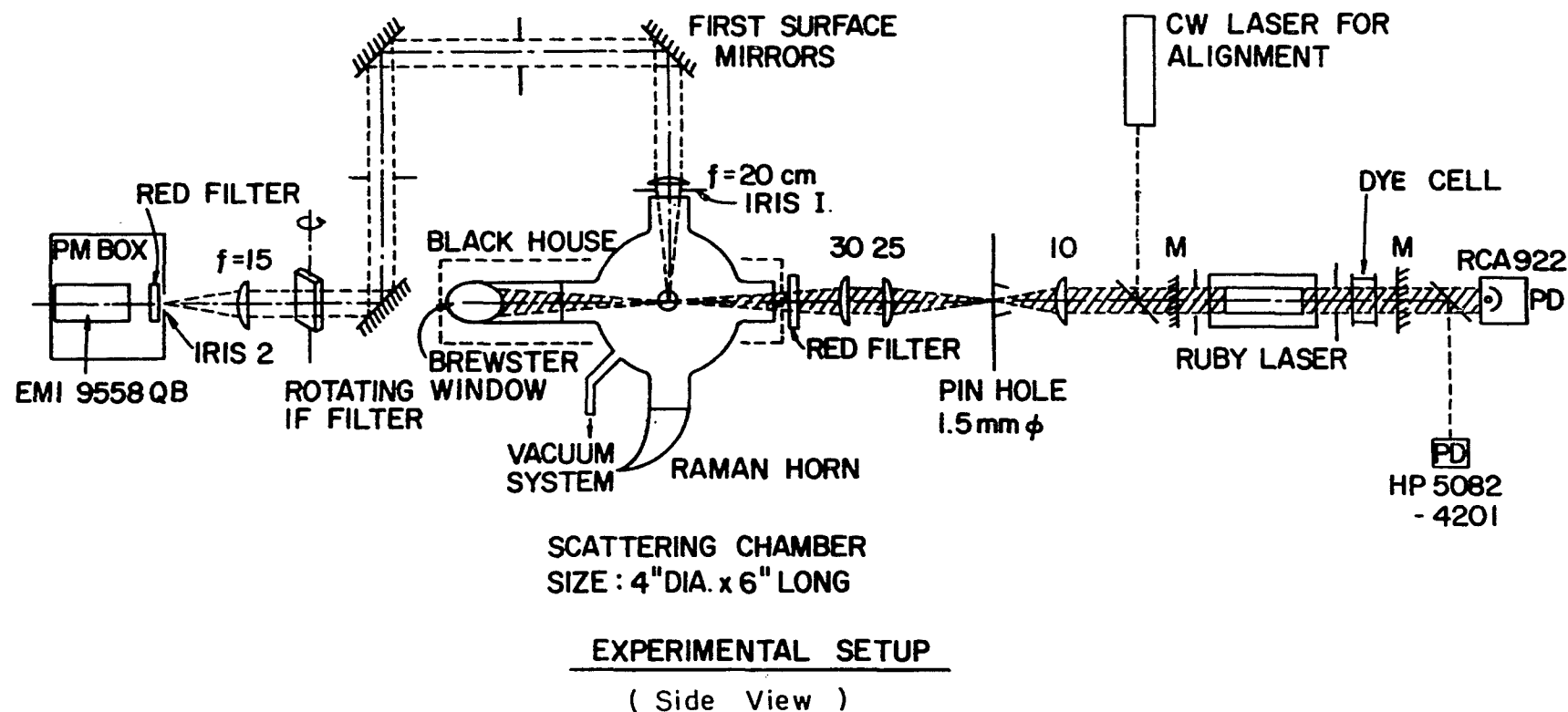


Fig. (IV B II) Thomson Scattering in Reduced Pressure

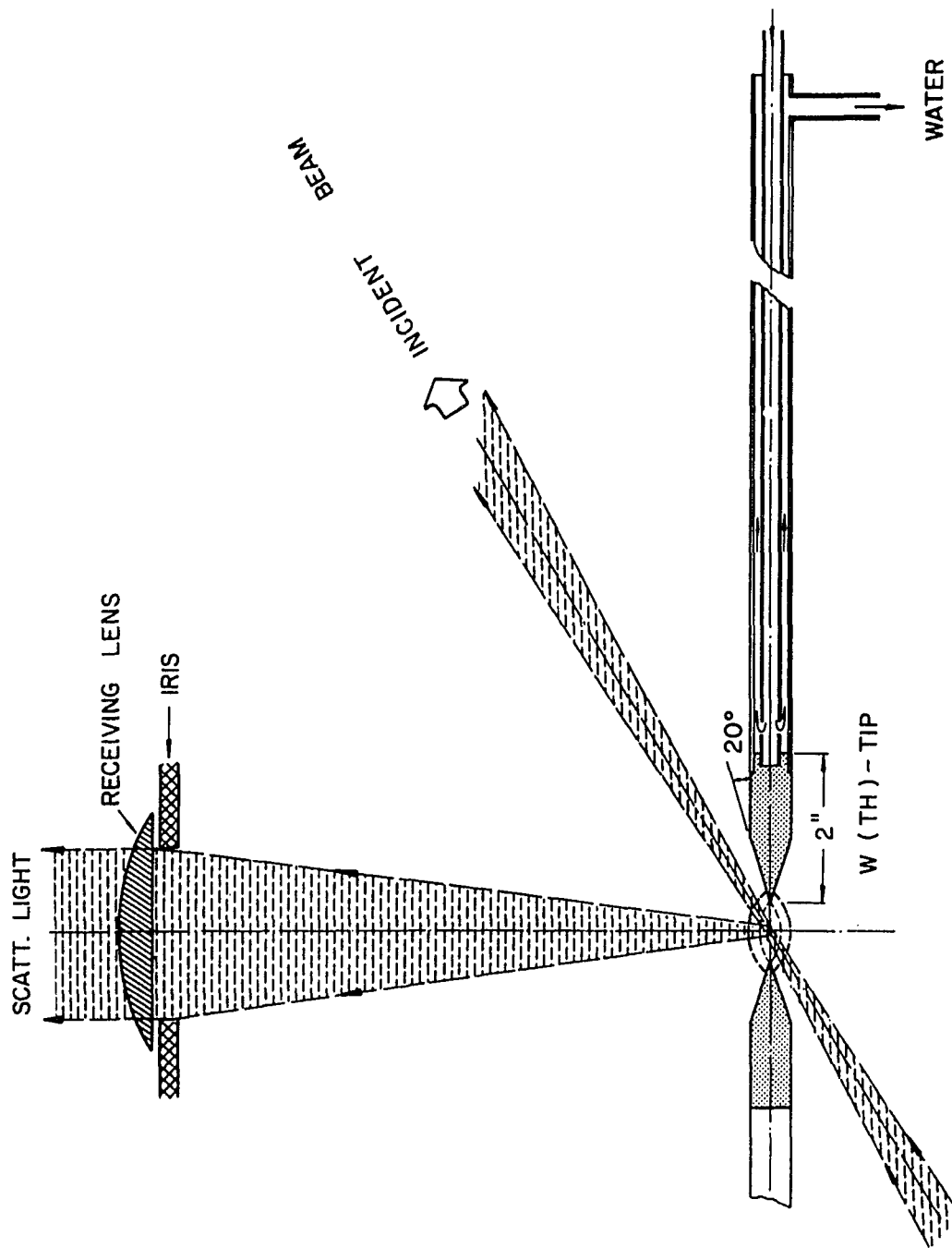


Fig. (IV B 12) Scattering Geometry

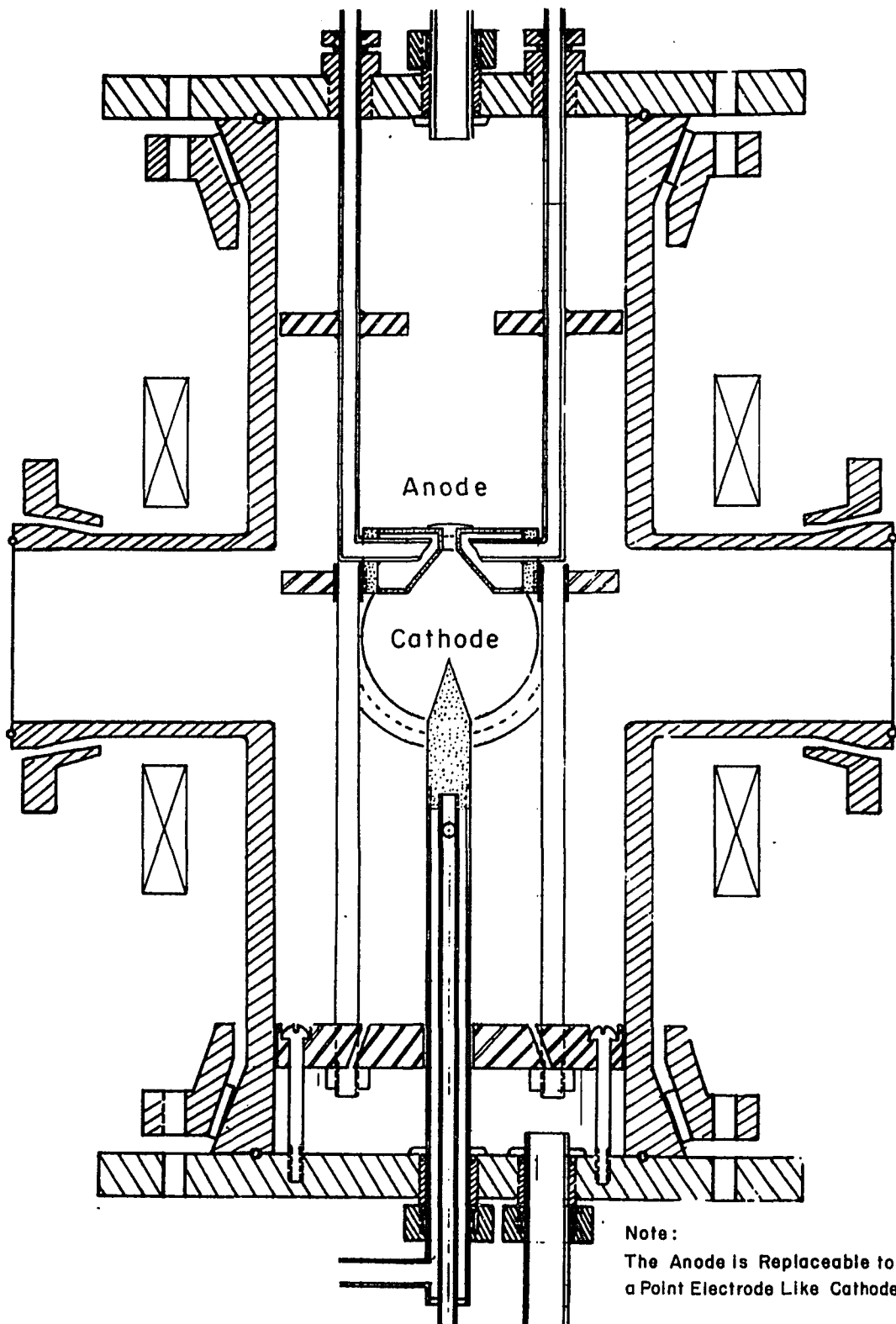


Fig. (IV B 13) Scattering Chamber (Top View)

lens. In addition, the glass wall of the scattering chamber is painted black on the outside. The scattered light is collected by an f/6 optical system and scanned by a tilting narrow-band pass (8 \AA) IF filter controlled by a precision rotator accurate to 1/10 of a degree. The scattered light is then focused onto an aperture of 5 mm \times 2 mm and the intensity is measured by an EM19558QB photomultiplier. The incident light is monitored by an RCA 922 vacuum photodiode (linearity range is less than $100\mu \text{ A}^{\circ}$) and both the outputs of photomultiplier and photodiode are displayed on a Tektronix 556 dual beam oscilloscope. The optical system is calibrated by Rayleigh scattering from dust-free argon at different pressures as shown in Fig. (IVB14) where the horizontal part is due to the scattering from wall of the chamber. Rayleigh scattering overcomes the wall scattering from above 200 Torr, which makes one select the range around 100 Torr pressure as the good experimental range for Thomson scattering. The stray light intensity has been reduced to 5×10^{-15} ($4 \times 10^{-2} \mu \text{W}$) of the incident laser intensity at $\Delta\lambda = 13 \text{ \AA}^{\circ}$. The Thomson scattered signal was observable experimentally for wavelengths shifted by more than 15 \AA° . Fig. (IVB15) shows a typical oscilloscope trace at $\Delta\lambda = 21.4 \text{ \AA}^{\circ}$ with a good S/N ratio of 5. The spectrum of scattered light together with that of the background stray light and plasma radiation are plotted in Fig. (IVB16). From the Rayleigh scattering data the electron density at $\Delta\lambda = 25 \text{ \AA}^{\circ}$ has been able to be calculated as $[4 \pm 0.2] \times 10^{20} \text{ m}^{-3}$. Error bars in

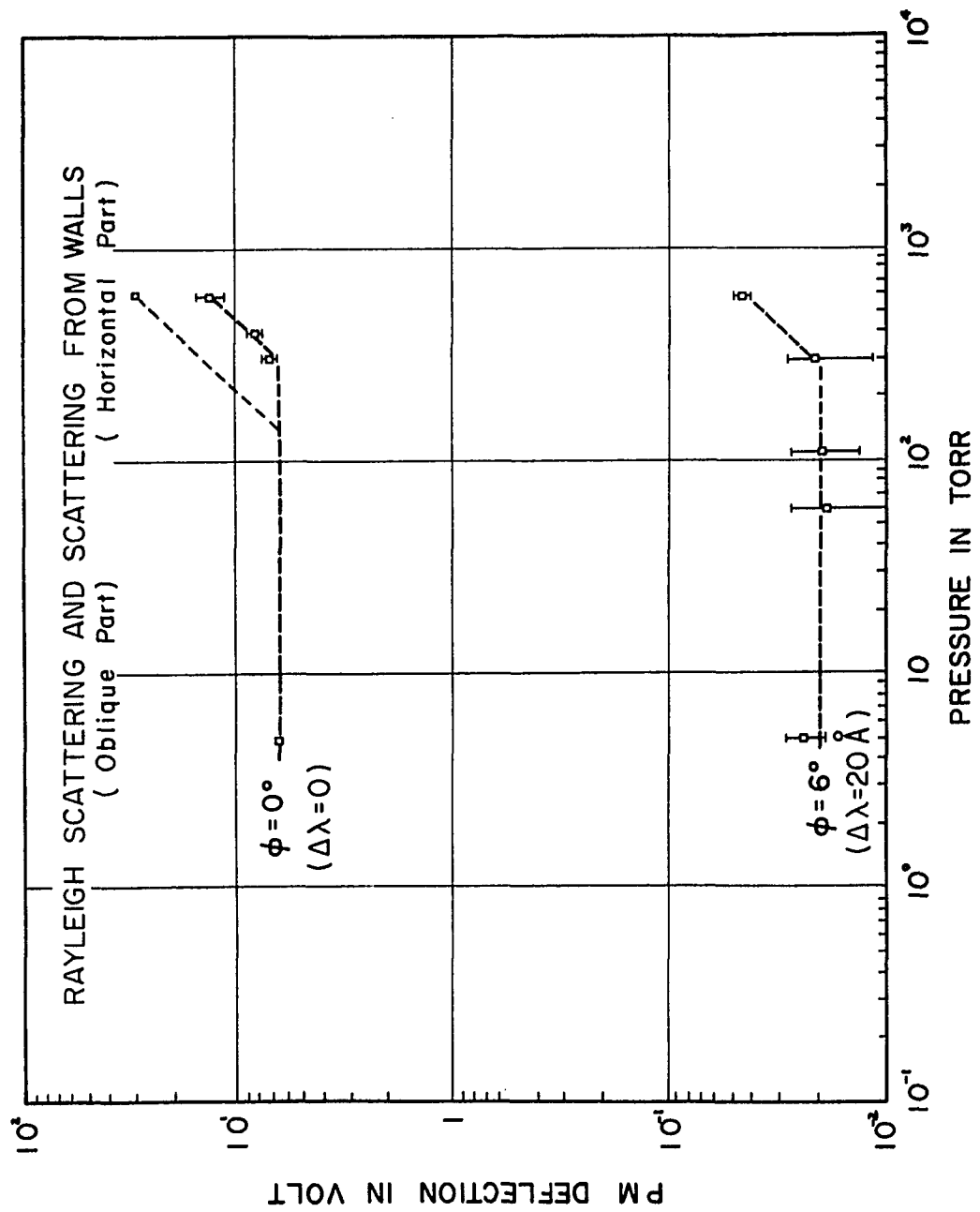


Fig. (IV B 14) Rayleigh and Wall Scattering

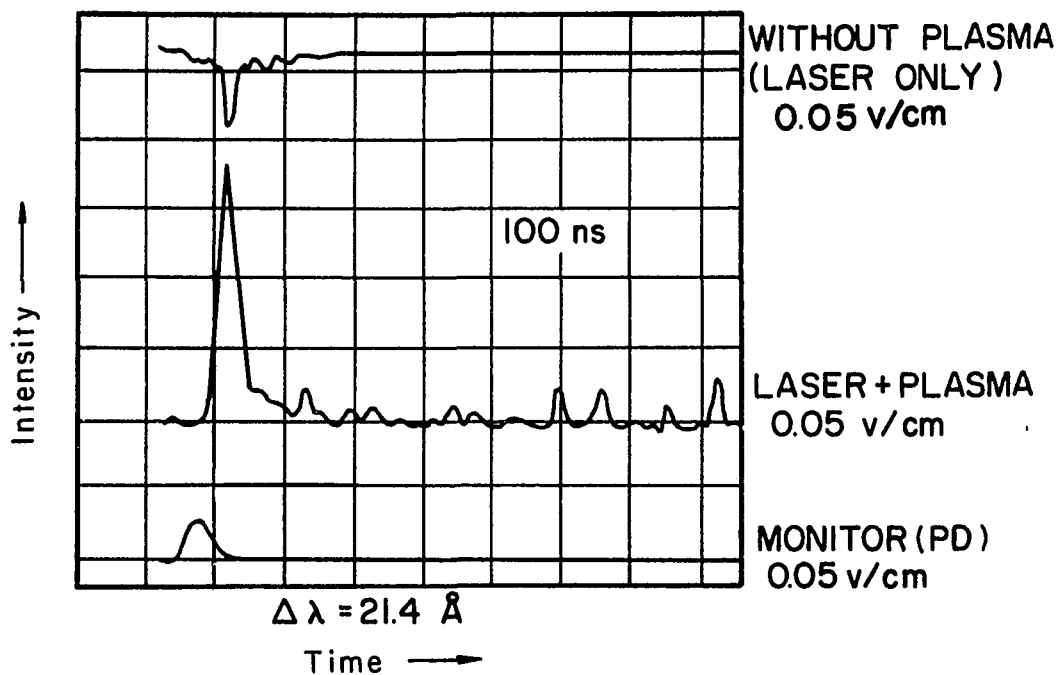


Fig. (IV B 15) Typical Oscilloscope Traces

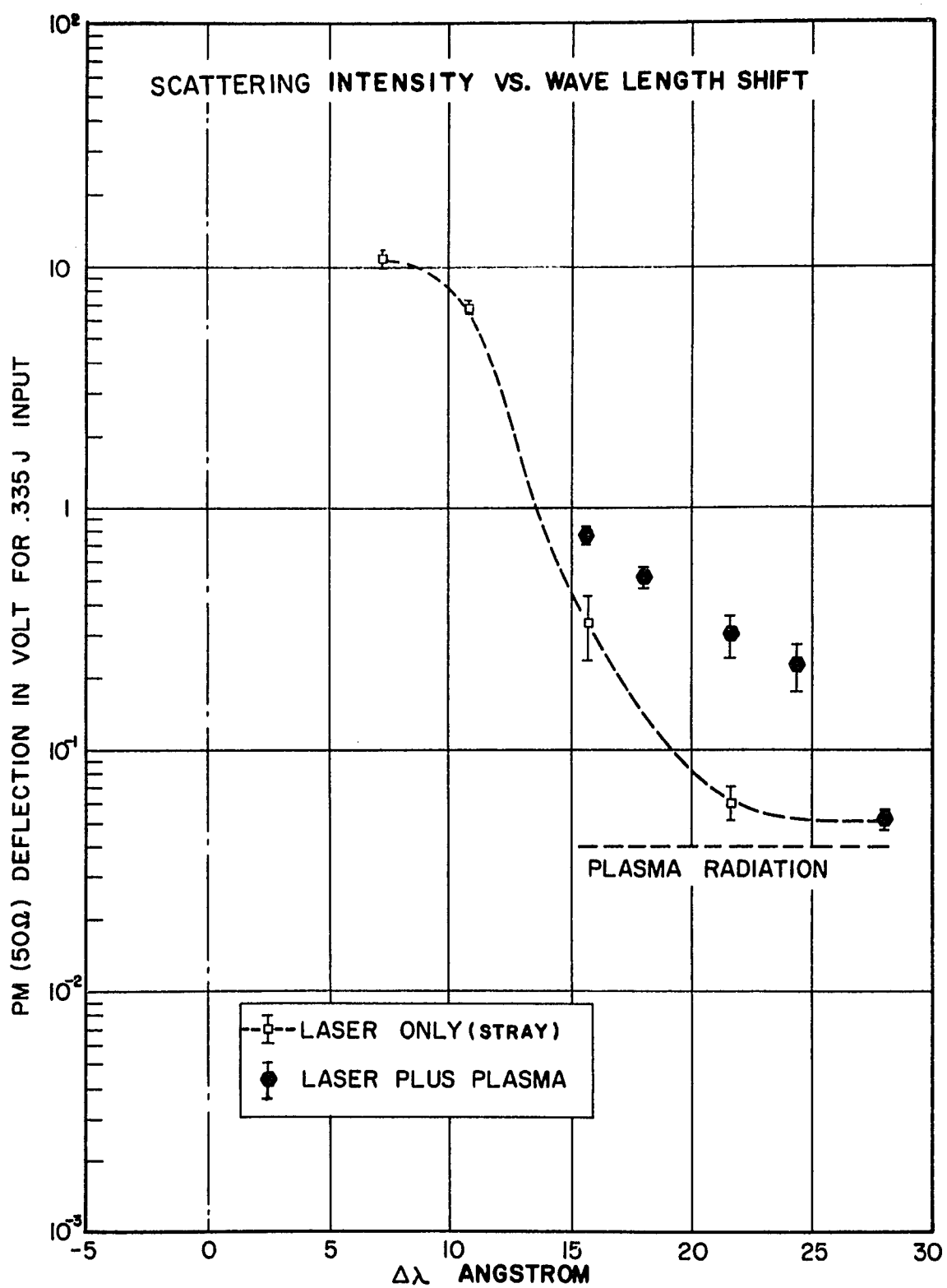


Fig. (IV B 16) Scattering Intensity Distribution

these figures denote the standard deviation of the mean of average 5 runs. Assuming a Maxwellian velocity distribution for the electrons, one can write the net scattered power intensity $I (= I_{\text{total}} - I_{\text{stray}})$ as

$$I = Ae^{-E/k_B T_e} \quad (\text{IVB24})$$

or

$$\ln I = - \frac{E}{k_B T_e} + \ln A \quad (\text{IVB25})$$

where A is a constant and E is the electron energy given by

$$E = \frac{1}{2} m v_e^2 = \frac{m}{2} \left(\frac{c}{2 \sin \frac{\theta}{2}} \frac{\Delta \lambda}{\lambda L} \right)^2 \text{ [eV]}$$

$$= \frac{1}{4} m c^2 \left(\frac{\Delta \lambda}{\lambda L} \right)^2 \text{ for } \theta = 90^\circ$$

$$= 2.60 \times 10^{-3} (\Delta \lambda)^2 \text{ for } \lambda_L = 6943 \text{ \AA}. \quad (\text{IVB26})$$

Here, v_e is the electron thermal velocity of \vec{k} component [direction satisfying the phase matching condition, see Fig. (IVA2)] and $\Delta \lambda$ is the wavelength shift in \AA units. Thus if the Maxwellian velocity distribution is assumed, the plot $\ln I$ against E should be a straight line and the average electron kinetic energy ($k_B T_e$) can be obtained from the

inverse of the slope or the energy at $1/e = 1/2$. 718 point of the linear curve. From Fig. (IVB17), the electron temperature $T_e = 0.979$ eV (11,400°K) was obtained at 5 mm position from the anode. Similar sets were obtained at 3 mm and 2 mm positions from the anode, whose data are shown in Table (IVB2).

Table (IVB2). Scattering Data

Wavelength Shift ° (Å)	Electron Energy E(eV)	Scattering Intensity I (Arbitrary)	nI
<u>at 3 mm from Anode</u>			
15.8	6.59×10^{-1}	4.3 ± 0.48	1.46
18.4	8.94×10^{-1}	3.6 ± 0.49	1.28
21.4	1.21	2.4 ± 0.62	0.88
24.5	1.59	1.7 ± 0.50	0.53
<u>at 2 mm from Anode</u>			
10	2.64×10^{-1}	5.3 ± 0.63	1.67
15	5.94×10^{-1}	4.32 ± 0.99	1.46
20	1.056	2.07 ± 0.60	0.72
25	1.650	1.26 ± 0.43	0.231

The data are plotted in Fig. (IVB18). The linear curves are theoretical least-square best fit obtained by the computer for each set of data. Figs. (IVB17) and (IVB18) are combined in Fig. (IVB19) adjusting the peak intensities to the same value at $E = 0$, which shows the variation

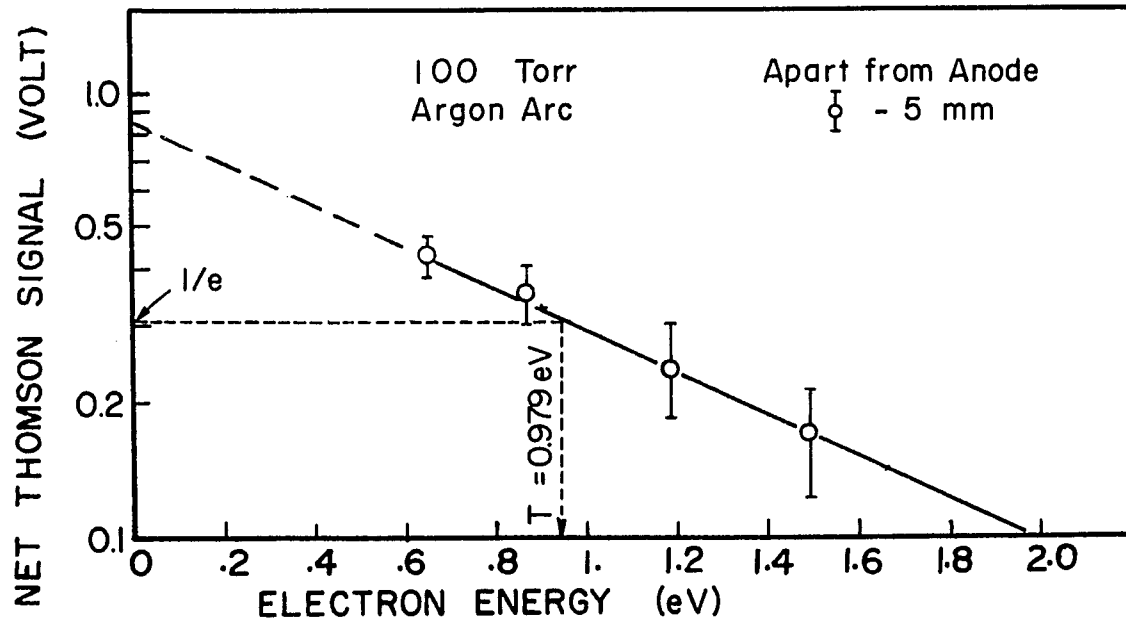


Fig. (IV B 17) Scattering Intensity vs. Electron Energy

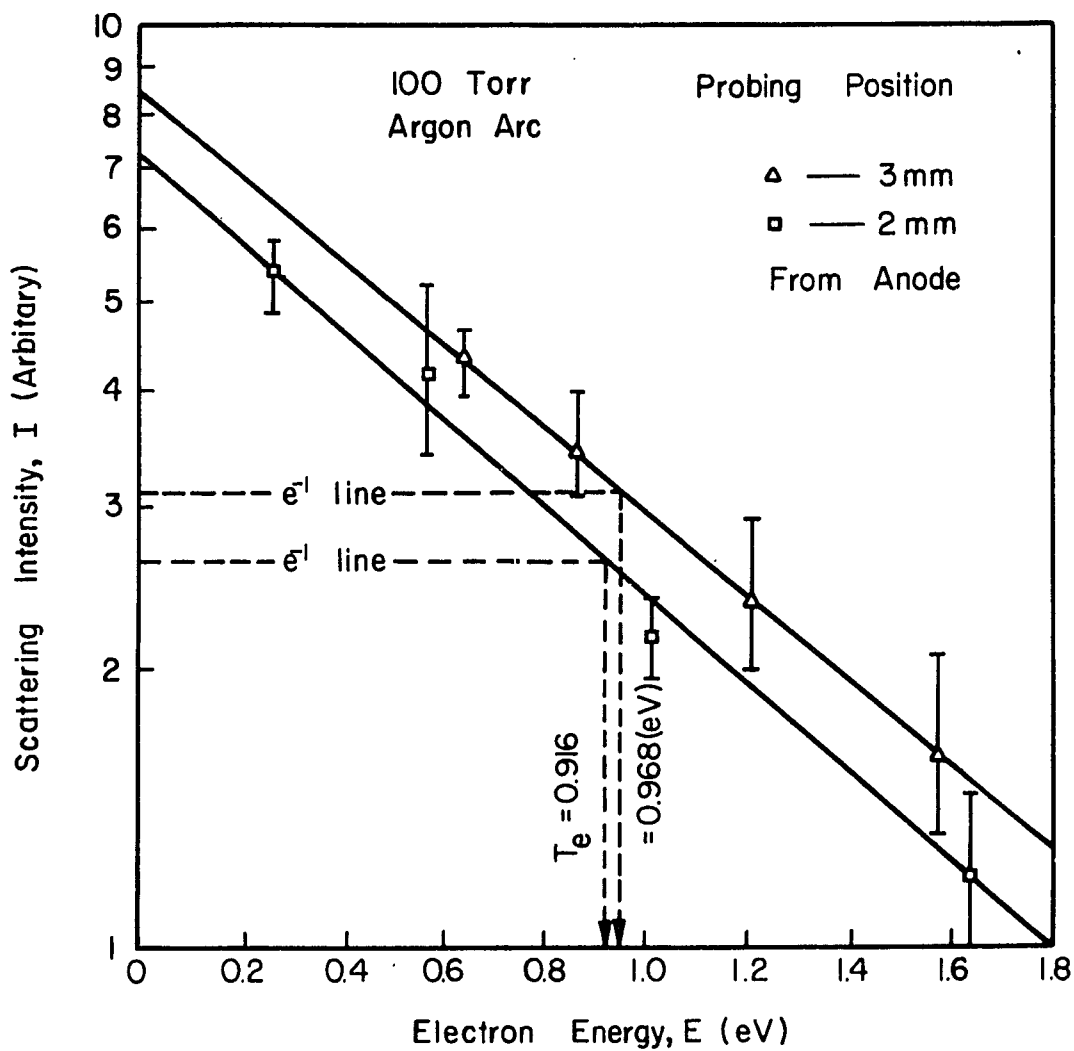


Fig (IVB18) Scattering Intensity vs. Electron Energy

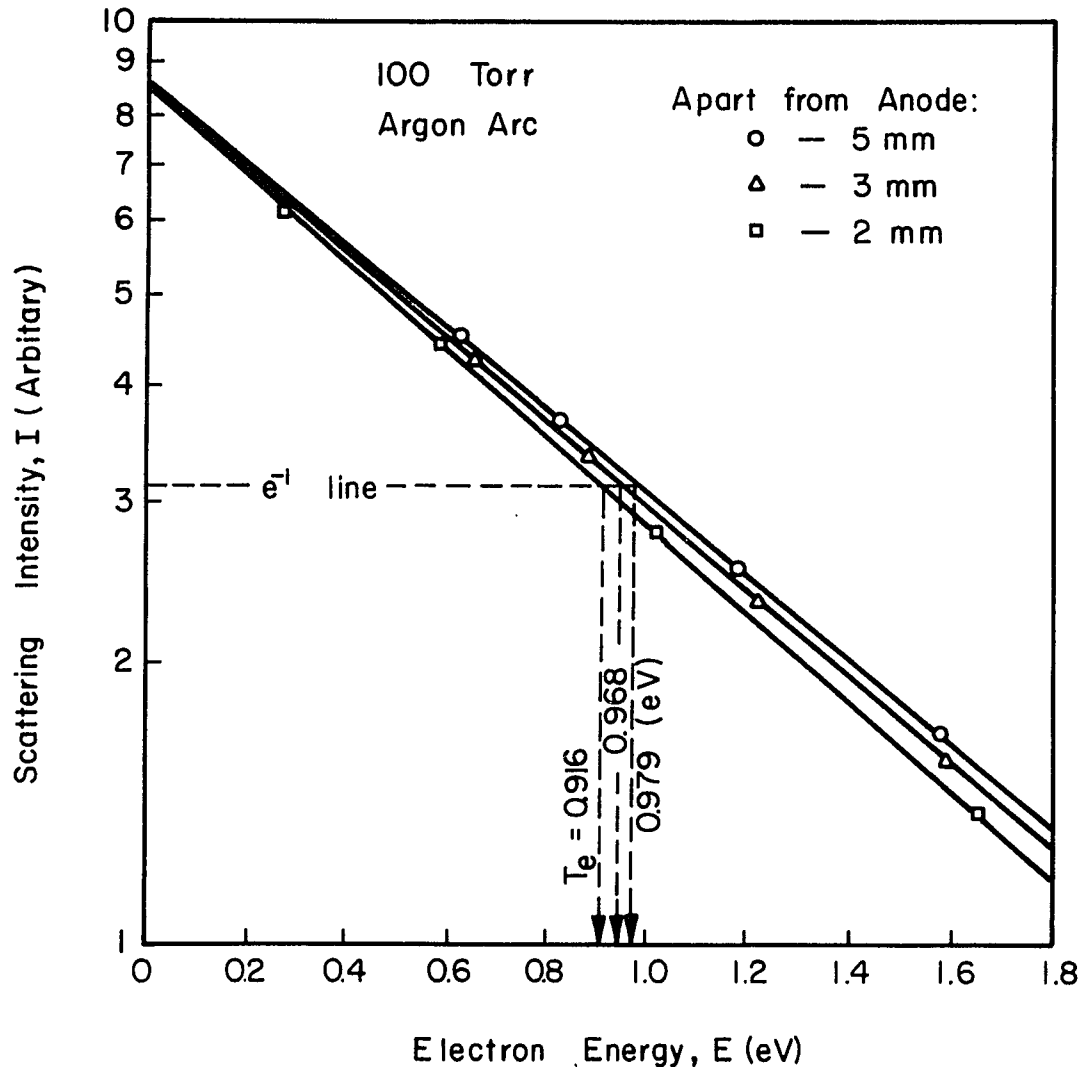


Fig (IVB19) Scattering Intensity vs. Electron Energy
(Electron Temperature Variation as a Function
of Position from Anode)

of electron temperature as a function of the position from the anode.

If the extrapolated intensity for $E = 0$ in Fig. (IVB17) is used, the electron density is calculated to be $n_e = (2.27 \pm 0.2) \times 10^{21} \text{ m}^{-3}$ at 5 mm position from the anode. Thus the Salpeter's alpha parameter given by Eq. (IVA16) is $\alpha_S = 2.50 \times 10^{-1}$, which shows that the 100 Torr pressure, 15 Amps arc is well in the pure Thomson scattering regime. Fig. (IVB20) shows the computer calculated electron Doppler broadened line for the data at 2 mm. The half intensity point corresponds to $\Delta\lambda = 16 \text{ \AA}$. From Eq. (IVA14), $T_e = 0.916 \text{ eV}$ is calculated, which is self-consistent with the temperature calculated at $1/e$ point of the straight curve in the $\ln I - E$ graph. The average electron thermal velocity corresponding to this temperature is obtained from the formula

$$v_e = \frac{c}{\sqrt{2}} \frac{\Delta\lambda}{\lambda L}$$

$$= 3.2 \times 10^4 \Delta\lambda (\text{\AA}), \text{ [m/sec]} \quad (\text{IVB27})$$

where $\Delta\lambda$ is the wavelength shift at half intensity point. Eq. (IVB27) gives $v_e = 4.96 \times 10^5 \text{ m/sec}$ which is the thermal velocity of the electrons moving toward the phase matching direction (45° with respect to the arc axis) at 2 mm position from the anode.

If the electron temperature measured by the Thomson scattering is equal to the Saha equilibrium temperature, the electron density

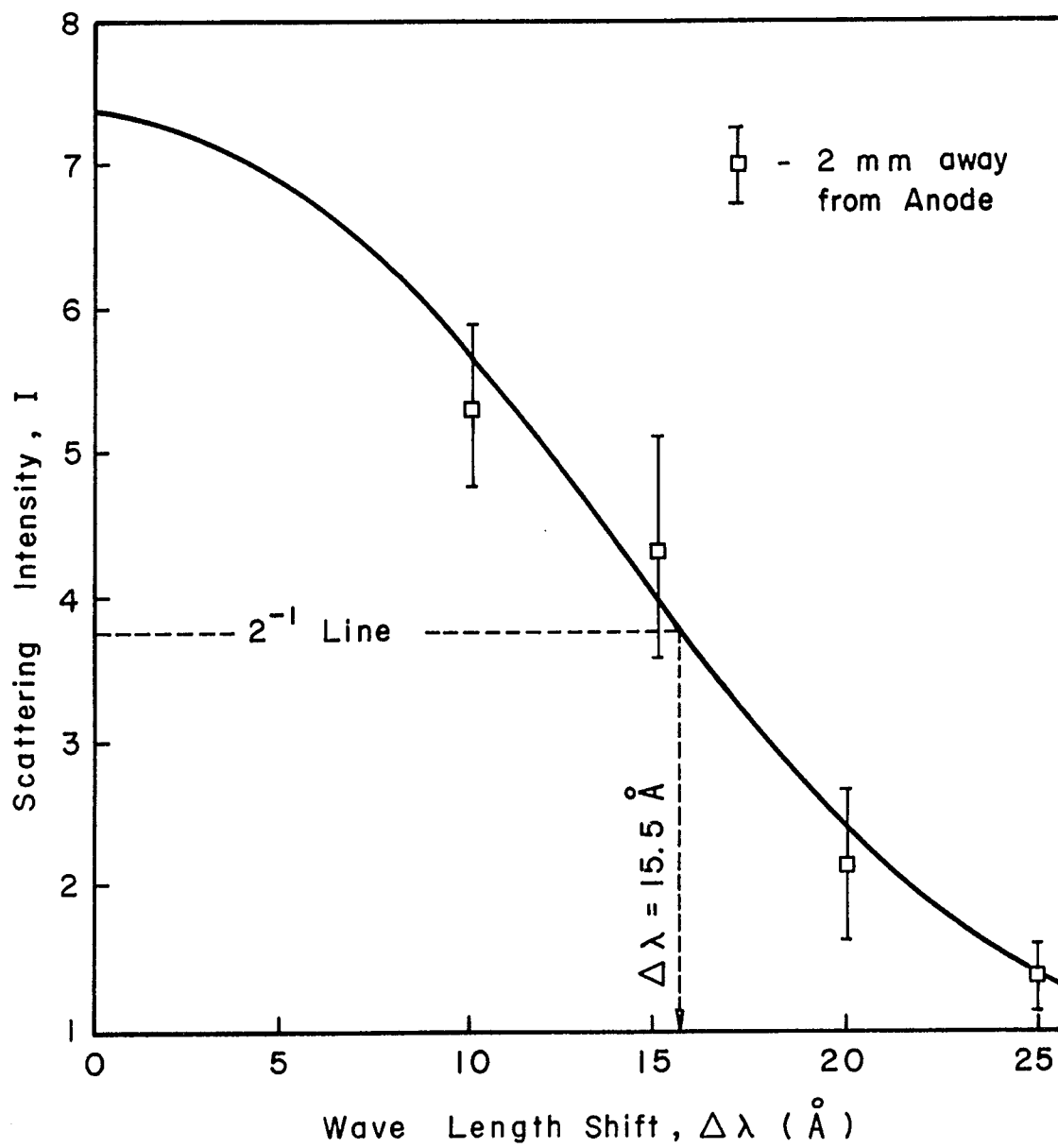


Fig. (IV B 20) Electron Doppler Broadened Line

should be $n_e = 4.5 \times 10^{22} \text{ m}^{-3}$ (from Fig. II A 1) which is one order higher than the value obtained from the scattering. In other words, the electron temperature measured by Thomson scattering is higher than the Saha equilibrium temperature 1,950°K. If the $T_e = T_{\text{Saha}}$ (Saha equilibrium temperature), $n_e = 4.3 \times 10^{22} \text{ m}^{-3}$ and $\alpha_S = 1.10$ whose scattering profile must be more or less flat topped or have a maximum at a frequency away from the center.

Fig. (IVB21) shows the electron temperature distribution on the arc axis, which shows the decreasing curve toward anode and implies a maximum near the center. Near the electrodes the background noise increases strongly due to the scattering from the sputtered electrode-surfaces. Although the reduction of the spot size can decrease the wall scattering in principle, it is limited in actuality for the following reason. The method of expansion of laser beam can make a spot size (ΔY) as small as the diffraction limit [$\Delta Y = 1.22\lambda (D/X_1) \approx 1.22\lambda$] if the F number of the focusing lens, $D/X_1 \approx 1$. See Fig. (IVB22). But the beam expansion increases the focusing angle which makes the beam hit the edge of the electrode (the electrode tip has flat surface of about 5 mm in the operational condition). Spot size can also be decreased if the higher transverse modes are suppressed by controlling the intra-cavity iris. But this can be applied only when the Thomson scattering S/N ratio is large. Present S/N ratio is 5 at most and the method is too limiting to be applied. Thus the scattering chamber will be

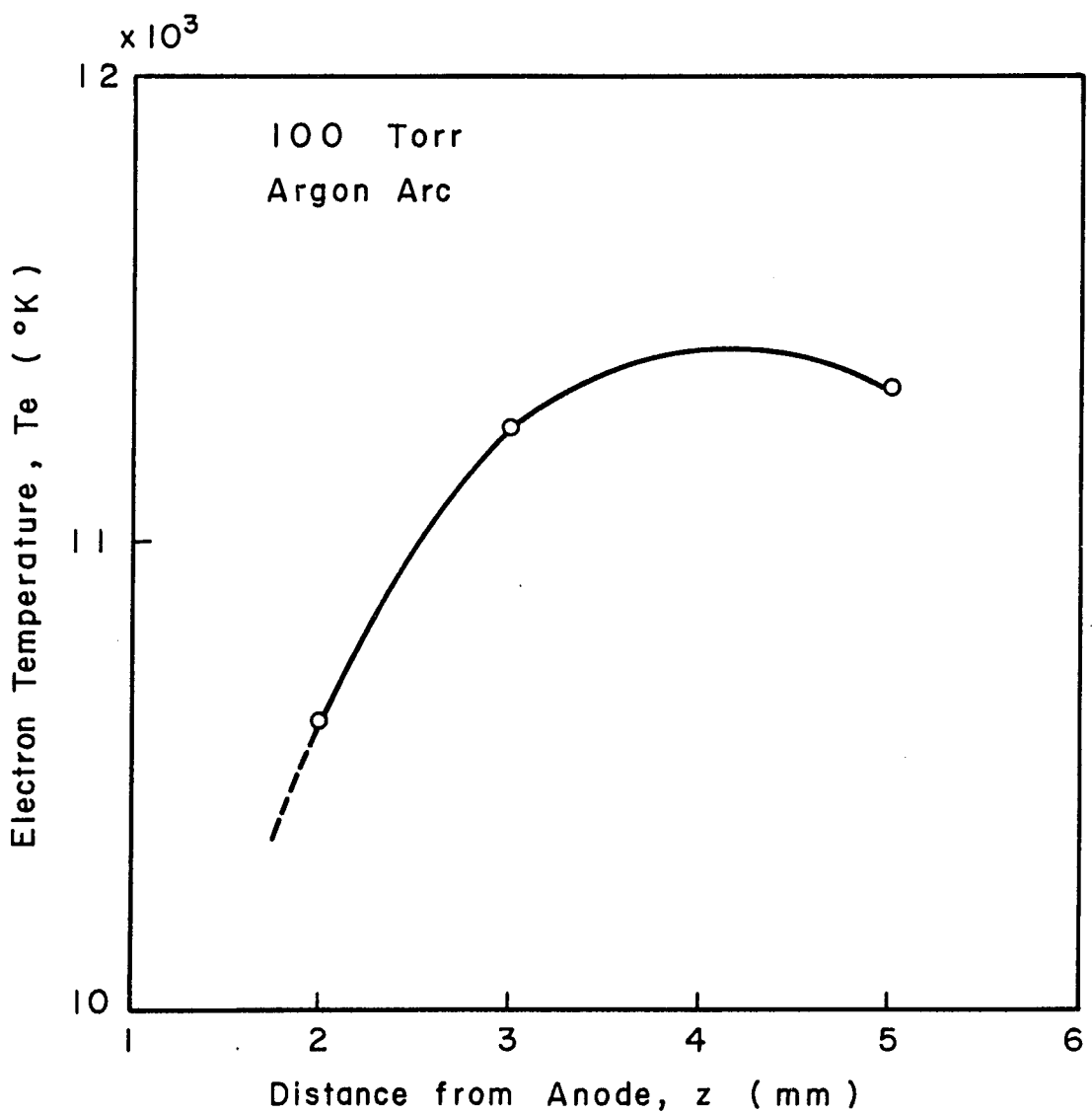


Fig. (IV B 21) Axial Electron Temperature Distribution

eliminated in the next experiment to operate in an open atmosphere so that the cleaning of the sputtered electrode surface becomes easy and that the higher Thomson scattering intensity results by the higher degree of ionization.

[IVB5] Experiments at Atmospheric Pressure

Fig. (IVB22) shows the experimental set up of the scattering experiment at atmospheric pressure. The spot size can be tuned by either controlling D/X_1 (F number of focusing lens or I_2 intra-cavity iris) shown in the figure. The arc device is shown in Fig. (IVB23) where fairly large water tanks are installed for efficient cooling of the electrodes. Gases are fed through the cathode to avoid oxidization of the electrode surfaces. A two-dimensional translation stage is employed for the spatial probing of the arc without moving the laser beam itself. Fig. (IVB24) shows the Rayleigh scattering result used for the intensity calibration of the system. It shows that the system behaves well in the sense that no foreign particles are present when gas is flowing through the orifice (1.6 mm ϕ). This is because the scattering is almost Rayleigh scattering as is seen from the polarization ratio S_{VV}/S_{VH} . The scattering profile is a convolution of the instrumental width of IF filter with the Rayleigh scattering signal. The rejection ratio of the filter is about 4 at the wavelength of the instrumental width (8 \AA°). Fig. (IVB25) shows the filter rejection ratio as a function of wavelength shift from the center frequency. It is seen that

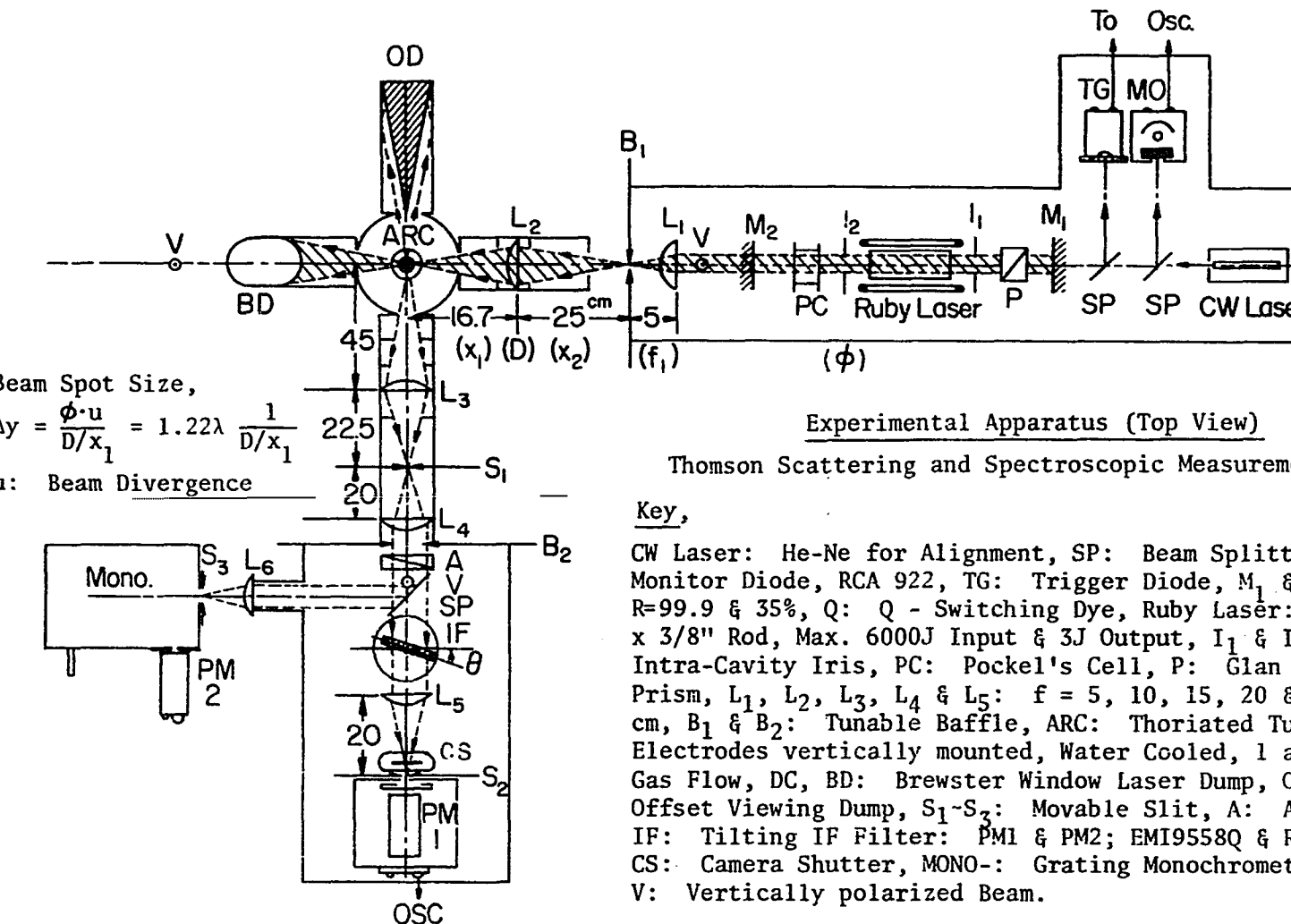


Fig. (IV B 22) Thomson Scattering Experiment in Atmospheric Pressure

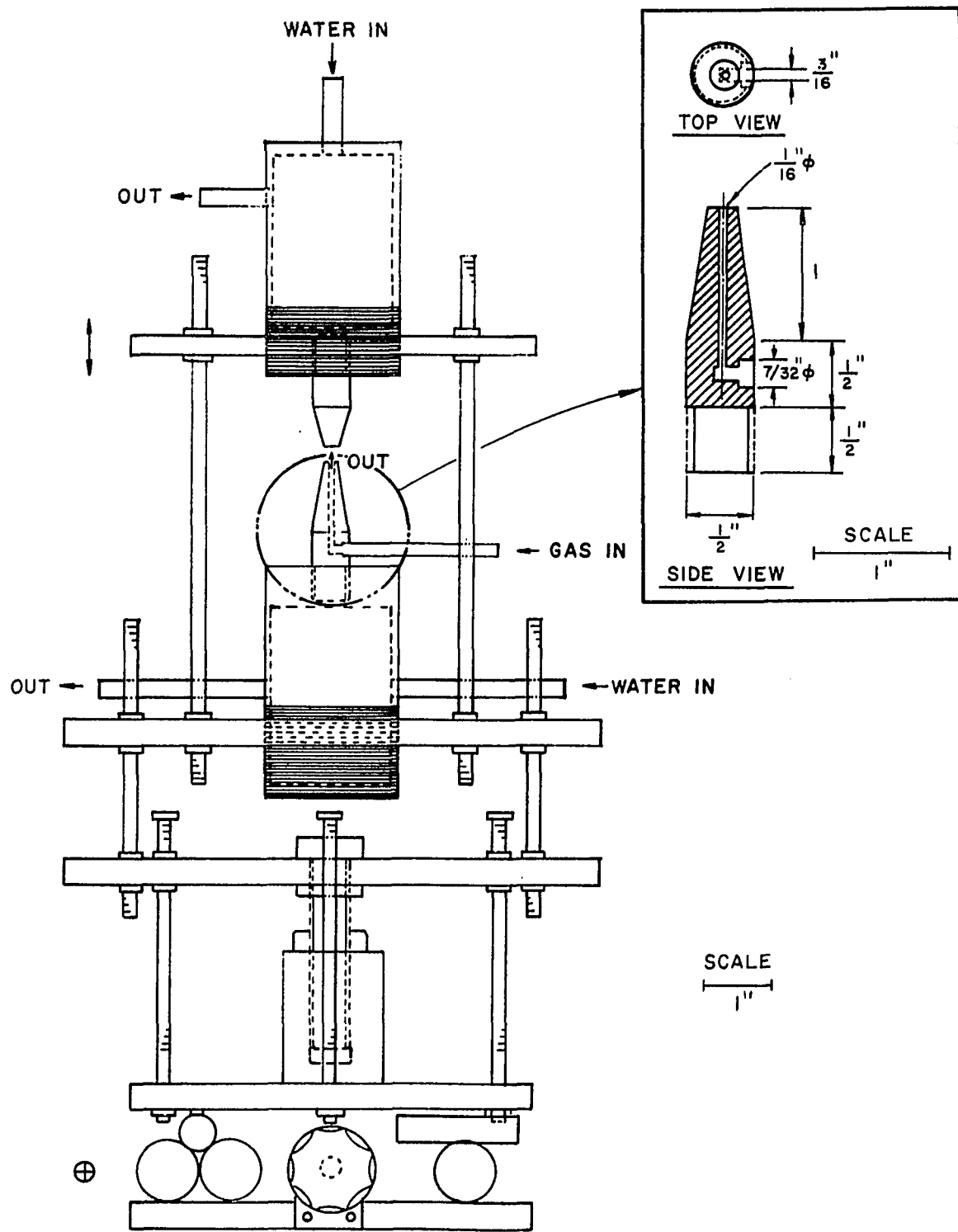


Fig. (IV B 23) Atmospheric Arc Device with Cooling, Gas Feeding and Translational Units

Stray Light Distribution, as a Convolution of the
Rayleigh Scattering Signal with the Instrument (IF Filter)
Response Profile.

Error Bars are Standard Error of the Mean for average 5 ($=n$) shots. ($x = \bar{x} \pm \alpha$, $\alpha = \sigma / \sqrt{n}$, σ : Standard Deviation.)

Test Gas: Argon, 2 atm.- ℓ /min., Scattering Volume: 3.14×10^{-3} cm $^{-3}$, Spot size = 500 μ , Received Photo Current: 6.8 mA (=55L) at $\Delta\lambda=0$ by EMI9958Q of 1280V.

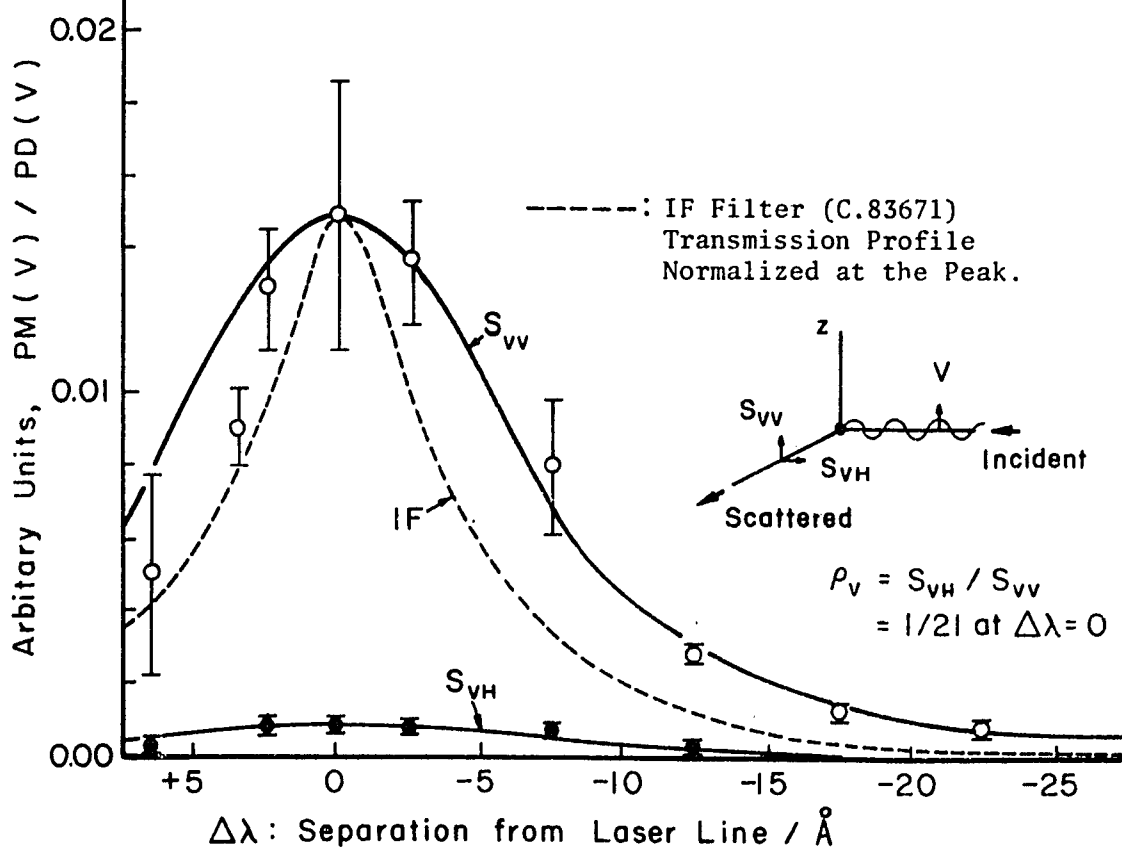


Fig. (IV B 24) Rayleigh Scattering from One Atmospheric Argon

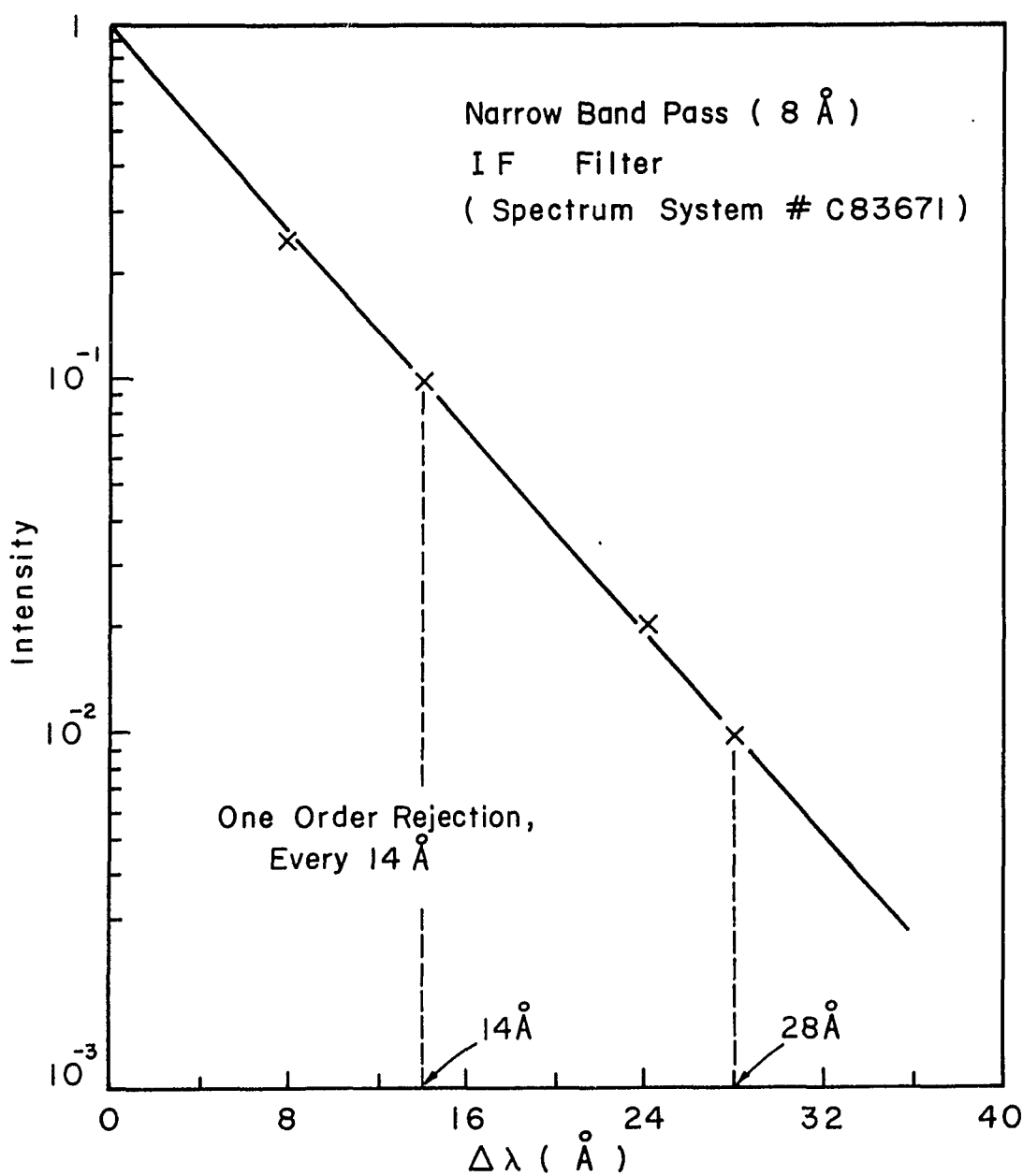


Fig. (IV B 25) Rejection Ratio of IF Filter

at $\Delta\lambda = 14 \text{ \AA}^{\circ}$ (or 1.75 times bandwidth) the intensity drops by one order of magnitude from the intensity at the center frequency.

The data of Fig. (IVB24) were taken in the early morning at least 24 hours after the last experiment. Once an experiment is started (or in the daytime) the background increases rapidly. Then the true Rayleigh scattering intensity from argon atoms must be the difference between the total intensity and that from foreign atoms. The contribution from the foreign atoms can be distinguished by an experiment in the helium environment because of the small Rayleigh scattering cross section (1.6% of argon). Fig. (IVB26) shows the calibration of this effect, where curve (2) is not a Rayleigh Scattering from He atoms (because it is too large) but the contribution from foreign atoms. The light beam is 3 mm away from the anode surface so that the wall scattering is negligible in this experiment. Thus the curve (3) = (1) - (2) in Fig. (IVB26) must be the true Rayleigh scattering, whose intensity can be used for the estimation of the electron density. At temperature 10^{40}K , the Rayleigh scattering from neutrals decrease to 4.2% of the intensity at room temperature (300°K), whose curve is (4) in Fig. (IVB26). If one can assume that the number density of foreign atoms also decreases at the same rate, the true background under the Thomson scattering experiment may be at most 10% of the Rayleigh scattering intensity at the room temperature. Therefore, if the wall scattering is

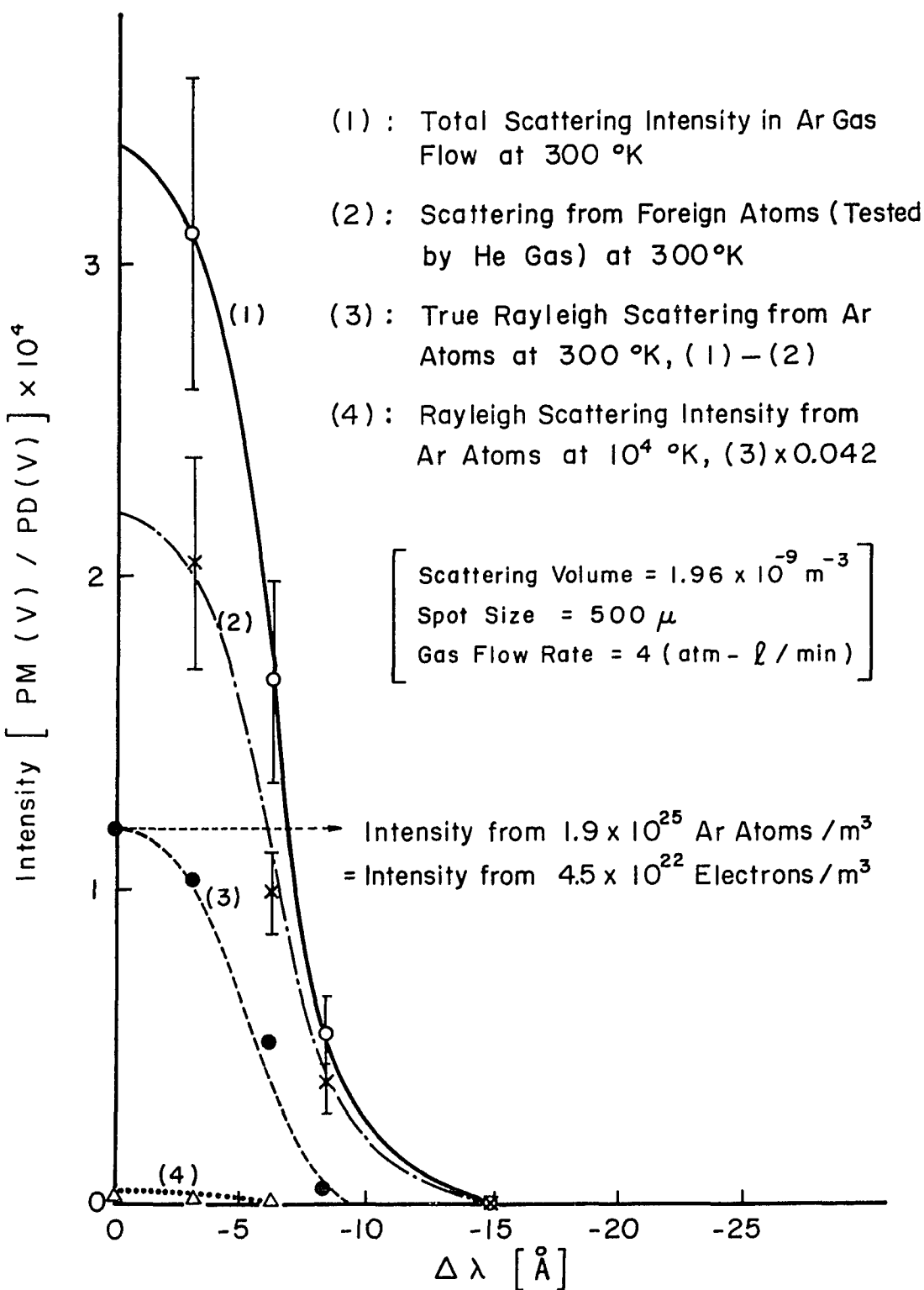


Fig. (IV B26) Scattering Intensity Calibration

negligible, the background to be subtracted is very small for plasmas whose electron density is of the order of 10^{22} m^{-3} .

On the other hand, when the wall scattering predominates over the scattering from neutral atoms, one has to subtract the background as was done in the experiment at reduced pressure. This effect has been checked by scanning the beam position toward the anode. The result is shown in Fig. (IVB27). The wall scattering builds up exponentially from about 2 mm position even when the spot size is 600μ . When the small amount of yellowish (sputtered or oxidized) material is deposited on the electrode surface, the intensity increases as shown by dashed curve in Fig. (IVB27). This means that even when the spot size (first Airy disc) is parted from the electrode surface, small amounts of side-lobe and stray light scattered from optical components are eventually hitting the surface. Therefore the practical experiment within 1 mm position becomes extremely difficult. The electrode surface had to be cleaned before every run by using NH_4OH liquid (which dissolve the oxidized tungsten chemicals, WO_3 , etc.).

The procedures of Thomson scattering experiment are very similar to the case explained in the preceding Section. Fig. (IVB28) shows a typical set of oscilloscope traces of Thomson scattering from 1 atm argon at 14 Amps, 32 Volts. It shows a large intensity at $\Delta\lambda \approx 15 \text{ \AA}$. Fig. (IVB29-a) shows the scattered intensity (normalized by the monitor intensity) distribution against $\Delta\lambda$ (wavelength shift) for a

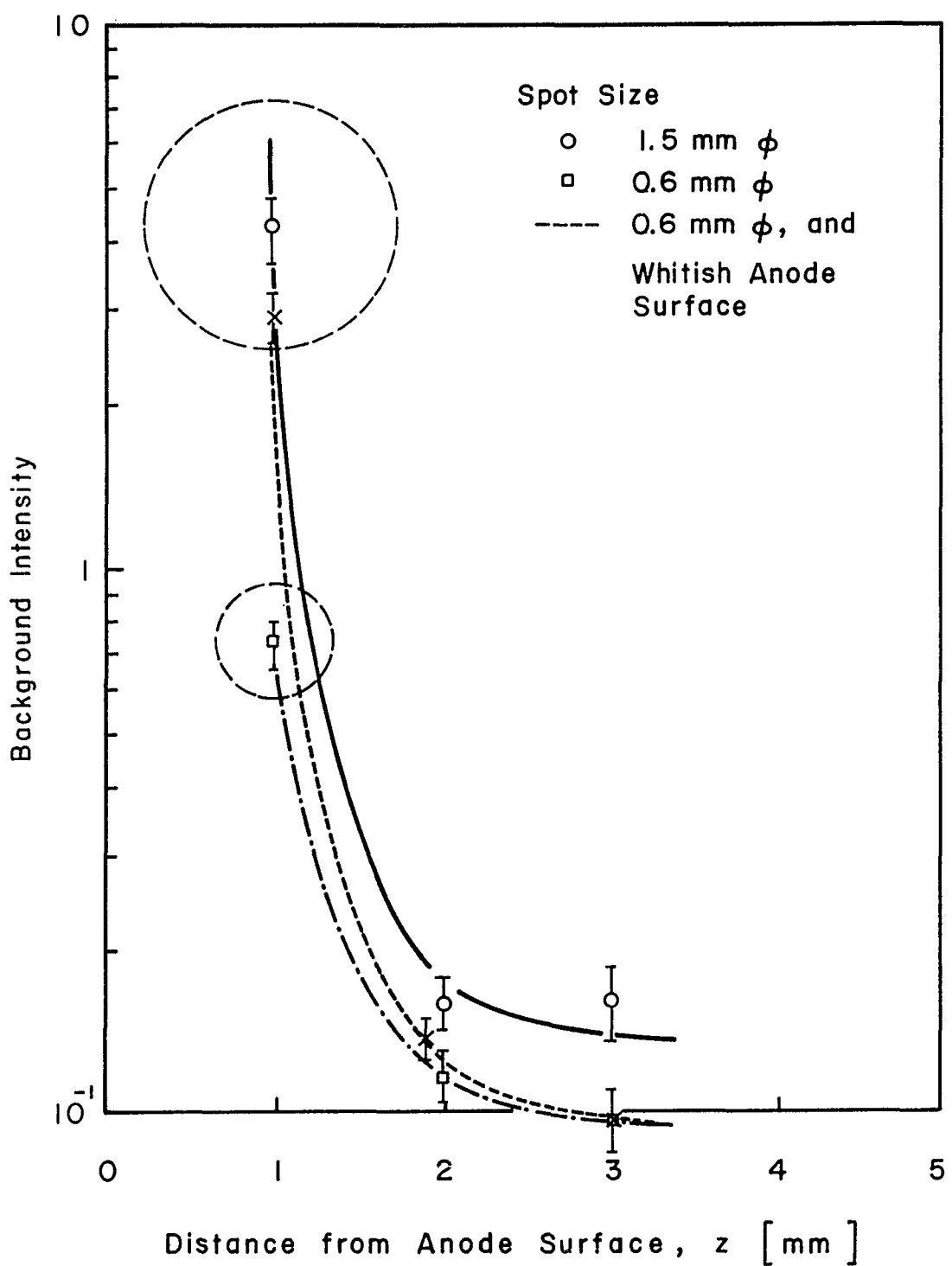


Fig. (IV B27) Background Intensity Distribution

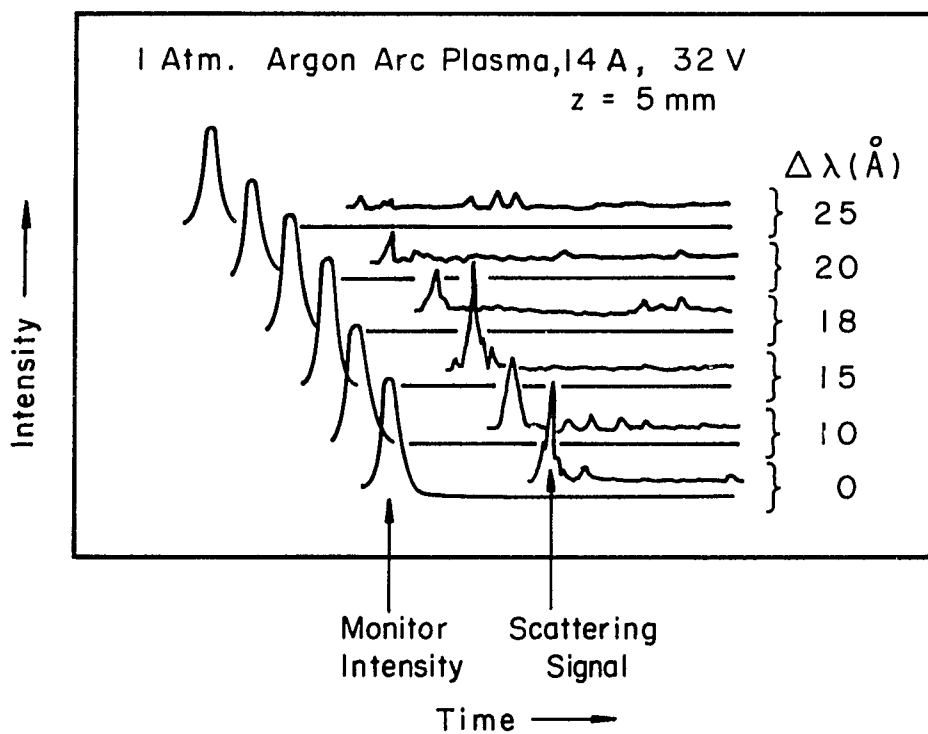


Fig. (IV B 28) Typical Oscilloscope Traces

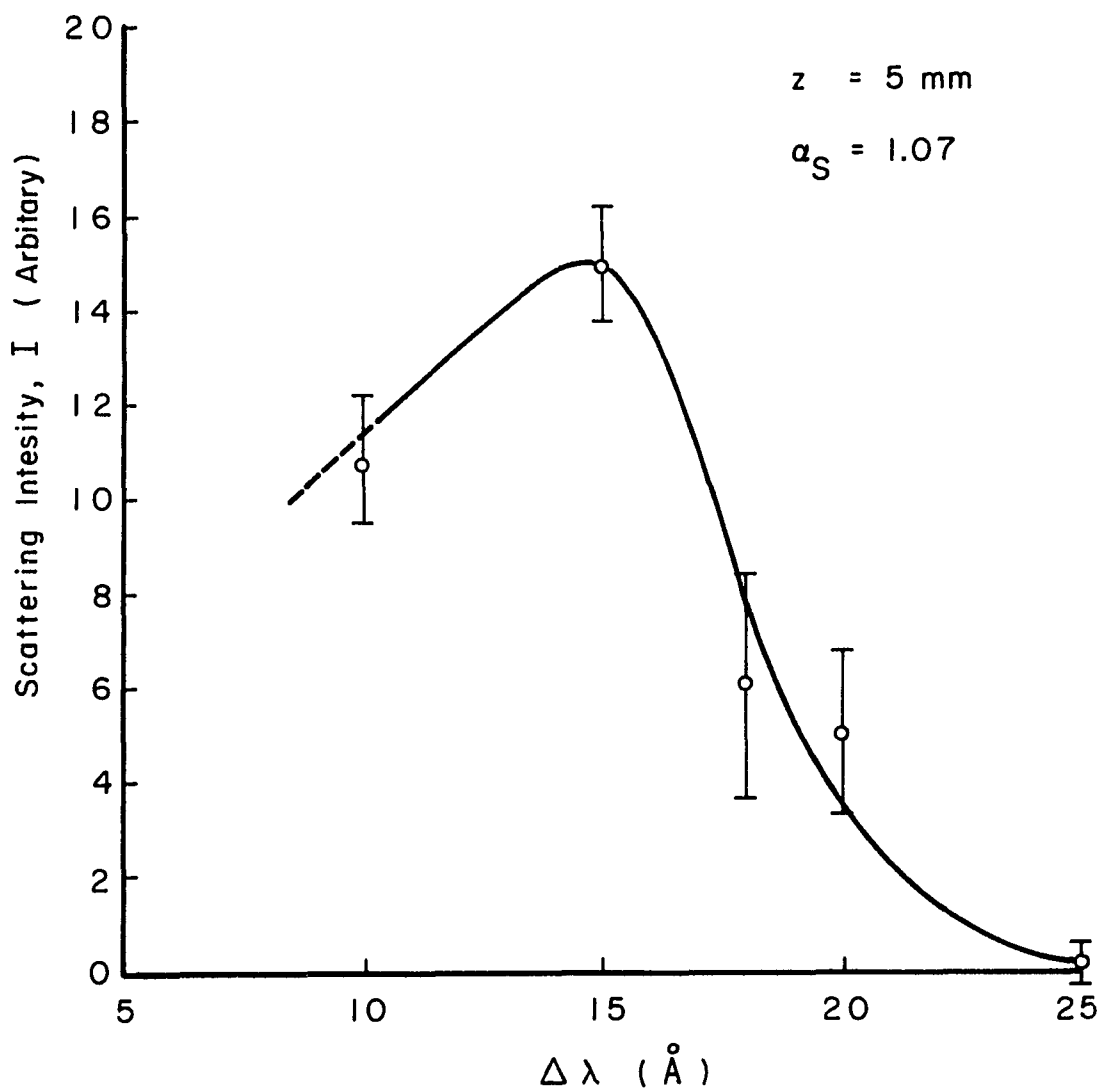


Fig. (IV B 29 - a) Scattering Intensity Distribution

plasma at 5 mm position from anode. This distribution clearly shows that the plasma is in the transition regime between pure Thomson and collective Thomson scattering. The theoretical best fit curve for Fig. (IVB29-a) indicates α_S (Salpeter's alpha parameter) = 1.07. Since α_S is a function of T_e and n_e one needs other data at a different scattering angle for the same plasma to calculate the exact plasma parameters. However we already know the electron temperatures at 100 Torr pressure. As is known, the electron temperature is almost constant (at low current) between 10 Torr and 10^3 Torr pressure⁷²⁾ and only the electron density changes due to the change of the initial neutral density and degree of ionization. If this can be assumed, we can calculate the electron density by the formula derived from Eq. (IVA16)

$$n_e = 3.7 \times 10^{22} \alpha_S^2 T_e (\text{°K}) / 11,606 \quad [\text{m}^{-3}] \quad (\text{IVB28})$$

Using the data at 5 mm position ($\alpha_S = 1.07$, $T_e = 11,350^\circ\text{K}$), Eq. (IVB28) yields $n_e = 4.14 \times 10^{22} \text{ m}^{-3}$. Similar experimental results are shown in Figs. (IVB29-b) and (IVB29-c) at 3 mm and 2 mm positions, respectively, where the temperature data are known. From Figs. (IVB29-b) and (IVB29-c) one can calculate that $n_e = 3.96 \times 10^{22} \text{ m}^{-3}$ at $z = 3 \text{ mm}$ ($\alpha_S = 1.05$) and $n_e = 3.38 \times 10^{22} \text{ m}^{-3}$ at $z = 2 \text{ mm}$ ($\alpha_S = 0.90$). The Saha equilibrium temperature to produce these electron densities will be discussed in the next Chapter. Fig. (IVB30) shows the electron density distribution calculated here.

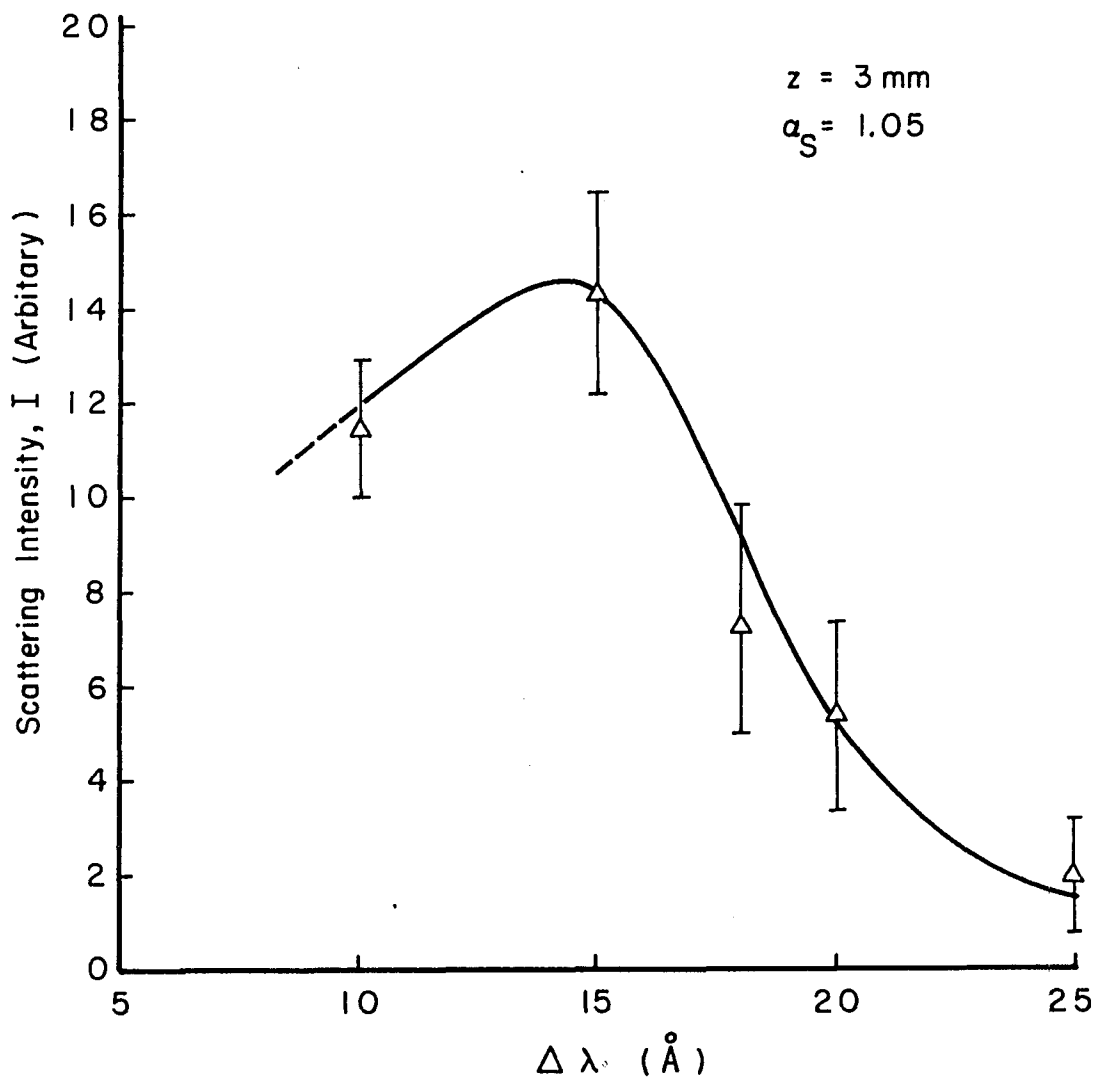


Fig. (IV B 29 - b) Scattering Intensity Distribution

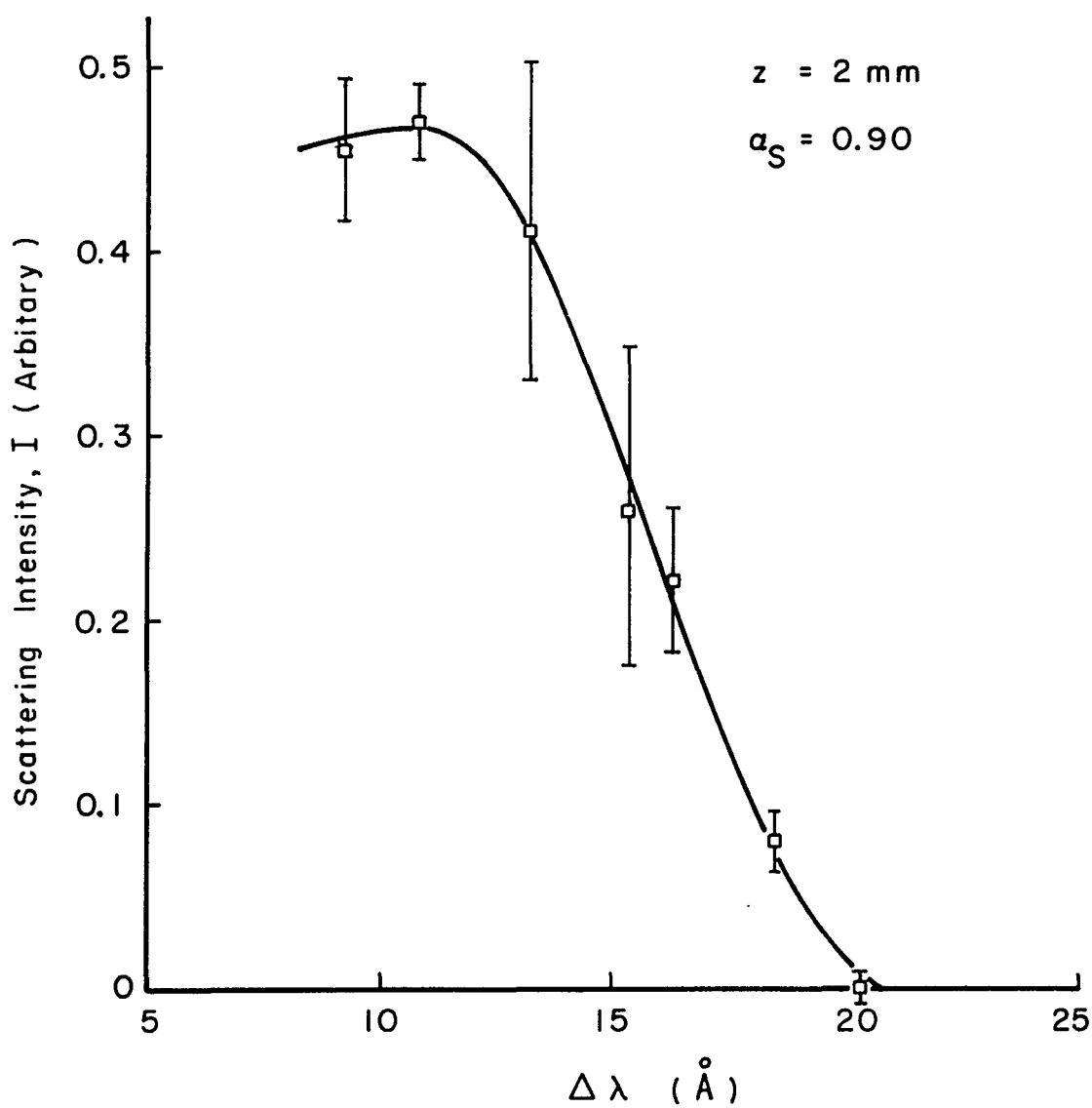


Fig. (IV B 29 - c) Scattering Intensity Distribution

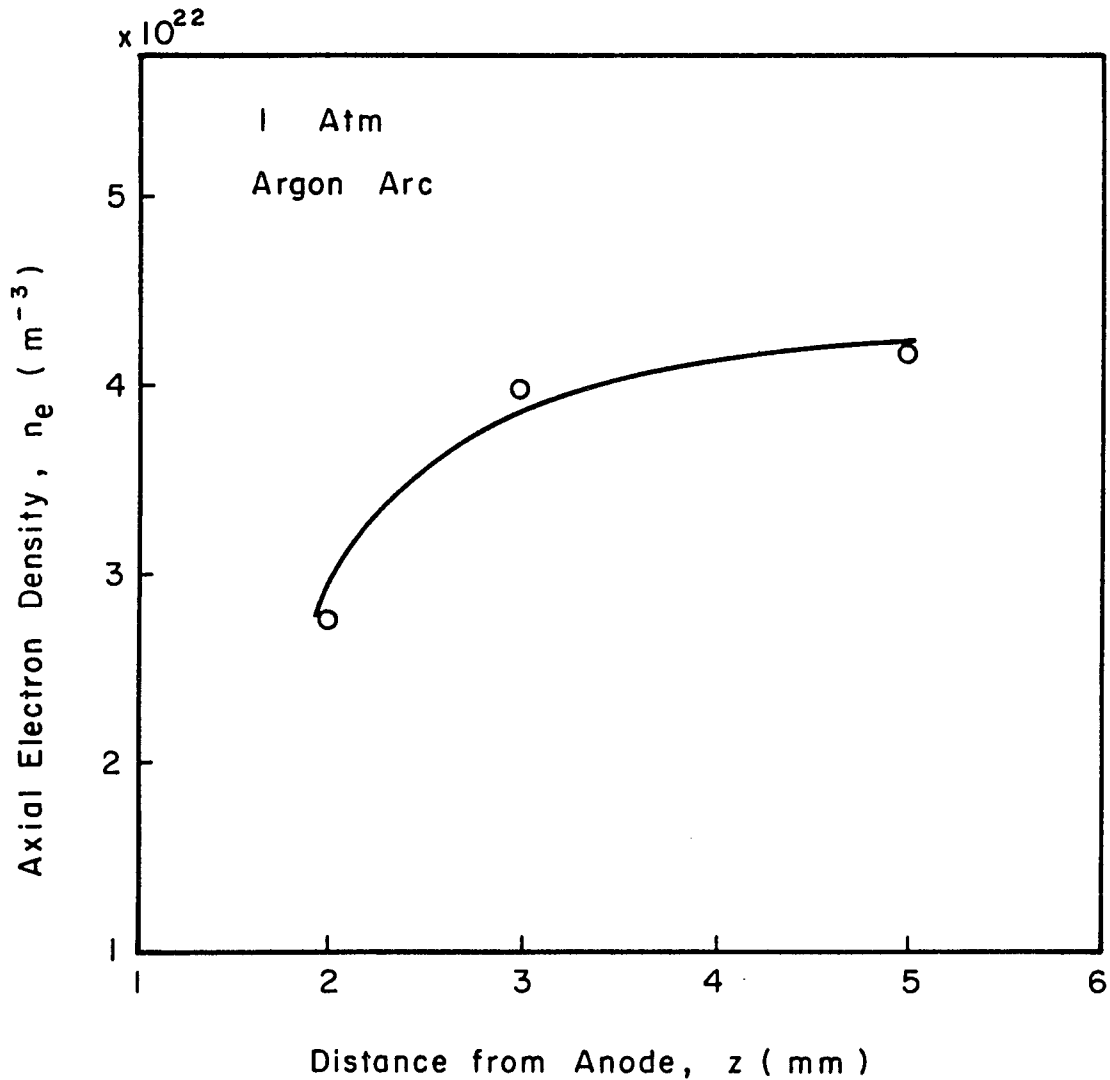


Fig. (IV B 30) Electron Density Distribution

[IVB6] Electrode Temperature Measurement

Fig. (IVB31) shows the experimental result of the measurement of temperatures in the anode. Five holes of $1/16''$ are drilled into the tungsten anode by $1/4''$ step. Using Chromel-Alumel thermocouple wires (Omega Clad, Max. heat resistance = 1350°C), the temperature distribution has been measured simultaneously at various arc currents. Since the size of the thermocouple points is made to be fitted exactly to that of the $1/16'' \phi$ hole, one can assume the thermal equilibrium between electrode and thermocouple. The electrode surface temperature at various currents can be obtained from the extrapolation of these curves.

[IVB7] Photographic Observation of Free Burning Arcs

Fig. (IVB32) shows the variation of schematic arc features corresponding to the gas flow rate (through the cathode hole). When the flow rate increases the hot cores located at the anode and cathode connect each other and the size of arc periphery decreases. The scattering data were obtained at the center of the core with diameter 1 mm. The background from the periphery and/or conductive part was too large to obtain reliable data. More precise measurement of the core diameter and intensity distribution may provide information of the current density.

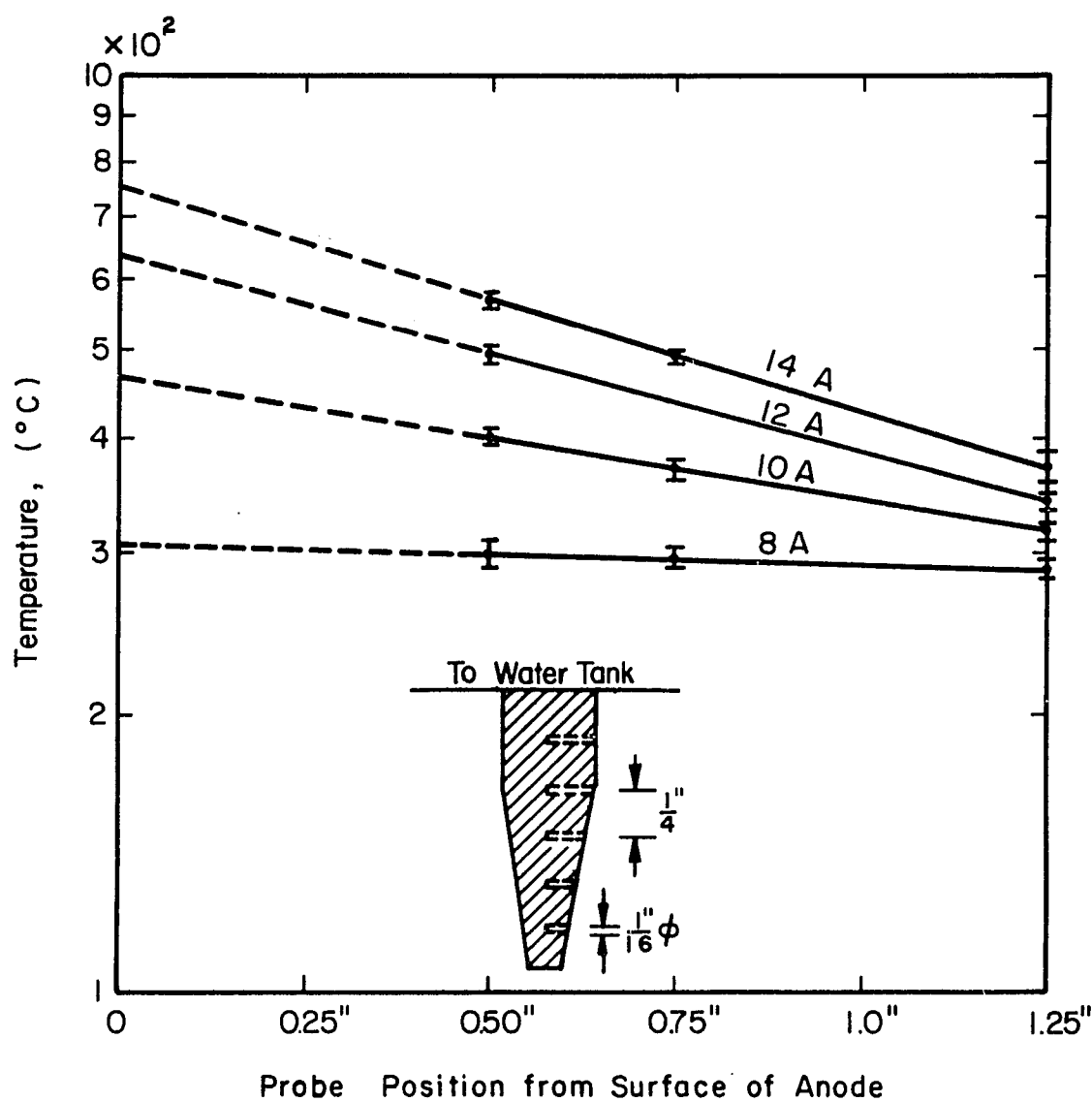


Fig. (IV B 31) Anode Temperature Measurement

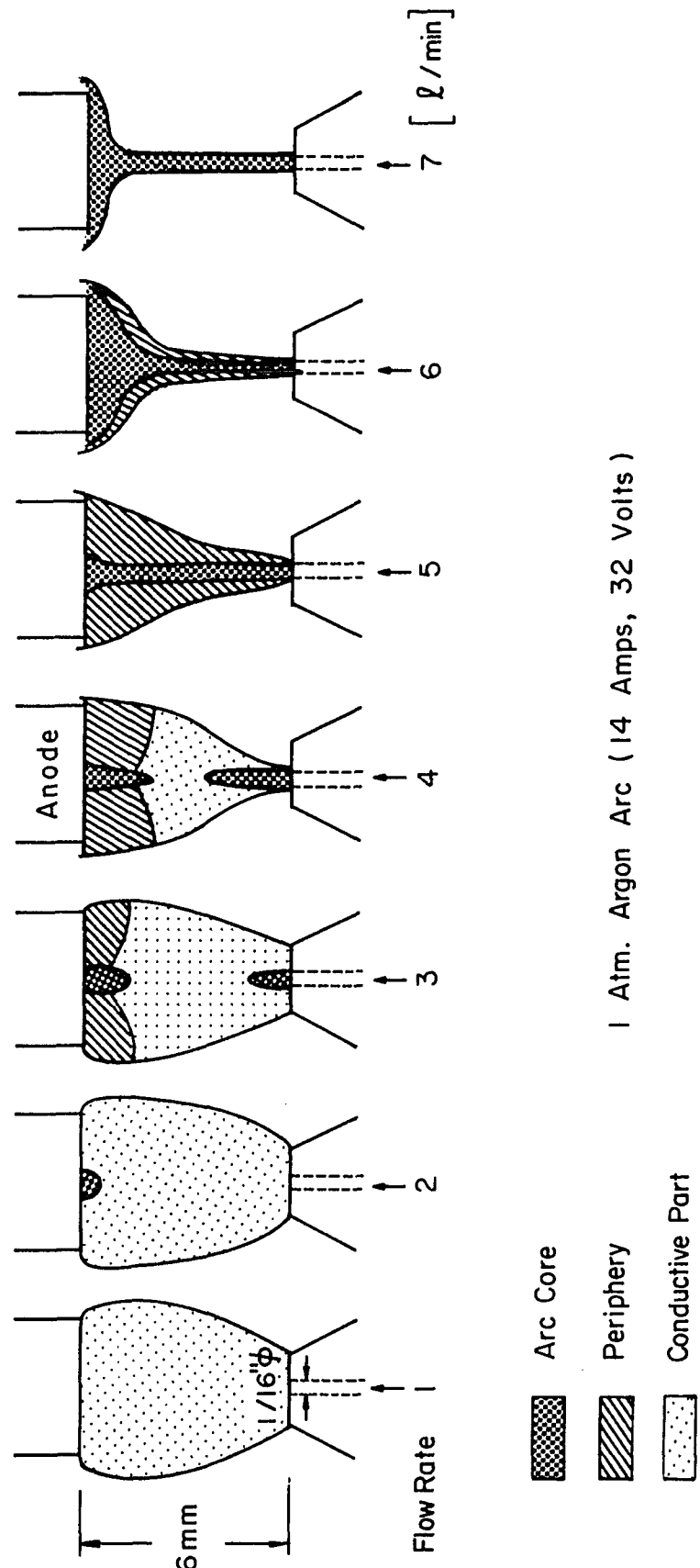


Fig. (IV B 32) Gas Flow Rate Dependency of Arc Feature

CHAPTER V

ANALYSES AND DISCUSSION

A. LTE VALIDITY IN THE LOW CURRENT ARGON ARC PLASMA

Table (VA1) shows the electron temperature (T_e) and electron density (n_e) obtained in the present Thomson scattering experiment. The Saha equilibrium temperature (T_{Saha}) required to give the same electron density as measured by the Thomson scattering as well as the difference temperature, $\Delta T_{Saha} \equiv T_e - T_{Saha}$ are also given. $\epsilon_{Saha} \equiv \Delta T_{Saha}/T_e$ is an index to indicate the degree of non-LTE, which is shown in the same table. One sees that the degree of non-LTE is clearly improved at 1 atm pressure than at 100 Torr pressure (for example, 1.32% compared with 28.5% at $z = 5$ mm). The results show that ϵ_{Saha} has a trend to increase toward the anode direction even though the electron temperature decreases for the same direction, which implies that the temperature of heavy particles decreases more rapidly than that of electrons (see Fig. VA1). Using the measured value of T_e and Eq. (IIA97), one can estimate the ion temperature (T_i). Eq. (IIA97) can be rewritten as

$$T_e^{1/2} (T_e - T_i)^{1/2} = 1.06 \times 10^6 E_z l_{ei}. \quad (\text{VA1})$$

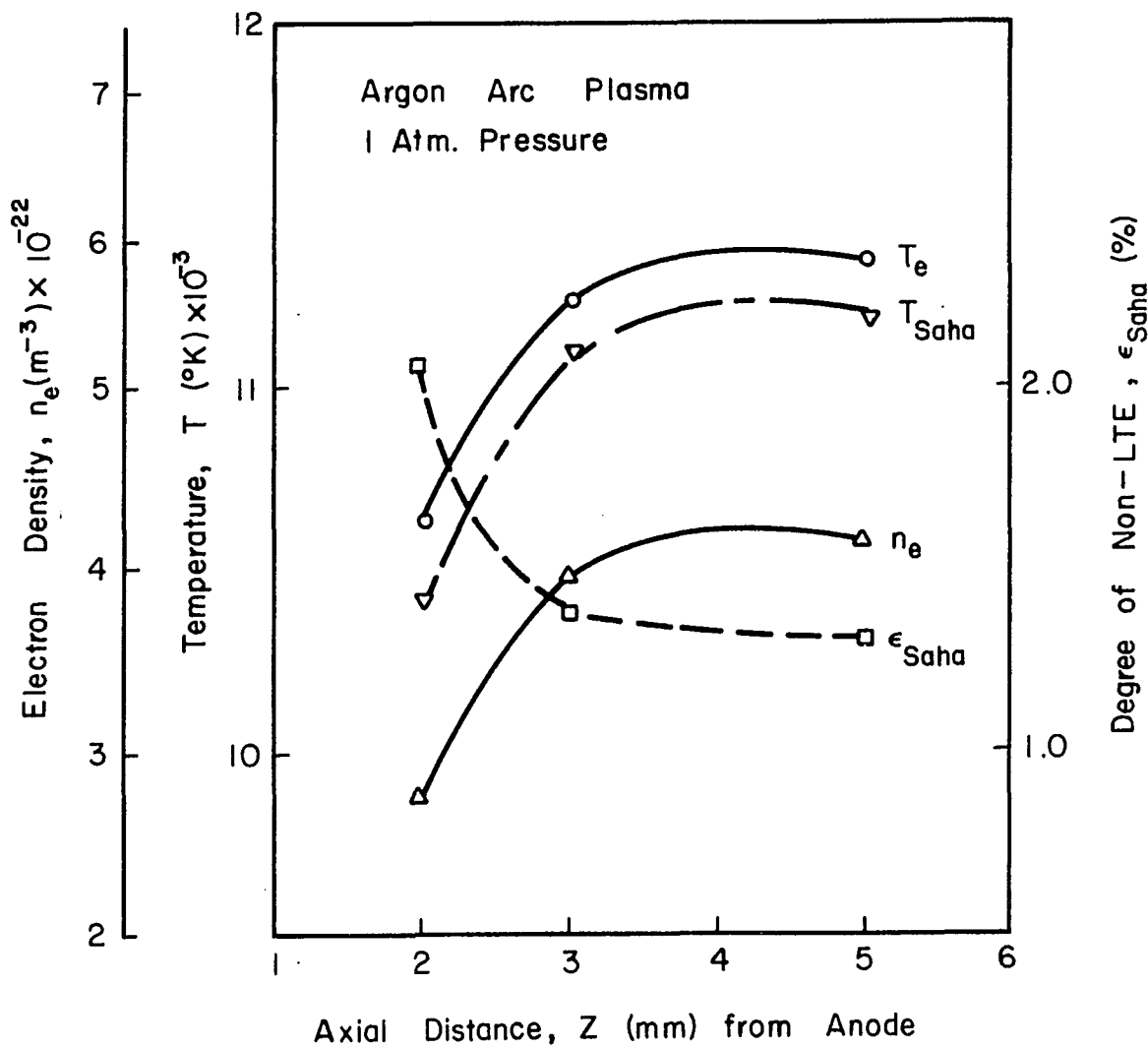


Fig (V A 1) Plasma Parameter Distribution

Table (VA1). Plasma Parameters at the Axis of 15 Amp Argon Arc. (Electrode Spacing, 6 mm)

Axial Position, z(mm)	5	3	2
<u>At 100 Torr Pressure</u>			
T_e ($^{\circ}$ K)	11,350	11,250	10,620
<u>At 100 Torr Pressure</u>			
n_e (m^{-3})	2.27×10^{21}	2.06×10^{21}	8.00×10^{20}
T_{Saha} ($^{\circ}$ K)	8,120	8,010	7,540
ΔT_{Saha} ($^{\circ}$ K)	3,230	3,240	3,080
ϵ_{Saha} (%)	28.5	28.8	29.0
<u>At 1 Atm Pressure</u>			
n_e (m^{-3})	4.14×10^{22}	3.96×10^{22}	2.75×10^{22}
α_s	1.07	1.05	0.90
T_{Saha} ($^{\circ}$ K)	11,200	11,100	10,400
ΔT_{Saha} ($^{\circ}$ K)	150	150	220
ϵ_{Saha} (%)	1.32	1.37	2.07

Note: T_e and n_e are data obtained by Thomson scattering,
 T_{Saha} is the Saha equilibrium temperature to produce n_e ,
 $\Delta T_{Saha} = T_e - T_{Saha}$, $\epsilon_{Saha} = \Delta T_{Saha}/T_e$, and T_e at 100 Torr pressure is assumed to be common also at 1 atm pressure.

Here l_{ei} can be calculated from Eq. (IIA19) as a function of T_e :

$$l_{ei} = 9.35 \times 10^9 T_e^2 (\text{°K}) / n_e \ln \Lambda, \text{ (for } z = 1\text{)} \quad (\text{VA2})$$

where Λ is given by Eq. (IIA14). According to Finkelnburg and Segal³²⁾, the arc electric field strength is about 10^3 V/m at the positive column in atmospheric pressure and almost independent of the arc current. Thus $E_z = 1 \times 10^3$ V/m is used for the calculation of Eq. (VA1). Then T_i can be calculated from Eq. (VA1) of the form:

$$T_i = T_e - \frac{1.12 \times 10^{12} E_z^2}{T_e} (l_{ei})^2 \cdot [\text{°K}] \quad (\text{VA3})$$

Table (VA2) shows the calculated values of T_i corresponding to the measured electron temperature T_e . Using the obtained T_i and T_e , one can have another degree of non-LTE, ϵ_{ne} as shown in Table (VA2):

Table (VA2). Degree of Non-LTE, ϵ_{NE} of 15 Amp Argon Arc at Atmospheric Pressure.

Axial Position z (mm)	5	3	2
T_e (°K)	11,350	11,250	10,620
l_{ei} (m)	3.75×10^{-6}	4.75×10^{-6}	5.25×10^{-6}
T_i (°K)	9,870	9,000	7,720
$\Delta T_i = (T_e - T_i)$	1,480	2,250	2,900
ϵ_{NE} (%) = $\Delta T_i / T_e$	13.0	20.0	27.3

From the above table one can see a similar spatial tendency of ϵ_{NE} as ϵ_{Saha} . If one takes into account much larger electric field distribution near the electrode, the magnitude of ϵ_{NE} becomes larger (or T_i becomes smaller) than the values listed in Table (VA2).

The calculated value of T_i is close to the equilibrium temperature predicted by the spectroscopic experiment shown in Fig. (IIA17), while the electron temperature is higher than the equilibrium temperature by average 20% as seen from Table (VA2). This magnitude of ϵ_{NE} is further predictable from the theory by Kruger⁵¹⁾ and from a recent experiment by Churchland et al.⁷³⁾. The latter observed very much higher electron temperature than the spectroscopically predicted temperature by a factor of 2.5 (= 250%) near the cathode and by about 50% at the positive column of a high current carbon arc. If the Saha equilibrium (or complete LTE up to the ground atoms) was assured for the analysis of those data (obtained by the absolute intensity measurement), this situation can be explained. So far obtained results of LTE validity for a present low current argon arc plasma are quite consistent from the predictions made in Chapters II and III. The degree of non-LTE at 15 Amps is higher than that of 200 Amp case³³⁾ by about 20 times (see Eq. IIA99).

B. ENERGY TRANSPORT ACROSS THE ARC PLASMA-ANODE INTERFACE

Here the energies transferred to the anode are calculated for the present arc using the theory developed in Section IIIB and the total energy is compared with the experimental value. First the conductive heat transfer rate given in Eq. (IIIB113) is calculated for an atmospheric 15 Amp argon arc using the following values: $j_e(0) = 2.9 \times 10^6$ Amps/m² (from Fig. IIIB4), which has been found to be very consistent with the photographic observation of the present arc at the diameter $R = 2.5$ mm and current $I = 15$ Amps; $j(\epsilon) \approx j_e(0)$; $U_A = 9.5$ Volt (from Fig. VA2); and $U_o(0) = U_i$ [Average ionization potential given by Eq. (IIIB2)] = $2.84 \times 10^{-4} T_e(\epsilon)$. Then Eq. (IIB113) becomes

$$q_{p \rightarrow A}^{\text{cond}}(0) = 2.9 \times 10^6 \{ 2.84 \times 10^{-4} T_e(\epsilon) + 9.5 \} + 0.9 \frac{k_T}{\delta_t} \{ T_i(\delta_t) - T_i(0) \}, \quad (\text{VA4})$$

where δ_t is the experimentally observed thermal boundary layer thickness. As can be seen from Fig. (IIB10-a), $T_e(\epsilon) \approx T_i(\epsilon) \approx T_i(0)$. The last approximation is justified since ϵ is very small compared to δ_t . The experimental values of $T_i(z)$ and $T_i(0)$ are given by Table (VA1) and Fig. (IVB31), respectively, which are plotted in Fig. (VA3). From Fig. (VA3), one sees that $T_i(\delta_t) = 9,800^\circ\text{K}$ (at $\delta_t = 5 \times 10^{-3}$ m) and $T_i(0) = 1,023^\circ\text{K}$. Thus from Fig. (IIA7), $k_T = 0.70 \text{ W/m}^\circ\text{K}$ at $T_i =$

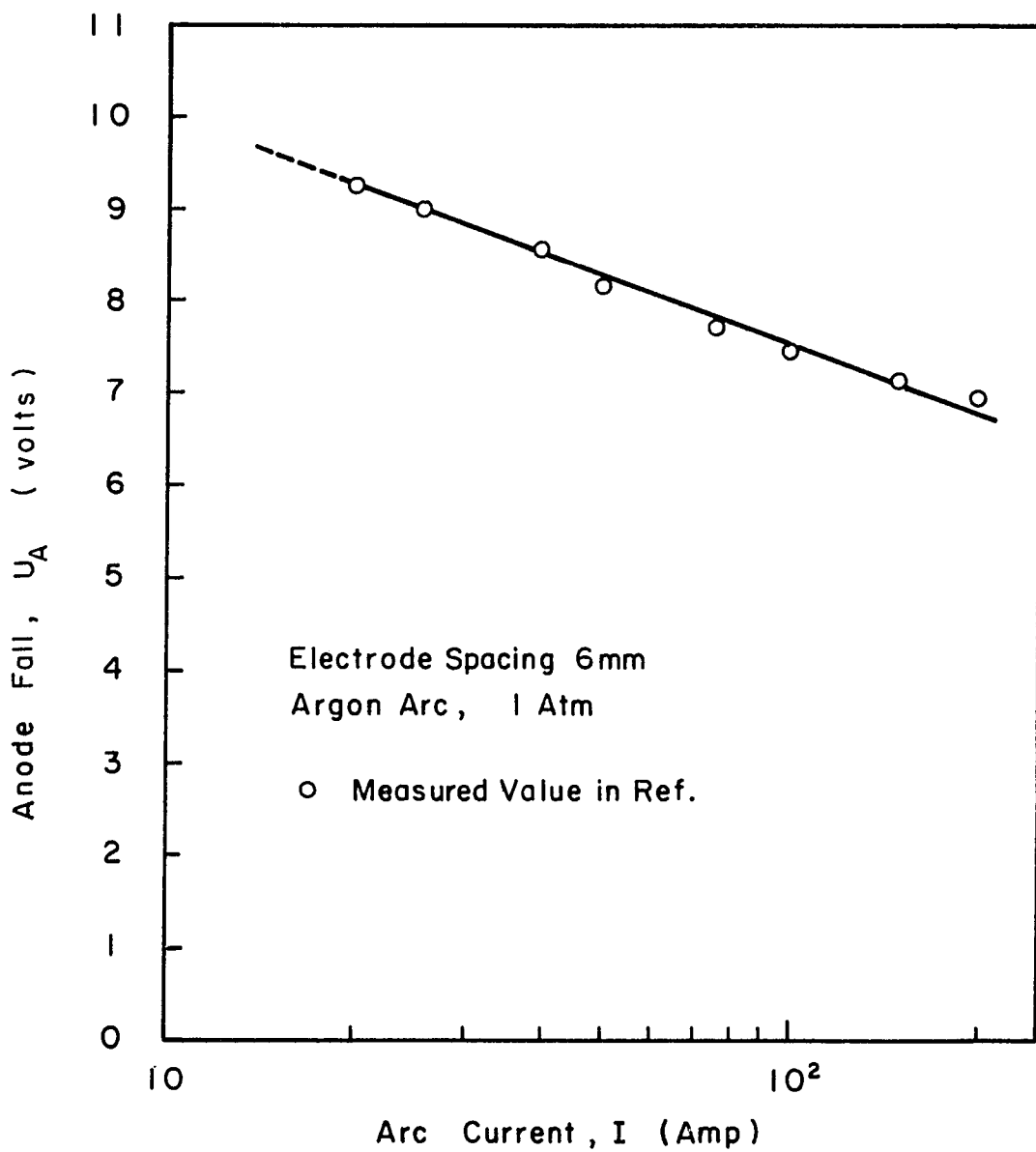


Fig. (V A 2)

Anode Fall Potential

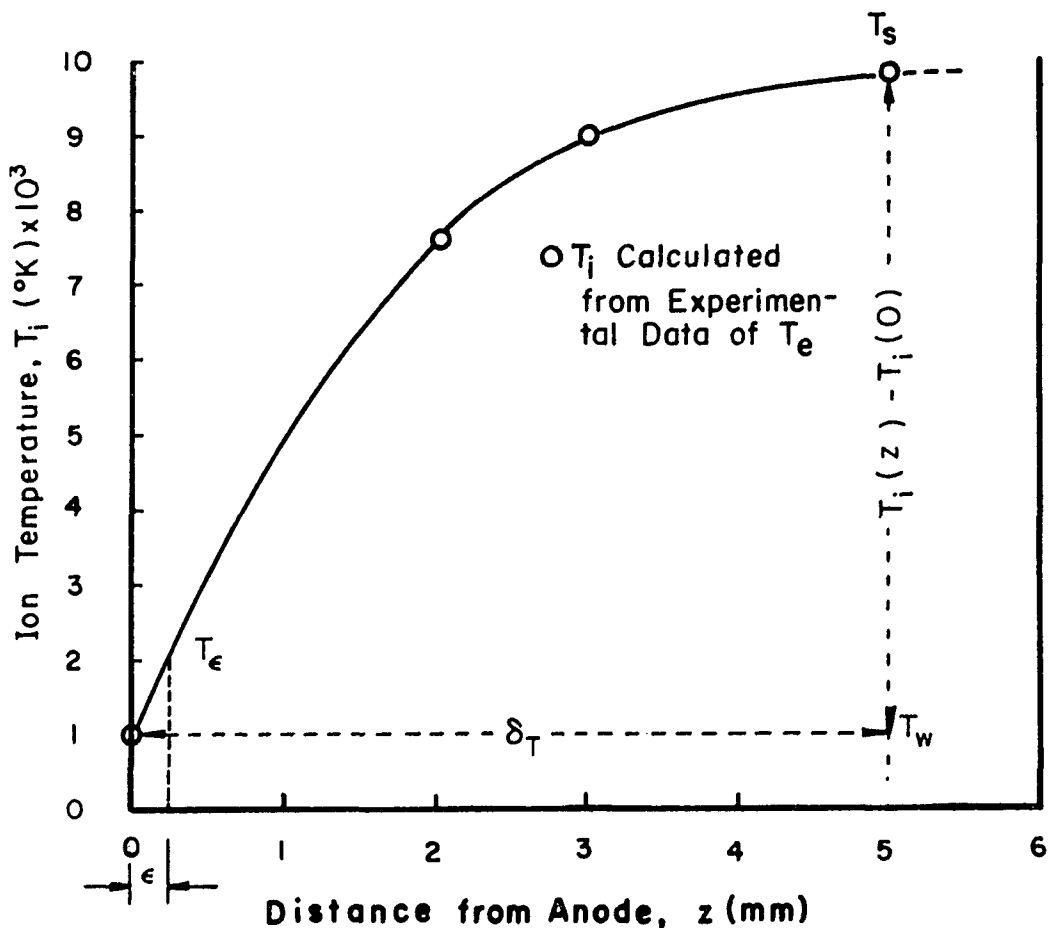


Fig. (VA 3) Static (Ion) Temperature Distribution

$9,800^{\circ}\text{K}$. These values are substituted into Eq. (VA4), which yields

$$q_{p \rightarrow A}^{\text{cond}}(0) = 2.85 \times 10^7 + 1.11 \times 10^5 \text{ [Watts/m}^2\text{]} \quad (\text{VA5})$$

The first term of Eq. (VA5) is the thermal energy carried by the electrons forming steady current of the arc while the second term is the thermal energy carried by the ions and atoms or the conductive heat transfer of static temperature in usual meaning. In other words, the first term can be regarded as the electric field correction for the second term. The second term is, however, only 1% of the first term and the absolute value is about 50 times smaller than that of the high current arc investigated by Schoeck¹⁰⁾. The larger δ_t observed due to non-existence of the free-stream temperature, which agrees with the prediction made for low current arcs in Section II A. Thus $T_i(\epsilon) \simeq T_i(0)$ in present case rather than $T_i(\epsilon) \simeq T_i(\delta_t)$, free-stream or maximum temperature. Next the heat due to the electrons accelerated by the thermionic work function of the electrode material is calculated for a thoriated tungsten anode using Eq. (IIB116):

$$\begin{aligned} q_{p \rightarrow A}^{\text{cond}}(0) &= j_e(0) \emptyset \\ &= (2.9 \times 10^6) \times 4.4 \\ &= 1.27 \times 10^7 \text{ [Watts/m}^2\text{]} \end{aligned} \quad (\text{VA6})$$

As is investigated in Section IIA (or see Eq. IIB85), the radiative heat transfer onto the anode surface is given by about 1% of the total conductive heat transfer, namely of Eq. (VA5) plus Eq. (VA6):

$$\begin{aligned} q_{p \rightarrow A}^{\text{rad}} &= 10^{-2} (2.86 + 1.27) \times 10^7 \\ &= 4.13 \times 10^5 \text{ [Watts/m}^2\text{].} \end{aligned} \quad (\text{VA7})$$

The reflected heat from the anode surface to the plasma is given by Eq. (IIB120). Of those, plasma heating due to the ablation is negligible since the present surface temperature (1023°K) is well below the melting point (3380°C for W, 1700°C for 100% Th). Power density of the reradiation is given by Eq. (IIB121). Using the measured wall temperature, $T_i(0) = T_w = 1023^{\circ}\text{K}$,

$$\begin{aligned} q_{A \rightarrow p}^{\text{rerad}} &= 7.1 \times 10^{-9} T_w^4 (\text{°K}) \\ &= 7.1 \times 10^3 \text{ [Watts/m}^2\text{]} \end{aligned} \quad (\text{VA8})$$

This is only 0.02% of the heat transferred to the anode from the plasma ($p \rightarrow A$). Thus the net heat transfer to the anode is approximately equal to the sum of Eqs. (VA5) through (VA7):

$$q_{p \rightarrow A} = 4.18 \times 10^7 \text{ [Watts/m}^2\text{]} \quad (\text{VA9})$$

Since the present arc area is $4.85 \times 10^{-6} \text{ m}^2$, the absolute thermal energy transferred per second to the anode surface is given by

$$P_{p \rightarrow A}^p = 2.03 \times 10^2 \text{ [Watts]} \quad (\text{VA10})$$

where the superscript p indicates that the total transport power has been obtained by the calculation in the plasma site.

On the other hand, the thermal energy carried away by coolant through the tungsten electrode can be calculated independently in the anode site from the anode temperature measurement shown in Fig. (IVB31). The curve of Fig. (IVB31) is expressed by

$$T(^{\circ}\text{K}) = 1.023 \times 10^3 \exp (-24.8 \chi), \quad (\text{VA11})$$

where χ is the distance measured from the anode surface toward the coolant in [m]. Then the conduction heat is calculated as

$$q(0) = -k_T \frac{\delta T}{\delta \chi} \Big|_{\chi=0} = 3.10 \times 10^6, \text{ [Watts/m}^2\text{]} \quad (\text{VA12})$$

where $k_T = 1.22 \times 10^2 \text{ [W/m } ^{\circ}\text{K}]$ was used for the heat conductivity of tungsten metal at $1,023^{\circ}\text{K}$. The effective area of the anode surface was 8 mm diameter during the experiment [the anode geometry is shown in Fig. (IVB31)]. Therefore the total energy per second which is calculated independently in the anode site (A) is

$$P_{p \rightarrow A}^A = 1.56 \times 10^2 \text{ [Watts].} \quad (\text{VA13})$$

This result is relatively good agreement (77%) compared with the value of Eq. (VA10) obtained in the plasma site (p). Much more precise measurement of the anode temperature distribution (for example two-dimensional temperature distribution) would have given better agreement. The convection would not heat the anode since the normal component of the hydrodynamic flow is zero at the anode surface as mentioned in Section IIB.

Since the maximum static temperature (9800°K) of the present arc is very close to 10^{40}K , the numerical results of examples exercised as $T \approx 10^{40}\text{K}$ in Section IIB can be used directly. The total input power is 520 Watts. The power stored at the anode boundary is (the total input power minus the power stored in the positive column)/2 if the equal energy partition is assumed between the anode and cathode boundaries. Thus the boundary power is 220 Watts from Fig. (IIB5) when no electric field correction is made and it is 206.4 Watts from Fig. (IIB7) when field correction is made. Then the total power transferred from plasma to the anode, 203 Watts given in Eq. (VA10) is 92.5% and 98.3% of the boundary powers without and with field correction, respectively. Since 100% boundary power is considered to be transported locally to the anode surface, the boundary power with electric field correction is more realistic.

Summing up the present results in terms of the energy partition, about 10% of the input power is stored in the positive column and about 45% is stagnated at the electrode boundary. And 98% of the boundary power is transferred locally onto the anode surface. The predominant transfer mechanism is due to the electron current (or electric field), namely the jU mode of Eq. (VA5) corresponds 68% and $j\phi$ mode of Eq. (VA6) corresponds 30% of the total heat transfer mechanism across the plasma-anode interface. The other modes due to the static temperature gradient and radiation are both about 1% contribution of the total as given in Eqs. (VA5) and (VA7), respectively.

C. THOMSON SCATTERING AS A PROBE FOR THE PLASMA-SOLID INTERFACE DIAGNOSTICS

Obviously Thomson scattering is the only one standard technique by which one can measure the electron temperature and density without imposing the LTE assumption for the plasma. For the energy transport of the arc, the electron flow plays a predominant role for the energy transfer as seen in the last Section VA and as seen in Section IIB the temperature can be calculated by the corresponding potential if the ionization potential is well defined. However if the LTE is not assumed for the plasma, direct measurement of the electron temperature is always required, especially at the plasma-solid interface. Thomson scattering is also the only one technique whose spatial resolution is in the order of wavelength of the probing light ($\sim 1\mu\text{m}$).

The electron temperature must be very high in the sheath due to the coupling with high electric field. The sheath is order of one ion-MFP length ($\sim 2\mu$ for 10^{40}K plasma) and the extended region is about 50 times ($\sim 100\mu$) the MFP length. Present experimental result (Fig. IVB27) shows that in order to measure z , the position from the anode surface, without being disturbed by the wall scattering, one needs about $z/2$ diameter spot size. This means that about 50μ diameter spot size is necessary to measure the extended region. To make 50μ diameter spot size is not difficult at all if it was in the space away from the anode surface. As mentioned in Section IVB, however, there exist practical difficulties when it is acutally applied on the plasma-anode interface

because of the limited S/N ratio and because of the geometrically limited spot size by the finite anode surface. In the practical experiment the minimum distance measurable was 500 μm from the anode surface, when the spot size was 200 μm and the anode surface area was 8 mm. Thus the observed region does not include the extended region of sheath.

Nevertheless, the diagnostics by Thomson scattering overwhelms the other diagnostic techniques. The electron temperature and density have been measured separately from the ion temperature and density. The static temperature was calculated from the measured electron density and the temperature gradient in the thermal boundary layer have been determined, which made possible the calculation of heat transfer flux by the conventional conduction. If the present plasma had a large S/N ratio and was relatively free from the sputtering, the measurement of the electron temperature distribution in the extended region of sheath would have been possible. Thus the evaluation from the Thomson scattering technique and the applicable minimum distance from the solid surface depends on the nature of the plasma to be used.

It should be emphasized finally that the diagnostics at the bulk of plasma are also very important for the study of the energy transport at the interface. Because, the diffusion characteristics are determined at the core not at the local periphery or plasma edge, as seen in Section

IIB. Further the energy stored at the interface can be calculated if the energy partition to the positive column is measured. Thus the measurement of plasma parameters and transport coefficients at the positive column is always required and sometimes good enough. In this case Thomson scattering becomes far more powerful. Especially the potentiality for the measurement of transport coefficients from the scattered spectra discussed in Section (VA) should be highly valued because no other method can measure the coefficients so locally and as tensor quantities. In addition, the capability of Thomson scattering for measuring the ion temperature is useful for the investigation of non-LTE and for the calculation of two-temperature model which aufheben the conventional transport study a step higher.

CHAPTER VI

CONCLUSION

A. SUMMARY

The important results and contributions of the present research are summarized here:

- (a) A comprehensive review of basic parameters of an argon arc has been carried out, providing more complete and accurate data than presently available in the literature. These parameters are necessary for accurate evaluation of the energy transport across the plasma-solid interface and in the bulk plasma.
- (b) Solution of the general energy transport equation of the arc plasma including all important source and dissipation terms in both the radial and axial direction is completed based on a one-temperature plasma model. A general thermal conductivity is introduced to take into account the temperature, density and pressure gradients in addition to the effect of the external electric field. The thermoelectric corrections on the thermal conductivities due to ∇T , ∇n , and ∇p

have been evaluated and found to be significant. A critical radius is found where the radial heat transfer flux has a maximum and from where non-LTE due to the ambipolar diffusion starts.

- (c) Correct boundary layer thicknesses and profiles have been obtained for the thermal boundary near the arc electrode and an exact formula has been obtained for the heat transfer flux across the boundary layer using a two-temperature plasma model to take into account the high electric fields and plasma inhomogeneities.
- (d) The degree of non-LTE both in the bulk plasma and in the boundary layer of an arc plasma under different experimental conditions due to the effects of high electric fields and plasma inhomogeneity has been investigated and discussed with reference to a plasma in Saha equilibrium.
- (e) Extensive computational work has been performed in collisional effects on the spectra of Thomson-scattered radiation from which transport coefficients such as coefficients of viscosity and thermal conductivity may be measured. Although the effects are too small to be measured on the present arc plasma, they are observable in plasmas with small Coulomb cutoff parameters. High current spark channels and laser-induced spark plasmas are examples.

- (f) Experimental measurements of electron temperature and density of an argon arc plasma at atmospheric and reduced pressures at different spatial points along the axis have been made and the degree of non-LTE has been studied in relation to the analysis of Part d above.
- (g) The individual rate of energy transport and the rate of heat transfer from the arc plasma to the anode surface have been calculated by using measured values and are in good agreement with the predicted values of the axial heat transfer rate calculated in Part b and Part c above. It has been found that the dominant mode of the thermal energy transport in the arc plasma is due to the electron flow. Further the correction for the electric field effect has been found to be important.

B. FUTURE WORK

One of the most needed future work for the study of plasma-solid interface energy transport will be the construction of a well-behaved plasma relatively free from sputtering. A magnetically and/or wall stabilized high current arc immersed in the argon (or helium) atmosphere is the candidate. Without this, laser light probe cannot diagnose the real interface (sheath) region because of the large scattering background due to the sputtered solid surface. If the sputtering can not be suppressed to a tolerable level, the laser holographic technique rather than the scattering technique will be useful for the measurement of the plasma density gradient in the interface.

Since the present results show that the dominant energy transport mechanism of the arc is due to the electron flow, precise measurements of the electric field by using a potential probe and of the current density in the interface are suggested to obtain much more self-consistent absolute values for various types of arcs. For the confirmation of the internal electric field correction, measurements of the radial temperature, density and pressure gradients are important and possible if the well-behaved high current arc is used. (In the low current arc as presently used, the background at periphery is too high to apply the Thomson scattering.)

For the study of non-LTE, a direct measurement of the ion temperature distribution is recommended. Thomson scattering in the

collective scattering regime can be used for that purpose although the present optics and spectroscopic system are not adequate devices.

When the ion temperature as well as the electron temperature are measured, it may be of interest to compare the result with a two-temperature plasma model which is possible to calculate using recently developed theories and computers.

Although it is not covered yet in this thesis, the investigation of the effects of magnetic field on the thermal conductivity tensor and of the nonlinear effects such as the turbulence and instabilities that may enhance the effective thermal conductivity especially at the plasma-solid interface are strongly recommended as future work.

This kind of energy transport study is highly desired, especially in the contemporary field of nuclear fusion research.

|

|

REFERENCES

1. Finkelnburg, W. and Maecker, H: Elektrische Bogen and Thermische Plasmen, in Handbuch der Physik, ed. S. Fliege, Berlin: Springer-Verlag (1956).
2. Spitzer, L., Jr.: Physics of Fully Ionized Gases, 2nd ed., Interscience Publisher (1962).
3. Braginskii, S. I. "Transport phenomena in a completely ionized two-temperature plasma," Soviet Phys. JETP 6, 358 (1958).
4. Kolesnikov, V. N.: Tr. Fiz Inst. Akad. Nauk USSR 30, 66 (1964). Or see, Holtgreven, W. L.: Plasma Diagnostics, North-Holland Publishing Company (1968).
5. Giannaris, R. J. and Incropera, F. P.: "Nonequilibrium effects in an atmospheric argon arc plasma," JQSRT 11, 291 (1971).
6. Kruger, C. H. and Mitcher, M.: "Kinetic theory of two-temperature plasmas," Phys. Fluids 10, 1953 (1967). Also see, Kruger, C. H.: "Nonequilibrium in confined-arc plasmas," Phys. Fluids 13, 1737 (1970).
7. Thomson, J. J.: Conduction of Electricity through Gases, 2nd ed. Cambridge University Press, New York, London (1935).
8. Compton, K. T.: "Theory of the electric arc," Phys. Rev. 21, 207 (1923).
9. Tonks, L. and Langmuir, L.: "A general theory of the plasma of an arc," Phys. Rev. 34, 876 (1929).
10. Schoeck, P. A.: "An investigation of the energy transfer to the anode of high intensity arcs," Ph. D. Thesis, University of Minnesota (1961).
11. Bird, R. B., W. E. Stewart and E. N. Lightfoot: Transport Phenomena, John Wiley and Sons, Inc. (1960).

12. Gebhart, B.: Heat Transfer, 2nd ed., McGraw-Hill, Inc. (1961).
13. Spitzer, L., Jr. and Harm: "Transport phenomena in a completely ionized gas," Phys. Rev. 89, 977 (1953).
14. Brown, S. C.: Introduction to electrical discharge in Gases, John Wiley and Sons, Inc. (1966).
15. Busz-Peukert, G. and Finkelnburg, W.: "Zum Anodenmechanismus des Thermischen Argonbogens," Z. Physik, 144, 244. (1954).
16. Block, J. J. and Finkelnburg, W.: "Uber die axiale Ausdehnung des Anondengallgebiets beim Kohlelichtbogen," Z. Naturforsch 8a, 758 (1953).
17. Emmons, H. W.: Recent developments in plasma heat transfer, 1965, page 420.
18. Cambel, A. B.: Plasma physics and magnetofluid mechanics, McGraw-Hill, New York, 1963.
19. Schreiber, P. W. and Hunter, A. M., II: "Argon and nitrogen plasma viscosity measurements," Phys. Fluids 14, 2696, (1971).
20. Penski, K.: "Variables of state and transport properties of an argon plasma," Chem. -Ing -Tech. 34, 84 (1962).
21. Maecker, H.: "Plasmastromungen in Lichbogen infolge eigenmagnetischer Kompression," Z. Physik 141, 198 (1955).
22. Wienecke, R.: "Uber as Auftreten von Dampfstrahlen in Kohlelichtbogen hoher Stromstraiken; I," Z. Physik 151, (1958).
23. Emmons, H. W.: "Arc measurement of high-temperature gas transport properties," Phys. Fluids 10, 1125 (1967).
24. Schreiber and Hunger, A. M., II: "Argon and nitrogen plasma viscosity measurement," Phys. Fluids 14, 2696 (1971).
25. Engel, A. von: Ionized Gases, 2nd ed. Oxford University Press (1965).
26. Caruso, A. and Cavalier, A.: "The structure of the collisionless plasma-sheath transition," Nuovo Cimento XXVI, 1389.

27. DuBois, D. F. and Gilinsky, V.: "Propagation of electromagnetic waves in plasma," *Phys. Rev.* 133, A1317 (1964); Also see Breginiskii, S. I.: *Soviet Phys. JETP* 6, 358.
28. Self, S. A.: "Exact solution of the collisionless plasma-sheath equation," *Phys. Fluids* 6, 1762 (1963).
29. Goldan, P. D. and Yadlowsky, E. J.: "Electron beam measurement of ion acoustic wave propagation," *Phys. Fluids* 14, 1990 (1971); also see *Ibid.* 13, 433 (1970); 13, 1055 (1970).
30. Hoyaux, M. F.: Arc physics, Springer Verlag, New York, Inc. (1968), page 157.
31. Kerrebrock, J. L.: Engineering aspects of magnetohydrodynamics, Columbia University Press, New York (1962).
32. Finkelnburg, W. and Segal, S. M.: "High temperature plasma properties from high current arc stream measurements," *Phys. Rev.* 80, 258 (1950).
33. Olsen, H. N.: "Thermal and electrical properties of argon arc plasma," *Phys. Fluids* 2, 614 (1959).
34. Dawson, J. M.: AEC research and development, Report MATT 428 (1965).
35. Eckert, E. R. G. and Pfender, E.: "Plasma heat transfer," Advances in plasma heat transfer, 4, edited by J. P. Hartnett and T. F. Iriine, Jr., Academic Press, New York (1967).
36. Thomson, W. B.: AERE, TM 73, Harwell, England (1954). The graph is listed on page 180 of Theory of ion flow dynamics (Dover, 1971) by Samaras, D. G.
37. Glasstone, S. and Loveuberg, R.H.: Controlled thermonuclear fusion, Van Nostrand Company, Inc., Princeton, (1960).
38. Hwnag, C. C.: "Spectroscopic intensity measurement of atmospheric-pressure helium arcs," *JQSRT* 12, 738 (1972).
39. Schmitz, G. Z. and Patt, H. J. Sine methode zur bestimmung von Materialfunktionen von Gasen aus den Temperaturverteilungen zylindersymmetrischer Lichtbögen," *Z. Physik* 167, 163 (1962).

40. Schmitz, G. Z.: "Zur theorie der wandstabilisierten Bogensanle," *Z. Naturforschung* 5A, 571 (1970).
41. Schmitz, G. Z. and Uhlenbusch, J.: "Zur mathematischen Beschreibung zylinder symmetrischer Lichtbogen," *Z. Physik* 12, 231 (1960).
42. Eckert, E. R. G.: Heat and mass transfer, McGraw-Hill (1959).
43. Frank, K.: Principle of heat transfer, 2nd ed., International Textbook Company (1965).
44. Weast, R. C.: Handbook of chemistry and physics, 50th ed. The Chemical Rubber Co. (1969).
45. Rieder, W.: *A. Physik* 146, 629 (1956).
46. Mason, R. C.: "Accomodation coefficient of mercury ions on a mercury surface," *Phys. Rev.* 47, 241 (1935).
47. Busz, G. and Finklenburg, W.: "Thermische Lichtbogen hoher Temperatur and Niedriger Brennapping," *Z. Physik*, 138, 212 (1954).
48. Bott, J. E.: "A spectroscopic investigation of a helium plasma," *JQSRT* 6, 807 (1966).
49. Hwang, C. C.: "Spectroscopic intensity measurement of atmospheric-pressure helium arcs," *JQSRT* 12, 783 (1972).
50. Griem, H. R.: Plasma spectroscopy, McGraw-Hill (1964).
51. Kruger, C. H.: "Nonequilibrium in confined-arc plasmas," *Phys. Fluids* 13, 1737 (1970).
52. Emmons, H. W.: "Arc measurement of high-temperature gas transport properties," *Phys. Fluids* 10, 1125 (1967).
53. Hwang, C. C. and Emmons, H. W.: "Investigation of helium arc at 10 atm pressure," *Phys. Fluids* 13, 2027 (1970).
54. Showdhury, S. S.: "The Composition of an argon plasma in Saha equilibrium, *JQSRT* 9, 129 (1969).

55. Gautam, M. S. and Anandarm, M. N.: "Computation of the composition of a highly ionized plasma in thermodynamic equilibrium,: Canada. J. Physics 49, 492 (1971).
56. Moore, C. W.: Atomic energy levels, Circular of NBS 497 (1949).
57. Thomson, J. J.: Conduction of electricity through gases, 2nd ed. p. 325, Cambridge University Press, New York, London (1935).
58. Born, M. and Wolf, E.: Principle of optics, 3rd ed. Pergamon Press (1965).
59. Niimura, M., Chan P. W., and Churchill, R. J.: "Coulomb collision corrected ion-acoustic line profiles,: JQSRT 12, 1319.
60. DuBois, D. F. and Gilinsky, V.: "Incoherent scattering of radiation by plasma I. Quantum mechanical calculation of scattering cross section," Phys. Rev. 133, A1308 (1964).
61. Salpeter, E. E.: "Electron density fluctuations in a plasma" Phys. Rev. 120, 1528 (1960).
62. Ichikawa, Y. H.: "On the kinetic equation for a high temperature plasma," Prog. Theoret. Phys. (Kyoto) 24, 1083 (1960).
63. Niimura, M., Chan, P. W. and Churchill, R. J.: "Effects of Coulomb collisions on the dispersion relation of longitudinal plasma oscillations," IEEE Transactions, Plasma Science 1, 46 (1973).
64. Niimura, M., Chan, P. W. and Churchill, R. J.: "Coulomb collision corrected electron plasma line profiles," J. Phys. Soc. Japan 34, 261 (1973).
65. Niimura, M., Chan, P. W., and Churchill, R. J.: "Numerical computations of Landau and collisional damping of plasma lines," JQSRT 12, 989 (1972).
66. Dougherty, J. P. and Farley, D. F.: "A theory of incoherent scattering of radio waves by a plasma," Proc. Roy Soc. (London) A259, 79 (1960).

67. Rostoker, M. N. and Rosenbluth, N.: "Scattering of electro-magnetic waves by a nonequilibrium plasma," *Phys. Fluids* 5, 776 (1962).
68. Kivelson, M. G. and DuBois, D. F., "Plasma conductivity at low frequencies and wave numbers," *Phys. Fluids* 7, 1578 (1964).
69. Malyshev, G. M., "Plasma diagnostics by light scattering on electrons," *Soviet Phys. -Tech. Phys.* 10, 1633 (1966).
70. Rudder, R. R., Rayleigh scattering of ruby laser light in neutral gases, the University of Michigan Ph. D. Thesis (1967), page 97.
71. Chan, P. W.: Scattering of laser light by laboratory plasmas, The University of British Columbia, Ph. D. Thesis (1966).
72. Somerville, J. M.: *The electric arc*, John Wiley and Sons, Inc. (1958).
73. Churchland, M. T., R. A. Nodwell and B. Ahlborn: "Electron temperature in a high current carbon arc," *Phys. Letters* 40A, 233 (1972).
74. Busz-Peuckert, G. and Finkelnburg, W.: "Zum Anodenmechanismus des Thermischen Argonbogens," *Z. Physik* 144, 244 (1956).

APPENDIX A

COMPUTER PROGRAM OF SAHA-EGGERT EQUATION

```

PROGRAM SAMAEQ
 1(INPUT,OUTPUT,TAPE5=INPUT,TAPE6=OUTPUT,FILNPLI
 000003      DIMENSION E1(10),OSC(10),OLG(10),NNMAX(10),DE1(10),UF(10),US(10),
 1UZ(10),DN(10),DIFF(10),PNMAX(10),NN(10,10)
 000003      DIMENSION AJ1(309),EL1(309),G1(309),EV1(309),
 1          AJ2(119),EL2(119),G2(119),EV2(119),
 1          AJ3(101),EL3(101),G3(101),EV3(101),
 1          AJ4( 37),EL4( 37),G4( 37),EV4( 37)
 000003      READ(5,200) (E1(I),OSC(I),OLG(I),NNMAX(I),I=1,4)
 000023      200 FORMAT(F7.3,F8.1,F8.1,4I1)
 000023      READ(5,201) (AJ1(N),EL1(N),N=1,309)
 000057      READ(5,201) (AJ2(N),EL2(N),N=1,119)
 000053      READ(5,201) (AJ3(N),EL3(N),N=1,101)
 000067      READ(5,201) (AJ4(N),EL4(N),N=1,37)
 000103      201 FORMAT(F5.1,F15.3)
 000103      WRITE(6,800)
 000107      800 FORMAT(1H1//20X, *THE COMPOSITION OF AN ARGON PLASMA IN SAMA EQUIL
 1BR|UM*5X,*DATA*//)
 000107      112X,*1*,5X,*E1()*,5X,*SC()*,5X,*LG()*,5X,*NNMAX()*
 000150      500 FORMAT(10X,13.5X,F7.3,5X,F8.1,5X,F8.1,5X,4I1)
 000150      WRITE(6,500)
 000154      801 FORMAT(1/12X,*1*,7X,*J()*,10X,*E()*,PCM+1)
 000154      WRITE(6,501) (N,AJ1(N),EL1(N),N=1,309)
 000151      WRITE(6,501) (N,AJ2(N),EL2(N),N=1,119)
 000166      WRITE(6,501) (N,AJ3(N),EL3(N),N=1,101)
 000203      WRITE(6,501) (N,AJ4(N),EL4(N),N=1,37)
 000220      501 FORMAT(10X,13.7X,F8.1,5X,F15.3)
 000220      WRITE(6,800)
 000224      800 FORMAT(1H1//5X,*RESULTS*//)
 000224      PI=3.1415927
 000226      EN=9.1091E-28
 000227      BK=1.38654E-16
 000231      HB=1.0545E-27
 000252      MW=6.6256E-27
 000234      E=4.80298E-10
 000255      EN=15.595
 C  FIXED VALUE
 000257      EN=1.0E16
 C  INITIAL GUESS,ZAV
 000240      ZAV=1.
 000242      DO 50 K=50,200,5
 000243      TEK=FLOAT(K)*100.
 000245      TEV=TEK/11605.7
 000247      50  ROD=SQRT(BK+TEK/(4.+PI)*(E**2)+EN*(1.+ZAV))
 000262      DO 1 I=1,4
 000263      DE1(I)=FLOAT(I)*E*500./ROD
 000267      DIFF(I)=E1(I)-DE1(I)
 000271      PNMAX(I)=SQRT((FLOAT(I)**2)+EN/DE1(I))
 1  CONTINUE
 000277      UF(1)=0.
 000301      UF(2)=0.
 000302      UF(3)=0.
 000303      UF(4)=0.
 000304      DO 5 N=1,309
 000305      G1(N)=2.*AJ1(N)+.
 000306      EV1(N)=EL1(N)+(1.2598E-4)
 000311

```

```

000313      UF(1)=G1(N1)/EXP(EV1(N1)/( TEV1)+UF(1)
000322      5    CONTINUE
000324      IF(EV1(309).LE.DIFF(1)) GO TO 6
000327      US(1)=0.
000330      GO TO 7
000330      6    US(1)=(2./3.)*(2.+0SG(1)+1.)*(2.+QLG(1)+1.)
000330      1.*PNMAX(1)+SORT(PNMAX(1))/EXP(DIFF(1)/( TEV1)
000331      7    UZ(1)=UF(1)+US(1)
000333      DO 8 N=1,119
000335      G2(N)=2.*AJ2(N1+1,
000336      EV2(N1)=EL2(N1)+(1.2598E-4)
000336      UF(2)=G2(N1)/EXP(EV2(N1)/( TEV1)+UF(2)
000337      8    CONTINUE
000337      IF(EV2(119).LE.DIFF(2)) GO TO 9
000338      US(2)=0.
000339      GO TO 10
000339      9    US(2)=(2./3.)*(2.+0SG(2)+1.)*(2.+QLG(2)+1.)
000339      1.*PNMAX(2)+SORT(PNMAX(2))/EXP(DIFF(2)/( TEV1)
000340      10   UZ(2)=UF(2)+US(2)
000342      DO 11 N=1,101
000344      G3(N)=2.*AJ3(N1+1,
000345      EV3(N1)=EL3(N1)+(1.2598E-4)
000345      UF(3)=G3(N1)/EXP(EV3(N1)/( TEV1)+UF(3)
000346      11   CONTINUE
000346      IF(EV3(101).LE.DIFF(3)) GO TO 12
000347      US(3)=0.
000348      GO TO 13
000348      12   US(3)=(2./3.)*(2.+0SG(3)+1.)*(2.+QLG(3)+1.)
000348      1.*PNMAX(3)+SORT(PNMAX(3))/EXP(DIFF(3)/( TEV1)
000349      13   UZ(3)=UF(3)+US(3)
000350      DO 14 N=1,37
000351      G4(N)=2.*AJ4(N1+1,
000352      EV4(N1)=EL4(N1)+(1.2598E-4)
000352      UF(4)=G4(N1)/EXP(EV4(N1)/( TEV1)+UF(4)
000353      14   CONTINUE
000353      IF(EV4(37).LE.DIFF(4)) GO TO 15
000354      US(4)=0.
000355      GO TO 16
000355      15   US(4)=(2./3.)*(2.+0SG(4)+1.)*(2.+QLG(4)+1.)
000355      1.*PNMAX(4)+SORT(PNMAX(4))/EXP(DIFF(4)/( TEV1)
000356      16   UZ(4)=UF(4)+US(4)
000357      UEC=2.+(EM+BK/(2.*P)+(MB+2))/((EM+BK/(2.*P)+(MB+2)))
000358      UE=UEC+TEK+SORT(TEK)
000359      DO 40 I=1,3
000360      RN(I+1,1)=(UE/EN)+(UZ(I+1)/UZ(I))/EXP(DIFF(I)/TEV1)
000361      40   CONTINUE
000362      DN(4)=(EM-RN(4,3)+RN(3,2))/(1.+2.*RN(3,2)+3.*RN(4,3)+RN(3,2))
000363      DN(3)=DN(4)/RN(4,3)
000364      DN(2)=DN(3)/RN(3,2)
000365      DN(1)=DN(2)/RN(2,1)
000366      DF=EN-(DN(2)+2.*DN(3)+5.*DN(4))
000367      DNT=DN(1)+DN(2)+DN(3)+DN(4)
000368      ZAVA=(DN(2)+4.*DN(3)+9.*DN(4))/EN
000369      TOL=1.E-10
000370      IF(ABS(ZAVA-ZAVL).LT. TOL) GO TO 51
000371      ZAV=ZAVA
000372      GO TO 50
000373      51   WRITE(6,502) TEK,EN,DN(1),DN(2),DN(3),DN(4),DNT,
```

```

1UZ(1),UZ(2),UZ(3),UZ(4),ZAVB,DF
000701 502 FORMAT(      5X, *T(K)=*,F7.1,3X,*EN=*,E10.3,3X,*A(1)=*,  

           1E10.3,3X,*A(11)=*,E10.3,3X,*A(111)=*,E10.3,3X,*A(IV)=*,E10.3,3X,  

           1*TOTAL=*,E10.3/  

           124X,*P(1)=*,E10.3,3X,*P(11)=*,E10.3,3X,*P(111)=*,E10.3,3X,*P(1V)=*  

           1,E10.3,3X,*ZAV=*,E10.3,3X,*DF=*,E10.3/  

           WRITE(6,802)
000701 502 FORMAT(/12X,*I=,6X,*DE1(1)=*, 9X,*DIFF(1)=*,9X,*PNMAX(1)=*)  

000705 503 WRITE(6,503) (I,DE1(I),DIFF(I),PNMAX(I),I=1,4)  

000724 503 FORMAT(10X,13.5X,E10.3,5X,E10.3,5X,E10.3)  

000724 503 WRITE(6,803)
000750 503 FORMAT(/12X,*I=,6X,*PF(1)=*,10X,*PS(1)=*)  

000750 504 WRITE(6,504) (I,UF(I),US(I),I=1,4)  

000745 504 FORMAT(10X,13.5X,E10.3,5X,E10.3)  

000745 50 CONTINUE  

000747 504 WRITE(6,506) UEC  

000755 506 FORMAT(/15X,*PEC=*,E10.3/  

000755 506 WRITE(6,804)
000761 506 FORMAT(/10X,*N=,6X,*J1(N)=,4X,*G1(N)=,12X,*E1(N) PCH=,6X,*E1(N) EV  

           1+)  

           506 WRITE(6,505) (N,AJ1(N),G1(N),EL1(N),EV1(N),N=1,300)  

001002 505 WRITE(6,805)
001006 505 FORMAT(/10X,*N=,6X,*J2(N)=,4X,*G2(N)=,12X,*E2(N) PCH=,6X,*E2(N) EV  

           1+)  

           505 WRITE(6,505) (N,AJ2(N),G2(N),EL2(N),EV2(N),N=1,110)  

001027 506 WRITE(6,806)
001033 506 FORMAT(/10X,*N=,6X,*J3(N)=,4X,*G3(N)=,12X,*E3(N) PCH=,6X,*E3(N) EV  

           1+)  

           506 WRITE(6,505) (N,AJ3(N),G3(N),EL3(N),EV3(N),N=1,101)  

001054 507 WRITE(6,807)
001060 507 FORMAT(/10X,*N=,6X,*J4(N)=,4X,*G4(N)=,12X,*E4(N) PCH=,6X,*E4(N) EV  

           1+)  

           507 WRITE(6,505) (N,AJ4(N),G4(N),EL4(N),EV4(N),N=1,37)  

001060 505 FORMAT(8X,13.6X,F4.2,4X,F5.2, 8X,F18.3,4X,E10.3/  

           505 END
001060

```